

**SENSORLESS AND EFFICIENCY OPTIMIZED INDUCTION MACHINE
CONTROL WITH ASSOCIATED CONVERTER PWM MODULATION
SCHEMES**

A Dissertation

Presented to

The Faculty of the Graduate School
Tennessee Technological University

By

Gan Dong

In Partial Fulfillment

Of the Requirements for the Degree

DOCTOR OF PHILOSOPHY

Engineering

December 2005

CERTIFICATE OF APPROVAL OF DISSERTATION

**SENSORLESS AND EFFICIENCY OPTIMIZED INDUCTION MACHINE
CONTROL WITH ASSOCIATED CONVERTER PWM MODULATION
SCHEMES**

By
Gan Dong

Graduate Advisory Committee:

Dr. Joseph O. Ojo, Chairperson

Date

Dr. Ghadir Radman

Date

Dr. Sastry Munukutla

Date

Dr. Brian M. O'Connor

Date

Dr. Mohamed A. Abdelrahman

Date

Approved for the Faculty:

Francis Otuonye
Associate Vice President for
Research and Graduate Studies

Date

ACKNOWLEDGEMENTS

I would like to take this opportunity to express my sincere appreciation to all the people who were directly or indirectly helpful in making this dissertation a success. First of all I would like to thank my advisor, Dr. Joseph O. Ojo, who is also the chairperson of my graduate committee, for his expert guidance and patience during the course of the research. I would also like to thank the other members of my committee, Dr. Ghadir Radman, Dr. Sastry Munukutla, Dr. Brian M. O'Connor, Dr. Mohamed A. Abdelrahman, and Dr. Joe N. Anderson for their effort in reviewing and evaluating my work.

I would also like to thank Zhiqiao Wu, Conard Murray, and L.V. Randolph for their invaluable help during the course of this project. I would like to express my special thanks to the US Office of Naval Research (ONR), the Department of Electrical and Computer Engineering and the Center for Energy Systems Research for the teaching and research assistantship provided during my graduate study.

I express my gratitude to my parents, my wife Dan, and my daughter Yuzhu for their moral support and encouragement during the course of my Ph.D. program.

TABLE OF CONTENTS

	Page
LIST OF FIGURES	ix
LIST OF TABLES	xxiv
CHAPTER 1	1
INTRODUCTION	1
1.1 Introduction.....	1
1.2 Literature Review.....	5
1.2.1 PWM Schemes in Three-Phase and Multi-Phase Voltage Source Inverters	5
1.2.2 Induction Motor Control.....	10
1.2.3 Efficiency Optimization.....	11
1.2.4 Sensorless Control of Induction Machines	13
1.2.5 Overmodulation Technique for VSI	17
1.3 Research Motivation	19
1.4 Scope of Work	22
CHAPTER 2	25
PWM SCHEMES IN THREE-PHASE AND MULTI-PHASE VOLTAGE SOURCE INVERTERS.....	25
2.1 Introduction.....	25
2.2 Carrier-Based PWM.....	26
2.3 Space Vector PWM.....	31
2.4 Generalized Discontinuous Modulation Scheme.....	40

	Page
2.5 Modulation Scheme for Multi-Phase Systems.....	47
2.5.1 Generalized Complex-Variable Q-D Reference Frame Transformation	49
2.5.2 Modulation Technique for Multi-Phase Converters	52
2.5.3 Modulation for Five-Phase Converters.....	54
2.5.4 Modulation for Six-Phase Converters.....	65
2.5.5 Experimental Results	74
2.5.6 Modulation Signals Calculation Using Turn-on Times for the Top Devices .	81
2.6 Conclusion	92
CHAPTER 3	93
INDUCTION MACHINE MODEL	93
3.1 Introduction.....	93
3.2 Operation Principle of a Three-phase Induction Motor.....	93
3.3 Three-phase Induction Motor Voltage Equations.....	96
3.4 Reference Frame Transformation	101
3.5 Three-phase Induction Motor Equivalent Circuit.....	104
3.5.1 Induction Machine Model Using Natural Variables.....	109
3.5.2 Induction Machine Model Using Flux Linkages	112
3.6 Parameters of Induction Machines.....	113
3.7 Conclusion	118
CHAPTER 4	119
VECTOR CONTROL OF INDUCTION MACHINE.....	119
4.1 Introduction.....	119

	Page
4.2 Fundamentals of Vector Control.....	120
4.3 Vector Control of Induction Machine.....	122
4.4 Derivation of Indirect Vector Control of Induction Machine.....	126
4.5 Input-output Feedback Linearization.....	128
4.6 Formulation of Indirect Vector Control Scheme of Induction Machine.....	135
4.7 Control Design for Indirect Vector Control Scheme of Induction Machine	139
4.8 Simulation Results	145
4.9 DSP Implementation and Experimental Results.....	150
4.9.1 Calculation of Rotor Flux Linkages.....	150
4.9.2 Per Unit Model and Base Values	156
4.9.3 Voltage / Current Sensing and Scaling.....	158
4.9.4 Speed Sensing and Scaling	160
4.9.5 Slip Estimation.....	161
4.9.6 Program Flowchart.....	163
4.10 Experimental Results	164
4.11 Conclusion	167
CHAPTER 5	168
EFFICIENCY OPTIMIZING CONTROL OF INDUCTION MOTOR USING NATURAL VARIABLES	168
5.1 Introduction.....	168
5.2 Induction Motor Model with Core Loss	169
5.3 Natural Variable Model and Total Loss Minimization.....	172

	Page
5.4 Formulation of Control Scheme.....	175
5.5 Speed Estimation	178
5.5.1 Using Imaginary Power	178
5.5.2 Using Rotor Voltage Equations	179
5.5.3 Using Rotor Voltage Equations (modified).....	183
5.6 Simulation Results	185
5.7 Experimental Results	189
5.8 Loss Minimization Using a Controller for the Loss Minimization Function	198
5.9 Conclusion	201
CHAPTER 6	203
SPEED ESTIMATION FOR INDUCTION MOTORS USING FULL-ORDER FLUX	
OBSERVERS	203
6.1 Introduction.....	203
6.2 Induction Machine Model.....	205
6.3 Full-order Flux Observer and Speed Estimation	207
6.4 Theory of MRAS (Model Reference Adaptive System).....	208
6.5 State Error Analysis and Transfer Function for Speed Estimation.....	213
6.6 Observer Gain Selection	218
6.7 D-decomposition Method	227
6.8 PI Control Parameters Selection	230
6.9 Formulation of Control Scheme.....	241
6.10 Simulation Results	244

	Page
6.11 Conclusion	253
CHAPTER 7	254
GENERALIZED OVER-MODULATION METHODOLOGY FOR CURRENT REGULATED THREE-PHASE VOLTAGE SOURCE CONVERTERS.....	254
7.1 Introduction.....	254
7.2 Linear PWM Modulation Schemes.....	255
7.3 Modulation in the Overmodulation Regions.....	259
7.4 Open-loop Voltage Generation	263
7.5 Current Regulation.....	269
7.6 Experimental Results	276
7.7 Conclusion	287
CHAPTER 8	289
CONCLUSIONS AND FUTURE WORK.....	289
8.1 Conclusions.....	289
8.2 Future Work.....	291
REFERENCES	293

LIST OF FIGURES

	Page
Figure 1.1 Schematic diagram of a voltage source inverter.....	3
Figure 2.1 A general three-phase voltage source converter.....	26
Figure 2.2 Illustration of carrier-based PWM using sine-triangle comparison method. (a) Modulation signal and carrier (triangle) signal. (b) the switching signal after the comparison.....	30
Figure 2.3 Carrier-based PWM generation. Ch2: modulation signal for phase A (0.6/div); Ch3: phase A voltage V_a (50V/div); Ch4: line to line voltage V_{ab} (50V/div).....	31
Figure 2.4 Transformation between reference frames.	33
Figure 2.5 Voltage space vector diagram for three-leg, three-phase voltage source converter including zero sequence voltages.	35
Figure 2.6a Existence functions of top devices in sectors I, II, III.	38
Figure 2.6b Existence functions of top devices in sectors IV, V, VI.....	39
Figure 2.7 Space vector PWM generation. Ch1: reference voltage for phase A (0.6/div); Ch2: modulation signal for phase A (0.6/div); Ch3: phase A voltage V_a (50V/div); Ch4: line to line voltage V_{ab} (50V/div).....	40
Figure 2.8 Time determination in sector I.	41

Figure 2.9 Generalized discontinuous PWM generation using $\alpha = 0.5 \cdot \{1 + \text{sgn}[\cos 3(\omega t + \delta)]\}$: (a) $\delta = 0^\circ$; (b) $\delta = -30^\circ$; (c) $\delta = -60^\circ$. Ch1: reference voltage for phase A (0.6/div); Ch2: modulation signal for phase A (0.6/div); Ch3: phase A voltage V_a (50V/div); Ch4: line to line voltage V_{ab} (50V/div).....	46
Figure 2.10 Feasible windings connections for five-phase machines : series connection of machines.	52
Figure 2.11 Feasible windings connections for six-phase machines : series connection of machines, six and three-phase machines.	52
Figure 2.12 Schematic diagram of a multi-phase voltage source converter.	53
Figure 2.13a Voltage space vector diagrams of a five-phase PWM inverter. (a) V_{qd1} ; (b) V_{qd2}	57
Figure 2.13b Voltage space vector diagrams of a five-phase PWM inverter. (a) V_{qd3} ; (b) V_{qd4} ; (c) V_o	58
Figure 2.14 Synthesis of the fundamental voltage in sector 1.	59
Figure 2.15a The space vector voltages for the six-phase converter. (a) V_{qd1} ; (b) V_{qd2} .	67
Figure 2.15b The space vector voltages for the six-phase converter. (a) V_{qd4} ; (b) V_{qd5} .	68
Figure 2.15c The space vector voltages for the six-phase converter. (a) V_{qd3} ; (b) V_o	69
Figure 2.16 Selection of voltage vectors in sector 1.....	70

Figure 2.17 Experimental result for five-phase system when $m_1 = 0.8$. (a) $m_3 = 0$, $\mu = 0.5$; (b) $m_3 = 0.2$, $V_{no} = 0$; (c) $m_3 = 0.2$, $\mu = 0.5$; (d) $m_3 = -0.2$, $V_{no} = 0$; (e) $m_3 = -0.2$, $\mu = 0.5$. Ch1: reference voltage for phase A (0.6/div), Ch2: modulation signal for phase A (0.6/div); Ch3: phase A voltage (50V/div); Ch4: line to line voltage V_{ab} (50V/div)..... 77

Figure 2.18a Experimental result for five-phase system when $m_1 = 1$. (a) $m_3 = 0.2$, $V_{no} = 0$; (b) $m_3 = 0.2$, $\mu = 0.5$; (c) $m_3 = -0.2$, $V_{no} = 0$; (d) $m_3 = -0.2$, $\mu = 0.5$. Ch1: Reference voltage for phase A (1.2/div); Ch2: modulation signal for phase A (1.2/div); Ch3: phase A voltage (50V/div); Ch4: line to line voltage V_{ab} (50V/div). 78

Figure 2.18b Experimental result for five-phase system when $m_1 = 1$. (a) $m_3 = 0.2$, $\delta = 0^\circ$; (b) $m_3 = 0.2$, $\delta = -36^\circ$; (c) $m_3 = -0.2$, $\delta = 0^\circ$; (d) $m_3 = -0.2$, $\delta = -36^\circ$. Ch1: reference voltage for phase A (1.2/div); Ch2: modulation signal for phase A (1.2/div); Ch3: phase A voltage (50V/div); Ch4: line to line voltage V_{ab} (50V/div). ($\mu = 0.5[1 + \text{sgn}(\cos 5(\omega t + \delta))]$)..... 79

Figure 2.19 Spectrum analysis of the line to line voltage V_{ad} (normalized with respect to the highest fundamental voltage) in the linear modulation region. (a) $m_1 = 0.8$, $m_3 = -0.2$; (b) $m_1 = 0.8$, $m_3 = 0.2$. 1: $V_{no} = 0$; 2: $\mu = 0.5$; 3: $\mu = 0.5[1 + \text{sgn}(\cos 5(\omega t + \delta))]$, $\delta = 0^\circ$; 4: $\mu = 0.5[1 + \text{sgn}(\cos 5(\omega t + \delta))]$, $\delta = -36^\circ$ 80

- Figure 2.20 Spectrum analysis of the line to line voltage V_{ad} (normalized with respect to the highest fundamental voltage) in the over-modulation region. (a) $m_1 = 1.5$, $m_3 = -0.2$; (b) $m_1 = 1.5$, $m_3 = 0.2$. 1: $V_{no} = 0$; 2: $\mu = 0.5$; 3: $\mu = 0.5[1 + \text{sgn}(\cos 5(\omega t + \delta))]$, $\delta = 0^\circ$; 4: $\mu = 0.5[1 + \text{sgn}(\cos 5(\omega t + \delta))]$, $\delta = -36^\circ$ 80
- Figure 2.21 Switching signals for the top devices in sector 1. 82
- Figure 2.22 Synthesis of fundamental and third harmonic voltages in a five-phase system. (a) Synthesizing reference voltage in sector 1 of V_{qd1} ; (b) Corresponding voltage vectors in V_{qd3} 83
- Figure 2.23 Experimental result for five-phase system when $m_1 = 0.7$, $m_3 = -0.2$. (a) $\mu = 0.5$; (b) $\delta = 0^\circ$; (c) $\delta = -36^\circ$ ($\mu = 0.5[1 + \text{sgn}(\cos 5(\omega t + \delta))]$). Ch1: Reference voltage for phase A (1.2/div); Ch2: Modulation signal for phase A (1.2/div); Ch3: Phase A voltage (50V/div); Ch4: Line to line voltage V_{ab} (50V/div). 88
- Figure 2.24 Experimental result for five-phase system when $m_1 = 0.7$, $m_3 = 0.2$. (a) $\mu = 0.5$; (b) $\delta = 0^\circ$; (c) $\delta = -36^\circ$ ($\mu = 0.5[1 + \text{sgn}(\cos 5(\omega t + \delta))]$). Ch1: Reference voltage for phase A (1.2/div); Ch2: Modulation signal for phase A (1.2/div); Ch3: Phase A voltage (50V/div); Ch4: Line to line voltage V_{ab} (50V/div). 89
- Figure 2.25 Experimental result for five-phase system when $m_1 = 1.4$, $m_3 = -0.2$. (a) $\mu = 0.5$; (b) $\delta = 0^\circ$; (c) $\delta = -36^\circ$ ($\mu = 0.5[1 + \text{sgn}(\cos 5(\omega t + \delta))]$). Ch1: reference voltage for phase A (1.2/div); Ch2: modulation signal for phase A (1.2/div); Ch3: phase A voltage (50V/div); Ch4: line to line voltage V_{ab} (50V/div). 90

Figure 2.26 Experimental result for five-phase system when $m_1 = 1.4$, $m_3 = 0.2$. (a) $\mu = 0.5$; (b) $\delta = 0^\circ$; (c) $\delta = -36^\circ$ ($\mu = 0.5[1 + \text{sgn}(\cos 5(\omega t + \delta))]$). Ch1: reference voltage for phase A (1.2/div); Ch2: modulation signal for phase A (1.2/div); Ch3: phase A voltage (50V/div); Ch4: line to line voltage V_{ab} (50V/div).....	91
Figure 3.1 Two-pole, three-phase, wye-connected symmetrical induction motor.	94
Figure 3.2 The equivalent phase circuit model of the induction machine.	97
Figure 3.3 Transformation between reference frames.	101
Figure 3.4 The qd0 equivalent circuit model of the induction machine in the arbitrary reference frame.	108
Figure 3.5 The phase model of the induction machine.	113
Figure 3.6 No-load test: (a) Mutual impedance vs phase voltage, (b) equivalent core loss resistance vs phase voltage.	115
Figure 3.7 Blocked rotor test: leakage impedance vs phase voltage.	117
Figure 3.8 The q-d equivalent circuit model of the induction machine including core loss resistance.	117
Figure 4.1 Idealized DC machine circuit diagram.	121
Figure 4.2 Phasor diagram of vector control of the induction machine.	123
Figure 4.3 Proposed indirect vector control scheme for the induction motor.	139
Figure 4.4 Linearization diagram for current control.	141
Figure 4.5 Poles location for 2nd Butterworth polynomial.	143
Figure 4.6 Indirect vector control diagram for induction machines.	145

Figure 4.7 Starting transients at no-load. (a) Speed command and actual speed; (b) electrical torque; (c) phase A voltage; (d) phase A current.	147
Figure 4.8 Response to the load change at steady state. (a) Speed command and actual speed; (b) electrical torque; (c) phase A voltage; (d) phase A current.	148
Figure 4.9 Response to the speed change after steady state. (a) Speed command and actual speed; (b) electrical torque; (c) speed command and actual speed; (d) electrical torque.....	149
Figure 4.10a Comparison of simulations of integration using a pure integrator and a LPF. (a) $\alpha_0 = 0, A_0 = 0$; (b) $\alpha_0 = \frac{\pi}{2}, A_0 = 0$	152
Figure 4.10b Comparison of simulations of integration using a pure integrator and a LPF. (a) $\alpha_0 = \pi, A_0 = 0$; (b) $\alpha_0 = 0, A_0 = -0.5$	153
Figure 4.11 Comparison of experimental results of integration using a pure integrator and a LPF. (a) Estimation of λ_{qs} from $(V_{qs} - r_s I_{qs})$, Ch1: $(V_{qs} - r_s I_{qs})$, Ch2: λ_{qs} ; (b) estimation of λ_{qs} and λ_{ds} using low pass filters, Ch1: λ_{qs} , Ch2: λ_{ds}	154
Figure 4.12 Voltage sensing and scaling block diagram (V_{ab}).	158
Figure 4.13 Current sensing and scaling block diagram (I_a).	159
Figure 4.14 Speed sensing and scaling block diagram.	161
Figure 4.15 Program flowchart.	163
Figure 4.16 Experimental results: the reference speed and actual speed when the reference speed is ramped up from 0 to 900rpm. Ch1: reference speed (545rpm/div); Ch2: actual speed (545rpm/div).	164

Figure 4.17a	Experimental results at steady state. (a) Reference and actual d-axis rotor flux linkages (0.6Wb/div); (b) reference q-axis stator currents (-1.65V, 3A/div); (c) reference d-axis stator current (-1.65V, 3A/div).....	165
Figure 4.17b	Experimental results at steady state. (a) Q- and d-axis stator current in stationary reference frame (6A/div); (b) q- and d-axis stator voltages in stationary reference frame (50V/div).....	166
Figure 4.18	Experimental results for speed regulation between -300rpm and 300rpm. Ch1: reference speed (273rpm/div); Ch2: actual speed (273rpm/div).....	167
Figure 5.1	The q-d equivalent circuit model of the induction machine including core loss resistance. (a) Q-axis; (b) d-axis.	170
Figure 5.2	Control scheme for induction motor with electrical loss minimization strategy.	178
Figure 5.3	Simulation of the rotor speed estimation including reactive power. (a) Reference and actual rotor speeds; (b) Reference and actual rotor speeds; (c) Developed electric torque.	180
Figure 5.4	Simulation of the rotor speed estimation using rotor voltage equations. (a) Reference and estimated rotor speeds; (b) reference and estimated rotor speeds... ..	182
Figure 5.5	Simulation of the rotor speed estimation using rotor voltage equations. (a) Reference and estimated rotor speeds; (b) reference and estimated rotor speeds... ..	184
Figure 5.6	Speed regulation and loss minimization for motor starting from zero speed to 300 rad/sec. (a) Developed torque; (b) reference and actual rotor speeds; (c) rotor flux linkage; (d) total electric loss.	185

Figure 5.7 Speed regulation and loss minimization for changing load torque. (a) Developed torque; (b) actual and command rotor speed; (c) square of rotor flux linkage; (d) total electric loss.....	187
Figure 5.8 Speed regulation and loss minimization for changing rotor speed. (a) Developed torque; (b) actual and command rotor speed; (c) square of rotor flux linkage; (d) total electric loss.....	187
Figure 5.9 Response to the speed change after steady state. (a) Reference speed and actual speeds; (b) electrical torque.....	188
Figure 5.10 Actual / estimated rotor speed corresponding to load change. (a) Reference and estimated speeds; (b) electric torque.....	188
Figure 5.11 Speed regulation from zero to 900 rpm. Ch1: reference rotor speed (545rpm/div); Ch2: actual rotor speed (545rpm/div); Ch3: square of rotor flux linkage (0.1Wb ² /div); Ch4: phase A current (6A/div).....	189
Figure 5.12 Speed regulation and loss minimization for changing rotor speed from zero to 900-600 rpm. Ch1: reference rotor speed (545rpm/div); Ch2: actual rotor speed (545rpm/div); Ch3: square of rotor flux linkage (0.1Wb ² /div); Ch4: phase A current (6A/div).....	190
Figure 5.13 Actual rotor speed and estimated rotor speed (using actual speed as feedback). Ch2: actual rotor speed (545rpm/div); Ch3: estimated rotor speed (545rpm/div).....	192

- Figure 5.14 Actual rotor speed, estimated rotor speed and filtered estimated rotor speed (without calculating the derivatives, using actual speed as feedback). Ch2: actual rotor speed (545rpm/div); Ch3: estimated rotor speed (545rpm/div); Ch4: filtered estimated rotor speed (545rpm/div). 193
- Figure 5.15 Actual rotor speed, estimated rotor speed and filtered estimated rotor speed (calculating the derivatives every 4 sampling period, using actual speed as feedback). Ch2: actual rotor speed (545rpm/div); Ch3: estimated rotor speed (545rpm/div); Ch4: filtered estimated rotor speed (545rpm/div). 194
- Figure 5.16 Reference rotor speed, actual rotor speed and estimated rotor speed (calculating the derivatives every 4 sampling period, using actual speed as feedback). Ch1: reference speed (545rpm/div); Ch2: measured speed (545rpm/div); Ch4: estimated speed (545rpm/div). 195
- Figure 5.17 Reference rotor speed, actual rotor speed and estimated rotor speed (calculating the derivatives every 4 sampling period, using actual speed as feedback). Ch1: reference speed (545rpm/div); Ch2: measured speed (545rpm/div); Ch4: estimated speed (545rpm/div). 195
- Figure 5.18 Experimental results for sensorless speed control. (a) 300 - 900rpm; (b) 300 - 600rpm. Ch1: reference speed (545rpm/div); Ch2: measured speed (545rpm/div); Ch4: estimated speed (545rpm/div). 196
- Figure 5.19 Speed regulation from zero to 600 rpm. Ch1: reference rotor speed (545rpm/div); Ch2: actual rotor speed (545rpm/div); Ch3: square of rotor flux linkage ($0.1\text{Wb}^2/\text{div}$); Ch4: phase A current (6A/div). 197

Figure 5.20 Speed regulation (300 – 600 rpm) showing rotor flux variation. Ch1: reference speed (273rpm/div); Ch2: estimated speed (273rpm/div); Ch3: rotor flux linkage (0.1Wb ² /div).....	198
Figure 5.21 The structures of controllers.....	200
Figure 5.22 Schematic diagram of the control algorithm.....	201
Figure 6.1 Structure of MRAS for speed estimation.....	209
Figure 6.2 Poles location for 4th Butterworth polynomial.....	219
Figure 6.3 $K_{11}, K_{12}, K_{21}, K_{22}$ with respect to ω_0 when L_m and r_r changes ($\omega_e = 377$ rad/s, $\omega_r = 375$ rad/s in motoring mode). (a) K_{11} ; (b) K_{12} ; (c) K_{21} ; (d) K_{22} . Solid line: $L_m = L_m^*$, $r_r = r_r^*$; Dotted line: $L_m = 1.25 L_m^*$, $r_r = 1.25 r_r^*$; Dashdot line: $L_m = 1.25 L_m^*$, $r_r = 0.75 r_r^*$; Dashed: $L_m = 0.75 L_m^*$, $r_r = 1.25 r_r^*$; Solid line (light): $L_m = 0.75 L_m^*$, $r_r = 0.75 r_r^*$	222
Figure 6.4 $K_{11}, K_{12}, K_{21}, K_{22}$ with respect to ω_0 when L_m and r_r changes ($\omega_e = 377$ rad/s, $\omega_r = 379$ rad/s in generating mode). (a) K_{11} ; (b) K_{12} ; (c) K_{21} ; (d) K_{22} . Solid line: $L_m = L_m^*$, $r_r = r_r^*$; Dotted line: $L_m = 1.25 L_m^*$, $r_r = 1.25 r_r^*$; Dashdot line: $L_m = 1.25 L_m^*$, $r_r = 0.75 r_r^*$; Dashed: $L_m = 0.75 L_m^*$, $r_r = 1.25 r_r^*$; Solid line (light): $L_m = 0.75 L_m^*$, $r_r = 0.75 r_r^*$	223
Figure 6.5 $K_{11}, K_{12}, K_{21}, K_{22}$ with respect to ω_0 under different operating conditions ($L_m = L_m^*$, $r_r = r_r^*$, $\omega_e = 377$ rad/s, 360 rad/s $\leq \omega_r \leq 390$ rad/s). (a) K_{11} ; (b) K_{12} ; (c) K_{21} ; (d) K_{22}	224

Figure 6.6 $K_{11}, K_{12}, K_{21}, K_{22}$ with respect to ω_0 under different operating conditions

($L_m = L_m^*$, $r_r = r_r^*$, $\omega_e = 188.5$ rad/s, 180 rad/s $\leq \omega_r \leq 195$ rad/s). (a) K_{11} ; (b) K_{12} ;
(c) K_{21} ; (d) K_{22} 225

Figure 6.7 t_{23} with respect to ω_0 under different operating conditions ($L_m = L_m^*$,

$r_r = r_r^*$, $\omega_e = 377$ rad/s, 360 rad/s $\leq \omega_r \leq 390$ rad/s). 231

Figure 6.8 Relationship between K_{wp} and K_{wi} at different slip frequencies.

($\omega_e = 377$ rad/s and -13 rad/s $\leq \omega_s \leq 17$ rad/s)..... 233

Figure 6.9 Relationship between K_{wp} and K_{wi} at different slip frequency. (a) $k = 0.0$; (b) $k = 0.2$; (c) $k = 0.4$; (d) $k = 0.5$; (e) $k = 0.8$; (f) $k = 1.0$.

($\omega_e = 377$ rad/s and -13 rad/s $\leq \omega_s \leq 17$ rad/s)..... 234

Figure 6.10 Relationship between K_{wp} and K_{wi} under parameter changes in motoring

mode ($k = 0.5$, $\omega_e = 377$ rad/s and $\omega_s = 17$ rad/s). 1: $r_r = 0.5r_r^*$, $L_m = 0.5L_m^*$; 2:

$r_r = 0.5r_r^*$, $L_m = 1.5L_m^*$; 3: $r_r = 1.5r_r^*$, $L_m = 0.5L_m^*$; 4: $r_r = 1.5r_r^*$, $L_m = 1.5L_m^*$. 236

Figure 6.11 Relationship between K_{wp} and K_{wi} under parameter changes in generating

mode ($k = 0.5$, $\omega_e = 377$ rad/s and $\omega_s = -13$ rad/s). 1: $r_r = 0.5r_r^*$, $L_m = 0.5L_m^*$; 2:

$r_r = 0.5r_r^*$, $L_m = 1.5L_m^*$; 3: $r_r = 1.5r_r^*$, $L_m = 0.5L_m^*$; 4: $r_r = 1.5r_r^*$, $L_m = 1.5L_m^*$. 236

Figure 6.12 Structure of PD controller used for speed regulation. 237

Figure 6.13 Relationship between K_{wrd} and K_{wrp} at different slip frequency. (a) $k = 0.0$;

(b) $k = 0.2$; (c) $k = 0.4$; (d) $k = 0.5$ (e) $k = 0.8$; (f) $k = 1.0$.

($\omega_e = 377$ rad/s and -13 rad/s $\leq \omega_s \leq 17$ rad/s)..... 239

Figure 6.14 Relationship between $K_{\text{wrđ}}$ and $K_{\text{wrđ}}$ under parameter changes in motoring

mode ($k = 0.5$, $\omega_e = 377$ rad/s and $\omega_s = 17$ rad/s). 1: $r_r = 0.5r_r^*$, $L_m = 0.5L_m^*$; 2:

$r_r = 0.5r_r^*$, $L_m = 1.5L_m^*$; 3: $r_r = 1.5r_r^*$, $L_m = 0.5L_m^*$; 4: $r_r = 1.5r_r^*$, $L_m = 1.5L_m^*$. 240

Figure 6.15 Relationship between $K_{\text{wrđ}}$ and $K_{\text{wrđ}}$ under parameter changes in generating

mode ($k = 0.5$, $\omega_e = 377$ rad/s and $\omega_s = -13$ rad/s). 1: $r_r = 0.5r_r^*$, $L_m = 0.5L_m^*$; 2:

$r_r = 0.5r_r^*$, $L_m = 1.5L_m^*$; 3: $r_r = 1.5r_r^*$, $L_m = 0.5L_m^*$; 4: $r_r = 1.5r_r^*$, $L_m = 1.5L_m^*$. 240

Figure 6.16 Rotor flux oriented control including full-order flux observer and adaptive

speed estimation..... 242

Figure 6.17 Starting transients and transients after change in load torque. (a) Reference,

actual, estimated speed; (b) developed torque; (c) slip..... 245

Figure 6.18 Starting transients and transients after change in load torque: reference,

actual and estimated speeds (a) during starting; (b) after starting; (c) at the steady

state; (d) zoomed around the reference speed..... 247

Figure 6.19 Starting transients and transients after change in load torque. (a) Difference

between actual and estimated q-axis currents; (b) difference between actual and

estimated d-axis currents..... 248

Figure 6.20 Starting transients and transients after change in load torque. (a) Regulation

of λ_{dr} ; (b) regulation of λ_{qr} ; (c) regulation of I_{qs} ; (d) regulation of I_{ds} 249

Figure 6.21 No-load flux linkages at steady state. (a) Actual q- and d-axis rotor flux linkages; (b) estimated q- and d-axis rotor flux linkages.....	250
Figure 6.22 Starting transients and transients after change in load torque. (a) Actual and estimated λ_{qs} ; (b) actual and estimated λ_{ds} ; (c) actual and estimated λ_{qr} ; (d) actual and estimated λ_{dr}	251
Figure 6.23 Response to the change in speed. (a) Reference, actual, estimated speed; (b) developed torque.....	252
Figure 7.1 (a) Schematic diagram of a voltage source inverter, (b) qdo voltages for the switching states.....	258
Figure 7.2 Voltage trajectories in the inverter. (a) Linear region; (b) over-modulation region I; (c) over-modulation region II.....	261
Figure 7.3 Relationship between crossover angle and modulation index in region I....	265
Figure 7.4 Relationship between holding angle and modulation index in region II.....	266
Figure 7.5 Relationship between the crossover / holding angle and modulation magnitude index.....	267
Figure 7.6 Mapping of the reference and actual modulation magnitude index for operation in the over-modulation region.....	268
Figure 7.7 Diagram of current regulation in all modulation regions.....	273
Figure 7.8 Simulation of current regulation for q- and d-axis currents. (a) Q-axis reference current; (b) q-axis actual current; (c) the output from the current controller for q-axis current; (d) d-axis reference current; (e) d-axis actual current; (f) the output from the current controller for d-axis current.....	274

Figure 7.9 Simulation of current regulation. (a) Phase A fundamental current during the transient; (b) phase A harmonic current during the transient; (c) phase A fundamental current at steady state in the overmodulation region; (d) phase A harmonic current at steady state in the overmodulation region.	275
Figure 7.10a Trajectory of V_q and V_d and the waveforms for V_q and V_d (0.6/div). (a) Linear modulation region; (b) overmodulation region I.	276
Figure 7.10b Trajectory of V_q and V_d and the waveforms for V_q and V_d (0.6/div). (a) Overmodulation region II; (b) six step operation.	277
Figure 7.11 Current regulation using space vector modulation. (a) Linear – over-modulation region I; (b) linear–overmodulation region II; (c) overmodulation region I–II. (1) reference q-axis current (3A/div), (2) measured fundamental q-axis current (3A/div), (3) reference d-axis current (3A/div), (4) measured fundamental d-axis current (3A/div), (R1) line-line voltage (200V/div), (R2) phase A measured (raw) current (6A/div).	280
Figure 7.12a Voltage ($V_q - V_d$) trajectories using space vector modulation (25V/div). (a) Linear to over-modulation region I transition; (b) linear to over-modulation region II transition.	282
Figure 7.12b Current waveforms of phase A. (a) Linear modulation region; (b) over-modulation region I; (c) over-modulation region II. Ch1: reference current (1.5A/div), Ch2: measured current (1.5A/div); Ch3: fundamental frequency current (1.5A/div); Ch4: harmonic current (0.6A/div).	283

Figure 7.13 Current regulation using discontinuous carrier-based modulation with gain G. (a) Linear – over-modulation region I; (b) linear–overmodulation region II; (c) overmodulation region I–II. Ch1: reference q-axis current (3A/div); Ch2: measured fundamental q-axis current (3A/div); Ch3: reference d-axis current (3A/div); Ch4: measured fundamental d-axis current (3A/div); ChR1: line-line voltage (200V/div), ChR2: phase A measured (raw) current (6A/div). 284

Figure 7.14 Current waveforms of phase A using discontinuous carrier-based modulation with gain G. (a) Linear modulation region; (b) over-modulation region II; (c) over-modulation region II. Ch1: reference current (1.5A/div); Ch2: measured current (1.5A/div); Ch3: fundamental frequency current (1.5A/div); Ch4: harmonic current (0.6A/div). 285

Figure 7.15 Current regulation using discontinuous carrier-based modulation without gain G. (a) Linear – over-modulation region I; (b) linear–overmodulation region II; (c) overmodulation region I–II. Ch1: reference q-axis current (3A/div); Ch2: measured fundamental q-axis current (3A/div); Ch3: reference d-axis current (3A/div); Ch4: measured fundamental d-axis current (3A/div); ChR1: line-line voltage (200V/div); ChR2: phase A measured (raw) current (6A/div). 286

LIST OF TABLES

	Page
Table 2.1 Switching modes of the three-phase voltage source inverter and corresponding stationary reference frame qdns voltages.....	34
Table 2.2 Device Switching times expressed in terms of reference voltages.....	42
Table 2.3 Device Switching times expressed in terms of reference line-line voltages...	43
Table 2.4 Average neutral voltage for all sectors	43
Table 2.5 Normalized times when the three top devices are turned on.	47
Table 2.6a Analysis on V_{o1} for V_{qd1} ($V_{qd2} = 0$).....	61
Table 2.6b Analysis on V_{o2} for V_{qd1} ($V_{qd2} = 0$).....	61
Table 2.6c Analysis on V_{oo} for V_{qd1} ($V_{qd2} = 0$).....	62
Table 2.7a Analysis on V_{o1} for V_{qd1} ($V_{qd2} = 0$).....	63
Table 2.7b Analysis on V_{o2} for V_{qd1} ($V_{qd2} = 0$).....	63
Table 2.7c Analysis on V_{oo} for V_{qd1} ($V_{qd2} = 0$).....	64
Table 2.8a Coefficients for $V_{a1}, V_{b1}, V_{c1}, V_{d1}, V_{e1}, V_{f1}$	71
Table 2.8b Coefficients for $V_{a1}, V_{b1}, V_{c1}, V_{d1}, V_{e1}, V_{f1}$ with coefficient α	71
Table 2.8c Coefficients for $V_{a2}, V_{b2}, V_{c2}, V_{d2}, V_{e2}, V_{f2}$	72
Table 2.8d Coefficients for $V_{a3}, V_{b3}, V_{c3}, V_{d3}, V_{e3}, V_{f3}$	72
Table 2.8e Coefficients for $V_{a3}, V_{b3}, V_{c3}, V_{d3}, V_{e3}, V_{f3}$ with coefficient α	73
Table 2.9 Calculation of the modulation signals in terms of turn-on times.....	84
Table 2.10a Calculation of the modulation signals in terms of line to line voltages.....	85
Table 2.10b Calculation of the modulation signals in terms of line to line voltages.....	85

	Page
Table 2.11 Calculation of the modulation signals m_a in terms of line to line voltages ..	86
Table 3.1 Parameters of the experimental induction motor	116
Table 7.1 The turn-on normalized times for three top devices	257
Table 7.2 The turn-on normalized times for three top devices in the over-modulation region	262

CHAPTER 1

INTRODUCTION

1.1 Introduction

Induction machines are widely used in the industry, serving as one of the most important roles during the energy conversion between electrical power and mechanical power. Based on the functionality, they are classified into two categories: induction generators and induction motors. Induction generators consume the mechanical energy and produce electrical power, which find the applications in the standing-alone electrical power generations and wind farms. Induction motors produce mechanical power while consuming the electrical power from the grid, which account for more than one half of the total electrical power consumed. Especially the induction machines with squirrel cage rotors are the dominant types due to the simple structures, easy connections, robust to severe operating conditions, low costs, and maintenance free features. They can be found in the applications as the important driving sources where a certain motion is required either linear or rotating ones. They are used to drive fans, pumps, compressors, power tools, mills, elevators, cranes, electrical vehicles, ships, etc.

The induction machines were initially applied in the cases where the speed was not required to change frequently since they are difficult to control compared with DC machines. During the last few decades, the feasible control of induction machines receives a lot of attentions due to the development of power electronics. The DC machines were applied for high performance speed and torque control since the air-gap

flux and armature current are regulated independently. It means that the torque is proportional to the armature current once the air-gap flux is fixed, which is very easy to control. The speed then can be regulated by the control of torque. In the induction machine, however, the torque is the cross-product of air-gap flux and stator currents, both of which have two axis components expressed in the q-d plane. All of these four components will affect the torque production if they are not zero, which is the general case. Apparently controlling the electric torque is much more complicated in the induction machines.

With the development of power electronics, the power semiconductor devices are being extensively used in the power electronic converters, which convert power from one form to another. The fast-switching devices and the techniques of DSP (Digital Signal Processor) provide the convenient ways to realize the complex control algorithms such that the induction machines can be controlled in different ways to satisfy certain requirements. This is done through controlling the voltages (magnitude, frequency and angle) applied to the machine through a VSI (Voltage Source Inverter) as shown in Figure 1.1. The VSI is a certain kind of DC/AC converter, which converts the DC voltage into AC voltage through PWM (Pulse Width Modulation) technique. The modulation signals are generated from the control algorithm, which are corresponding to the voltages with certain magnitude, frequency and angle. These signals are then compared with a high frequency carrier signal to generate the pulses, which are generally positive when the modulation signals are greater than the carrier signal and negative when the modulation signals are smaller than the carrier signal. When these pulses are applied to

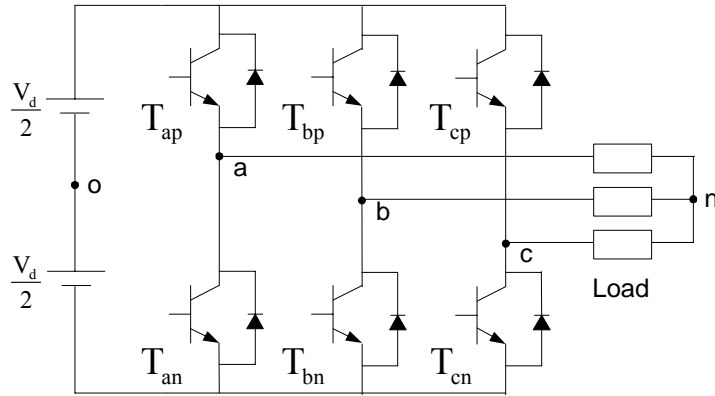


Figure 1.1 Schematic diagram of a voltage source inverter.

switch on and off the switching devices, the fundamental voltage that is embedded in the output voltage pulses will be the same as the desired voltages.

With the help of the control algorithm and voltage source inverter, a torque expression similar to that of DC machines can be achieved for the induction machine, which finds a lot of high performance applications. The torque equation can be simplified if the angle between the stator current and rotor flux linkage vectors is controlled although the torque is originally the cross-product of these two vectors. For example, if one of the rotor flux linkage components is regulated to be zero, the torque equation will change to the product of two components only, one component comes from the rotor flux linkage and the other one comes from the stator current. The desired torque can be produced when these two components are regulated separately.

From the application point of view, the vectors in q-d plane are not visible and the magnitudes of some quantities are of more importance including the flux, current, electric torque etc. These quantities are all scalars that are independent of any reference frame. The reference frame is usually selected as the synchronous one, in which all the time changing quantities in the stationary reference frame become DC quantities

corresponding to a particular steady-state operating condition to facilitate the control. The transformation is then necessary between the stationary reference frame and synchronous reference frame since the measured quantities and the modulation signals are in the stationary reference frame. However, these transformations can be saved if it is possible to use these scalars in the control and everything can be done in the stationary reference frame.

One of the most popular control objectives is to control the speed of the induction machine to the reference speed. The speed is generally measured using speed sensors or calculated from the absolute position sensors. These speed or position sensors are expensive and thus increase the total cost of the whole drive system. At the same time, the installation of the speed or position sensors requires more space and increases the chances of fault and also the complexity of the system. Thus the research on the speed control of induction machines has moved to the sensorless speed control, which eliminates the need of installing speed sensor in order to reduce the cost, or for operation in special conditions. Speed sensorless control is basically the algorithm of speed estimation that can infer the required measurement from other more easily available measurements like voltages and currents.

In the normal operation, the induction machines are operated under the rated condition. However, in the case of emergency or abnormal situations, the induction machines are required to generate the output that is more than rated. Thus the voltage source inverter will have to operate into the overmodulation region to get more voltage output although the output voltages are not pure sinusoidal any more. The extreme case is that the phase voltages are square waves, in which the fundamental voltages reach the

maximum value. Special manners have to be adopted in order to reduce the torque oscillations due to the introduction of harmonic components in the voltages and currents. It is expected that the induction machine can still go back to the normal operating condition once the problem resulting from abnormal operation is fixed. This capability of operating in the overmodulation region could increase the stability of the whole drive system and gives more output torque.

1.2 Literature Review

The review on the various works previously done related to the induction machine control is necessary in the sense of defining the research scope. It is also helpful to find the appropriate way of conducting current research under the present conditions by examining different methods since different methods have their own advantages and disadvantages. The PWM modulation technique is the first that needs to be studied because it is the basis of implementing the induction machine control. Then different methods of the induction machine control are discussed. The approaches of loss minimization and the speed estimation techniques are highlighted. At last the methods mentioned in the literatures regarding the overmodulation technique are reviewed.

1.2.1 PWM Schemes in Three-Phase and Multi-Phase Voltage Source Inverters

The general three-phase voltage source inverter feeding a three-phase load is shown in Figure 1.1. The main purpose of this topology is to generate a three-phase voltage

source with controllable amplitude, phase angle and frequency. Pulse width modulation (PWM) techniques used in three phase voltage source converters can be classified into two categories : carrier-based PWM and space vector PWM. The PWM technique using sine triangle intersection was first proposed by Schönung and Stemmler in 1964 [2.1]. Due to the ease of implementation, the sinusoidal PWM has been found in a wide range of applications. However the output range of its linear operation is limited to 78.5 percent of the maximum fundamental voltage generated by the six-step operation. Thus the usage of the DC bus voltage is not efficient. Then the direct digital technique or the space vector modulation technique was proposed by Pfaff, Weschta and Wick in 1982 [2.2]. And the development of micro-controllers made the implementation of direct digital technique possible at the same time. This scheme became more and more popular due to its efficient utilization of the DC link voltage, possible optimization of the output distortion and switching losses, and compatibility with the digital controller. It has been widely used for high performance three-phase drive systems and it showed that the absence of neutral current path in star-connected three-phase systems provides the degree of freedom in determining the duty cycles of the switching devices. This degree of freedom is achieved by partitioning the two null states. The equivalent degree of freedom in sine-triangle comparison method is also observed by injection of appropriate zero sequence signal. Since the voltage between the load neutral and the reference of the DC source can take any value, this zero sequence signal is used to alter the duty cycle of the switching devices and alternatively the modulation signals. Appropriate zero sequence signal injection could increase the linear range of the voltage generation, improve the waveform quality and reduce switching losses without affecting the effective output. It

has been shown that the linear range of the output voltage was increased to 90.7 percent of the maximum fundamental voltage generated from the six-step operation. Some other techniques were developed for harmonic elimination in order to suppress the lower ordered harmonics. The third harmonic injection (THIPWM) techniques explain that by adding the third harmonic component to the fundamental voltages for a three-phase inverter [2.3], it is possible to obtain a line-to-line output voltage that is 15 percent greater than that obtained when pure sinusoidal modulation is employed and the line-to-line voltage is undistorted.

The discontinuous modulation technique was developed first and illustrated that the scheme resulted in high voltage linearity range, reduced switching losses, and superior current waveform. The scheme had a poor performance in the lower modulation region and it is desirable to operate when the modulation index is relatively high. It is found that the harmonic loss in the higher modulation region can be greatly reduced by using an optimal modulation for minimum switching loss. The correlation between the carrier-based PWM and space vector PWM was established by changing the duty cycle weights of the zero states. It was proved that the modified space vector PWM could be implemented as triangle comparison method by adding the zero sequence voltage to the fundamental voltages. Hava developed a high performance generalized discontinuous PWM algorithm [2.4], which employed conventional space-vector PWM in the low modulation region and generalized discontinuous PWM algorithms in higher modulation region.

Multi-phase electric machines powered with multi-phase converters are being seriously considered for several high power applications in order to achieve higher torque

per ampere and improve system reliability in applications such as aerospace, electric ship propulsion, electric locomotive, and hybrid electric vehicles. When a converter leg is lost, multi-phase machines are able to produce a higher fraction of their rated torques with little pulsations when compared to the three-phase machines. Five and six phase machines have improved torque capabilities when the stator windings are injected with phase currents comprising of the fundamental and third harmonic components, which individually interact with the fundamental and third harmonic airgap flux densities, each of them produces an average, non-pulsating electromagnetic torque [2.5, 2.11-2.13]. The third harmonic air-gap flux density is enhanced with the use of concentrated stator windings in induction machines, the generation of quasi-rectangular back EMF waveforms in permanent magnet machines or rotor structure configuration in synchronous reluctance machines [2.6, 2.14-2.15]. Recently, it has been shown that when inverter fed multi-phase electric machines with either odd or even phase numbers are connected in series with other machines with same or lower phase numbers, they can be independently speed controlled using conventional vector control methodology [2.7-2.9].

Applying what is referred to as space vector decomposition technique to the 64 switching states of the six-phase converter, the output voltages are decomposed into three voltage sets (d-q), (x-y), and (o₁-o₂) which are used to synthesize three set of balanced voltages. The time required to turn on selected switching states in each of the converter sectors to synthesize desired phase voltages for the dual winding three-phase induction machines are calculated by solving a set of linear voltage averaging equations. For dual winding machines of [2.17, 2.18], the synthesis of the fundamental phase voltages corresponding to the (d-q) set and suppressing (setting to zero) the (x-y), and (o₁-o₂) were

considered. Further sequencing of the selected switching states are required in order to minimize switching losses and improve waveforms in the implementation of the continuous and discontinuous space vector PWM (SVPWM) [2.18]. Modulation strategies for a six-phase converter driving various stator winding connections of a three-phase dual winding induction machine to synthesize fundamental voltages have been reported [2.19]. In [2.20], the three-phase unified PWM method for three-phase converters was extended to n-phase inverters to synthesize sinusoidal phase voltages which were achieved by applying times of available switching states to approximate the desired phase voltages. Offset voltages comprising of the instantaneous maximum and minimum values of the phase voltages are added to the modulation signals to improve the voltage utilization of the dc bus. SVPWM method for five phase machines based on multiple d-q space concepts was presented to synthesize both balanced five phase fundamental and third harmonic voltages required to improve torque capability [2.21]. Resolving the 32 states into two d-q different space vectors for the fundamental and third harmonic voltages, the switching time required for turning on the selected voltage vectors are calculated for each sector. Furthermore, it is shown that by adding appropriate offset voltages to the modulation signals corresponding to the fundamental and third harmonic voltages to produce flat-top modulation waveforms, the converter voltage gain of the five-phase converter is improved.

1.2.2 Induction Motor Control

There are a lot of control schemes applied for the induction motor drives including the scalar control, direct torque control, adaptive control, and vector / field oriented control. The vector control of induction machines emerges with the development of modern power electronics and is very popular since it can be used to get similar performance as the DC machine. The basic idea of vector control is that the similar torque expression compared with DC machines can be derived once the air-gap flux is aligned on one of the two axes in q-d plane, which means one of the two axis flux is zero (i.e. $\lambda_q = 0$). This method can be applied in different reference frames resulting the stator, air-gap and rotor flux oriented vector control schemes [4.2-4.3].

In the case of induction machines, the rotor flux oriented control is usually employed although it is possible to implement stator flux oriented and also magnetizing flux oriented control. The stator / rotor flux linkages of the induction machines are necessary for the vector control. In terms of the methods of obtaining the flux linkages, the field oriented induction machine drive systems are classified into two categories : the direct field oriented system and the indirect field oriented system. In the former case, the flux quantities (magnitude and angle) are directly measured by using Hall-effect sensors, search coils, tapped stator windings of the machine or calculated from the so-called flux model. For the indirect field oriented control system, the magnitude and space angle of the flux linkages are obtained by utilizing the monitored stator currents and the rotor speed. The space angle of the flux linkage is then obtained as the sum of the monitored rotor angle (corresponding to the rotor speed) and the computed reference value of the

slip angle (corresponding to the slip frequency). The indirect field oriented control is still receiving wide attention although some sensorless control strategies have been proposed in the last few years [4.1-4.4]. The exact estimation of rotor position is one of the key issues in the vector control system.

The scalar control is receiving some attentions since they can be used for the efficiency optimization [4.5-4.6]. From the application point of view, only the magnitudes of some quantities are important including the flux, current, electric torque etc. These quantities are all scalars that are constants in any reference frame. Using these quantities as the control variables leads to the scalar control, which can be used for the loss minimization since the real power and losses are also scalars. One of the advantage of using the scalars as the state variables is that no reference frame transformation is required. It is known that the transformation and reverse transformation between the stationary and synchronous reference frames are necessary since the control is preferred to be done in the synchronous reference frame while the measured quantities and the modulation signals are in the stationary reference frame. If all of the state variables are scalars, it means that these variables can be calculated in the stationary reference frame. However, there are some disadvantages of the calculations using the AC signals, which are not desirable since the calculations using AC signals could result into some error.

1.2.3 Efficiency Optimization

Efficiency improvement of motor drives has been an area of active research within the last twenty years occasioned by the increasing need to better utilize electric power in

this era of increasing demand. Since induction machines are known as the greatest consumers of electric power, much work has been done to improve their design and steady-state operation. The efficiency that decreases with increasing loss can be improved by minimizing both the electrical and mechanical losses. However, the mechanical losses are difficult to minimize once the machine is designed, manufactured and put into operation. These losses include the ones due to the wind friction and bearing friction. Some of the electrical losses are also difficult to minimize, which include the stray losses. But the electrical losses are dominated by the copper and core losses and the overall system efficiency is improved when they are minimized. Copper loss reduces with decreasing stator and rotor currents while the core loss essentially increases with increasing air-gap flux density. A study of the copper and core loss components reveals that their trends conflict – when the core loss increases, the copper loss tends to decrease. However, for a given load torque, there is an air-gap flux density at which the total loss is minimized. Hence, electrical loss minimization process ultimately comes down to the selection of the appropriate air-gap flux density of operation. Since the air-gap flux density must be variable when the load is changing, control schemes in which the (rotor, air-gap) flux linkage is constant will yield sub-optimal efficiency operation especially when the load is light.

There are two main approaches followed in the literature for loss minimization of electric machines - model based and on-line power search optimization based methods. In the model based scheme, the loss is defined in terms of measured machine parameters, which is minimized using what is called as the loss model controllers [5.1-5.3]. The on-line power search optimization method uses the measured input power to the motor and

perturbs control variables until the measured power is the minimum for the particular operating condition [5.5-5.6]. It would appear with good justification that these efficiency improvement schemes find their greatest utility under steady and quasi-steady-state operating conditions.

There has been some work done on the efficiency optimization of high performance drives. The classical vector control algorithms need some modifications to include core loss effect and in the determination of the reference currents or flux linkages, without which the decoupling between the flux and torque current components are compromised [5.4]. A most recent proposal in a series of papers dealing with the sensorless speed vector control of induction machines, operating at high efficiency in which core loss is accounted for, shows with simulation and experimental results, that in the sensorless mode of operation, high agility and high efficiency are feasible [5.7]. Recently, papers have been presented dealing with loss minimization and high performance speed (torque) control of synchronous and permanent magnet machines. The nonlinear control schemes are based on feedback linearization and decoupling methods using motor models in which core loss is represented with core loss resistances [5.8-5.10].

1.2.4 Sensorless Control of Induction Machines

The speed control is quite common in the most induction motor applications. Traditionally the speed information of the induction motor is measured or calculated using a rotor position / speed sensor. The resolvers and rotary encoders are the most widely used types, which are classified into two categories. One is the absolute optical

encoder that can be used to sense the exact rotor position while the other one is the incremental optical encoder that is used for the calculation of rotor speed only. One of the advantage of installing speed sensors is that the measurement is almost independent of the machine control itself. The precision can be very high when the high resolution sensor is used. So it is regarded as an accurate method for the speed measurement. However, the speed sensors are difficult or not allowed to install due to the space limitation and severe environment conditions in some applications. The installation increases the possibility of failures due to the extension of shaft. And another most important issue is the cost of the speed sensor, which takes a large portion of total cost for the auxiliary equipment of induction motor control. In the last few years, a lot of research has been done on the techniques for eliminating the physical speed or position sensor and replacing it with speed estimation schemes.

The speed estimation basically is the algorithm that can infer the measurement required from other more easily available measurements like voltages and currents. The speed estimation techniques that have been developed can be classified into three categories. The first one is using the motor back EMF to determine the rotational speed of the rotor [6.1]. The stator or rotor flux is estimated from the stator voltage equations and the speed is obtained using the estimated flux linkages and the rotor voltage equations. The model reference adaptive system (MRAS) [6.2] is an alternative method that uses the rotor flux estimated from stator voltage equations as the reference model and the rotor voltage equations as the adaptive model. The speed is then obtained by the use of an adaptive law having the cross product of the two estimated flux linkages as inputs. The idea of using imaginary power as the basis of speed estimation has its own advantages

since the speed estimator does not involve pure integrations to get the flux linkages. The method of this category performs very well except in very low speed range because the state voltages provided by the inverter are difficult to measure and the errors are relatively high for the low speed operation.

The second technique is based on detecting the rotor slot harmonics in the stator currents [6.3]. The effect of rotor slot harmonics on the currents flowing into the machine is used to detect the rotor speed. This method works well above some minimum speed and the algorithm is quite complex compared with other methods. And the last technique is based on detecting the saliency in the rotor [6.4]. This technique measures the response of the machine when a persistent, high frequency excitation, distinct from the fundamental excitation is applied via the inverter. According to the type of high frequency excitation and the signal processing technique used to estimate the rotor or flux position, they can be classified into two main categories. One is injecting a carrier signal superimposed on the fundamental excitation and is generally distinct from the PWM switching excitation created by the inverter. The other one is creating an excitation by the PWM switching of the inverter by modifying modulation signals. The advantage of this method is that the detection of rotor position or speed is almost independent of the actual speed. Hence, it can be used even for the zero speed measurement. The disadvantages are the distortion of the voltages, currents and flux linkages in the machine due to the introduction of extra high frequency signals. Also the degree of saliency depends on the machine itself and the effect is not significant especially for the induction machines.

The full-order observer system is an alternative method of the first category. It has received a lot of attentions since the currents and flux linkages in the motor are always

needed for the control. Especially when they are used together with the adaptive speed observer, an effective sensorless control can be formulated. The definitions of full-order observers have been shown in some papers [6.5-6.8]. Some of them used the stator currents and rotor flux linkages as the state variables [6.5-6.6] and some used the stator and rotor flux linkages as the state variables [6.8]. The machine model in terms of the chosen state variables is derived first and then the full-order flux observer model is defined. The adaptive speed estimation is proposed based on the chosen error function, in which actual stator currents and the estimated flux linkages are used.

In the paper by Hisao Kubota [6.6], the stator currents and rotor flux linkages are used as the state variables in the stationary reference frame. The state observer, which estimates the stator current and the rotor flux linkages together, is defined in terms of the estimated states and the observer gains as the difference between the estimated and actual stator currents. The Lyapunov's theorem is utilized to drive the speed adaptive mechanism. The observer gain matrix is calculated so that the observer poles are proportional to those of the motor itself. The adaptive observer is stable in usual operation since the induction motor itself is stable. The direct field oriented control without speed sensors is used for the experiments and a particular set of PI control parameters is selected in the paper for the speed adaptive estimation.

In the paper by Geng Yang [6.5], similar full-order observer is defined and the form of observer gain is even exactly the same as that in [6.6]. The idea of MRAS is applied, in which the motor model is considered as a reference model and the observer model as an adjustable model. The error between the states from two models is used to derive an adaptive mechanism to adjust estimated speed. The error function is chosen based on the

Popov's criterion and it turns out to be the same as that in [6.6]. The estimation of stator resistance is also proposed. A vector-controlled speed sensorless system is used for the experiments and a constant gain is chosen for the observer.

The full-order flux observers for sensorless induction motors are analyzed and designed in [6.8], in which the stator and rotor flux linkages are chosen as the state variables. The angular speed of the reference frame is included in the model equations, which means that the observer can operate in any reference frame. The speed estimation is based on the component of the current estimation error that is perpendicular to the estimated rotor flux linkages. The speed adaptive observer is studied via small signal linearization using a synchronous reference frame in order to obtain a steady-state operating point. The transfer function from the estimation error of the speed to the estimation error of the current is derived and closed-loop transfer function between the estimated speed and actual speed is also derived. Certain expressions are shown in the paper on the selection of speed-adaptation gain and observer gain.

1.2.5 Overmodulation Technique for VSI

In most motor drive and utility applications, three-phase voltage source converters are required to operate in the over-modulation regions to improve steady-state capabilities and dynamic system performance. They are even supposed to transit from the linear modulation region into the over-modulation and six-step modes seamlessly especially when inserted in the closed-loop current regulated systems. With the development of microprocessors and digital signal processors, space vector and carrier-

based PWM schemes have become very popular PWM methods for three-phase voltage source converters. Space vector modulation computes the duty cycles of the switches and minimizes the switching actions during the transitions between two successive space vectors to obtain the optimal switching pattern. Similar switching and voltage generating characteristics are also achieved using carrier-based triangle intersection modulation schemes which generate switching pulses by comparing a high frequency carrier signal with modulation signals which may be continuous or discontinuous. The generalized discontinuous carrier-based triangle intersection modulation scheme with its various variants, have been developed and their advantages and disadvantages in the linear and over-modulation regions have received significant attentions [7.1-7.3]. The direct digital space vector PWM modulation (SVPWM) method in which the two null states are utilized for the same time, has become very popular in the industry since it generates less harmonic voltages and provides a more efficient use of the DC source voltage. The relationship between the two modulation schemes when operating in the linear region has been established [7.3].

When space vector converters operate in the over-modulation region, the sum of the normalized switching times of the two active states, used to synthesize the reference voltages is greater than unity. The switching times of the active states are therefore scaled down in order to make the sum of the normalized time to be unity in the process of which the reference voltage is decreased. To synthesize the desired voltage reference, an off-line calculation method based on the scaled times is used to determine the switching trajectory of the converter to ensure that the fundamental component of the synthesized voltage equals the reference voltage [7.4]. Comparatively, the implementation of

generalized carrier-based PWM is much easier. It is proved that the same voltage can be generated through injecting zero sequence voltage. The magnitude of reference signal needs to be increased to generate higher voltage in the overmodulation region while the angle information remains the same [7.6]. Issues of current regulation, speed or torque control of motor drives, when operating in the converter over-modulation regions, have recently been considered when the SVPWM and GDPWM methods are implemented [7.5-7.6]. Dynamic over-modulation GDPWM characteristics are degraded because of the phase error between the reference and output voltages while the current control degradation is shown due to the load harmonic currents in the SVPWM implementation.

1.3 Research Motivation

The current research is motivated from the literature review given in the above because there is still a lot of research work that could be explored further. Some extensions can always be made based on the work previously done. In the case of PWM modulation scheme, the modulation techniques for the three-phase system have been explored comprehensively. However, this is the simplest case if the multi-phase system is considered that has more than three phases. The application of multi-phase systems is receiving more and more attentions due to their advantages. The corresponding modulation methods are still under exploration since there are multiple solutions and each has its own feature. For the three-phase system, the modulation methods using both sine-triangle comparison or space vector approaches have been generalized. The question for the multi-phase system is, whether it is possible to get the similar generalized zero

sequence voltage equation and then the modulation signals. This is possible by going through the similar process as finding the modulation schemes for the three-phase system. Unlike the three-phase system, some assumptions have to be made in order to reach the solution since there are a lot of voltage vectors that can be used to synthesize the desired voltages and it is not possible to use all of them. Also the other benefit of multi-phase modulation is that it could be used to drive more than one motor, which makes the generalized modulation scheme more useful.

The control of induction machines using natural variables was earlier proposed as a scalar approach. But the scalars are very often considered with other non-scalar variables together to solve some problems. Very little research work has been done on the control by just using the scalars as the states and so the advantages of using scalars are not exhibited extensively. The simulation and experimental works that have been done are not sufficient. Also the formulation of minimizing the losses in the machine using natural variables is not set up yet. Due to the large amount of industrial applications, energy saving in the induction machines is becoming more and more important. Once the loss minimization is formulated using the natural variables, everything could be done by using the same variables and it could result a lot of advantages.

Regarding the rotor speed estimation, some simple methods are still receiving a lot of attentions although some complicated methods have been reported. The sensorless approach using only one of the rotor voltage equations has been reported before. But the fact is that both rotor voltage equations could be used and a better estimation could result. This kind of estimation is classified as one type of the open-loop approaches using back-EMF calculations. The other category is the closed-loop estimation that utilizes certain

kind of adaptive mechanism to drive the estimated speed to the reference speed through defining some error functions. So the advantage is that the estimated speed converges to the actual speed unless the states are estimated incorrectly. The full-order flux observer has been implemented successfully and shown as a good method of speed estimation at the speed above zero. However, there are some important issues that are not addressed very well including the selection of the observer gains and the controller parameters for the speed estimation. These values are often chosen according to the experience by trial and error. But there must some methods that can be used to define the certain ranges so that the system is stable. Also these values are changing under different operating conditions including motoring and regenerating modes, which is not desirable. Now the question is whether it is possible to find the range such that a set of parameters work for all different operating conditions. This can be done based on the transfer function analysis to make the system stable. Certain criterions for the parameters selection can also be set up instead of picking up the parameters from the air. For example, the observer gain can be chosen by locating the poles using Butterworth polynomial or some other methods.

The over-modulation techniques have been studied using the space vector method. The reference voltage vector used to determine the switching is modified from the space vector diagram in order to generate the desired fundamental voltage when it is out of the realizable range. But the idea behind the space vector is the time calculation for the states. Is it possible to realize the over-modulation technique by examining the times calculated from the original reference voltages directly? The answer is confirmative. The normalized time spent on the top device is set to unity when it is greater than unity and

this leads to a new modulation. The equivalence between the carrier-based PWM and space vector PWM has been already found. But this kind of equivalence is not explored when they are applied for the operation in the over-modulation region. Also the difference between these two methods is not shown clearly. And the application of over-modulation techniques in the motor drive control remains a big problem.

1.4 Scope of Work

The research is carried out using one horsepower induction machine and the implementation is being implemented using a TI DSP (TMS320LF2407). The organization of the dissertation is as follows.

Chapter 2 reviews the modulation technique of carrier-based PWM and space vector PWM for the three-phase system. The equivalence is set up between these two methods and then the modulation technique is extended to the multi-phase system in the example of five and six phases. The generalized transformation is defined first to draw the space vector diagrams. The zero sequence voltage expressions are calculated in all sectors by choosing the appropriate active and null states. Then these expressions are generalized and added to the reference voltage to generate the modulation signals. The possibility of generating the voltages more than the fundamental one is explored and this approach can be used to drive two machines in series.

Chapter 3 presents the induction machine model. The stator and rotor voltage equations are expressed in both stationary and synchronous reference frames. The general transformations that could be used in the control are shown explicitly including the

Clarke, Park transformations and the corresponding reverse ones. The expressions in the synchronous reference are derived from the equations in the stationary reference frame using the transformations.

Chapter 4 illustrates the rotor flux oriented control of the induction machine. The basic idea of rotor flux orientation is presented and then the control scheme is derived for the speed control. This scheme is verified through simulation and then implemented using DSP. The implementation procedures are discussed in detail including the measurements and a lot of considerations in the DSP programming, which are also useful for the implementation of other different schemes.

Chapter 5 lays out the control scheme of induction machines using natural variables from the definition of natural variables. The minimum electrical loss strategy is formulated using the same variables, including the stator and rotor copper loss and stator core loss. The resultant optimum rotor flux is then used as the reference one and the whole scheme is simulated for the speed control. Also the sensorless approach using both rotor voltage equations is simulated and it gives much better estimation result. The experiments are conducted to verify the proposed formulation and the sensorless method.

Chapter 6 explores one of the closed-loop speed estimations using the full-order flux observer. The process of designing a full-order flux observer system is illustrated and the emphasis is given on the selection of observer gain and control parameters for the speed estimation. The 4th order Butterworth polynomial and D-decomposition methods are applied to determine these parameters to ensure the system stability. Appropriate parameters are chosen to make the system stable under both motoring and regenerating

modes. The simulation results show the characteristics of the full-order flux observer and the effectiveness of proposed method of selecting parameters.

Chapter 7 proposes a new over-modulation scheme using the concept of space vector. It has higher voltage gain compared with the traditional scaling method. The equivalence between the carrier-based PWM and space vector PWM is found and the applications in the current regulation are explored. The idea of eliminating the harmonic current in stationary reference frame is proposed in order to generate high fundamental voltages in the over-modulation region. Both PWM methods are implemented and the comparison is made on the analysis of advantages and disadvantages.

CHAPTER 2
PWM SCHEMES IN THREE-PHASE AND MULTI-PHASE VOLTAGE SOURCE
INVERTERS

2.1 Introduction

A general three-phase voltage source inverter feeding a three-phase load is shown in Figure 2.1. The main purpose of this topology is to generate a three-phase voltage source with controllable amplitude, phase angle, and frequency. Three-phase DC/AC voltage source inverters are extensively used in motor drives, active filters, and power flow controllers and uninterruptible power supplies (UPS) using various pulse width modulation (PWM) strategies. There are totally six power semiconductor devices, which can be transistors, MOSFETs, IGBTs, or any other components that can operate as switches and transfer power. The input DC source is usually obtained from a single-phase or three-phase diode-bridge rectifier with an LC or C filter. Various voltages can be generated from the voltage source converter by turning on and off the switches under certain combinations.

First, the modulation techniques using carrier-based PWM and space vector PWM are analyzed systematically. Then the modulation scheme for three-phase system is extended to multi-phase systems in general. The general transformation is defined and the voltage vectors that are used to synthesize the desired voltage are drawn in the case of five- and six-phase systems. It is possible to derive the similar zero sequence expressions

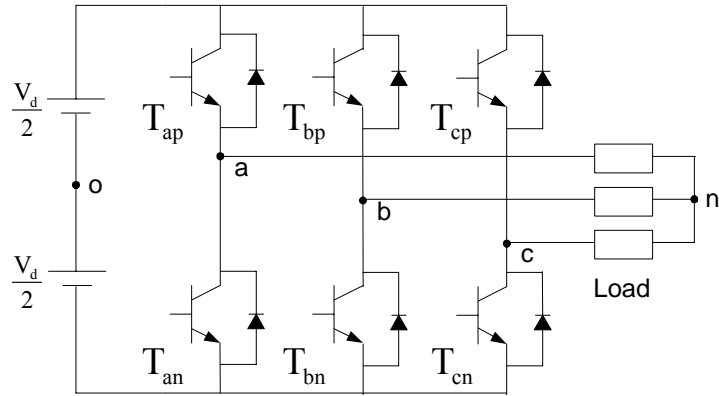


Figure 2.1 A general three-phase voltage source converter.

for the multi-phase systems to get the generalized carrier-based PWM approach. The insertion of third harmonic component makes it feasible to increase fundamental component and the usage of the DC bus voltage [2.5, 2.6]. The special application of the multi-phase voltage source converters is also discussed in driving multiple machines in series, which finds the advantages of saving switching devices although the losses increase due to the current with multiple harmonic components [2.7 – 2.9].

2.2 Carrier-Based PWM

It can be seen that the two switching devices on the same leg cannot be turned on at the same time. Otherwise it will short the voltage source. Also they are not supposed to be turned off at the same time, which will result in the uncertain voltage to the connected phase. Thus the nature of the two switches on the same leg is complementary. The turn-on and turn-off sequences of a switching device are represented by an existence function, which has a value of unity when it is turned on and becomes zero when it is turned off. In

general, an existence function of a two-level converter comprising of switching devices T_{ij} is represented by S_{ij} , $i = a, b, c$ and $j = p, n$ where i represents the load phase to which the device is connected, and j signifies top (p) and bottom (n) device of the inverter leg. Hence, S_{ap} , S_{an} which take values of zero or unity, are, respectively, the existence functions of the top device (T_{ap}) and bottom device (T_{an}) of the inverter leg which is connected to phase 'a' load.

$$\begin{aligned}
 S_{ap} + S_{an} &= 1 \\
 S_{bp} + S_{bn} &= 1 \\
 S_{cp} + S_{cn} &= 1
 \end{aligned} \tag{2.1}$$

In the ideal case, the voltage drop across the switch is immediately zero when the switch is turned on and the current flowing through the switch is zero when the switch is turned off. So at any time, the output voltage from the VSI can be expressed as

$$\begin{aligned}
 \frac{V_d}{2}(S_{ap} - S_{an}) &= V_{an} + V_{no} \\
 \frac{V_d}{2}(S_{bp} - S_{bn}) &= V_{bn} + V_{no} \\
 \frac{V_d}{2}(S_{cp} - S_{cn}) &= V_{cn} + V_{no}
 \end{aligned} \tag{2.2}$$

Since the switching functions for the two switching devices are dependent, it is convenient to use only one switching function to represent the switching status of each leg, which is always chosen as the switching function of upper device. So the turn-on and turn-off actions of the switches produce series of rectangular waveform and the ratio between the on-duration and a full cycle is defined as duty cycle, which is varying between 0 and 1. It is thus evident that varying the duty cycle of the switching device will result into variable output voltage. Both fundamental component and harmonic

components are buried in the series of pulses, in which only the fundamental component is necessary. Then (2.2) can be rewritten as

$$\begin{aligned}\frac{V_d}{2}(2S_{ap} - 1) &= V_{an} + V_{no} \\ \frac{V_d}{2}(2S_{bp} - 1) &= V_{bn} + V_{no} \\ \frac{V_d}{2}(2S_{cp} - 1) &= V_{cn} + V_{no}\end{aligned}\tag{2.3}$$

The switching or existence function is a series of modulation pulse whose magnitude is either unity or zero. A Fourier series approximation of this function is given as

$$\begin{aligned}S_{ap} &= \frac{1}{2} \cdot (1 + M_{ap}) \\ S_{bp} &= \frac{1}{2} \cdot (1 + M_{bp}) \\ S_{cp} &= \frac{1}{2} \cdot (1 + M_{cp})\end{aligned}\tag{2.4}$$

where M_{ap} , M_{bp} , M_{cp} are the carrier-based modulation signals comprising fundamental frequency component. They vary between -1 and 1 when operating in the linear modulation range.

In order to generate the desired fundamental voltage, the pulse width modulation is necessarily applied in three steps. The first step is to calculate the fundamental voltages with certain frequency, which is also called modulation signals that are required by the load. Then these modulation signals are compared with a much higher frequency triangle signal to generate PWM signals between 0 and 1. These PWM signals are amplified and used as the driving signals to the switching devices. The out voltage pulses are then

applied to the load, which result in a nearly sinusoidal current when the load is inductive in most cases. For a three-phase voltage source converter, there are three reference signals that are compared with the same carrier signal, which is generally a high frequency triangle wave. The ratio between the magnitude of the reference signal and half of the DC bus voltage is defined as the modulation index.

$$M = \frac{V^*}{\frac{V_d}{2}} \quad (2.5)$$

The carrier-based PWM using sine-triangle comparison is illustrated in Figure 2.2, in which the sinusoidal modulation signal is compared with the high frequency triangle carrier signal. When the modulation signal is greater than the triangle carrier signal, the output signal is high, which is used to drive the upper device of the phase to be ON state. The corresponding lower device is then off and the phase is connected to the positive rail of the DC bus. Whenever the modulation signal is less than the triangle carrier signal, the output signal is low, which is used to drive the lower device of the phase to be ON state. The corresponding upper device is then off and the phase is shorted to the negative rail of the DC bus. Assuming the frequency of the triangle signal is high enough, the fundamental component that can be extracted from the voltage pulses is almost equal to the reference signal. The output voltage is linear to the reference signal until the magnitude of the reference signal reaches $V_{dc}/2$, which is the maximum fundamental voltage that can be achieved. The maximum fundamental voltage that is generated from six-step operation is $(2/\pi)V_{dc}$. The linear operation range is limited to 78.5 percent. This limit is overcome by the alternative technique known as space vector modulation.

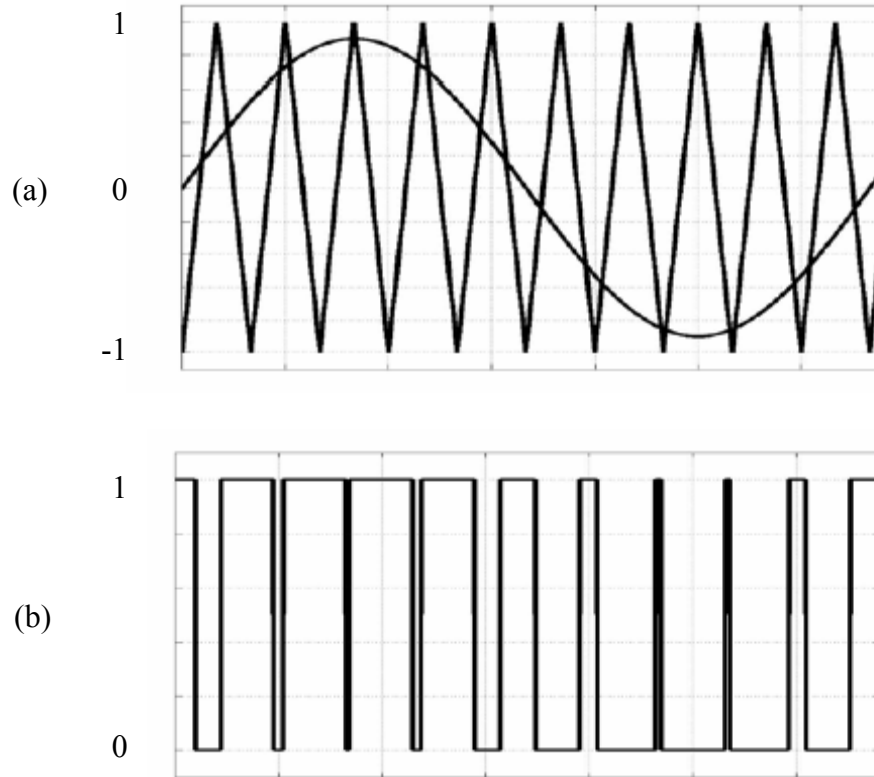


Figure 2.2 Illustration of carrier-based PWM using sine-triangle comparison method. (a) Modulation signal and carrier (triangle) signal. (b) the switching signal after the comparison.

The modulation signal generated from TI TMS320LF2407 DSP evaluation board is shown in Figure 2.3, in which the phase and line to line voltages are also shown.

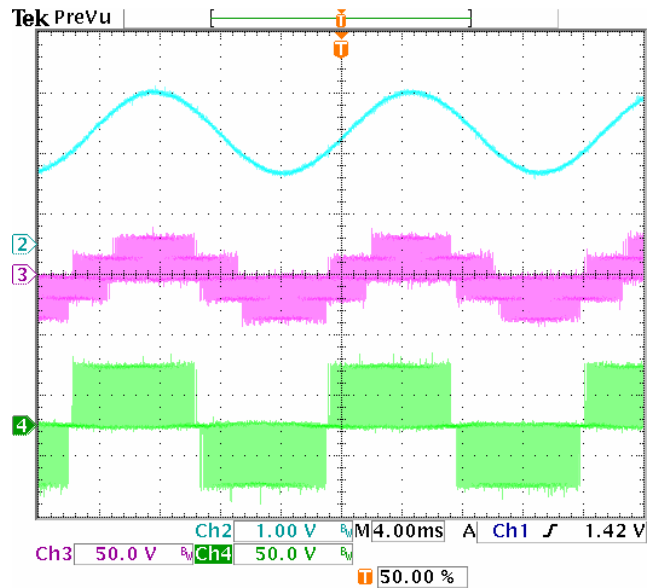


Figure 2.3 Carrier-based PWM generation. Ch2: modulation signal for phase A (0.6/div);
Ch3: phase A voltage V_a (50V/div); Ch4: line to line voltage V_{ab} (50V/div).

2.3 Space Vector PWM

Space vector PWM is the direct digital PWM method and uses the combination of possible modes to realize the desired reference voltages. As seen from Figure 2.1, there are totally six switching devices and only three of them are independent. The combination of these three switching states gives out eight possible operation modes. At any time, the inverter has to operate in one of these modes. Certain modes can be selected to synthesize the desired voltage in each switching period. All of the eight modes are shown in Table 2.1. Then the voltages corresponding to all of eight modes can be expressed in the q-d stationary reference frame.

For the three-wire system as shown in Figure 2.1, the sum of three phase voltages is zero. Then the voltage between the load neutral and the reference point of DC voltage is determined from (2.3).

$$\begin{aligned} \frac{V_d}{2}(2S_{ap} + 2S_{bp} + 2S_{cp} - 3) &= 3V_{no} \\ V_{no} &= \frac{V_d}{3} \left(S_{ap} + S_{bp} + S_{cp} - \frac{3}{2} \right) \end{aligned} \quad (2.6)$$

After substituting the above voltage into (2.3) again, the phase voltages can be expressed in terms of three switching functions and the DC bus voltage.

$$\begin{aligned} V_{ap} &= \frac{V_d}{3} (2S_{ap} - S_{bp} - S_{cp}) \\ V_{bp} &= \frac{V_d}{3} (-S_{ap} + 2S_{bp} - S_{cp}) \\ V_{cp} &= \frac{V_d}{3} (-S_{ap} - S_{bp} + 2S_{cp}) \end{aligned} \quad (2.7)$$

The general transformation between different reference frame (abc stationary reference frame and q-d reference frame) is illustrated in Figure 2.4, in which f represents any quantity in the certain frame including the voltage, current, flux linkage etc. And the corresponding transformation matrix (both the transformation and the inverse transformation) is shown in (2.8) assuming the angle between these two reference frames is θ .

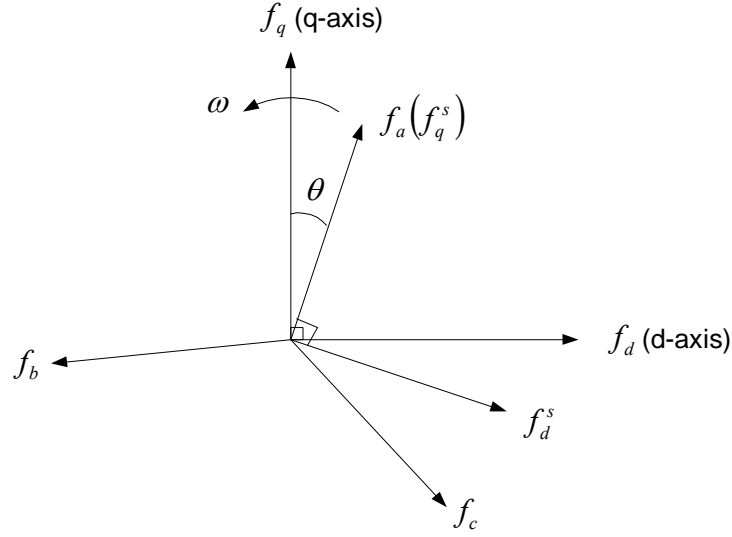


Figure 2.4 Transformation between reference frames.

$$\begin{bmatrix} f_q \\ f_d \\ f_0 \end{bmatrix} = \frac{2}{3} \begin{bmatrix} \cos \theta & \cos\left(\theta - \frac{2\pi}{3}\right) & \cos\left(\theta + \frac{2\pi}{3}\right) \\ \sin \theta & \sin\left(\theta - \frac{2\pi}{3}\right) & \sin\left(\theta + \frac{2\pi}{3}\right) \\ \frac{1}{2} & \frac{1}{2} & \frac{1}{2} \end{bmatrix} \begin{bmatrix} f_a \\ f_b \\ f_c \end{bmatrix} \quad (2.8)$$

$$\begin{bmatrix} f_a \\ f_b \\ f_c \end{bmatrix} = \begin{bmatrix} \cos \theta & \sin \theta & 1 \\ \cos\left(\theta - \frac{2\pi}{3}\right) & \sin\left(\theta - \frac{2\pi}{3}\right) & 1 \\ \cos\left(\theta + \frac{2\pi}{3}\right) & \sin\left(\theta + \frac{2\pi}{3}\right) & 1 \end{bmatrix} \begin{bmatrix} f_q \\ f_d \\ f_0 \end{bmatrix}$$

In the space vector PWM, the transformation between abc and stationary q-d reference frames is needed just for the voltages. Then the voltages in q-d reference frame are calculated for all eight modes using (2.9) assuming the sum of three-phase voltages is zero. The voltage between the load neutral and the reference point of DC voltage is calculated from (2.6).

$$\begin{aligned}
V_{qp} &= V_{an} = \frac{V_d}{3}(2S_{ap} - S_{bp} - S_{cp}) \\
V_{dp} &= \frac{1}{\sqrt{3}}(-V_{bn} + V_{cn}) \\
&= \frac{1}{\sqrt{3}}(-S_{bp} + S_{cp}) \\
V_{pn} &= \frac{V_d}{3}\left(S_{ap} + S_{bp} + S_{cp} - \frac{3}{2}\right)
\end{aligned} \tag{2.9}$$

Table 2.1 Switching modes of the three-phase voltage source inverter and corresponding stationary reference frame qdns voltages

Mode	S_{ap}	S_{bp}	S_{cp}	V_{qp}	V_{dp}	V_{pn}
U_0	0	0	0	0	0	$-\frac{V_d}{2}$
U_5	0	0	1	$-\frac{V_d}{3}$	$\frac{V_d}{\sqrt{3}}$	$-\frac{V_d}{6}$
U_3	0	1	0	$-\frac{V_d}{3}$	$-\frac{V_d}{\sqrt{3}}$	$-\frac{V_d}{6}$
U_4	0	1	1	$-\frac{2V_d}{3}$	0	$\frac{V_d}{6}$
U_1	1	0	0	$\frac{2V_d}{3}$	0	$-\frac{V_d}{6}$
U_6	1	0	1	$\frac{V_d}{3}$	$\frac{V_d}{\sqrt{3}}$	$\frac{V_d}{6}$
U_2	1	1	0	$\frac{V_d}{3}$	$-\frac{V_d}{\sqrt{3}}$	$\frac{V_d}{6}$
U_7	1	1	1	0	0	$\frac{V_d}{2}$

These modes and corresponding q-d-o voltages are shown in Figure 2.5, which is also called as the space vector diagram.

In order to synthesize the desired three-phase voltages, these voltages are transformed into the stationary reference frame as V_{qd}^* as shown in Figure 2.5. The general transformation for any three-phase voltage set is

$$\begin{aligned}
 V_{qs}^* &= \frac{2}{3} \left(V_{an} - \frac{1}{2} V_{bn} - \frac{1}{2} V_{cn} \right) \\
 V_{ds}^* &= \frac{2}{3} \left(-\frac{\sqrt{3}}{2} V_{bn} + \frac{\sqrt{3}}{2} V_{cn} \right) \\
 V_{os}^* &= \frac{2}{3} \left(\frac{1}{2} V_{an} + \frac{1}{2} V_{bn} + \frac{1}{2} V_{cn} \right)
 \end{aligned} \tag{2.10}$$

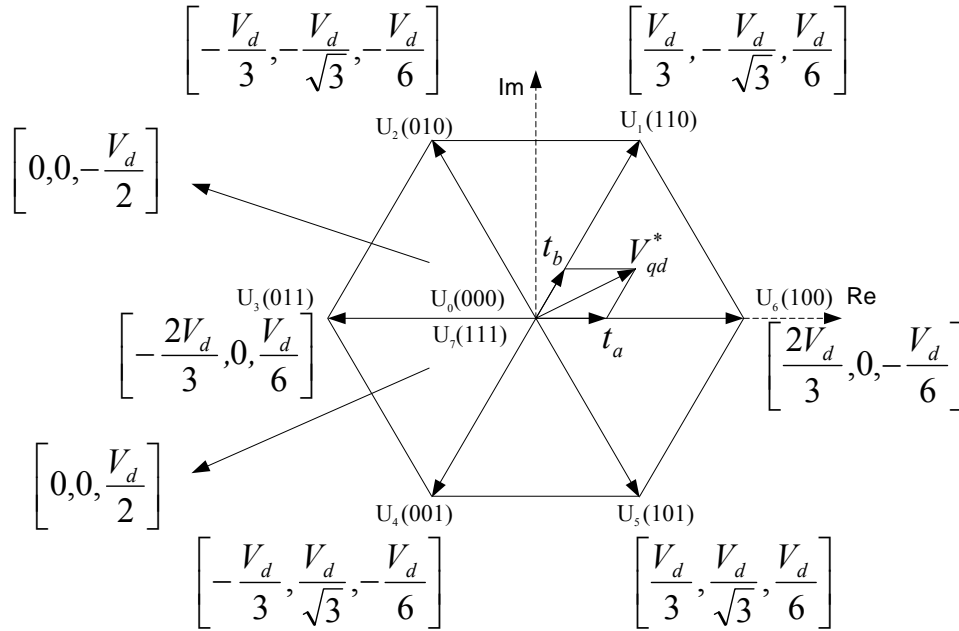


Figure 2.5 Voltage space vector diagram for three-leg, three-phase voltage source converter including zero sequence voltages.

For the balanced case, V_{os}^* is equal to zero. However, in general

$$V_{pn} = V_{os}^* + V_{no} \quad (2.11)$$

This reference voltage vector is then used to calculate the turn-on times of the inverter switching devices required to synthesize a reference three-phase balanced voltage set. In general, the three-phase balanced voltages expressed in the stationary reference frame, situated in the appropriate sector in Figure 2.5, are approximated by the time-average over a sampling period (inverter switching period, T_s) of the two adjacent active q-d voltage vectors and the two zero states U_0 and U_7 in order to minimize the number of switching during transient. If the normalized times (with respect to modulator sampling time or inverter switching period, T_s) of the four voltage vectors termed as V_{qda} , V_{qdb} , V_{qd0} , V_{qd7} are t_a , t_b , t_0 , t_7 respectively. The q and d components of the reference voltage V_{qd}^* and the zero sequence voltage are approximated as

$$\begin{aligned} V_{qs}^* &= V_{qpa}t_a + V_{qpb}t_b + V_{qp0}t_0 + V_{qp7}t_7 \\ V_{ds}^* &= V_{dpa}t_a + V_{dpb}t_b + V_{dp0}t_0 + V_{dp7}t_7 \\ <V_{no} + V_{os}^* >= V_{pna}t_a + V_{pnb}t_b + V_{pn0}t_0 + V_{pn7}t_7 \end{aligned} \quad (2.12)$$

where V_{os} is the zero sequence voltage due to the three-phase reference voltages. It is observed that both V_{qd0} and V_{qd7} do not influence the values of t_a and t_b .

$$\begin{bmatrix} V_{qs}^* \\ V_{ds}^* \end{bmatrix} = \begin{bmatrix} V_{qpa} & V_{qpb} \\ V_{dpa} & V_{dpb} \end{bmatrix} \begin{bmatrix} t_a \\ t_b \end{bmatrix} \quad (2.13)$$

So the times for the two active states are calculated as

$$\begin{bmatrix} t_a \\ t_b \end{bmatrix} = \begin{bmatrix} V_{qpa} & V_{qpb} \\ V_{dpa} & V_{dpb} \end{bmatrix}^{-1} \begin{bmatrix} V_{qs}^* \\ V_{ds}^* \end{bmatrix}$$

$$\begin{aligned}
t_a &= \frac{V_{dpb} \cdot V_{qs}^* - V_{qpb} \cdot V_{ds}^*}{V_{qpa} V_{dpb} - V_{qpb} V_{dpa}} \\
t_b &= \frac{-V_{dpa} \cdot V_{qs}^* + V_{qpa} \cdot V_{ds}^*}{V_{qpa} V_{dpb} - V_{qpb} V_{dpa}}
\end{aligned}
\tag{2.14}$$

In general, the sum of these two times is less than 1 when the inverter works in the linear modulation region. Hence the time left has to be utilized by the two null states.

$$\begin{aligned}
t_c &= 1 - t_a - t_b \\
t_0 &= \alpha \cdot t_c \\
t_7 &= (1 - \alpha) \cdot t_c
\end{aligned}
\tag{2.15}$$

where $0 \leq \alpha \leq 1$. In general, it has been shown that the best voltage synthesis is achieved when the converter is operating in the linear modulation region when $\alpha = 0.5$.

One of the most frequently used sequences to synthesize a reference voltage vector that is rotating counter-clockwise for all six sectors is shown in Figure 2.6. In each sector, the starting and ending conditions for all upper switching devices are state mode 0 while the state mode 7 happens in the middle of the switching period. The minimum switching is achieved by this arrangement.

The modulation signal generated from DSP is shown in Figure 2.7, in which the reference phase voltage, phase, and line to line voltages are also shown.

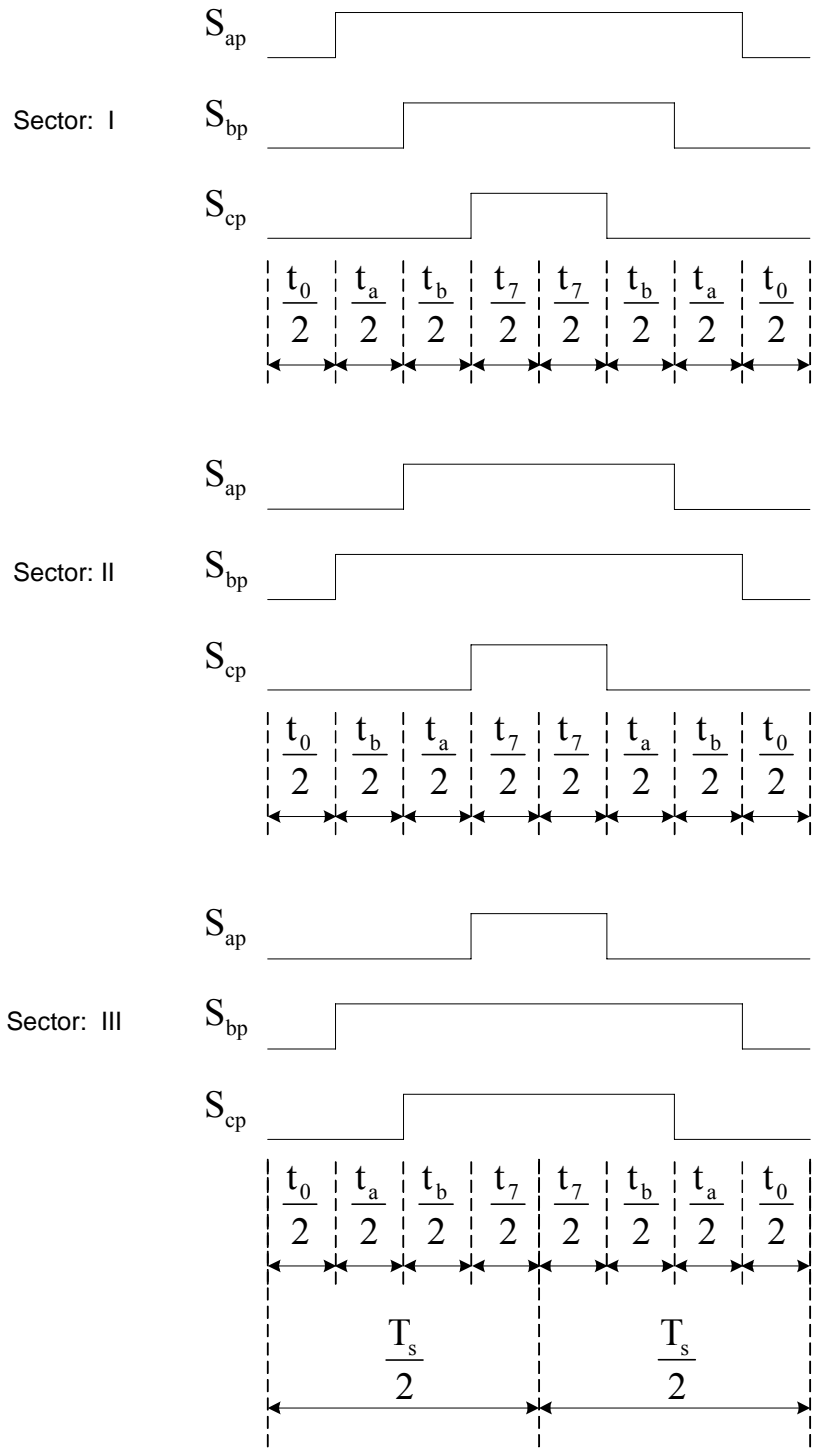


Figure 2.6a Existence functions of top devices in sectors I, II, III.

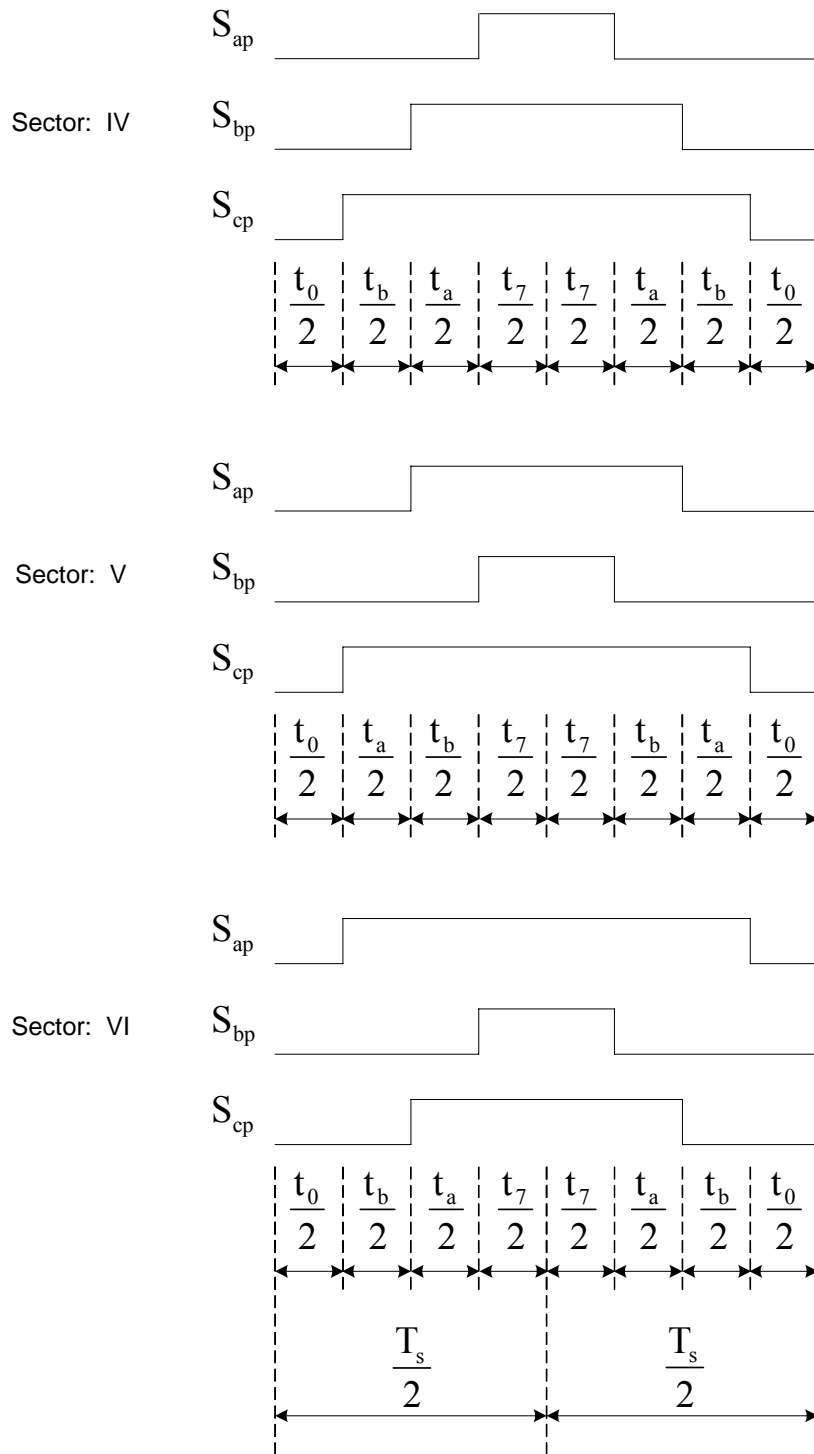


Figure 2.6b Existence functions of top devices in sectors IV, V, VI.

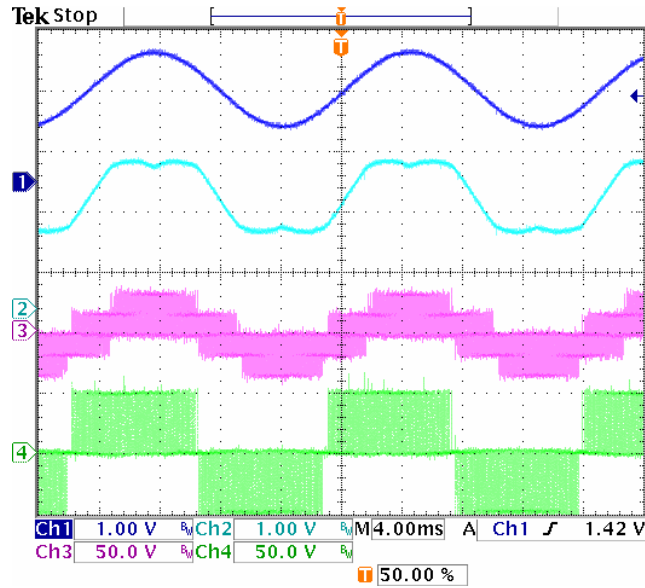


Figure 2.7 Space vector PWM generation. Ch1: reference voltage for phase A (0.6/div); Ch2: modulation signal for phase A (0.6/div); Ch3: phase A voltage V_a (50V/div); Ch4: line to line voltage V_{ab} (50V/div).

2.4 Generalized Discontinuous Modulation Scheme

The generalized discontinuous carrier-based PWM modulation for the three-leg voltage source converter is made possible by the appropriate definition of the neutral voltage V_{no} . As mentioned in the above section, the time durations for those two active modes are determined by the reference voltages. However, the distribution factor between two null modes (0 and 7) is not determined yet. It means that different value for α can be chosen to generate different zero sequence voltages to satisfying the particular operation objective. One of the major problems faced by the voltage source inverter in the high power application is that the switching loss is extremely high compared with the power that can be transferred. If the switching devices can be clamped to either the

positive or negative rails of the DC link voltage during some switching periods, the effective switching frequency will reduce and the switching loss will also decrease. But the line-line voltages remain the same. This is so-called discontinuous PWM and there are different types of discontinuous PWM schemes. Since all of these different schemes are based on the selection of α , it is possible to derive the general expression that is used to generate all the possibilities.

The average neutral voltage, V_{no} , can be determined using the method of space vector modulation and the voltages of the three-phase voltage source converter. As seen from (2.10), the zero sequence voltage is determined by the selection of α since t_a and t_b are calculated from the desired balance reference voltages. For example, in sector I, the switching times for the two active modes are calculated as

$$V_{qpa} = \frac{2}{3}V_d, V_{dpa} = 0; V_{qpb} = \frac{1}{3}V_d, V_{dpb} = -\frac{1}{\sqrt{3}}V_d$$

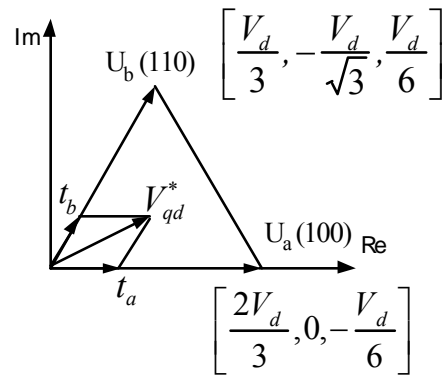


Figure 2.8 Time determination in sector I.

$$\begin{aligned}
t_a &= \frac{V_{dpb} \cdot V_{qs}^* - V_{qpb} \cdot V_{ds}^*}{V_{qpa}V_{dpb} - V_{qpb}V_{dpa}} = \frac{3V_{qs}^* + \sqrt{3}V_{ds}^*}{2V_d} \\
t_b &= \frac{-V_{dpa} \cdot V_{qs}^* + V_{qpa} \cdot V_{ds}^*}{V_{qpa}V_{dpb} - V_{qpb}V_{dpa}} = \frac{-\sqrt{3}V_{ds}^*}{V_d}
\end{aligned} \tag{2.16}$$

Similarly the times in other sectors can be calculated as shown in Table 2.2.

Then these times can be further expressed in terms of reference phase voltages and even the line-line voltages in Table 2.3 using the inverse transformation.

$$\begin{aligned}
V_{an} &= V_{qs} + V_{os} \\
V_{bn} &= -\frac{1}{2}V_{qs} - \frac{\sqrt{3}}{2}V_{ds} + V_{os} \\
V_{cn} &= -\frac{1}{2}V_{qs} + \frac{\sqrt{3}}{2}V_{ds} + V_{os}
\end{aligned} \tag{2.17}$$

Table 2.2 Device Switching times expressed in terms of reference voltages

Sector	I	II	III
t_a	$\frac{3V_{qs}^* + \sqrt{3}V_{ds}^*}{2V_d}$	$\frac{3V_{qs}^* - \sqrt{3}V_{ds}^*}{2V_d}$	$\frac{-\sqrt{3}V_{ds}^*}{V_d}$
t_b	$\frac{-\sqrt{3}V_{ds}^*}{V_d}$	$\frac{-3V_{qs}^* - \sqrt{3}V_{ds}^*}{2V_d}$	$\frac{-3V_{qs}^* + \sqrt{3}V_{ds}^*}{2V_d}$

Sector	IV	V	VI
t_a	$\frac{-3V_{qs}^* - \sqrt{3}V_{ds}^*}{2V_d}$	$\frac{-3V_{qs}^* + \sqrt{3}V_{ds}^*}{2V_d}$	$\frac{\sqrt{3}V_{ds}^*}{V_d}$
t_b	$\frac{\sqrt{3}V_{ds}^*}{V_d}$	$\frac{3V_{qs}^* + \sqrt{3}V_{ds}^*}{2V_d}$	$\frac{3V_{qs}^* - \sqrt{3}V_{ds}^*}{2V_d}$

Table 2.3 Device Switching times expressed in terms of reference line-line voltages

Sector	I	II	III	IV	V	VI
t_a	$\frac{V_{ab}}{V_d}$	$\frac{V_{ac}}{V_d}$	$\frac{V_{bc}}{V_d}$	$\frac{V_{ba}}{V_d}$	$\frac{V_{ca}}{V_d}$	$\frac{V_{cb}}{V_d}$
t_b	$\frac{V_{bc}}{V_d}$	$\frac{V_{ba}}{V_d}$	$\frac{V_{ca}}{V_d}$	$\frac{V_{cb}}{V_d}$	$\frac{V_{ab}}{V_d}$	$\frac{V_{ac}}{V_d}$
Max voltage	$V_{ap} - V_{os}$	$V_{bp} - V_{os}$	$V_{bp} - V_{os}$	$V_{cp} - V_{os}$	$V_{cp} - V_{os}$	$V_{ap} - V_{os}$
Min voltage	$V_{cp} - V_{os}$	$V_{cp} - V_{os}$	$V_{ap} - V_{os}$	$V_{ap} - V_{os}$	$V_{bp} - V_{os}$	$V_{bp} - V_{os}$

The average neutral voltage for each sector can be generalized in terms of the calculated times as shown in Table 2.4.

The general expression for the average neutral voltage can be derived by considering Tables 2.3 and 2.4 together and expressing the average zero sequence voltage in terms of the maximum and minimum reference phase voltages. For example, in sector 1,

$$V_{\max} = V_{ap} - V_{os}, V_{\min} = V_{cp} - V_{os} \text{ and } V_{bp} - V_{os} = -(V_{\max} + V_{\min})$$

$$t_a = \frac{V_{ab}}{V_d} = \frac{2V_{\max} + V_{\min}}{V_d}, t_b = \frac{V_{bc}}{V_d} = \frac{-V_{\max} - 2V_{\min}}{V_d}$$

$$t_c = 1 - t_a - t_b = 1 - \frac{V_{\max} - V_{\min}}{V_d}$$

Table 2.4 Average neutral voltage for all sectors

Sectors	I, III, V	II, IV, VI
$\langle V_{no} \rangle$	$\frac{V_d}{6}(t_b - t_a) + \frac{V_d}{2}(1 - 2\alpha)t_c$	$\frac{V_d}{6}(t_a - t_b) + \frac{V_d}{2}(1 - 2\alpha)t_c$

$$\begin{aligned}
\langle V_{no} \rangle &= \frac{V_d}{6}(t_b - t_a) + \frac{V_d}{2}(1 - 2\alpha)t_c \\
&= \frac{-V_{\max} - V_{\min}}{2} + \frac{V_d}{2}(1 - 2\alpha) \left(1 - \frac{V_{\max} - V_{\min}}{V_d}\right) \\
&= \frac{V_d}{2}(1 - 2\alpha) - \alpha V_{\min} - (1 - \alpha)V_{\max}
\end{aligned} \tag{2.18}$$

After calculating the average zero sequence voltages for all six sectors, the equation (2.18) becomes the general expression for the average zero sequence voltage. In the case of carrier-based PWM, this zero sequence voltage is added to the fundamental component to generate the modulation signal, which is compared with a carrier signal. The final modulation signal is

$$M_{ip} = \frac{2V_{ip}}{V_d} + (1 - 2\alpha) - \alpha \frac{2V_{\min}}{V_d} - (1 - \alpha) \frac{2V_{\max}}{V_d} \tag{2.19}$$

where $i = a, b, c$ representing three phases.

In the implementation of this modulation scheme, the null-state partition parameter (α) can take any form (constant or time-varying) ranging between 0 and 1. The choice of α affects the average neutral voltage between the load star-point and the inverter reference point. In the conventional space vector modulation, α is generally taken as 0.5. When α is either 0 or 1 and for any depth of modulation magnitude, each switching device ceases to switch for a total of 120 degrees per fundamental cycle. Under the above condition, the switching losses and effective inverter switching frequency are significantly reduced. However, other functions of α may be used, which may lead to performance improvement of the modulator. The selection of α gives rise to an infinite number of possible carrier-based PWM modulation signals, some of which have been

discovered and referred to as the generalized discontinuous PWM. The generalized discontinuous modulation signal is obtained when [2.10]:

$$\alpha = \frac{1}{2} \{1 + \text{sgn}[\cos 3(\omega t + \delta)]\} \quad (2.20)$$

where $\text{sgn}(X)$ is 1, 0 and -1 when X is positive, zero, and negative, respectively. By varying the modulation angle δ , various discontinuous modulation signals are generated. In general, it has been shown that the best voltage synthesis when the inverter is operating in the linear modulation region and $\alpha = 0.5$. In the over-modulation regions, the generalized discontinuous scheme is most appropriate with a promise of enlarged voltage linearity, if the appropriate modulation angle δ is utilized.

For the direct implementation (space vector PWM), this is realized by selecting the appropriate α and calculating the equivalent on-durations for three top switching devices. Then the existence functions shown in Figure 2.6 are applied when the reference voltage is located in one of six sectors.

The modulation signals generated from DSP are shown in Figure 2.9, in which the reference phase voltage, phase and line to line voltages are also shown. By varying δ , the difference in the modulation signals can be seen clearly in the figures below.

The turn-on times for the three top devices corresponding to the three legs are listed in Table 2.5. All of these times are within 0 and 1 (normalized with respect to the switching period). These times can actually be used as the modulation signals. And the same PWM signals will be generated if the carrier triangle signal is limited within 0 and 1 instead of within -1 and 1, and then used for the comparison as in the above sine-triangle PWM method.

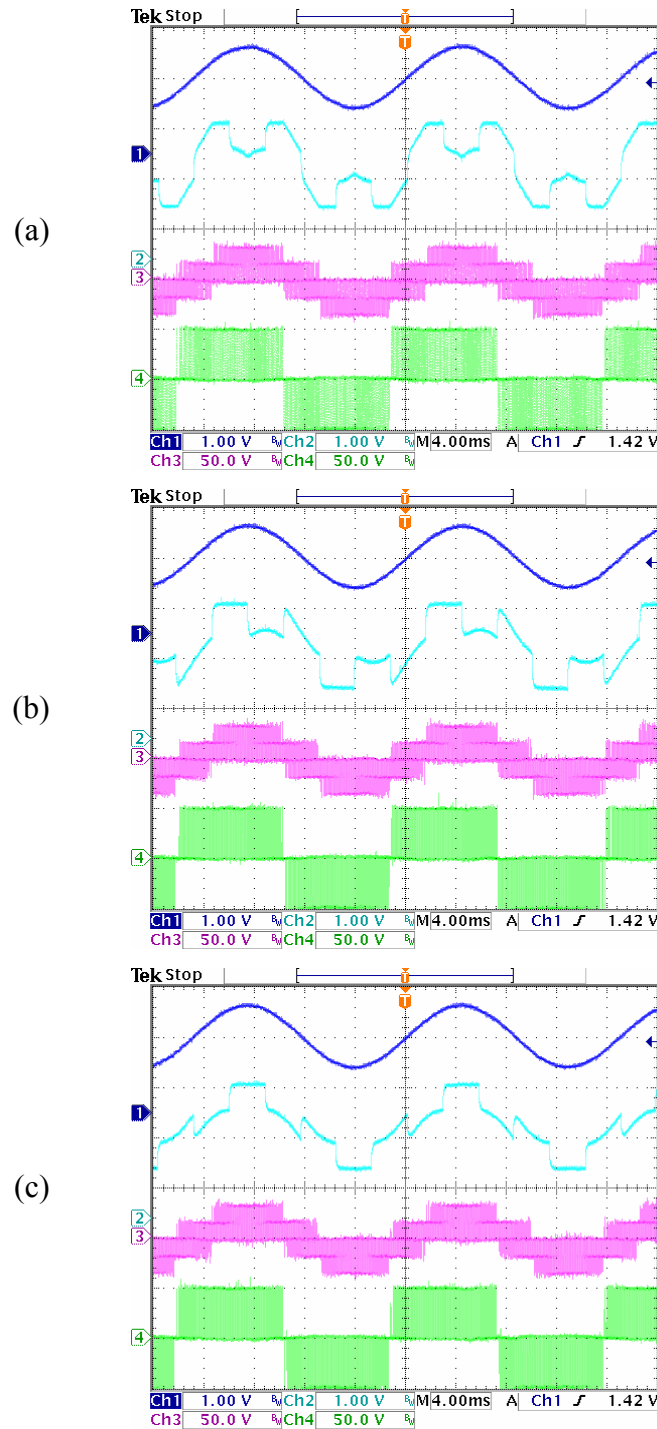


Figure 2.9 Generalized discontinuous PWM generation using $\alpha = 0.5 \cdot \{1 + \text{sgn}[\cos 3(\omega t + \delta)]\}$: (a) $\delta = 0^\circ$; (b) $\delta = -30^\circ$; (c) $\delta = -60^\circ$. Ch1: reference voltage for phase A (0.6/div); Ch2: modulation signal for phase A (0.6/div); Ch3: phase A voltage V_a (50V/div); Ch4: line to line voltage V_{ab} (50V/div).

Table 2.5 Normalized times when the three top devices are turned on.

Sector	I	II	III	IV	V	VI
τ_{ap}	$t_a + t_b + t_7$	$t_a + t_7$	t_7	t_7	$t_b + t_7$	$t_a + t_b + t_7$
τ_{bp}	$t_b + t_7$	$t_a + t_b + t_7$	$t_a + t_b + t_7$	$t_a + t_7$	t_7	t_7
τ_{cp}	t_7	t_7	$t_b + t_7$	$t_a + t_b + t_7$	$t_a + t_b + t_7$	$t_a + t_7$

2.5 Modulation Scheme for Multi-Phase Systems

In all multi-phase electric machines, multi-phase converters are required to deliver currents of different frequencies either for use of single machines requiring fundamental and third harmonic currents to improve torque capability or to achieve independent control of serially connected motors needing many fundamental frequency currents for the mutually decoupled machines. Traditionally, the multi-phase converters use hysteresis-type current controllers to impress the required currents. Although very simple to implement, its inherent nonlinearity, the varying switching frequency of the converters lead to uneven distribution of losses in the switching devices of the converter. This then constrains the converter thermal design and selection of converter filtering elements. Hence it is not the optimum control scheme for high power applications where efficiency optimization and ease of converter cooling are premium design requirements. It is desirable therefore to use control schemes that ensure defined converter switching frequency such as the space vector PWM and carrier-based sine-triangle PWM modulation to command the load phase voltages that impress the commanded multi-frequency (non-sinusoidal) phase currents. The feasibility of controlling individual

components of the non-sinusoidal phase currents of multi-phase motors using synchronous reference frame current controllers and voltage source converters has been established. Each current component in their individual synchronous reference frames yields constant dc qd quantities which with the classical PI controllers and decoupling schemes can be regulated without phase and magnitude errors [2.16]. The outputs of the controllers are commanded phase voltages for each frequency component which are used to synthesize the converter output voltages.

While existing multi-motor drives use a common dc bus to drive converters, each feeding a three-phase motor which are individually and independent controlled. The multi-phase machines provide the opportunity that two or more machines can be connected in series by using single inverter. It is envisaged that multiphase machines with other serially connected motors fed with single multi-phase converters will deliver the advantages of few converter legs and associated control circuitry without comprising the independent controllability of the individual drives.

This section presents the generalized carrier-based continuous and discontinuous PWM techniques to generate all the possible voltage components of multiphase converters with special attention paid to the five and six phase variants. Carrier-based sine-triangle modulation scheme is preferred in multiphase converters when compared to the digitally implemented space vector because of its simplicity of implementation either digitally or analogically (it requires calculation of switching times and sequencing of the switching states). With the proposed modulation, it is possible with a single five phase converter to drive a five phase machine connected in series with another five-phase machine with a transposed winding arrangement which are independently controlled

while improving the torque capability of the first five phase motor. Similarly, a six-phase converter with appropriate carrier-based modulation scheme to be determined, produces balanced fundamental and third harmonic voltages for a six-phase machine in addition to a balanced three-phase voltage set or two-phase voltage set for three- or two-phase machines connected in series with the six-phase machine.

2.5.1 Generalized Complex-Variable Q-D Reference Frame Transformation

The expressions for the stationary reference frame transformation for the variables of n-phase machines are determined from the machine impedance matrix. When the machine is balanced, the impedance matrix is circulant in which case its eigenvectors correspond to the columns of the nth phase stationary reference frame transformation expressed in complex-variable form [2.22, 2.23]. Hence, the stationary reference frame transformation $T(0)$ and its inverse for n phase balanced system are given respectively, as

$$T(0) = \frac{1}{n} \begin{bmatrix} 1 & 1 & 1 & \cdots & 1 \\ 1 & a^1 & a^2 & \cdots & a^{(n-1)} \\ 1 & a^2 & a^4 & \cdots & a^{2(n-1)} \\ \vdots & \vdots & \vdots & \ddots & \vdots \\ 1 & a^{(n-1)} & a^{2(n-1)} & \cdots & a^{(n-1)^2} \end{bmatrix} \quad (2.21)$$

$$T(0)^{-1} = \begin{bmatrix} 1 & 1 & 1 & \cdots & 1 \\ 1 & a^{-1} & a^{-2} & \cdots & a^{-(n-1)} \\ 1 & a^{-2} & a^{-4} & \cdots & a^{-2(n-1)} \\ \vdots & \vdots & \vdots & \ddots & \vdots \\ 1 & a^{-(n-1)} & a^{-2(n-1)} & \cdots & a^{-(n-1)^2} \end{bmatrix} \quad (2.22)$$

where $a = e^{j\alpha}$ and $\alpha = \frac{2\pi}{n}$.

For five phase balanced variables f_a, f_b, f_c, f_d, f_e , the generalized qd arbitrary reference frame transformed variables expressed in the complex-variable form are

$$f_0 = 1/5[f_a + f_b + f_c + f_d + f_e] \quad (2.23a)$$

$$f_{qd1} = 1/5[f_a + af_b + a^2 f_c + a^3 f_d + a^4 f_e] e^{-j\varphi_{e1}} \quad (2.23b)$$

$$f_{qd2} = 1/5[f_a + a^2 f_b + a^4 f_c + a f_d + a^3 f_e] e^{-j\varphi_{e2}} \quad (2.23c)$$

$$f_{qd3} = 1/5[f_a + a^3 f_b + af_c + a^4 f_d + a^2 f_e] e^{-j\varphi_{e3}} \quad (2.23d)$$

$$f_{qd4} = 1/5[f_a + a^4 f_b + a^3 f_c + a^2 f_d + af_e] e^{-j\varphi_{e4}} \quad (2.23e)$$

For the six-phase balanced variables, $f_a, f_b, f_c, f_d, f_e, f_f$, the generalized qd arbitrary reference frame transformed variables expressed in the complex-variable form are

$$f_0 = 1/6[f_a + f_b + f_c + f_d + f_e + f_f] \quad (2.24a)$$

$$f_{qd1} = 1/6[f_a + af_b + a^2 f_c + a^3 f_d + a^4 f_e + a^5 f_f] e^{-j\varphi_{e1}} \quad (2.24b)$$

$$f_{qd2} = 1/6[f_a + a^2 f_b + a^4 f_c + f_d + a^2 f_e + a^4 f_f] e^{-j\varphi_{e2}} \quad (2.24c)$$

$$f_{qd3} = 1/6[f_a + a^3 f_b + f_c + a^3 f_d + f_e + a^3 f_f] e^{-j\varphi_{e3}} \quad (2.24d)$$

$$f_{qd4} = 1/6[f_a + a^4 f_b + a^2 f_c + f_d + a^4 f_e + a^2 f_f] e^{-j\varphi_{e4}} \quad (2.24e)$$

$$f_{qd5} = 1/6[f_a + a^5 f_b + a^4 f_c + a^3 f_d + a^2 f_e + af_f] e^{-j\varphi_{e5}} \quad (2.24f)$$

$\varphi_{ei} = \omega_{ei}t + \varphi_i$, $i = 1, 2, \dots, n$, ω_{ei} are the rotating frequencies of the reference frames and the initial angles are φ_i .

Multi-phase motor windings produce a torque-producing rotating field only if the spatial displacement angles of its phase windings are equal to the temporal displacement angles of the phase currents. The transformed quantities comprise of zero, positive and negative sequence components of which only the positive and negative sequence components produce average torque. Hence, the positive, negative and zero sequence motor magnetomotive force (MMF) can be determined by transforming the MMFs produced by the phases using (2.23-24) for five and six phase machines. It is assumed that the fundamental components of the n-phase machine winding functions are mutually displaced by $2\pi/n$ in the positive sequence and the phase currents are also spatially displaced by the same angle, but sequenced in all possible orders. For the five phase machine, (2.23a) gives the zero sequence component, two positive sequences are produced by (2.23b-23c) and negative sequence MMFs are also produced by (2.23d-23e). Hence, the windings producing the two positive sequence MMFs can be connected as shown in Figure 2.10. For the third harmonic MMF of the windings, a positive sequence MMF is produced only with the use of 2.23(b). From this analysis and Figure 2.10, it is inferred that average torques can be produced with the serial connection of two five-phase winding machines with phase current transposition in the second machine. A balanced third harmonic current in the first machine will also produce an average torque interacting with its third harmonic MMF. Hence the five-phase converter feeding the machine must generate up to three voltage components. Similar considerations lead to Figure 2.11 for the six-phase machines. The feasible serial connections shown in Figure 2.11 consist of a six-phase and a three-phase machine for which the six-phase converter delivers possible two voltage components for the two machines.

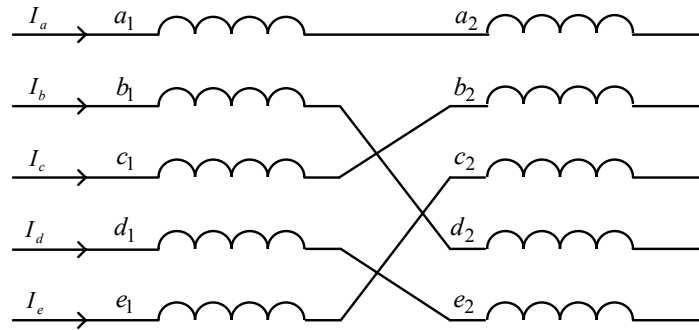


Figure 2.10 Feasible windings connections for five-phase machines : series connection of machines.

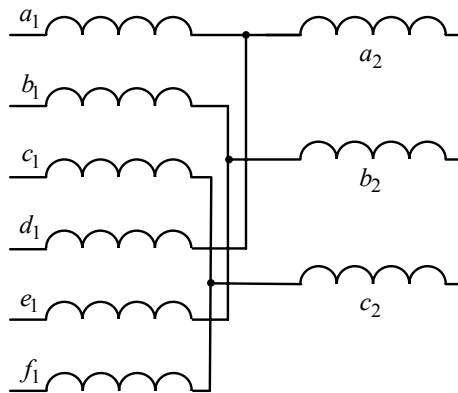


Figure 2.11 Feasible windings connections for six-phase machines : series connection of machines, six and three-phase machines.

2.5.2 Modulation Technique for Multi-Phase Converters

Figure 2.12 shows a schematic diagram of a multi-phase voltage source converter. The switching of the devices are described by switching functions which take values of one and zero when the devices are turned on or turned off, respectively.

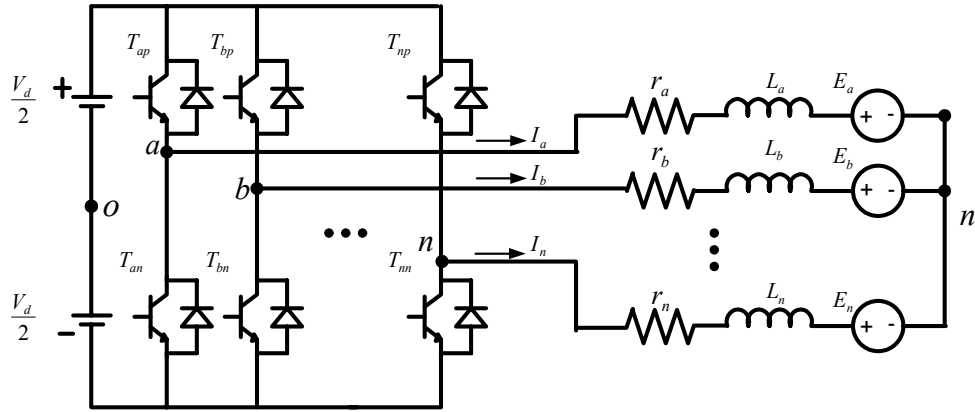


Figure 2.12 Schematic diagram of a multi-phase voltage source converter.

The switching functions of the top devices are S_{ip} ($i = a, b, c, \dots, n$) are complimentary with the switching functions of the bottom devices. The n-phase voltages are therefore expressed as

$$\frac{V_d}{2} \cdot (2S_{ip} - 1) = V_{in} + V_{no},$$

$$S_{ip} = \frac{1}{2} \cdot (1 + M_{ip}), \quad i = a, b, c, d, e, \dots, n \quad (2.25)$$

S_{ip} and M_{ip} are the switching functions and the modulation signals for the i^{th} leg, respectively. The neutral voltage is V_{no} and the phase voltages are V_{in} . The expression for the modulation signals which are compared with a high frequency triangle waveform using sine-triangle carrier-based PWM technique to synthesize the desired phase voltages V_{in} (which may be multi-frequency, in general) is given as

$$M_{ip} = \frac{V_{in} + V_{no}}{V_d / 2} \quad (2.26)$$

The neutral voltage V_{no} in (2.25) is indeterminate and can take any realistic values. When V_{no} is set equal to zero or is a continuous function of time, continuous modulation signals and a continuous carrier-based modulation scheme result. However the performance of the converter can be enhanced with the selection of an appropriate expression of the average neutral sequence voltage like it is done in three-phase, two level converters to achieve discontinuous, continuous, and space vector carrier-based PWM modulation [2.10, 2.24]. In this section, the stationary reference frame transformed converter phase voltages are used to determine the expression for the average neutral voltage which substituted in (2.26) yields the equation for the modulation signals.

2.5.3 Modulation for Five-Phase Converters

A five-phase voltage source converter with an input DC voltage given as V_d has 32 switching modes, 30 of which are active and the other two are null modes. The converter is to generate the five phase voltages ($V_{an}, V_{bn}, V_{cn}, V_{dn}, V_{en}$) comprising of sum of all or some of the voltage sets ($V_{an1}, V_{bn1}, V_{cn1}, V_{dn1}, V_{en1}$), ($V_{an2}, V_{bn2}, V_{cn2}, V_{dn2}, V_{en2}$) and ($V_{an13}, V_{bn13}, V_{cn13}, V_{dn13}, V_{en13}$) expressed as ($\alpha = 2\pi / 5$):

$$\begin{aligned}
 V_{an1} &= V_1 \cos(\omega_e t + \gamma) \\
 V_{bn1} &= V_1 \cos(\omega_e t + \gamma - \alpha) \\
 V_{cn1} &= V_1 \cos(\omega_e t + \gamma - 2\alpha) \\
 V_{dn1} &= V_1 \cos(\omega_e t + \gamma - 3\alpha) \\
 V_{en1} &= V_1 \cos(\omega_e t + \gamma - 4\alpha)
 \end{aligned} \tag{2.27a}$$

$$\begin{aligned}
V_{an13} &= V_{13} \cos 3(\omega_e t + \beta) \\
V_{bn13} &= V_{13} \cos 3(\omega_e t + \beta - \alpha) \\
V_{cn13} &= V_{13} \cos 3(\omega_e t + \beta - 2\alpha) \\
V_{dn13} &= V_{13} \cos 3(\omega_e t + \beta - 3\alpha) \\
V_{en13} &= V_{13} \cos 3(\omega_e t + \beta - 4\alpha)
\end{aligned} \tag{2.27b}$$

$$\begin{aligned}
V_{an2} &= V_2 \cos(\omega_2 t + \xi) \\
V_{bn2} &= V_2 \cos(\omega_2 t + \xi - 2\alpha) \\
V_{cn2} &= V_2 \cos(\omega_2 t + \xi - 4\alpha) \\
V_{dn2} &= V_2 \cos(\omega_2 t + \xi - \alpha) \\
V_{en2} &= V_2 \cos(\omega_2 t + \xi - 3\alpha)
\end{aligned} \tag{2.27c}$$

The phase angles of the voltages are ξ , γ , β . The phase and neutral voltages from (2.25) for the five-phase converter are

$$\begin{aligned}
V_d S_{ap} - \frac{V_d}{2} &= V_{an} + V_{no} \\
V_d S_{bp} - \frac{V_d}{2} &= V_{bn} + V_{no} \\
V_d S_{cp} - \frac{V_d}{2} &= V_{cn} + V_{no} \\
V_d S_{dp} - \frac{V_d}{2} &= V_{dn} + V_{no} \\
V_d S_{ep} - \frac{V_d}{2} &= V_{en} + V_{no} \\
V_{no} &= \frac{V_d}{5} (S_{ap} + S_{bp} + S_{cp} + S_{dp} + S_{ep}) - \frac{V_d}{2}
\end{aligned} \tag{2.28}$$

Hence, for balanced phase voltages, the converter phase and neutral voltages are given as

$$\begin{aligned}
V_{an} &= \frac{V_d}{5} (4S_{ap} - S_{bp} - S_{cp} - S_{dp} - S_{ep}) \\
V_{bn} &= \frac{V_d}{5} (-S_{ap} + 4S_{bp} - S_{cp} - S_{dp} - S_{ep}) \\
V_{cn} &= \frac{V_d}{5} (-S_{ap} - S_{bp} + 4S_{cp} - S_{dp} - S_{ep}) \\
V_{dn} &= \frac{V_d}{5} (-S_{ap} - S_{bp} - S_{cp} + 4S_{dp} - S_{ep}) \\
V_{en} &= \frac{V_d}{5} (-S_{ap} - S_{bp} - S_{cp} - S_{dp} + 4S_{ep})
\end{aligned} \tag{2.29}$$

Substituting (2.29) into (2.23), the stationary reference frame qd voltages for each of the four components are calculated and displayed in Figure 2.13. It is however, observed that space vectors V_{qd1} and V_{qd4} are complex conjugates, so are V_{qd2} and V_{qd3} . Hence, only two space vectors V_{qd1} and V_{qd2} are used for voltage synthesis. V_{qd1} generates the fundamental frequency voltages (2.27a) and V_{qd2} produces the third harmonic voltages (2.27b) required for the third harmonic machine MMF for torque production or voltages in (2.27c) to interact with the transposed second five phase machine connected with the first machine. The voltage vectors of the neutral voltage V_o are used for the determination of the average neutral voltage required in (2.26).

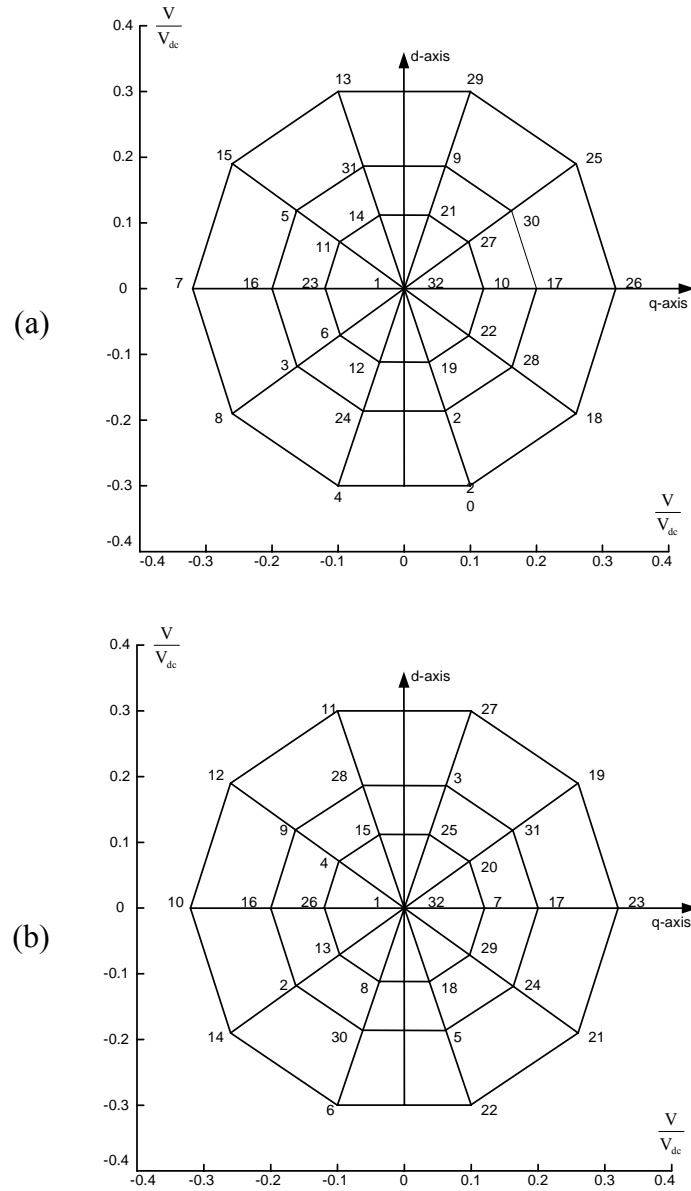


Figure 2.13a Voltage space vector diagrams of a five-phase PWM inverter. (a) V_{qd1} ; (b)

V_{qd2} .

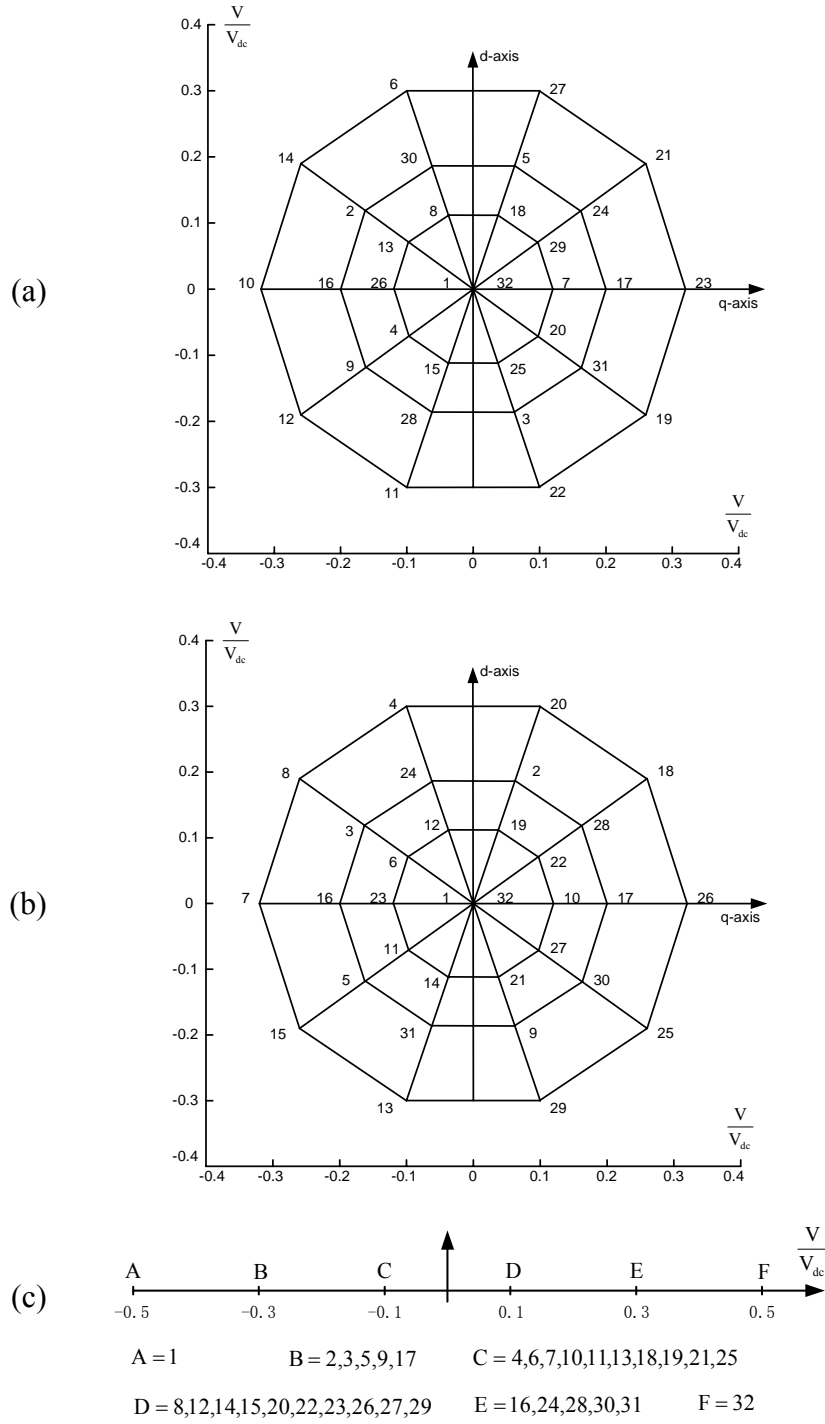


Figure 2.13b Voltage space vector diagrams of a five-phase PWM inverter. (a) V_{qd3} ; (b)

V_{qd4} ; (c) V_o .

Vectors with the largest values in V_{qd1} give the least magnitude voltages in V_{qd2} , while the middle valued vectors in V_{qd1} are corresponding to the middle valued vectors in V_{qd2} . Active vectors used to synthesize voltages are chosen as the outer and middle vectors in V_{qd1} as shown in Figure 2.14.

Reference voltages V_{qd1}^* and V_{qd2}^* in any sector of the space vector are synthesized by time-averaging some four active and two null voltage vectors as illustrated in Figure 2.14 for sector 1. In sector 1 of the V_{qd1} space vector, the active modes are [17(V_{qd11}), 25(V_{qd14}), 26(V_{qd12}), 30(V_{qd13})] and the two null vectors are [1(V_{qd101}) and 32(V_{qd132})]. The corresponding voltage vectors in V_{qd2} are also selected. Since the qd voltages of the null vectors are zero, the linear equations for determining the averaging times for the vectors are

$$\begin{aligned} V_{qd1} &= V_{qd11}t_1 + V_{qd12}t_2 + V_{qd13}t_3 + V_{qd14}t_4 + V_{qd101}t_{01} + V_{qd132}t_{032} \\ V_{qd2} &= V_{qd21}t_1 + V_{qd22}t_2 + V_{qd23}t_3 + V_{qd24}t_4 + V_{qd201}t_{01} + V_{qd232}t_{032} \end{aligned} \quad (2.30)$$

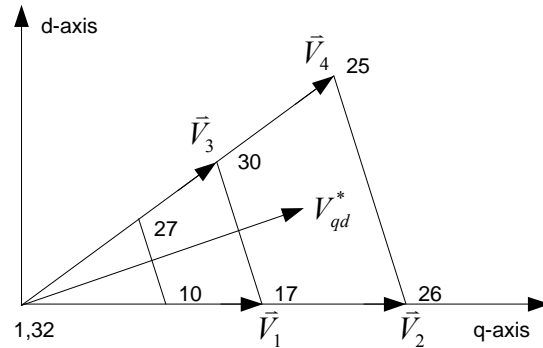


Figure 2.14 Synthesis of the fundamental voltage in sector 1.

The time ratio between two null states (1 and 32) are defined as $t_{01} = \mu t_c$, $t_{032} = (1 - \mu)t_c$ with the variable μ ranging between zero and unity. With $t_c = 1 - (t_1 + t_2 + t_3 + t_4)$, the average neutral voltage corresponding to the selected voltage vectors for sector 1 is

$$\begin{aligned}
 V_o &= \frac{V_d}{2} \left[\frac{4}{5}(-t_1 + t_3) + \frac{2}{5}(t_2 - t_4) + \frac{6}{5}(1 - 2\mu) \right. \\
 &\quad \left. - \frac{6}{5}(1 - 2\mu)(t_1 + t_2 + t_3 + t_4) \right] \\
 V_{o1} &= \frac{4}{5}(-t_1 + t_3) \\
 V_{o2} &= \frac{2}{5}(t_2 - t_4) \\
 V_{oo} &= (t_1 + t_2 + t_3 + t_4)
 \end{aligned} \tag{2.31}$$

The expressions for times t_1 , t_2 , t_3 , and t_4 obtained from (2.30) are substituted into (2.31) yielding the neutral sequence voltage in terms of V_{qd1} and V_{qd2} . Calculations similar to (2.30-31) are done for all the ten sectors of V_{qd1} for which ten expressions are obtained for the average neutral voltages. Using the inverse stationary reference frame transformations (2.22) the qd voltages in the equations for the ten average neutral voltages are expressed in terms of the phase voltages (V_{an} , V_{bn} , V_{cn} , V_{dn} , V_{en}). It is further desirable to reduce the complexity of these expressions and unify them by expressing them in terms of the instantaneous maximum and minimum phase voltages V_{\max} , V_{\min} . When the q- and d-axis reference voltages are expressed in terms of phase voltages, the times spent on the voltage vectors can be calculated. The coefficients of the phase voltages are shown in Table 2.6, which is corresponding to the condition when $V_{qd2} = 0$.

Table 2.6a Analysis on V_{o1} for V_{qd1} ($V_{qd2} = 0$)

Sector	-0.2211	0.5789	0.5789	-0.2211	-0.7155
1	V_a	V_b	V_c	V_d	V_e
2	V_b	V_a	V_e	V_d	V_c
3	V_b	V_c	V_d	V_e	V_a
4	V_c	V_b	V_a	V_e	V_d
5	V_c	V_d	V_e	V_a	V_b
6	V_d	V_c	V_b	V_a	V_e
7	V_d	V_e	V_a	V_b	V_c
8	V_e	V_d	V_c	V_b	V_a
9	V_e	V_a	V_b	V_c	V_d
10	V_a	V_e	V_d	V_c	V_b

Table 2.6b Analysis on V_{o2} for V_{qd1} ($V_{qd2} = 0$)

Sector	0.1789	-0.4683	-0.4683	0.1789	0.5789
1	V_a	V_b	V_c	V_d	V_e
2	V_b	V_a	V_e	V_d	V_c
3	V_b	V_c	V_d	V_e	V_a
4	V_c	V_b	V_a	V_e	V_d
5	V_c	V_d	V_e	V_a	V_b
6	V_d	V_c	V_b	V_a	V_e
7	V_d	V_e	V_a	V_b	V_c
8	V_e	V_d	V_c	V_b	V_a
9	V_e	V_a	V_b	V_c	V_d
10	V_a	V_e	V_d	V_c	V_b

Table 2.6c Analysis on V_{oo} for V_{qd1} ($V_{qd2} = 0$)

Sector	0.7236	0.4472	-0.4472	-0.7236	0
1	V_a	V_b	V_c	V_d	V_e
2	V_b	V_a	V_e	V_d	V_c
3	V_b	V_c	V_d	V_e	V_a
4	V_c	V_b	V_a	V_e	V_d
5	V_c	V_d	V_e	V_a	V_b
6	V_d	V_c	V_b	V_a	V_e
7	V_d	V_e	V_a	V_b	V_c
8	V_e	V_d	V_c	V_b	V_a
9	V_e	V_a	V_b	V_c	V_d
10	V_a	V_e	V_d	V_c	V_b

These tables can be further simplified as in Table 2.7. In the case of sector 1, V_a and V_d are the maximum and minimum phase voltages respectively. V_e can be expressed in terms of V_a and V_d as $V_e = 1.618 \cdot (V_a + V_d)$ since

$$\begin{aligned}
 V_a + V_d &= V \cos(\omega t) + V \cos(\omega t - 3\beta) \\
 &= 2V \cos\left(\omega t - \frac{3}{2}\beta\right) \cos\left(\frac{3}{2}\beta\right) \\
 &= -2V \cos(\omega t - 4\beta) \cos\left(\frac{3}{2}\beta\right) \\
 &= 0.618 \cdot V_e
 \end{aligned}$$

$$V_a = V_{\max}$$

$$V_d = V_{\min}$$

Table 2.7a Analysis on V_{o1} for V_{qd1} ($V_{qd2} = 0$)

Sector	-0.8000	-0.8000	-1.2944
1	V_a	V_d	V_e
2	V_b	V_d	V_c
3	V_b	V_e	V_a
4	V_c	V_e	V_d
5	V_c	V_a	V_b
6	V_d	V_a	V_e
7	V_d	V_b	V_c
8	V_e	V_b	V_a
9	V_e	V_c	V_d
10	V_a	V_c	V_b

Table 2.7b Analysis on V_{o2} for V_{qd1} ($V_{qd2} = 0$)

Sector	0.6472	0.6472	1.0472
1	V_a	V_d	V_e
2	V_b	V_d	V_c
3	V_b	V_e	V_a
4	V_c	V_e	V_d
5	V_c	V_a	V_b
6	V_d	V_a	V_e
7	V_d	V_b	V_c
8	V_e	V_b	V_a
9	V_e	V_c	V_d
10	V_a	V_c	V_b

Table 2.7c Analysis on V_{o0} for V_{qd1} ($V_{qd2} = 0$)

Sector	$a_1 : 0.7236$	$a_2 : 0.4472$	$a_3 : a_2 \cdot 0.618$ $= 0.2764$	$a_1 + a_3 = 1$
1	$V_a - V_d$	$V_b - V_c$	$V_a - V_d$	$V_a - V_d$
2	$V_b - V_d$	$V_a - V_e$	$V_b - V_d$	$V_b - V_d$
3	$V_b - V_e$	$V_c - V_d$	$V_b - V_e$	$V_b - V_e$
4	$V_c - V_e$	$V_b - V_a$	$V_c - V_e$	$V_c - V_e$
5	$V_c - V_a$	$V_d - V_e$	$V_c - V_a$	$V_c - V_a$
6	$V_d - V_a$	$V_c - V_b$	$V_d - V_a$	$V_d - V_a$
7	$V_d - V_b$	$V_e - V_a$	$V_d - V_b$	$V_d - V_b$
8	$V_e - V_b$	$V_d - V_c$	$V_e - V_b$	$V_e - V_b$
9	$V_e - V_c$	$V_a - V_b$	$V_e - V_c$	$V_e - V_c$
10	$V_a - V_c$	$V_e - V_d$	$V_a - V_c$	$V_a - V_c$

The average neutral voltage in sector 1 can be expressed as (2.32a) ($0 \leq \mu \leq 1$).

Similarly the average neutral voltage in sector 4 can be expressed as (2.32b), in which

$V_c = V_{\max}$, $V_e = V_{\min}$. After tedious and time-consuming calculations for all sectors, the

generalized average neutral voltage is given as (2.32c).

$$V_0 = (-0.8 - 1.2944 \cdot 1.618 + 0.6472 + 1.0472 \cdot 1.618) \cdot (V_a + V_d) + \frac{3}{5}(1 - 2\mu)\frac{V_d}{2} - \frac{3}{5}(1 - 2\mu)(V_a - V_d) \quad \text{- Sector 1} \quad (2.32a)$$

$$V_0 = (-0.8 - 1.2944 \cdot 1.618 + 0.6472 + 1.0472 \cdot 1.618) \cdot (V_c + V_e) + \frac{3}{5}(1 - 2\mu)\frac{V_d}{2} - \frac{3}{5}(1 - 2\mu)(V_c - V_e) \quad \text{- Sector 4} \quad (2.32b)$$

$$V_0 = -0.5528 \cdot (V_{\max} + V_{\min}) + \frac{3}{5}(1 - 2\mu)\frac{V_d}{2} - \frac{3}{5}(1 - 2\mu)(V_{\max} - V_{\min}) \quad (2.32c)$$

When $\mu = 0.5$, the neutral voltage depends on the sum of the instantaneous maximum

and minimum voltages of the phase voltages which is similar is what is arrived at by

intuition in [2.21]. Converter operation in the under-modulation region is best when $\mu = 0.5$. When the desired phase magnitudes are high, requiring operation in the over-modulation region, by varying μ as a function time thereby using V_o to clamp the switching devices to the upper or lower voltage rail is desirable.

2.5.4 Modulation for Six-Phase Converters

The six-phase converter phase and neutral voltages when the load voltages are balanced are given as

$$\begin{aligned}
 V_{an} &= \frac{V_d}{6} (5S_{ap} - S_{bp} - S_{cp} - S_{dp} - S_{ep} - S_{fp}) \\
 V_{bn} &= \frac{V_d}{6} (-S_{ap} + 5S_{bp} - S_{cp} - S_{dp} - S_{ep} - S_{fp}) \\
 V_{cn} &= \frac{V_d}{6} (-S_{ap} - S_{bp} + 5S_{cp} - S_{dp} - S_{ep} - S_{fp}) \\
 V_{dn} &= \frac{V_d}{6} (-S_{ap} - S_{bp} - S_{cp} + 5S_{dp} - S_{ep} - S_{fp}) \\
 V_{en} &= \frac{V_d}{6} (-S_{ap} - S_{bp} - S_{cp} - S_{dp} + 5S_{ep} - S_{fp}) \\
 V_{fn} &= \frac{V_d}{6} (-S_{ap} - S_{bp} - S_{cp} - S_{dp} - S_{ep} + 5S_{fp}) \\
 V_{no} &= \frac{V_d}{6} (S_{ap} + S_{bp} + S_{cp} + S_{dp} + S_{ep} + S_{fp}) - \frac{V_d}{2}
 \end{aligned} \tag{2.33}$$

The six space vector diagrams for the six-phase converter corresponding to the stationary reference frame transformations (2.24) are shown in Figure 2.15. The voltage vectors V_{qd1} , V_{qd5} are complex conjugates as also the vectors V_{qd2} and V_{qd4} . Hence V_{qd1}

is used to synthesize a fundamental frequency voltage set (2.34a), $(V_{an1}, V_{bn1}, V_{cn1}, V_{dn1}, V_{en1}, V_{fn1})$. V_{qd2} produces a second voltage set (2.34b), which is three phase $(V_{an2}, V_{bn2}, V_{cn2}, V_{dn2}, V_{en2}, V_{fn2})$ and V_{qd3} generates the third voltage set (2.34c) which is two-phase $(V_{an3}, V_{bn3}, V_{cn3}, V_{dn3}, V_{en3}, V_{fn3})$. At the same time, a third harmonic voltage set (2.34d) $(V_{an13}, V_{bn13}, V_{cn13}, V_{dn13}, V_{en13}, V_{fn13})$ can be produced. The neutral voltage V_o is again used to determine the average neutral voltage.

$$\begin{aligned}
V_{an1} &= V_1 \cos(\omega_e t + \gamma) \\
V_{bn1} &= V_1 \cos(\omega_e t + \gamma - \alpha) \\
V_{cn1} &= V_1 \cos(\omega_e t + \gamma - 2\alpha) \\
V_{dn1} &= V_1 \cos(\omega_e t + \gamma - 3\alpha) \\
V_{en1} &= V_1 \cos(\omega_e t + \gamma - 4\alpha) \\
V_{fn1} &= V_1 \cos(\omega_e t + \gamma - 5\alpha)
\end{aligned} \tag{2.34a}$$

$$\begin{aligned}
V_{an2} &= V_{dn2} = V_2 \cos(\omega_2 t + \xi) \\
V_{bn2} &= V_{en2} = V_2 \cos(\omega_2 t + \xi - 2\pi/3) \\
V_{cn2} &= V_{fn2} = V_2 \cos(\omega_2 t + \xi + 2\pi/3)
\end{aligned} \tag{2.34b}$$

$$\begin{aligned}
V_{an3} &= V_{cn3} = V_{en3} = V_3 \cos(\omega_3 t + \psi) \\
V_{bn3} &= V_{dn3} = V_{fn3} = V_3 \cos(\omega_3 t + \psi - \pi)
\end{aligned} \tag{2.34c}$$

$$\begin{aligned}
V_{an13} &= V_{13} \cos 3(\omega_e t + \beta) \\
V_{bn13} &= V_{13} \cos 3(\omega_e t + \beta - \alpha) \\
V_{cn13} &= V_{13} \cos 3(\omega_e t + \beta - 2\alpha) \\
V_{dn13} &= V_{13} \cos 3(\omega_e t + \beta - 3\alpha) \\
V_{en13} &= V_{13} \cos 3(\omega_e t + \beta - 4\alpha) \\
V_{fn13} &= V_{13} \cos 3(\omega_e t + \beta - 5\alpha)
\end{aligned} \tag{2.34d}$$

To obtain the modulation signal expressions needed for the generation of some or all of the possible voltage combinations, the equation of the neutral voltage is required.

However, a choice has to be made on the selection of the voltage vectors to be used to synthesize the desired voltages since there are many combinations that yield the same result.

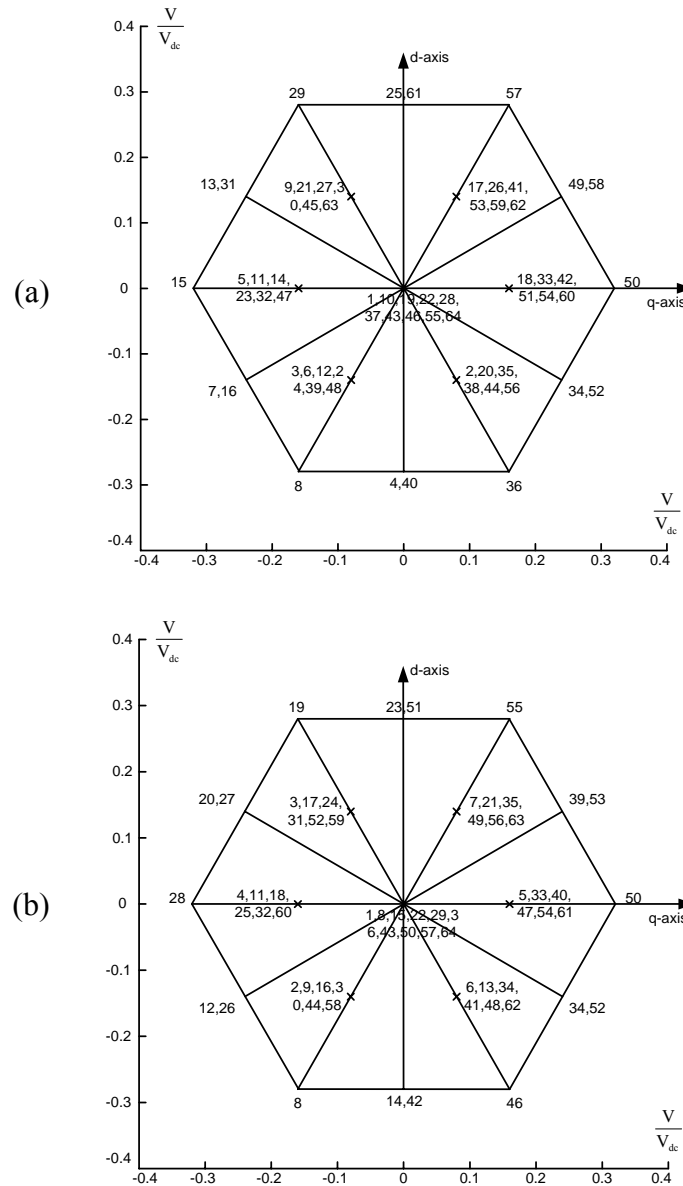


Figure 2.15a The space vector voltages for the six-phase converter. (a) V_{qd1} ; (b) V_{qd2} .

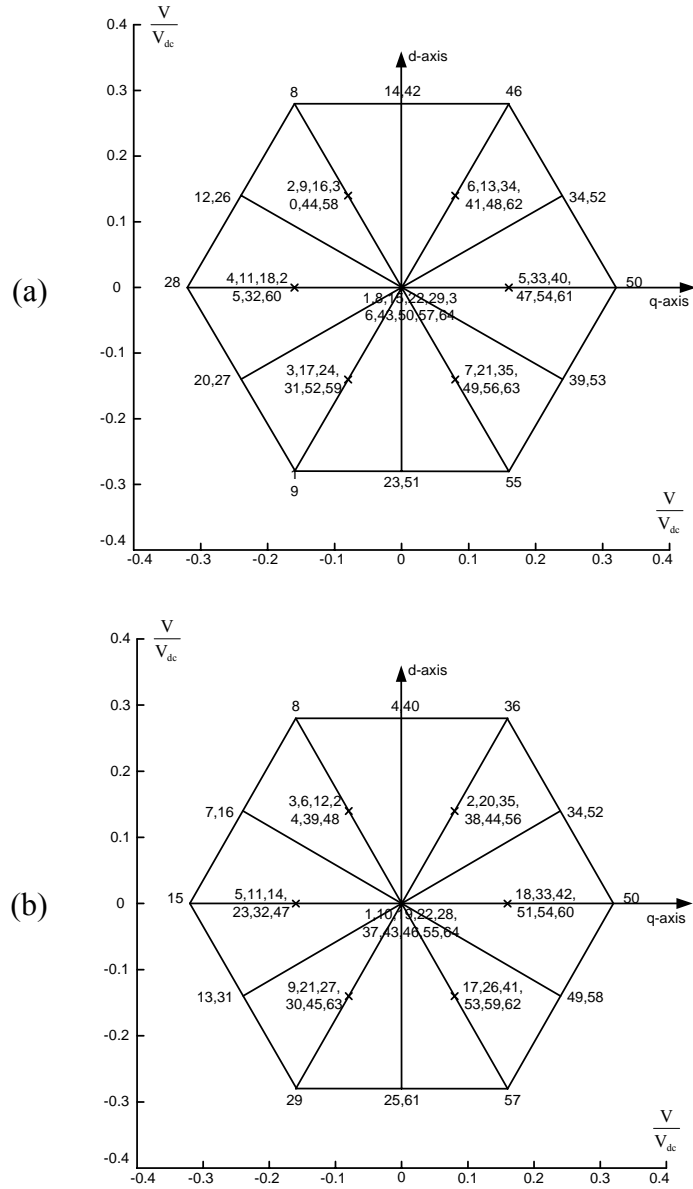


Figure 2.15b The space vector voltages for the six-phase converter. (a) V_{qd4} ; (b) V_{qd5} .

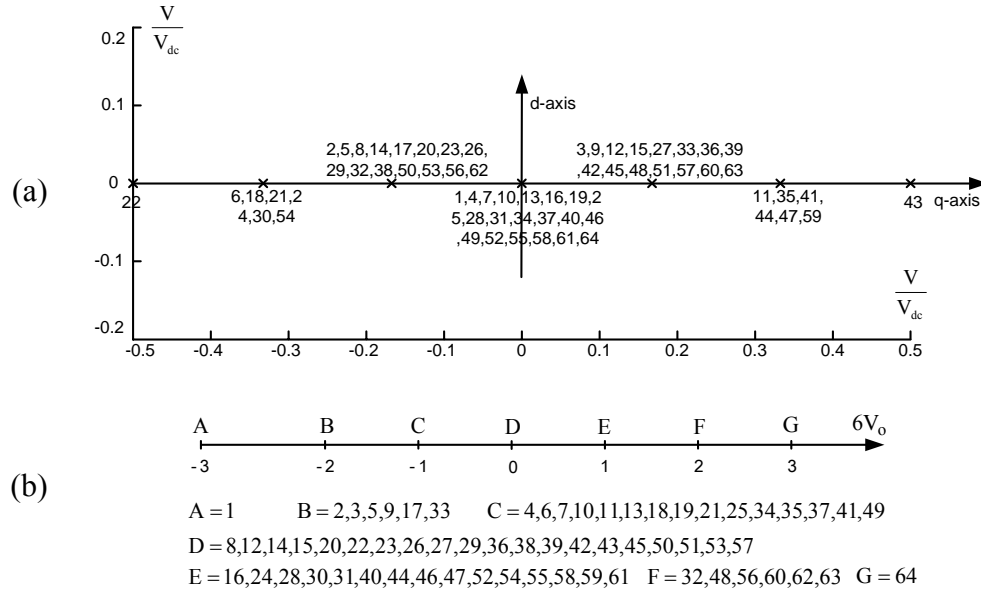


Figure 2.15c The space vector voltages for the six-phase converter. (a) V_{qd3} ; (b) V_o .

The determination of the average neutral voltage when it is desired to synthesize all the three possible voltages requires the use of the three space vector voltages V_{qd1} , V_{qd2} , and V_{qd3} . The voltage vectors of V_{qd1} used to generate the three voltage sets in sector 1 are shown in Figure 2.16, however this selection is not unique. The times these voltage vectors and their corresponding V_{qd2} and V_{qd3} components are turned-on are shown in Figure 2.16. These vectors in V_{qd1} with their corresponding components in the V_{qd2} and V_{qd3} are time-averaged to synthesize the reference voltages, V_{qd1}^* , V_{qd2}^* , and V_{qd3}^* .

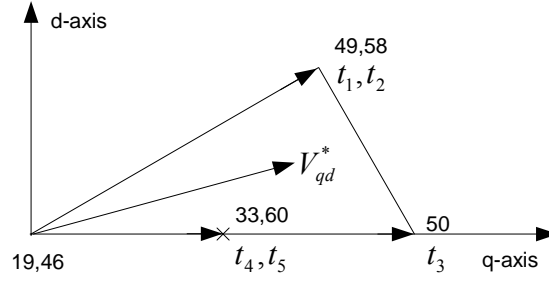


Figure 2.16 Selection of voltage vectors in sector 1.

The time-averaged voltage equations used to determine the turn-on times of the devices corresponding to the selected voltage vectors are

$$\begin{aligned}
 V_{qd1} &= V_{qd11}t_1 + V_{qd12}t_2 + V_{qd13}t_3 + V_{qd14}t_4 + V_{qd15}t_5 + V_{qd119}t_{019} + V_{qd146}t_{046} \\
 V_{qd2} &= V_{qd21}t_1 + V_{qd22}t_2 + V_{qd23}t_3 + V_{qd24}t_4 + V_{qd25}t_5 + V_{qd219}t_{019} + V_{qd246}t_{046} \\
 V_{qd3} &= V_{qd31}t_1 + V_{qd32}t_2 + V_{qd33}t_3 + V_{qd34}t_4 + V_{qd35}t_5 + V_{qd319}t_{019} + V_{qd346}t_{046}
 \end{aligned}
 \tag{2.35}$$

The corresponding average neutral voltage for sector 1 is expressed as

$$\begin{aligned}
 V_o &= V_{o49}t_1 + V_{o58}t_2 + V_{o50}t_3 + V_{o33}t_4 + V_{o60}t_5 + V_{o19}t_{019} + V_{o46}t_{046} \\
 t_6 &= 1 - (t_1 + t_2 + t_3 + t_4 + t_5)
 \end{aligned}
 \tag{2.36}$$

When the q- and d-axis reference voltages are expressed in terms of phase voltages, the times spent on the voltage vectors can be calculated. And V_o can be expressed in terms of the phase voltages in Table 2.8. In sector 1, the maximum and minimum voltages in V_{qd1} are V_a and V_d . The maximum and minimum voltages in V_{qd2} are V_a , V_d and V_c , V_f . The maximum and minimum voltages in V_{qd3} are V_a , V_c , V_e and V_b , V_d , V_f . The average neutral voltage in sector 1 can be expressed as 2.37(a) ($0 \leq \mu \leq 1$). Similarly in sector 4, the maximum and minimum voltages in V_{qd1} are V_b and V_e . The maximum and minimum voltages in V_{qd2} are V_b , V_e and V_a , V_d . The maximum and

Table 2.8a Coefficients for V_{a1} , V_{b1} , V_{c1} , V_{d1} , V_{e1} , V_{f1}

Sector	V_{a1}	V_{b1}	V_{c1}	V_{d1}	V_{e1}	V_{f1}
1	-1/3	-1/6	1/6	1/3	1/6	-1/6
2	-1/6	-1/3	-1/6	1/6	1/3	1/6
3	-1/6	-1/3	-1/6	1/6	1/3	1/6
4	1/6	-1/6	-1/3	-1/6	1/6	1/3
5	1/6	-1/6	-1/3	-1/6	1/6	1/3
6	1/3	1/6	-1/6	-1/3	-1/6	1/6
7	1/3	1/6	-1/6	-1/3	-1/6	1/6
8	1/6	1/3	1/6	-1/6	-1/3	-1/6
9	1/6	1/3	1/6	-1/6	-1/3	-1/6
10	-1/6	1/6	1/3	1/6	-1/6	-1/3
11	-1/6	1/6	1/3	1/6	-1/6	-1/3
12	-1/3	-1/6	1/6	1/3	1/6	-1/6

Table 2.8b Coefficients for V_{a1} , V_{b1} , V_{c1} , V_{d1} , V_{e1} , V_{f1} with coefficient α

Sector	V_{a1}	V_{b1}	V_{c1}	V_{d1}	V_{e1}	V_{f1}
1	2/3	1/3	-1/3	-2/3	-1/3	1/3
2	1/3	2/3	1/3	-1/3	-2/3	-1/3
3	1/3	2/3	1/3	-1/3	-2/3	-1/3
4	-1/3	1/3	2/3	1/3	-1/3	-2/3
5	-1/3	1/3	2/3	1/3	-1/3	-2/3
6	-2/3	-1/3	1/3	2/3	1/3	-1/3
7	-2/3	-1/3	1/3	2/3	1/3	-1/3
8	-1/3	-2/3	-1/3	1/3	2/3	1/3
9	-1/3	-2/3	-1/3	1/3	2/3	1/3
10	1/3	-1/3	-2/3	-1/3	1/3	2/3
11	1/3	-1/3	-2/3	-1/3	1/3	2/3
12	2/3	1/3	-1/3	-2/3	-1/3	1/3

Table 2.8c Coefficients for V_{a2} , V_{b2} , V_{c2} , V_{d2} , V_{e2} , V_{f2}

Sector	V_{a2}	V_{b2}	V_{c2}	V_{d2}	V_{e2}	V_{f2}
1	-1/3	1/6	1/6	-1/3	1/6	1/6
2	1/6	-1/3	1/6	1/6	-1/3	1/6
3	1/6	-1/3	1/6	1/6	-1/3	1/6
4	1/6	1/6	-1/3	1/6	1/6	-1/3
5	1/6	1/6	-1/3	1/6	1/6	-1/3
6	-1/3	1/6	1/6	-1/3	1/6	1/6
7	-1/3	1/6	1/6	-1/3	1/6	1/6
8	1/6	-1/3	1/6	1/6	-1/3	1/6
9	1/6	-1/3	1/6	1/6	-1/3	1/6
10	1/6	1/6	-1/3	1/6	1/6	-1/3
11	1/6	1/6	-1/3	1/6	1/6	-1/3
12	-1/3	1/6	1/6	-1/3	1/6	1/6

Table 2.8d Coefficients for V_{a3} , V_{b3} , V_{c3} , V_{d3} , V_{e3} , V_{f3}

Sector	V_{a3}	V_{b3}	V_{c3}	V_{d3}	V_{e3}	V_{f3}
1	-1/6	1/6	-1/6	1/6	-1/6	1/6
2	1/6	-1/6	1/6	-1/6	1/6	-1/6
3	1/6	-1/6	1/6	-1/6	1/6	-1/6
4	-1/6	1/6	-1/6	1/6	-1/6	1/6
5	-1/6	1/6	-1/6	1/6	-1/6	1/6
6	1/6	-1/6	1/6	-1/6	1/6	-1/6
7	1/6	-1/6	1/6	-1/6	1/6	-1/6
8	-1/6	1/6	-1/6	1/6	-1/6	1/6
9	-1/6	1/6	-1/6	1/6	-1/6	1/6
10	1/6	-1/6	1/6	-1/6	1/6	-1/6
11	1/6	-1/6	1/6	-1/6	1/6	-1/6
12	-1/6	1/6	-1/6	1/6	-1/6	1/6

Table 2.8e Coefficients for V_{a3} , V_{b3} , V_{c3} , V_{d3} , V_{e3} , V_{f3} with coefficient α

Sector	V_{a3}	V_{b3}	V_{c3}	V_{d3}	V_{e3}	V_{f3}
1	1/3	-1/3	1/3	-1/3	1/3	-1/3
2	-1/3	1/3	-1/3	1/3	-1/3	1/3
3	-1/3	1/3	-1/3	1/3	-1/3	1/3
4	1/3	-1/3	1/3	-1/3	1/3	-1/3
5	1/3	-1/3	1/3	-1/3	1/3	-1/3
6	-1/3	1/3	-1/3	1/3	-1/3	1/3
7	-1/3	1/3	-1/3	1/3	-1/3	1/3
8	1/3	-1/3	1/3	-1/3	1/3	-1/3
9	1/3	-1/3	1/3	-1/3	1/3	-1/3
10	-1/3	1/3	-1/3	1/3	-1/3	1/3
11	-1/3	1/3	-1/3	1/3	-1/3	1/3
12	1/3	-1/3	1/3	-1/3	1/3	-1/3

minimum voltages in V_{qd3} are V_b , V_d , V_f and V_a , V_c , V_e . The average neutral voltage in sector 4 can be expressed as (2.37b). After tedious and time-consuming calculations for all sectors, the generalized average neutral voltage is given as (2.37c).

$$\begin{aligned}
 V_o = & \frac{V_d}{2}(1-2\mu) + \left(-\frac{2}{3}V_{a1} + \frac{1}{3}V_{d1} \right)(1-2\mu) \\
 & - \frac{1}{2}(V_{a1} + V_{d1}) - V_{a2} + \frac{1}{2}(-V_{a3} + V_{b3})(1-2\mu) \quad \text{- Sector 1}
 \end{aligned} \tag{2.37a}$$

$$\begin{aligned}
 V_o = & \frac{V_d}{2}(1-2\mu) + \left(-\frac{2}{3}V_{b1} + \frac{1}{3}V_{e1} \right)(1-2\mu) \\
 & - \frac{1}{2}(V_{b1} + V_{e1}) - V_{b2} + \frac{1}{2}(-V_{b3} + V_{a3})(1-2\mu) \quad \text{- Sector 4}
 \end{aligned} \tag{2.37b}$$

$$\begin{aligned}
 V_o = & \frac{V_d}{2}(1-2\mu) + \left(-\frac{2}{3}V_{\max 1} + \frac{1}{3}V_{\min 1} \right)(1-2\mu) \\
 & - \frac{1}{2}(V_{\max 1} + V_{\min 1}) - V_{\max 2} + \frac{1}{2}(-V_{\max 3} + V_{\min 3})(1-2\mu)
 \end{aligned} \tag{2.37c}$$

The instantaneous maximum and minimum values of V_{in1} , V_{in2} , V_{in3} ($i = a, b, c, d, e, f$) are $V_{\max 1}$, $V_{\max 2}$, $V_{\max 3}$ and $V_{\min 1}$, $V_{\min 2}$, $V_{\min 3}$, respectively.

2.5.5 Experimental Results

The carrier-based PWM modulation technique for the five-phase system has been implemented using a TI DSP TMS320LF2407 EVM. The reference fundamental voltage magnitude and the third harmonic voltage magnitude are given as $V_1 = m_1 \cdot V_d / 2$, $V_{13} = m_3 \cdot V_d / 2$, where m_1 and m_3 are the modulation index for the fundamental and third harmonic voltages, respectively. For the experiment, $V_d = 50 \text{ V}$. For the first waveform shown in Figure 2.17, $m_1 = 0.8$ and $m_3 = -0.2$.

For the first waveform shown in Figure 2.17, $m_1 = 0.8$ and $\mu = 0.5$, which is corresponding to the space vector PWM for the generation of fundamental voltage in the linear region for the five-phase system. Then the third harmonic voltage with magnitude $m_3 = 0.2$ is considered for both cases: added to and subtracted from the fundamental voltage. It is seen that the modulation signals at the middle (top waveform of Figure 2.17(d, e)) are reduced or flattened when the peaks of the two reference voltages are out of phase with each other. When the neutral voltage corresponding to $\mu = 0.5$ is added to the reference voltage signals, the flatness of the middle portion of the composite modulation signal increases signifying that a higher fundamental voltage can be generated in the linear region compared to the condition when the neutral voltage is excluded from the modulation signal expression. It is recalled that $\mu = 0.5$ corresponds

to SVPWM in the three-phase converter, which is known for good waveforms for operation in the under-modulation region. However, this kind of flatness cannot be observed when the third harmonic voltage is in phase with the fundamental voltage.

Discontinuous PWM modulation is recommended especially when the over-modulation region is approached in which case the devices are clamped to the positive and negative rails for some times during each switching period. In the regions where the devices are clipped, the devices are completely turned on reducing the switching loss and effective switching frequency. Defining μ as in (2.38), it varies with time and by changing or fixing δ the waveforms can be appropriately shifted with respect to the fundamental voltage to clamp at the appropriate regions of the phase current waveforms and to change the converter voltage gain.

$$\mu = \frac{1}{2}[1 + \text{sgn}(\cos 5(\omega t + \delta))] \quad (2.38)$$

In Figure 2.18, the modulation index of the fundamental voltage is increased to 1 (with respect to half of the dc link voltage) in order to check the performance in the over-modulation region. The waveforms corresponding to the modulation without any zero sequence voltage and with the space vector approach are shown in Figure 2.18a. The waveforms shown in Figure 2.18b correspond to when the neutral voltage corresponding to $\delta = 0^\circ, -36^\circ$ is added to the modulation signals. It is observed that within each fundamental cycle, the top and bottom devices are clamped to the top and bottom rails keeping the device turned on for some angle. In Figures 2.18a(a, b) and 2.18b(a, b), the peaks of the fundamental and harmonic modulation signals coincide and hence reduce the possible phase voltage magnitude that can be synthesized. With the neutral voltage corresponding to $\mu = 0.5$ added, the composite modulation waveform in Figure 2.18a(b)

flattens increasing the voltage gain and giving better waveforms when compared to the condition when the neutral voltage signal is excluded. However this is not the case when m_f is increased to 1.5 as shown in the spectrum analysis in Figure 2.19. In Figure 2.18b, where a discontinuous neutral voltage signal is added to the modulation signals, the devices are clamped to the rails for some angle giving different voltage gain in the over-modulation region of operation. In Figure 2.18a(d) when the third harmonic voltage is out of phase with the fundamental voltage, the modulation signal is reduced into the linear modulation region although the original fundamental signal is right on the margin. It means that the linear range for the fundamental voltage can be extended by injecting the third harmonic component and further improved by adding the appropriate zero sequence voltage.

The spectrum analysis has been done based on one of the line-line voltages to examine the effects of different modulation schemes on the generation of fundamental and third harmonic voltages. Figure 2.19 shows the FFT results for the four modulation schemes when different zero sequence voltage is applied. It is seen that the application of discontinuous PWM leads to the increase of the fundamental component when the reference fundamental and third harmonic voltages are out of phase in the linear modulation region. When these two reference voltages are in phase, the fundamental component generated increases or decreases depending on the angle δ used. However, the discontinuous PWM generates less fundamental voltages when the inverter operates in the over-modulation region as shown in Figure 2.20. Hence the discontinuous PWM can be used to generate the desired voltages and the voltages generated depend on the magnitudes and phase angles of the components of reference voltages.

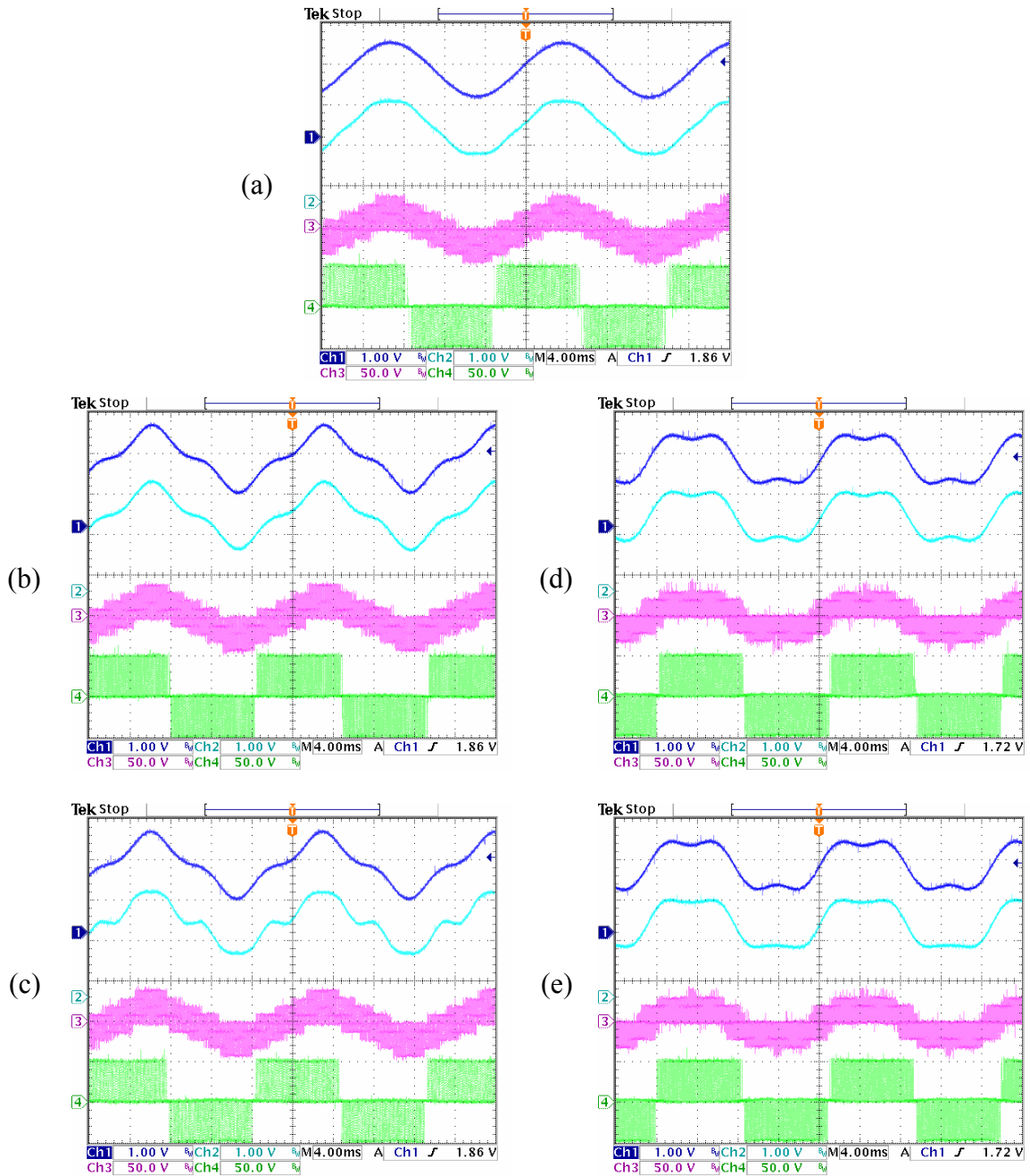


Figure 2.17 Experimental result for five-phase system when $m_1 = 0.8$. (a) $m_3 = 0$, $\mu = 0.5$; (b) $m_3 = 0.2$, $V_{no} = 0$; (c) $m_3 = 0.2$, $\mu = 0.5$; (d) $m_3 = -0.2$, $V_{no} = 0$; (e) $m_3 = -0.2$, $\mu = 0.5$. Ch1: reference voltage for phase A (0.6/div), Ch2: modulation signal for phase A (0.6/div); Ch3: phase A voltage (50V/div); Ch4: line to line voltage V_{ab} (50V/div).

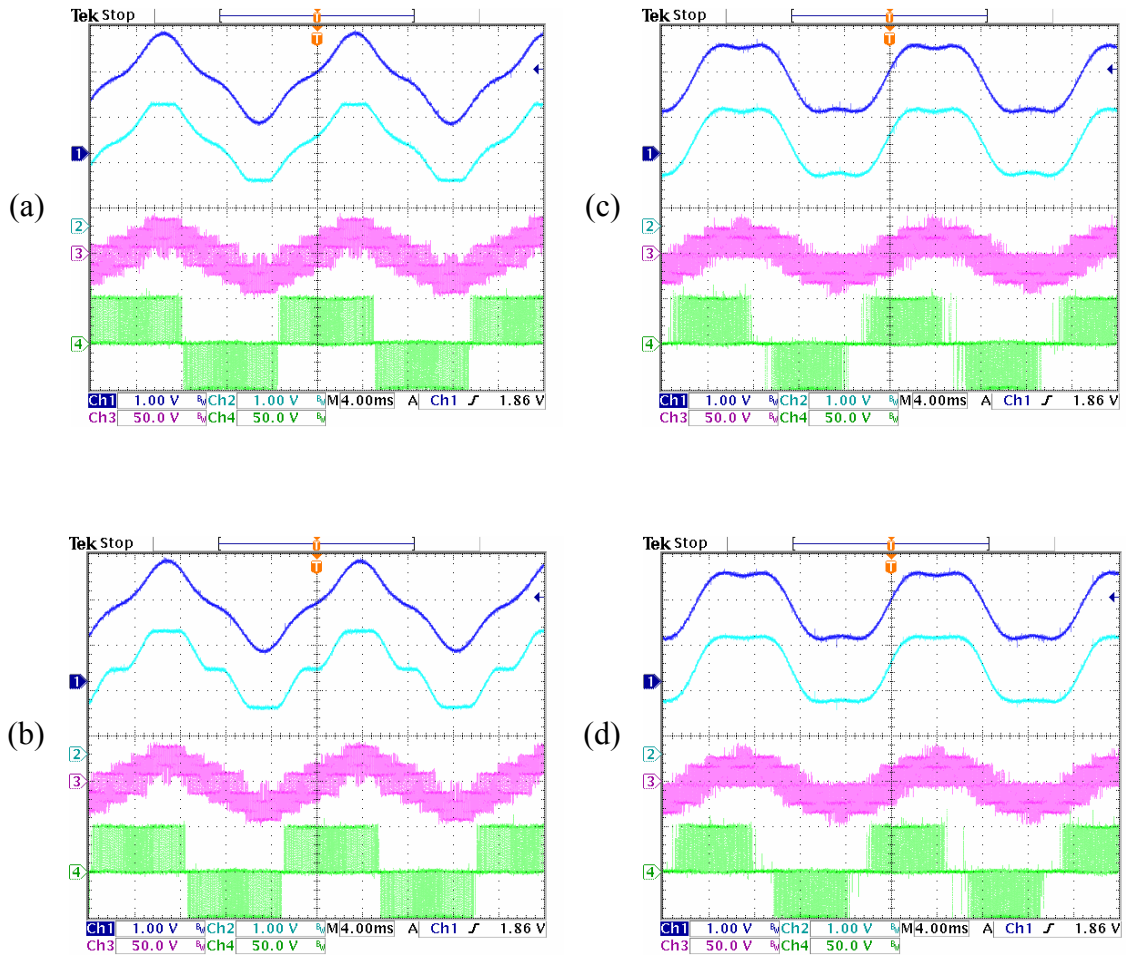


Figure 2.18a Experimental result for five-phase system when $m_1 = 1$. (a) $m_3 = 0.2$, $V_{no} = 0$; (b) $m_3 = 0.2$, $\mu = 0.5$; (c) $m_3 = -0.2$, $V_{no} = 0$; (d) $m_3 = -0.2$, $\mu = 0.5$. Ch1: Reference voltage for phase A (1.2/div); Ch2: modulation signal for phase A (1.2/div); Ch3: phase A voltage (50V/div); Ch4: line to line voltage V_{ab} (50V/div).

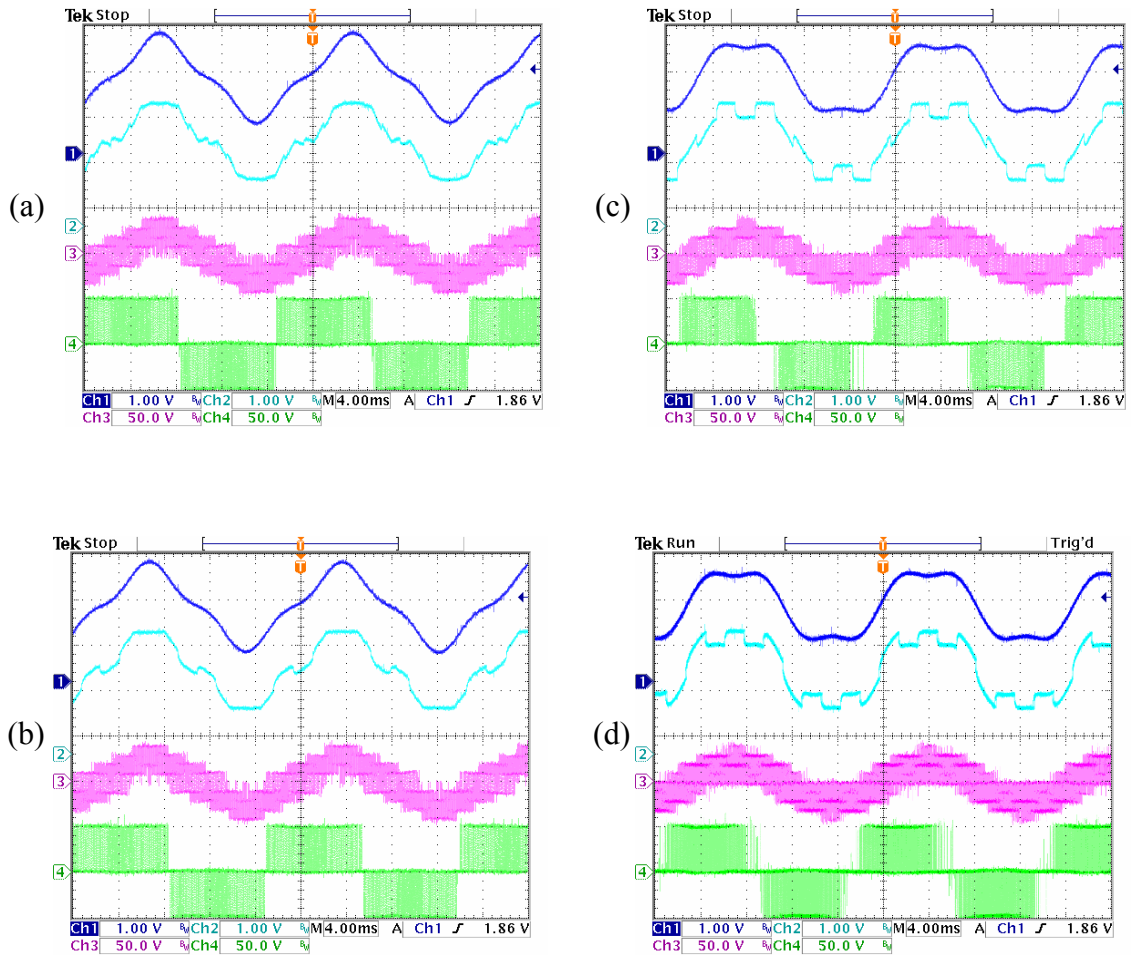


Figure 2.18b Experimental result for five-phase system when $m_1 = 1$. (a) $m_3 = 0.2$, $\delta = 0^\circ$; (b) $m_3 = 0.2$, $\delta = -36^\circ$; (c) $m_3 = -0.2$, $\delta = 0^\circ$; (d) $m_3 = -0.2$, $\delta = -36^\circ$. Ch1: reference voltage for phase A (1.2/div); Ch2: modulation signal for phase A (1.2/div); Ch3: phase A voltage (50V/div); Ch4: line to line voltage V_{ab} (50V/div).

$$(\mu = 0.5[1 + \text{sgn}(\cos 5(\omega t + \delta))])$$

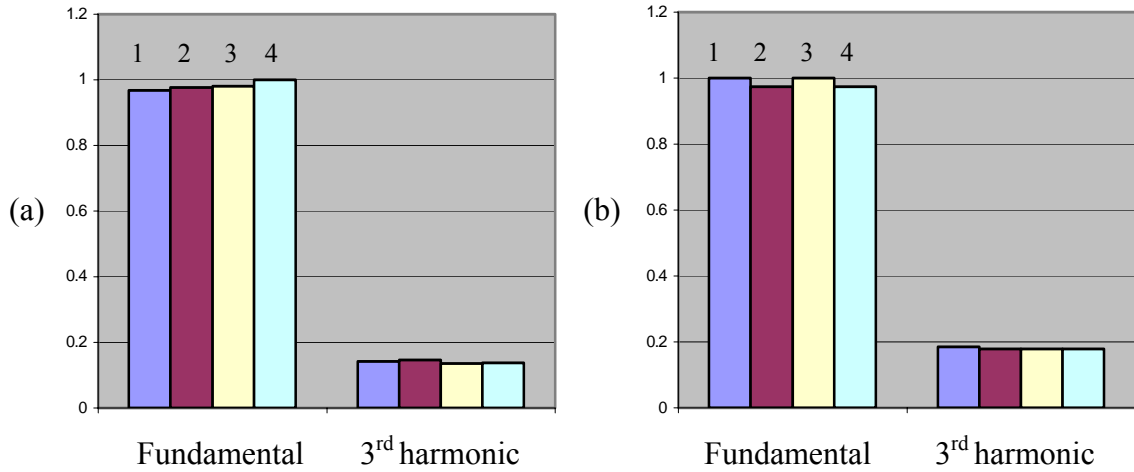


Figure 2.19 Spectrum analysis of the line to line voltage V_{ad} (normalized with respect to the highest fundamental voltage) in the linear modulation region. (a) $m_1 = 0.8$, $m_3 = -0.2$;
 (b) $m_1 = 0.8$, $m_3 = 0.2$. 1: $V_{no} = 0$; 2: $\mu = 0.5$; 3: $\mu = 0.5[1 + \text{sgn}(\cos 5(\omega t + \delta))]$, $\delta = 0^\circ$;
 4: $\mu = 0.5[1 + \text{sgn}(\cos 5(\omega t + \delta))]$, $\delta = -36^\circ$.

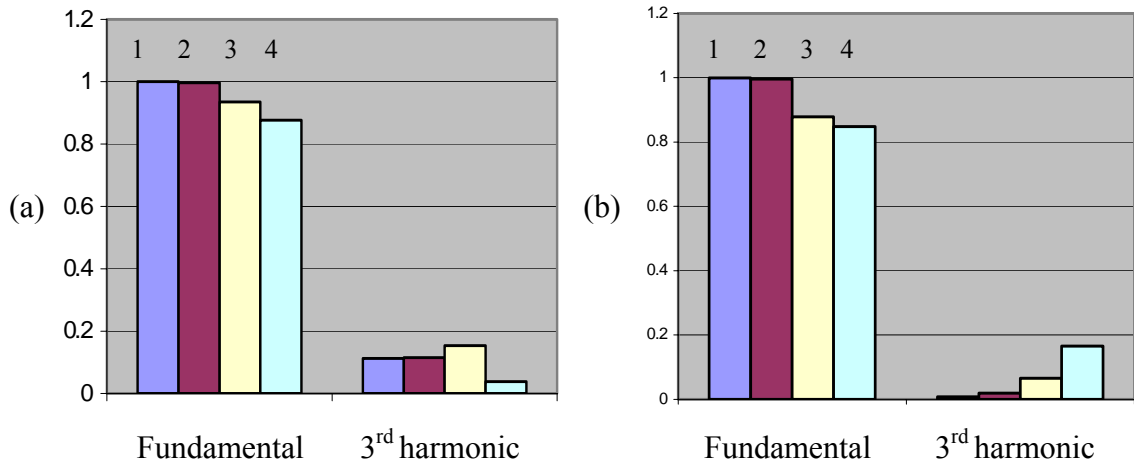


Figure 2.20 Spectrum analysis of the line to line voltage V_{ad} (normalized with respect to the highest fundamental voltage) in the over-modulation region. (a) $m_1 = 1.5$, $m_3 = -0.2$;
 (b) $m_1 = 1.5$, $m_3 = 0.2$. 1: $V_{no} = 0$; 2: $\mu = 0.5$; 3: $\mu = 0.5[1 + \text{sgn}(\cos 5(\omega t + \delta))]$, $\delta = 0^\circ$;
 4: $\mu = 0.5[1 + \text{sgn}(\cos 5(\omega t + \delta))]$, $\delta = -36^\circ$.

The phase angle between the fundamental and third harmonic voltages significantly affects the voltage gain of the converter as illustrated in Figures 2.17 and 2.18. In many applications, the reference voltages (equivalently, the modulation signals) and the phase angles between them, which are the outputs of controllers, are independently determined by closed-loop control laws. The neutral voltage signal can therefore be used to modify the composite modulation signals in order to better the converter utility. For better results in terms of waveform quality, voltage gain and switching loss reduction, the definitions of μ and the selection of δ are very crucial.

2.5.6 Modulation Signals Calculation Using Turn-on Times for the Top Devices

In the carrier-based PWM, the modulation signals are calculated by adding the zero sequence voltage to the reference signals. The final modulation signals normalized with respect to $V_d/2$ are between -1 and 1 in the linear modulation region. The PWM signals are determined by comparing the modulation signals with the triangle carrier signal with magnitude -1 and 1 .

Figure 2.21 shows the switching signals for the top devices in sector 1 in a five-phase system. It is seen that the normalized modulation signals for the five top devices are equal to the ratio between the individual turn-on time for the top devices and the switching period. Thus the alternative approach of finding the modulation signal without calculating the zero sequence voltage is to sum up the turn-on times for the top devices and then use them as the modulation signals, which are compared with the triangle carrier signal between 0 and 1 to generate the PWM signals. The normalized turn-on times for

the active states that are used to synthesize the desired voltages are determined first. Then the turn-on times for the individual devices are summed up and treated as the modulation signals. Now the modulation signal is within the range 0 and 1.

For the five phase system with consideration of generating both fundamental and third harmonic components, the turn-on times for the active states are calculated based on the space vector diagram for the fundamental component as shown in Figure 2.22. In sector I, the outer four voltage vectors are selected to synthesize the desired fundamental voltage. At the the same time, the corresponding voltage vectors in V_{qd3} are determined and used to synthesize the desired third harmonic voltage. The voltage equations that are used to calculate the times are

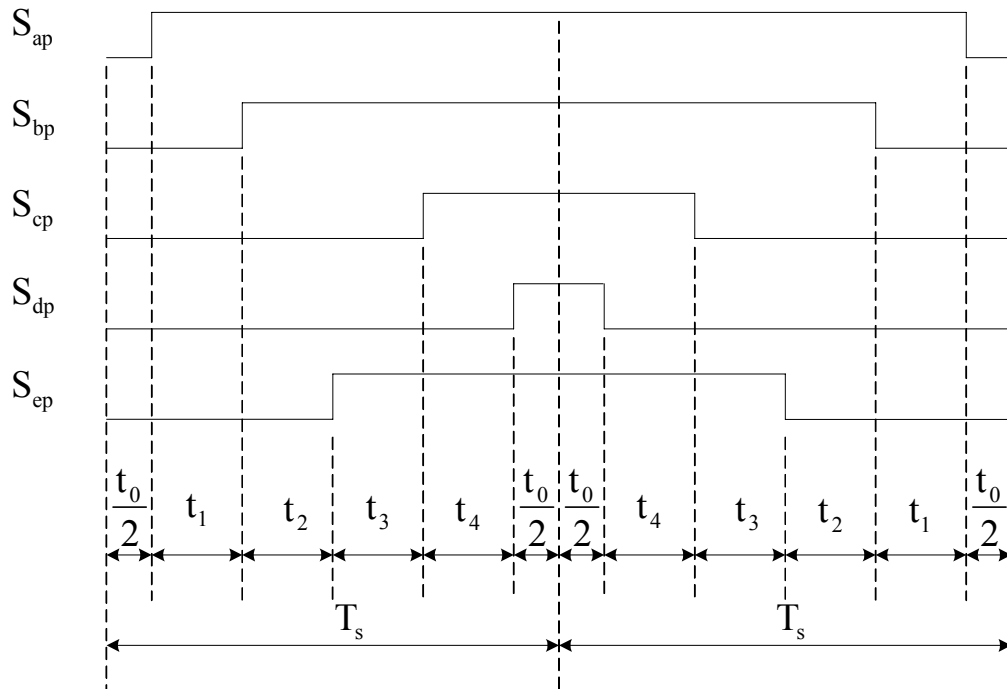


Figure 2.21 Switching signals for the top devices in sector 1.

$$V_{qd1} = V_{qd11}t_1 + V_{qd12}t_2 + V_{qd13}t_3 + V_{qd14}t_4 + V_{qd101}t_{01} + V_{qd132}t_{032}$$

$$V_{qd3} = V_{qd31}t_1 + V_{qd32}t_2 + V_{qd33}t_3 + V_{qd34}t_4 + V_{qd301}t_{01} + V_{qd332}t_{032}$$

where t_1, t_2, t_3, t_4 are the corresponding times spent on the four active states as shown in Figure 2.22. The same pattern applies to all the other sectors.

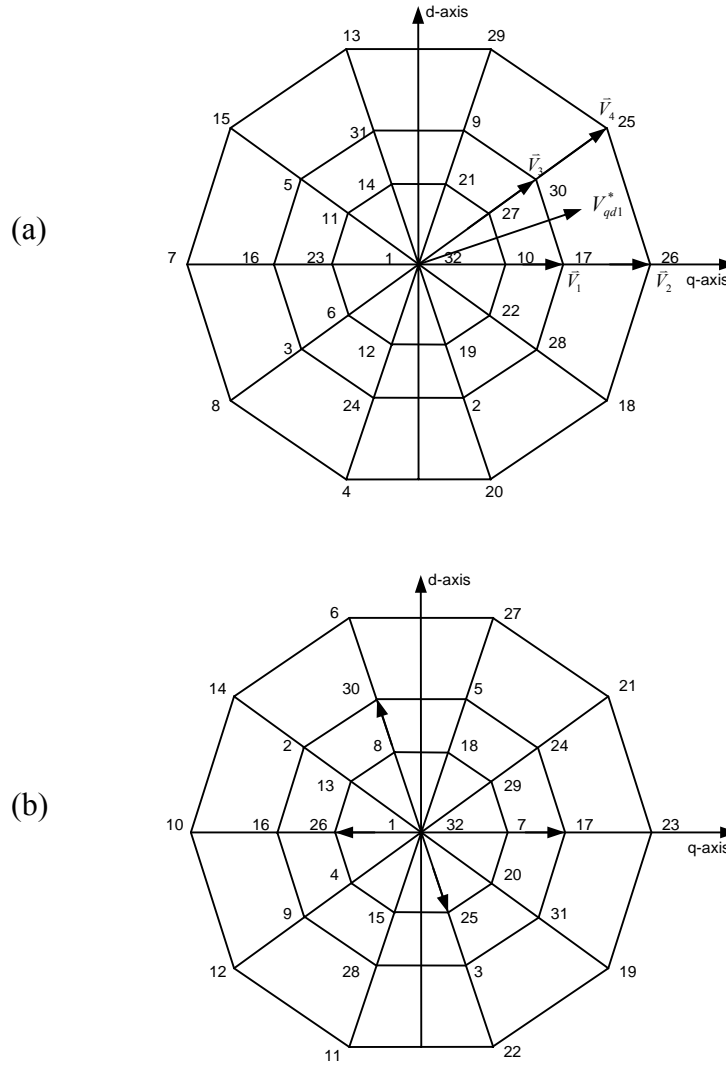


Figure 2.22 Synthesis of fundamental and third harmonic voltages in a five-phase system. (a) Synthesizing reference voltage in sector 1 of V_{qd1} ; (b) Corresponding voltage vectors in V_{qd3} .

The turn-on times for the top devices, which are the modulation signals also, are determined as

$$m_a = m_{a1} + (1 - \alpha)[1 - (t_1 + t_2 + t_3 + t_4)]$$

$$m_b = m_{b1} + (1 - \alpha)[1 - (t_1 + t_2 + t_3 + t_4)]$$

$$m_c = m_{c1} + (1 - \alpha)[1 - (t_1 + t_2 + t_3 + t_4)]$$

$$m_d = m_{d1} + (1 - \alpha)[1 - (t_1 + t_2 + t_3 + t_4)]$$

$$m_e = m_{e1} + (1 - \alpha)[1 - (t_1 + t_2 + t_3 + t_4)]$$

where m_{a1} , m_{b1} , m_{c1} , m_{d1} and m_{e1} are determined corresponding to Table 2.9.

The turn-on times for the top devices, which are the modulation signals also, are determined as shown in Table 2.10.

Table 2.9 Calculation of the modulation signals in terms of turn-on times

Sector	m_{a1}	m_{b1}	m_{c1}	m_{d1}	m_{e1}
1	$t_1 + t_2 + t_3 + t_4$	$t_2 + t_3 + t_4$	t_3	0	$t_2 + t_3$
2	$t_1 + t_2 + t_4$	$t_1 + t_2 + t_3 + t_4$	$t_1 + t_4$	0	t_1
3	$t_2 + t_3$	$t_1 + t_2 + t_3 + t_4$	$t_2 + t_3 + t_4$	t_3	0
4	t_1	$t_1 + t_2 + t_4$	$t_1 + t_2 + t_3 + t_4$	$t_1 + t_4$	0
5	0	$t_2 + t_3$	$t_1 + t_2 + t_3 + t_4$	$t_2 + t_3 + t_4$	t_3
6	0	t_1	$t_1 + t_2 + t_4$	$t_1 + t_2 + t_3 + t_4$	$t_1 + t_4$
7	t_3	0	$t_2 + t_3$	$t_1 + t_2 + t_3 + t_4$	$t_2 + t_3 + t_4$
8	$t_1 + t_4$	0	t_1	$t_1 + t_2 + t_4$	$t_1 + t_2 + t_3 + t_4$
9	$t_2 + t_3 + t_4$	t_3	0	$t_2 + t_3$	$t_1 + t_2 + t_3 + t_4$
10	$t_1 + t_2 + t_3 + t_4$	$t_1 + t_4$	0	t_1	$t_1 + t_2 + t_4$

Table 2.10a Calculation of the modulation signals in terms of line to line voltages

Sector	m_{a1}	m_{b1}	m_{c1}	m_{d1}	m_{e1}
1	$V_{ad1}+V_{ad3}$	$V_{bd1}+V_{bd3}$	$V_{cd1}+V_{cd3}$	0	$V_{ed1}+V_{ed3}$
2	$V_{ad1}+V_{ad3}$	$V_{bd1}+V_{bd3}$	$V_{cd1}+V_{cd3}$	0	$V_{ed1}+V_{ed3}$
3	$V_{ae1}+V_{ae3}$	$V_{be1}+V_{be3}$	$V_{ce1}+V_{ce3}$	$V_{de1}+V_{de3}$	0
4	$V_{ae1}+V_{ae3}$	$V_{be1}+V_{be3}$	$V_{ce1}+V_{ce3}$	$V_{de1}+V_{de3}$	0
5	0	$V_{ba1}+V_{ba3}$	$V_{ca1}+V_{ca3}$	$V_{da1}+V_{da3}$	$V_{ea1}+V_{ea3}$
6	0	$V_{ba1}+V_{ba3}$	$V_{ca1}+V_{ca3}$	$V_{da1}+V_{da3}$	$V_{ea1}+V_{ea3}$
7	$V_{ab1}+V_{ab3}$	0	$V_{cb1}+V_{cb3}$	$V_{db1}+V_{db3}$	$V_{eb1}+V_{eb3}$
8	$V_{ab1}+V_{ab3}$	0	$V_{cb1}+V_{cb3}$	$V_{db1}+V_{db3}$	$V_{eb1}+V_{eb3}$
9	$V_{ac1}+V_{ac3}$	$V_{bc1}+V_{bc3}$	0	$V_{dc1}+V_{dc3}$	$V_{ec1}+V_{ec3}$
10	$V_{ac1}+V_{ac3}$	$V_{bc1}+V_{bc3}$	0	$V_{dc1}+V_{dc3}$	$V_{ec1}+V_{ec3}$

Table 2.10b Calculation of the modulation signals in terms of line to line voltages

Sector	$(1-\alpha)[1-(t_1+t_2+t_3+t_4)]$
1	$(1-\alpha)[1-(V_{ad1}+V_{ad3})]$
2	$(1-\alpha)[1-(V_{bd1}+V_{bd3})]$
3	$(1-\alpha)[1-(V_{be1}+V_{be3})]$
4	$(1-\alpha)[1-(V_{ce1}+V_{ce3})]$
5	$(1-\alpha)[1-(V_{ca1}+V_{ca3})]$
6	$(1-\alpha)[1-(V_{da1}+V_{da3})]$
7	$(1-\alpha)[1-(V_{db1}+V_{db3})]$
8	$(1-\alpha)[1-(V_{eb1}+V_{eb3})]$
9	$(1-\alpha)[1-(V_{ec1}+V_{ec3})]$
10	$(1-\alpha)[1-(V_{ac1}+V_{ac3})]$

Table 2.11 Calculation of the modulation signals m_a in terms of line to line voltages

Sector	m_a
1	$(V_{ad1} + V_{ad3}) + (1 - \alpha)[1 - (V_{ad1} + V_{ad3})]$
2	$(V_{ad1} + V_{ad3}) + (1 - \alpha)[1 - (V_{bd1} + V_{bd3})]$
3	$(V_{ae1} + V_{ae3}) + (1 - \alpha)[1 - (V_{be1} + V_{be3})]$
4	$(V_{ae1} + V_{ae3}) + (1 - \alpha)[1 - (V_{ce1} + V_{ce3})]$
5	$0 + (1 - \alpha)[1 - (V_{ca1} + V_{ca3})]$
6	$0 + (1 - \alpha)[1 - (V_{da1} + V_{da3})]$
7	$(V_{ab1} + V_{ab3}) + (1 - \alpha)[1 - (V_{db1} + V_{db3})]$
8	$(V_{ab1} + V_{ab3}) + (1 - \alpha)[1 - (V_{eb1} + V_{eb3})]$
9	$(V_{ac1} + V_{ac3}) + (1 - \alpha)[1 - (V_{ec1} + V_{ec3})]$
10	$(V_{ac1} + V_{ac3}) + (1 - \alpha)[1 - (V_{ac1} + V_{ac3})]$

The proposed method of using the turn-on times for the top switching devices as the modulation signals is implemented to generate both fundamental and third harmonic voltages. The carrier-based PWM is used to generate the PWM signals through comparing the modulation signals with the high-frequency triangle signal with magnitude between 0 and 1. Figures 2.23 and 2.24 show the experimental results when the inverter is operating in the linear modulation region. The third harmonic voltage with magnitude $m_3 = 0.2$ is subtracted from and added to the fundamental voltage with magnitude $m_1 = 0.7$ in Figures 2.23 and 2.24 respectively. Figures 2.25 and 2.26 shows the experimental results when the inverter is operating in the over-modulation region, in which $m_1 = 1.4$ and $m_3 = 0.2$. The third harmonic voltage is subtracted from and added to the fundamental voltage in Figure 2.25 and Figure 2.26, respectively.

Different modulation schemes are implemented to see the effects. The first one is the space vector modulation when $\mu = 0.5$ while the second and third ones are corresponding to the discontinuous modulations when $\delta = 0^\circ, -36^\circ$. It is seen that the modulation signals at the middle are flattened when the peaks of the two reference voltages are out of phase with each other. When the neutral voltage corresponding to $\mu = 0.5$ is added to the reference voltage signals, the flatness of the middle portion of the composite modulation signal increases, which means that a higher fundamental voltage can be generated in the linear region compared to the condition when the neutral voltage is excluded from the modulation signal expression. However, this kind of flatness cannot be observed when the third harmonic voltage is in phase with the fundamental voltage.

In the case of discontinuous PWM with different angle δ , the waveforms can be appropriately shifted with respect to the fundamental voltage to clamp at the appropriate regions of the phase current waveforms and to change the converter voltage gain.

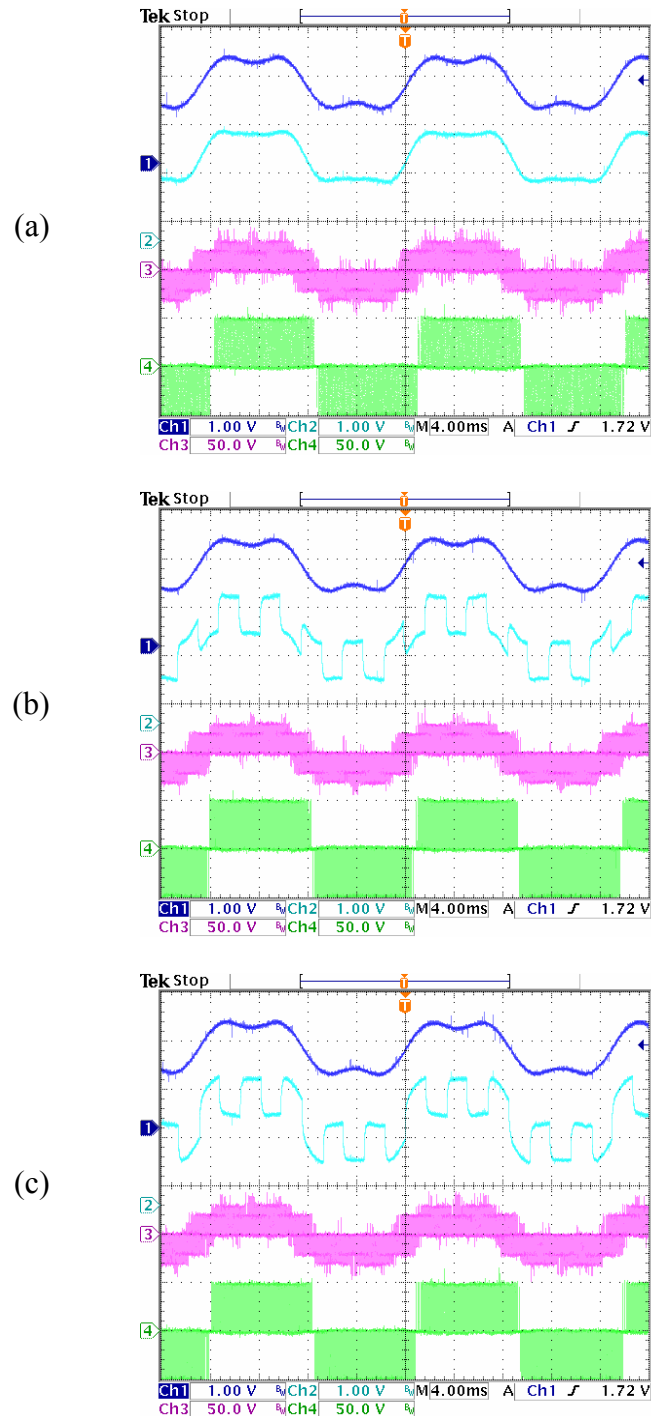


Figure 2.23 Experimental result for five-phase system when $m_1 = 0.7$, $m_3 = -0.2$. (a) $\mu = 0.5$; (b) $\delta = 0^\circ$; (c) $\delta = -36^\circ$ ($\mu = 0.5[1 + \text{sgn}(\cos 5(\omega t + \delta))]$). Ch1: Reference voltage for phase A (1.2/div); Ch2: Modulation signal for phase A (1.2/div); Ch3: Phase A voltage (50V/div); Ch4: Line to line voltage V_{ab} (50V/div).

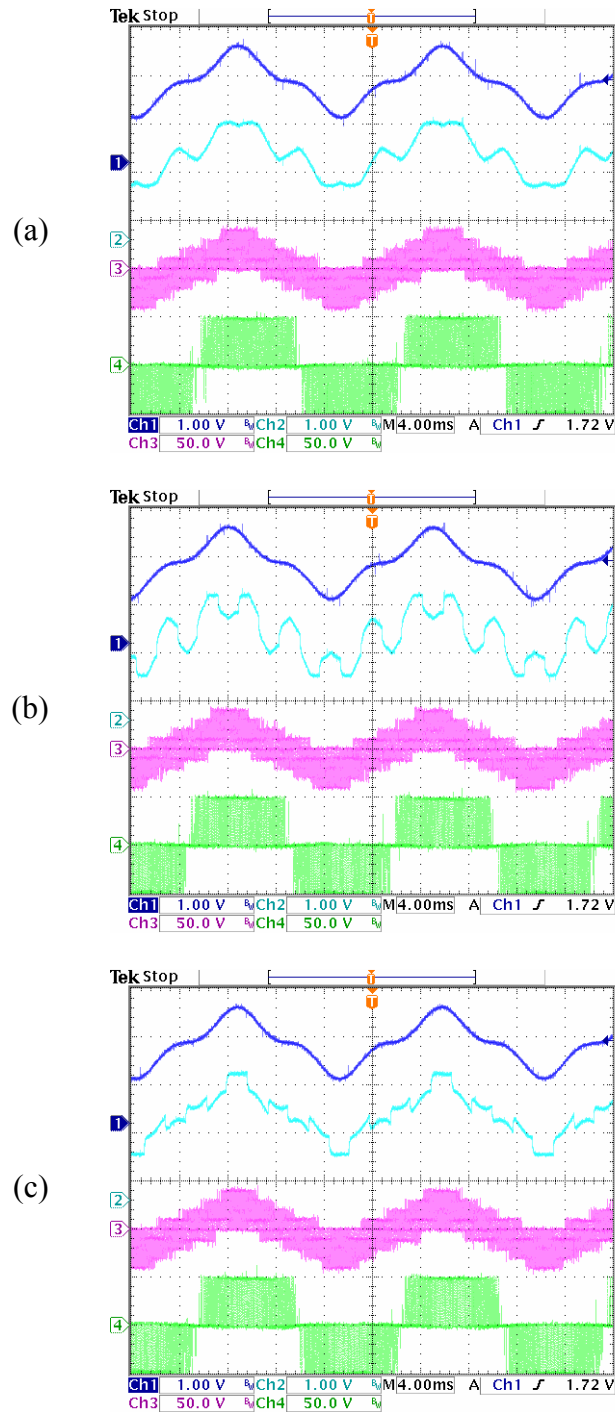


Figure 2.24 Experimental result for five-phase system when $m_1 = 0.7$, $m_3 = 0.2$. (a) $\mu = 0.5$; (b) $\delta = 0^\circ$; (c) $\delta = -36^\circ$ ($\mu = 0.5[1 + \text{sgn}(\cos 5(\omega t + \delta))]$). Ch1: Reference voltage for phase A (1.2/div); Ch2: Modulation signal for phase A (1.2/div); Ch3: Phase A voltage (50V/div); Ch4: Line to line voltage V_{ab} (50V/div).

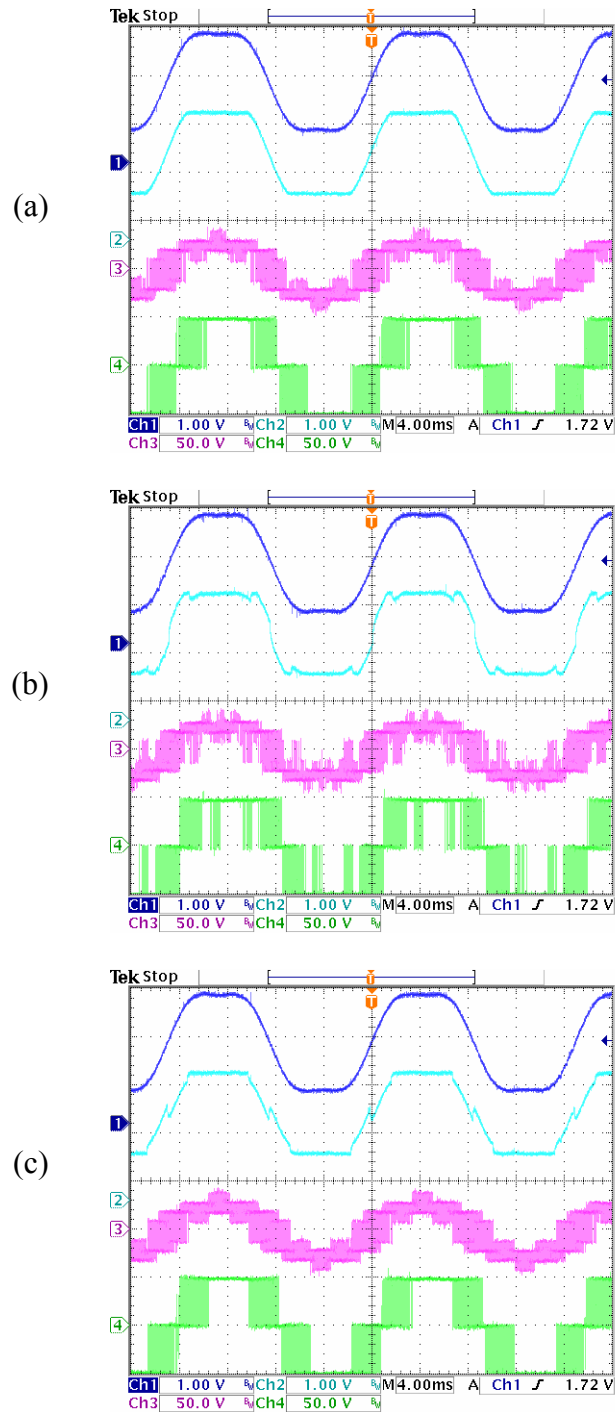


Figure 2.25 Experimental result for five-phase system when $m_1 = 1.4$, $m_3 = -0.2$. (a) $\mu = 0.5$; (b) $\delta = 0^\circ$; (c) $\delta = -36^\circ$ ($\mu = 0.5[1 + \text{sgn}(\cos 5(\omega t + \delta))]$). Ch1: reference voltage for phase A (1.2/div); Ch2: modulation signal for phase A (1.2/div); Ch3: phase A voltage (50V/div); Ch4: line to line voltage V_{ab} (50V/div).

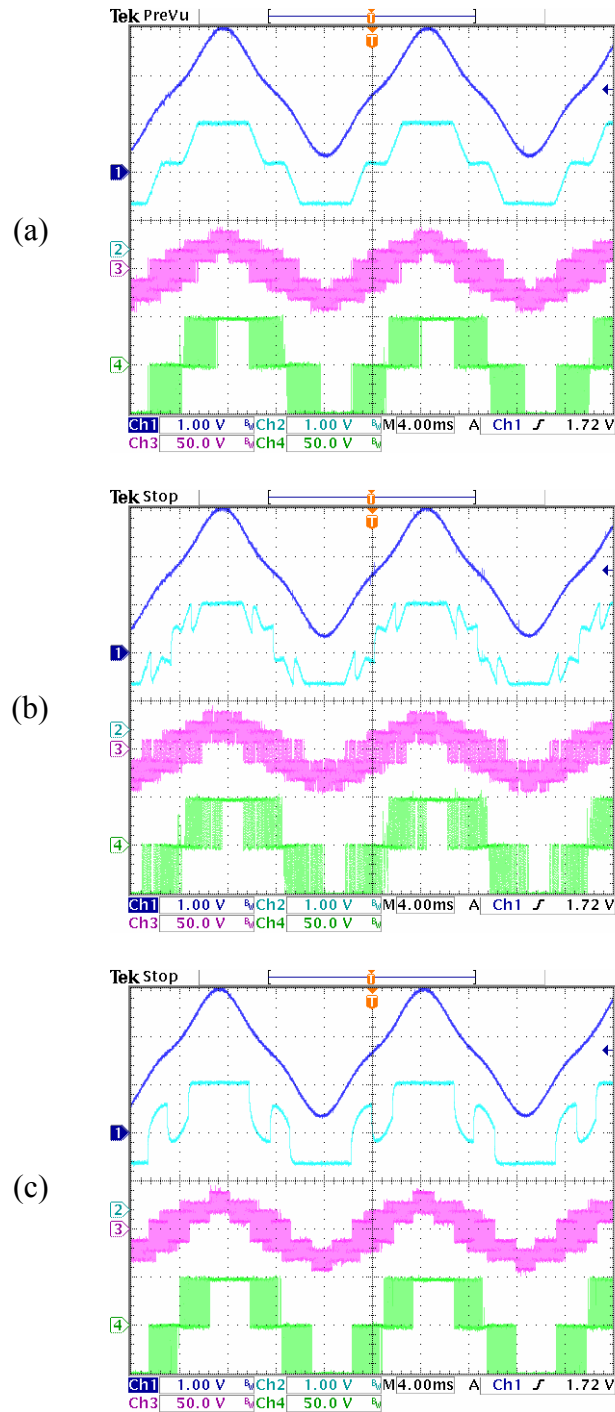


Figure 2.26 Experimental result for five-phase system when $m_1 = 1.4$, $m_3 = 0.2$. (a) $\mu = 0.5$; (b) $\delta = 0^\circ$; (c) $\delta = -36^\circ$ ($\mu = 0.5[1 + \text{sgn}(\cos 5(\omega t + \delta))]$). Ch1: reference voltage for phase A (1.2/div); Ch2: modulation signal for phase A (1.2/div); Ch3: phase A voltage (50V/div); Ch4: line to line voltage V_{ab} (50V/div).

2.6 Conclusion

This chapter shows the equivalence between the carrier-based PWM and space vector PWM for the three-phase system through derivation of the modulation scheme. Then the modulation technique is extended to the multi-phase system in the example of five and six phases. The generalized transformation is defined and the concept of space vector is applied to calculate the zero sequence voltage expressions in all sectors by choosing the appropriate active and null states. Then these expressions are generalized and added to the reference voltage to generate the modulation signals. The experimental results for the five-phase system validate the possibility of generating the voltages more than the fundamental one and this approach can be used to drive two machines in series.

CHAPTER 3

INDUCTION MACHINE MODEL

3.1 Introduction

Induction motors have been widely used in the industrial drive system as a means of converting electric power to mechanical power. With the development of the vector control technology, the induction machine drive systems offer high performance as well as independent control on torque and flux linkages, which is similar to that of the DC machine. Furthermore, it is possible to drive the induction machines above their rated speed through flux weakening, which also finds a lot of industrial applications.

In this chapter, the operation principle of a three-phase induction motor is explained. Then the stator and rotor voltage equations and the torque equations are derived. The transformation to the arbitrary reference frame is established for the convenience of analysis. These equations are the basis that is necessary for the analysis of vector control and any other control approach.

3.2 Operation Principle of a Three-phase Induction Motor

Any type of induction motors can be represented by a simplified model with two poles. The winding arrangement of a two-pole, three-phase, wye-connected symmetrical induction motor is shown in Figure 3.1. The stator windings are identical with equivalent turns and resistance. The rotor windings are also approximated as identical windings with

equivalent turns and resistance, which may be a forged squirrel cage type or a wound type. Both stator and rotor windings are approximated as sinusoidally distributed windings and the air gap is assumed uniform.

In general, the induction motor is operated with the stator windings connected to a balanced three-phase voltage source and the rotor windings short-circuited. The balanced three-phase current is then generated in the stator windings, which are sinusoidally distributed in space with 120° electrical degrees phase shift. These currents with the help of stator winding distribution establish a rotating air-gap magneto-magnetic force (MMF)

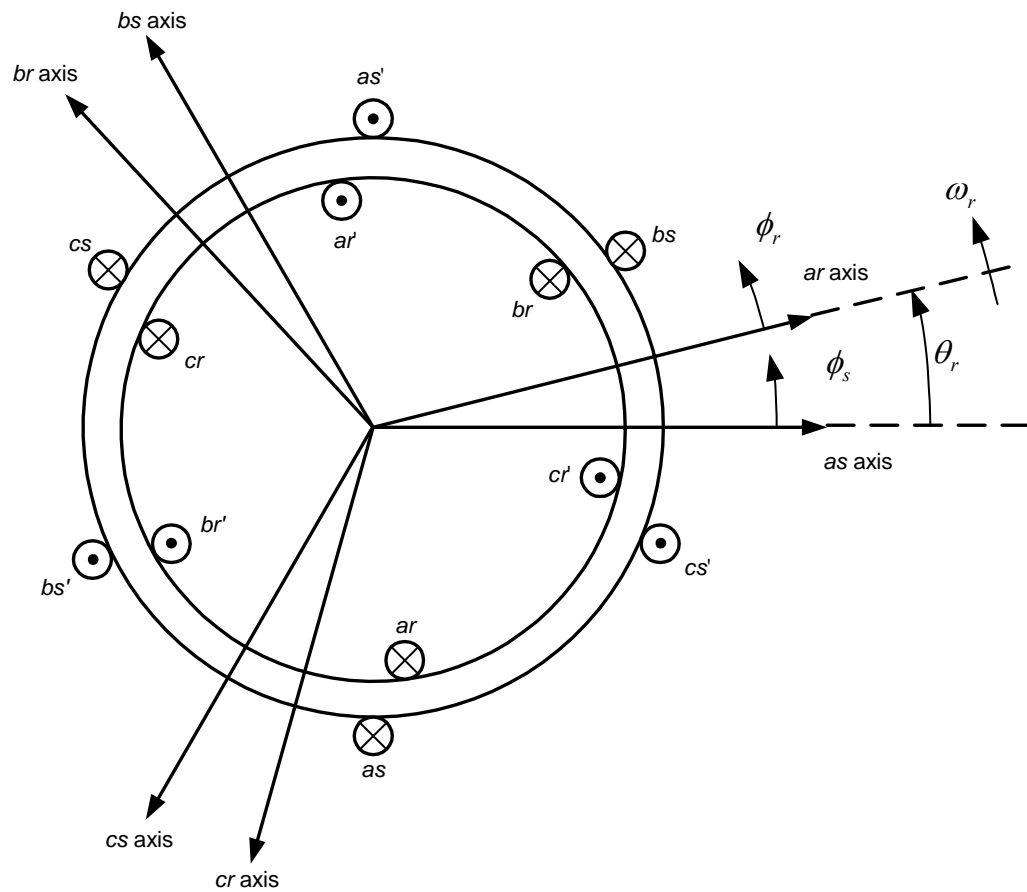


Figure 3.1 Two-pole, three-phase, wye-connected symmetrical induction motor.

as in the case of the synchronous machine, which rotates about the air gap at the speed determined by the stator voltages/currents frequency and the number of poles.

$$\omega_e = (P/2)\omega_m \quad (3.1)$$

where ω_e and ω_m are the electrical and mechanical speeds in radian/second and P is the number of poles of stator windings. When the rotor speed in electrical degrees is different from this synchronous speed, three-phase balanced currents will be induced in the rotor windings to counter the change of flux linkages from Lenz's law. The difference between the rotor speed in electrical degrees and the synchronous speed is defined as the slip frequency.

$$\omega_s = \omega_e - \omega_r \quad (3.2)$$

This is the frequency of the current flowing in the rotor windings. The induced rotor currents also produce an air-gap MMF, which rotates at the speed corresponding to the frequency of rotor currents relative to the rotor. It means that the air-gap MMF generated from the stator currents rotates at the same speed of that established from the rotor currents. These two MMFs can be seen as two sets of magnetic poles and they are interacted with each other to produce the torque. It is clear that two MMFs have to exist in order to generate the electric torque, which can be resulted from the currents or excited from the permanent magnets as in the permanent magnet machine. In the case of induction motor, they are generated from both currents in the stator and rotor windings, which mean the rotor speed in electrical degrees has to be different from the synchronous speed in order to produce the electric torque and run the motor. Otherwise there is no current induced in the rotor windings and therefore no torque produced. The induction machine is classified into motoring and generating modes depending on the sign of the

slip frequency. If the slip frequency is greater than zero, the machine is running as an induction motor and the electric power is consumed by the machine and converted into mechanical power through the rotor. The stator current flows into the machine. If the slip frequency is less than zero, the machine runs as an induction generator and the stator current flows out of the stator. The mechanical power from the rotor shaft is then transformed into electric power and then consumed by the load connected to the stator.

3.3 Three-phase Induction Motor Voltage Equations

A two-pole, three-phase wye-connected induction machine is shown in Figure 3.1. The stator windings of which are identical, sinusoidally distributed in space with a phase displacement of 120° (electrical degrees), with N_s equivalent turns and phase resistance, r_s . Similarly, the rotor is assumed to be symmetrical with three-phase windings displaced in space by the angle of 120° (electrical degrees), with N_r equivalent turns and phase resistance r_r . The voltage equations for the stator and the rotor are given as

$$\begin{aligned} V_{as} &= r_s I_{as} + p\lambda_{as} \\ V_{bs} &= r_s I_{bs} + p\lambda_{bs} \end{aligned} \tag{3.3}$$

$$\begin{aligned} V_{cs} &= r_s I_{cs} + p\lambda_{cs} \\ V_{ar} &= r_r I_{ar} + p\lambda_{ar} \\ V_{br} &= r_r I_{br} + p\lambda_{br} \end{aligned} \tag{3.4}$$

$$V_{cr} = r_r I_{cr} + p\lambda_{cr}$$

where V_{as} , V_{bs} , and V_{cs} are the three-phase stator voltages with the supply frequency while V_{ar} , V_{br} , and V_{cr} are the three-phase rotor voltages induced from the stator with the slip frequency. I_{as} , I_{bs} , and I_{cs} are the three-phase stator currents while I_{ar} , I_{br} , and I_{cr} are the

three-phase rotor currents. r_s and r_r are the stator and rotor phase resistance respectively. λ_{as} , λ_{bs} , and λ_{cs} are the three-phase stator flux linkages while λ_{ar} , λ_{br} , and λ_{cr} are the three-phase rotor flux linkages. p represents the derivative term d/dt . The above relationship can be seen clearly after the space model of the induction motor is expressed as the phase circuit model as shown in Figure 3.2.

Then it is necessary to derive the machine inductances in order to have the equivalent circuit model. In a magnetically linear system, the self-inductance of a winding is the ratio of the flux linked by a winding to the current flowing in the same winding with all other winding currents zero. Mutual inductance is the ratio of flux linked by one winding due to the current flowing in a second winding with all other winding currents zero. In the case of the induction machine, the air-gap is uniform. So the flux density due to current in the as winding with all other currents zero is obtained as

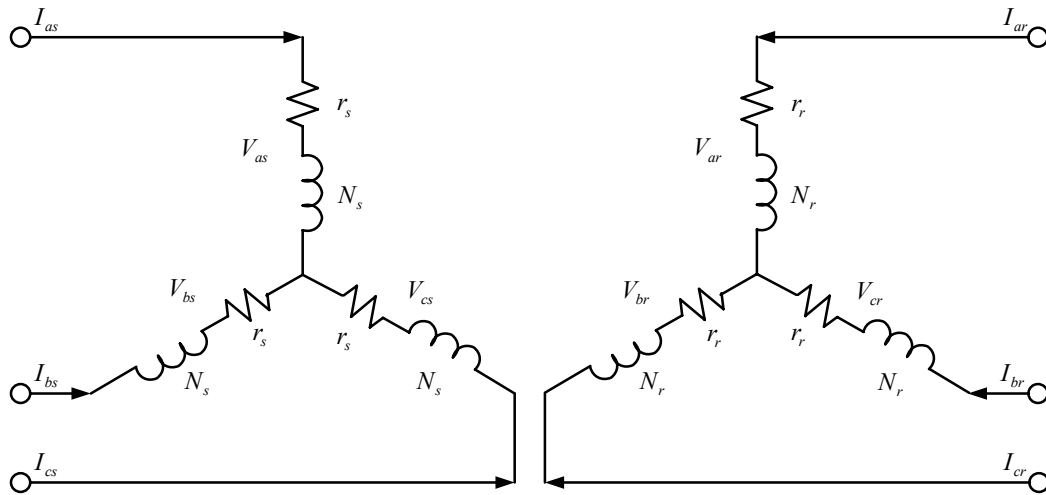


Figure 3.2 The equivalent phase circuit model of the induction machine.

$$\begin{aligned}
B_a(\phi_s) &= \frac{\mu_0 \cdot \text{MMF}(\phi_s)}{g} \\
&= \mu_0 \frac{N_s}{2} I_{as} \cos(\phi_s)
\end{aligned} \tag{3.5}$$

where g is the length of the air-gap and ϕ_s is the angular displacement of the stator.

Similarly, the flux density with all currents zero except I_{bs} and I_{cs} are

$$\begin{aligned}
B_b(\phi_s) &= \mu_0 \frac{N_s}{2} I_{bs} \cos\left(\phi_s - \frac{2\pi}{3}\right) \\
B_c(\phi_s) &= \mu_0 \frac{N_s}{2} I_{cs} \cos\left(\phi_s + \frac{2\pi}{3}\right)
\end{aligned} \tag{3.6}$$

Then the flux is determined by performing a surface integral over the open surface of a single turn as

$$\Phi(\phi_s) = \int_{\phi_s}^{\phi_s + \pi} B_a(\xi) r l d\xi \tag{3.7}$$

where r is the average radius of the air gap of the machine and l is the axial length of the air gap. For the sinusoidally distributed as winding, the turns function can be expressed as

$$N_{as}(\phi_s) = -\frac{N_s}{2} \sin(\phi_s) \tag{3.8}$$

So the total flux linkages of the as winding due to the current flowing only in the as winding is

$$\begin{aligned}
\lambda_{as} &= L_{ls} I_{as} + \int N_{as}(\phi_s) \int_{\phi_s}^{\phi_s + \pi} B_a(\xi) r l d\xi d\phi_s \\
&= L_{ls} I_{as} + \left(\frac{N_s}{2}\right)^2 \frac{\mu_0 \pi r l}{g} I_{as}
\end{aligned} \tag{3.9}$$

The self-inductance of the as winding is obtained by dividing the above equation by I_{as} .

$$\begin{aligned}
L_{asas} &= L_{ls} + \left(\frac{N_s}{2}\right)^2 \frac{\mu_0 \pi r l}{g} \\
&= L_{ls} + L_{ms}
\end{aligned} \tag{3.10}$$

where L_{ms} is the stator magnetizing inductance. The self-inductances of phase b and c have the same expression since the three phases are assumed symmetrical.

The mutual inductance between the two stator windings as and bs can be determined in the similar way by first computing the flux linking the as winding due to the current flowing in the bs winding. In this case,

$$\begin{aligned}
\lambda_{as} &= \int N_{as}(\phi_s) \int_{\phi_s}^{\phi_s+\pi} B_b(\xi) r l d\xi d\phi_s \\
&= -\frac{1}{2} \left(\frac{N_s}{2}\right)^2 \frac{\mu_0 \pi r l}{g} I_{bs}
\end{aligned} \tag{3.11}$$

The mutual inductance between as winding and bs winding is obtained by dividing the above equation by I_{bs} .

$$\begin{aligned}
L_{asbs} &= -\frac{1}{2} \left(\frac{N_s}{2}\right)^2 \frac{\mu_0 \pi r l}{g} \\
&= -\frac{1}{2} L_{ms}
\end{aligned} \tag{3.12}$$

The mutual inductances between phase b and c and between phase c and a have the same expression since the three phases are assumed symmetrical.

It follows that the rotor self-inductances for three phases are equal to

$$\begin{aligned}
L_{arar} &= L_{lr} + \left(\frac{N_r}{2}\right)^2 \frac{\mu_0 \pi r l}{g} \\
&= L_{lr} + L_{mr}
\end{aligned} \tag{3.13}$$

where L_{mr} is the rotor magnetizing inductance.

The mutual inductances between any two rotor windings are

$$\begin{aligned} L_{arbr} &= -\frac{1}{2} \left(\frac{N_r}{2} \right)^2 \frac{\mu_0 \pi r l}{g} \\ &= -\frac{1}{2} L_{mr} \end{aligned} \quad (3.14)$$

The mutual inductances between the stator and rotor windings can be determined using the same method. All of these mutual inductances are

$$L_{sr} = \left(\frac{N_s}{2} \right) \left(\frac{N_r}{2} \right) \frac{\mu_0 \pi r l}{g} \quad (3.15)$$

$$L_{asar} = L_{bsbr} = L_{cscar} = L_{sr} \cos \theta_r \quad (3.16)$$

$$L_{asbr} = L_{bscr} = L_{csar} = L_{sr} \cos \left(\theta_r + \frac{2\pi}{3} \right) \quad (3.17)$$

$$L_{ascr} = L_{bsar} = L_{csbr} = L_{sr} \cos \left(\theta_r - \frac{2\pi}{3} \right) \quad (3.18)$$

Then the flux linkages for the stator windings can be written as

$$\begin{aligned} \lambda_{as} &= L_{asas} I_{as} + L_{asbs} I_{bs} + L_{ascs} I_{cs} + L_{asar} I_{ar} + L_{asbr} I_{br} + L_{ascr} I_{cr} \\ \lambda_{bs} &= L_{bsas} I_{as} + L_{bsbs} I_{bs} + L_{bscs} I_{cs} + L_{bsar} I_{ar} + L_{bsbr} I_{br} + L_{bscr} I_{cr} \\ \lambda_{cs} &= L_{csas} I_{as} + L_{csbs} I_{bs} + L_{cscs} I_{cs} + L_{csar} I_{ar} + L_{csbr} I_{br} + L_{cscr} I_{cr} \end{aligned} \quad (3.19)$$

And the flux linkages for the rotor windings are

$$\begin{aligned} \lambda_{ar} &= L_{aras} I_{as} + L_{arbs} I_{bs} + L_{arcs} I_{cs} + L_{arar} I_{ar} + L_{arbr} I_{br} + L_{arcr} I_{cr} \\ \lambda_{br} &= L_{bras} I_{as} + L_{brbs} I_{bs} + L_{brcs} I_{cs} + L_{brar} I_{ar} + L_{brbr} I_{br} + L_{brcr} I_{cr} \\ \lambda_{cr} &= L_{cras} I_{as} + L_{crbs} I_{bs} + L_{crcs} I_{cs} + L_{crar} I_{ar} + L_{crbr} I_{br} + L_{crcr} I_{cr} \end{aligned} \quad (3.20)$$

3.4 Reference Frame Transformation

In the above derivations, all signals including phase voltages and currents are time-changing and all the inductances are time-changing also. All these ac variables increase the complexity of analyzing the machine. Fortunately various transformation theories were established to make the analysis in a much easier way. The basic idea is to transform the ac signals into dc signals, which are constant corresponding to a particular operating condition. After the analysis is done and the result comes out, the results are then transformed back to get the ac signals through the inverse transformation. This process is realized by the transformation between the stationary and synchronous reference frames, which are rotating at zero and synchronous (ω_e) speeds. However, this reference frame can be rotating at any arbitrary speed in general. So it is desired to get the general form of the transformation and then apply it in the particular applications.

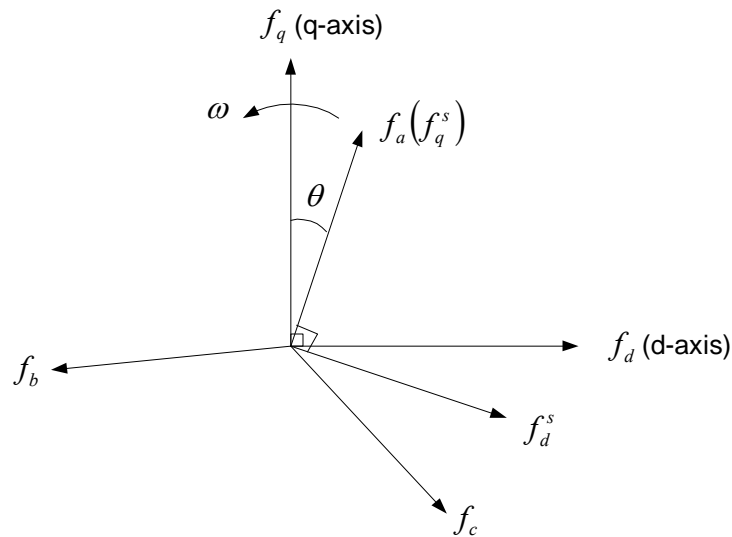


Figure 3.3 Transformation between reference frames.

The general transformation from the stationary abc reference frame to qd0 reference frame rotating at the arbitrary speed ω (rad/s) is shown in Figure 3.3 and defined in (3.21).

$$\begin{bmatrix} f_q \\ f_d \\ f_0 \end{bmatrix} = \frac{2}{3} \begin{bmatrix} \cos \theta & \cos\left(\theta - \frac{2\pi}{3}\right) & \cos\left(\theta + \frac{2\pi}{3}\right) \\ \sin \theta & \sin\left(\theta - \frac{2\pi}{3}\right) & \sin\left(\theta + \frac{2\pi}{3}\right) \\ \frac{1}{2} & \frac{1}{2} & \frac{1}{2} \end{bmatrix} \begin{bmatrix} f_a \\ f_b \\ f_c \end{bmatrix} = K \cdot \begin{bmatrix} f_a \\ f_b \\ f_c \end{bmatrix} \quad (3.21)$$

where $\theta = \omega t + \theta_0$, which represents the instant angle between two reference frames. f can be any variable in the corresponding reference frame including voltages, currents, flux linkages, inductance, etc.

In the case of transforming the variables in the abc stationary reference frame into the synchronous reference frame, $\omega = \omega_e$. The transformation can be done using (3.21) directly. However, six sine/cosine functions are necessarily calculated, which introduce a lot of calculation burden and not preferred especially in the digital implementation. The alternative way is to transform states in the abc stationary reference frame into the qd0 stationary reference frame (Clarke transformation). And then the final transformation is done through transforming the states in the qd0 stationary reference frame in to the qd0 synchronous reference frame (Park transformation). By this way, only two sine/cosine functions are calculated, which save a lot of calculation time. The Clarke transformation can be derived from the general transformation expression by forcing $\omega = 0$.

$$\begin{aligned}
f_q^s &= \frac{2}{3} \left(f_a - \frac{1}{2} f_b - \frac{1}{2} f_c \right) \\
f_d^s &= \frac{1}{\sqrt{3}} (-f_b + f_c) \\
f_0^s &= \frac{1}{3} (f_a + f_b + f_c)
\end{aligned} \tag{3.22}$$

Note that the third expression, which represents the zero sequence component, remains the same in the arbitrary reference frame. So it will not be put together with the qd expressions in the following analysis. Assuming the states in the abc stationary reference frame are balanced, which means

$$f_a + f_b + f_c = 0 \tag{3.23}$$

Then the Clarke transformation is rewritten as

$$\begin{aligned}
f_q^s &= f_a \\
f_d^s &= \frac{1}{\sqrt{3}} (-f_b + f_c) \\
&= \frac{1}{\sqrt{3}} (-f_a - 2f_b) \\
&= \frac{1}{\sqrt{3}} (f_a + 2f_c)
\end{aligned} \tag{3.24}$$

From Figure 3.3, the Park transformation between the qd0 stationary and synchronous reference frames is

$$\begin{bmatrix} f_q \\ f_d \end{bmatrix} = \begin{bmatrix} \cos \theta & -\sin \theta \\ \sin \theta & \cos \theta \end{bmatrix} \begin{bmatrix} f_q^s \\ f_d^s \end{bmatrix} \tag{3.25}$$

After the analysis is done in the synchronous reference frame, the results need to be transformed back into the abc stationary reference frame. The general inverse transformation is

$$\begin{bmatrix} f_a \\ f_b \\ f_c \end{bmatrix} = \begin{bmatrix} \cos \theta & \sin \theta & 1 \\ \cos\left(\theta - \frac{2\pi}{3}\right) & \sin\left(\theta - \frac{2\pi}{3}\right) & 1 \\ \cos\left(\theta + \frac{2\pi}{3}\right) & \sin\left(\theta + \frac{2\pi}{3}\right) & 1 \end{bmatrix} \begin{bmatrix} f_q \\ f_d \\ f_0 \end{bmatrix} = K^{-1} \cdot \begin{bmatrix} f_q \\ f_d \\ f_0 \end{bmatrix} \quad (3.26)$$

The inverse Park and Clarke transformations are

$$\begin{bmatrix} f_q^s \\ f_d^s \end{bmatrix} = \begin{bmatrix} \cos \theta & \sin \theta \\ -\sin \theta & \cos \theta \end{bmatrix} \begin{bmatrix} f_q \\ f_d \end{bmatrix} \quad (3.27)$$

$$\begin{aligned} f_a &= f_q^s \\ f_b &= -\frac{1}{2}f_q^s - \frac{\sqrt{3}}{2}f_d^s \\ f_c &= -\frac{1}{2}f_q^s + \frac{\sqrt{3}}{2}f_d^s \end{aligned} \quad (3.28)$$

3.5 Three-phase Induction Motor Equivalent Circuit

To facilitate the following analysis, the abbreviations are used

$$\begin{aligned} f_{abcs} &= [f_{as} \quad f_{bs} \quad f_{cs}]^T \\ f_{abcr} &= [f_{ar} \quad f_{br} \quad f_{cr}]^T \end{aligned} \quad (3.29)$$

Then the flux linkages in the stator and rotor windings can be expressed in terms of the stator and rotor currents as

$$\begin{bmatrix} \lambda_{abcs} \\ \lambda_{abcr} \end{bmatrix} = \begin{bmatrix} L_s & L_{sr} \\ L_{sr}^T & L_r \end{bmatrix} \begin{bmatrix} I_{abcs} \\ I_{abcr} \end{bmatrix} \quad (3.30)$$

and

$$L_s = \begin{bmatrix} L_{ls} + L_{ms} & -\frac{1}{2}L_{ms} & -\frac{1}{2}L_{ms} \\ -\frac{1}{2}L_{ms} & L_{ls} + L_{ms} & -\frac{1}{2}L_{ms} \\ -\frac{1}{2}L_{ms} & -\frac{1}{2}L_{ms} & L_{ls} + L_{ms} \end{bmatrix} \quad (3.31)$$

$$L_r = \begin{bmatrix} L_{lr} + L_{mr} & -\frac{1}{2}L_{mr} & -\frac{1}{2}L_{mr} \\ -\frac{1}{2}L_{mr} & L_{lr} + L_{mr} & -\frac{1}{2}L_{mr} \\ -\frac{1}{2}L_{mr} & -\frac{1}{2}L_{mr} & L_{lr} + L_{mr} \end{bmatrix} \quad (3.32)$$

$$L_{sr} = L_{sr} \begin{bmatrix} \cos(\theta_r) & \cos(\theta_r + \beta) & \cos(\theta_r - \beta) \\ \cos(\theta_r - \beta) & \cos(\theta_r) & \cos(\theta_r + \beta) \\ \cos(\theta_r + \beta) & \cos(\theta_r - \beta) & \cos(\theta_r) \end{bmatrix} \quad (3.33)$$

where $\beta = \frac{2\pi}{3}$.

In order to derive the equivalent circuit, it is necessary to transform all signals into the same side of the machine, either stator side or rotor side. And there is a turn ratio between these two sides corresponding to the definition of flux linkages. It is preferred to transform the flux linkages on the rotor side into the stator side. Then the flux linkages and the voltage equations are expressed in terms of machine variables referred to the stator windings as

$$\begin{bmatrix} \lambda_{abc} \\ \lambda_{abc}' \end{bmatrix} = \begin{bmatrix} L_s & (L_{sr})' \\ (L_{sr})^T & L_r' \end{bmatrix} \begin{bmatrix} I_{abc} \\ I_{abc}' \end{bmatrix} \quad (3.34)$$

$$\begin{bmatrix} V_{abc} \\ V_{abc}' \end{bmatrix} = \begin{bmatrix} r_s + pL_s & pL_{sr}' \\ p(L_{sr})^T & r_r' + pL_r' \end{bmatrix} \begin{bmatrix} I_{abc} \\ I_{abc}' \end{bmatrix} \quad (3.35)$$

where

$$I_{abc}' = \frac{N_r}{N_s} I_{abc}, \quad V_{abc}' = \frac{N_r}{N_s} V_{abc}, \quad \lambda_{abc}' = \frac{N_r}{N_s} \lambda_{abc}$$

$$L_{sr}' = \frac{N_r}{N_s} L_{sr}, \quad r_r' = \left(\frac{N_r}{N_s}\right)^2 r_r, \quad L_r' = \left(\frac{N_s}{N_r}\right)^2 L_r.$$

In order to facilitate the analysis, the voltage equations are generally transformed into the synchronous reference frame. This process is done through multiplying both sides of (3.34 ~ 35) by K .

$$K \cdot \begin{bmatrix} \lambda_{abc}' \\ \lambda_{abc}' \end{bmatrix} = K \cdot \begin{bmatrix} L_s & (L_{sr})' \\ (L_{sr}^T)' & L_r' \end{bmatrix} \cdot (K^{-1} \cdot K) \cdot \begin{bmatrix} I_{abc}' \\ I_{abc}' \end{bmatrix}$$

$$K \cdot \begin{bmatrix} V_{abc}' \\ V_{abc}' \end{bmatrix} = K \cdot \begin{bmatrix} r_s + pL_s & pL_{sr}' \\ p(L_{sr}^T)' & r_r' + pL_r' \end{bmatrix} \cdot (K^{-1} \cdot K) \cdot \begin{bmatrix} I_{abc}' \\ I_{abc}' \end{bmatrix}$$

After substituting the transformation matrix into this expression,

$$\begin{bmatrix} \lambda_{qd0s}' \\ \lambda_{qd0r}' \end{bmatrix} = \begin{bmatrix} K \cdot L_s \cdot K^{-1} & K \cdot (L_{sr})' \cdot K^{-1} \\ K \cdot (L_{sr}^T)' \cdot K^{-1} & K \cdot L_r' \cdot K^{-1} \end{bmatrix} \cdot \begin{bmatrix} I_{qd0s}' \\ I_{qd0r}' \end{bmatrix}$$

$$V_{qd0s}' = r_s I_{qd0s}' + \omega \lambda_{dqs}' + p \lambda_{qd0s}'$$

$$V_{qd0r}' = r_r' I_{qd0r}' + (\omega - \omega_r) \lambda_{dqr}' + p \lambda_{qd0r}' \quad (3.36)$$

where

$$\lambda_{qd0s}' = [\lambda_{qs}' \quad \lambda_{ds}' \quad \lambda_{0s}']^T, \quad \lambda_{qd0r}' = [\lambda_{qr}' \quad \lambda_{dr}' \quad \lambda_{0r}']^T,$$

$$\lambda_{dqs}' = [\lambda_{ds}' \quad \lambda_{qs}' \quad 0]^T, \quad \lambda_{dqr}' = [\lambda_{dr}' \quad \lambda_{qr}' \quad 0]^T,$$

$$K \cdot L_s \cdot K^{-1} = \begin{bmatrix} L_{ls} + L_m & 0 & 0 \\ 0 & L_{ls} + L_m & 0 \\ 0 & 0 & L_{ls} \end{bmatrix},$$

$$K \cdot L_r' \cdot K^{-1} = \begin{bmatrix} L_{lr}' + L_m & 0 & 0 \\ 0 & L_{lr}' + L_m & 0 \\ 0 & 0 & L_{lr}' \end{bmatrix},$$

$$K \cdot (L_{sr}') \cdot K^{-1} = K \cdot (L_{sr}')^T \cdot K^{-1} = \begin{bmatrix} L_m & 0 & 0 \\ 0 & L_m & 0 \\ 0 & 0 & 0 \end{bmatrix},$$

$$L_m = \frac{3}{2} L_{ms}.$$

These voltage equations are frequently written in expanded form.

$$\begin{aligned} V_{qs} &= r_s I_{qs} + \omega \lambda_{ds} + p \lambda_{qs} \\ V_{ds} &= r_s I_{ds} - \omega \lambda_{qs} + p \lambda_{ds} \end{aligned} \quad (3.37)$$

$$V_{0s} = r_s I_{0s} + p \lambda_{0s}$$

$$\begin{aligned} V_{qr}' &= r_r' I_{qr}' + (\omega - \omega_r) \lambda_{dr}' + p \lambda_{qr}' \\ V_{dr}' &= r_r' I_{dr}' - (\omega - \omega_r) \lambda_{qr}' + p \lambda_{dr}' \end{aligned} \quad (3.38)$$

$$V_{0r}' = r_r' I_{0r}' + p \lambda_{0r}'$$

And the expressions for the flux linkages in expanded form are

$$\begin{aligned} \lambda_{qs} &= L_{ls} I_{qs} + L_m (I_{qs} + I_{qr}') \\ \lambda_{ds} &= L_{ls} I_{ds} + L_m (I_{ds} + I_{dr}') \end{aligned} \quad (3.39)$$

$$\lambda_{0s} = L_{ls} I_{0s}$$

$$\begin{aligned} \lambda_{qr}' &= L_{lr}' I_{qr}' + L_m (I_{qs} + I_{qr}') \\ \lambda_{dr}' &= L_{lr}' I_{dr}' + L_m (I_{ds} + I_{dr}') \end{aligned} \quad (3.40)$$

$$\lambda_{0r}' = L_{lr}' I_{0r}'$$

From (3.37 ~ 40), the qd0 equivalent circuit of the induction machine in an arbitrary reference frame rotating at speed ω is shown in Figure 3.4. The equivalent circuit in the

synchronous reference frame can be derived by making $\omega = \omega_e$. The advantage of using the synchronous reference frame is that the applied voltages after the transformation are DC quantities and then the currents can be solved easily. Since all the quantities in the rotor are referred to the stator side in the convenience of analysis, the sign of “prime” in the rotor equations will be ignored in the following analysis.

The dynamic equation of the induction machine is given as

$$p\omega_r = \frac{P}{2J}(T_e - T_L) \quad (3.41)$$

in which the electric torque can be calculated using flux linkages and currents as

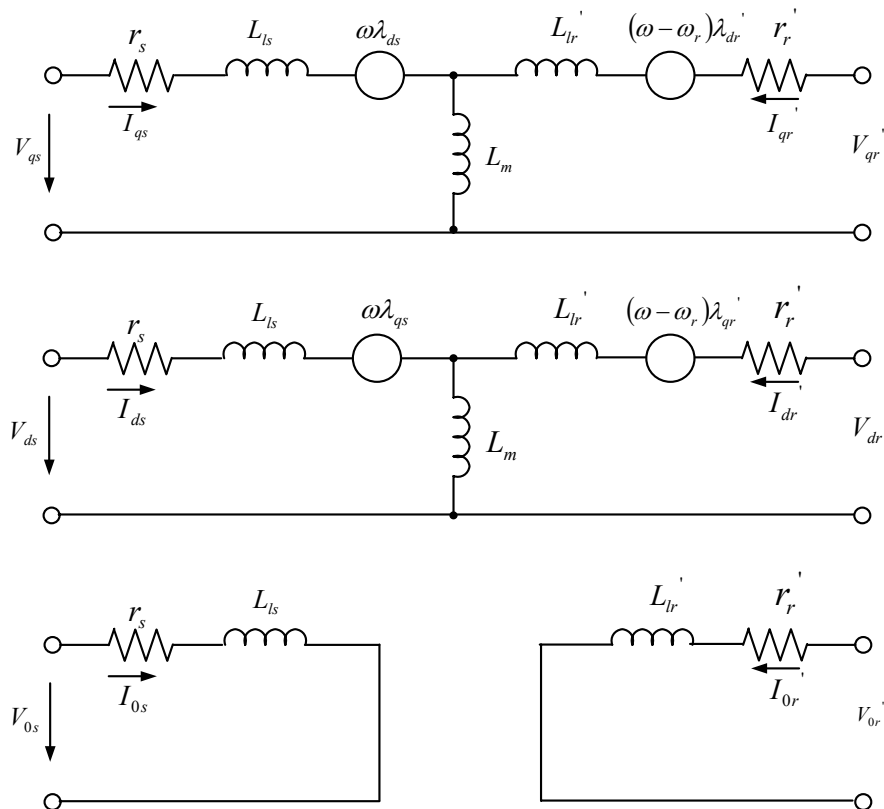


Figure 3.4 The qd0 equivalent circuit model of the induction machine in the arbitrary reference frame.

$$\begin{aligned}
T_e &= \frac{3P}{4} \cdot \frac{L_m}{L_r} \cdot (\lambda_{dr} I_{qs} - \lambda_{qr} I_{ds}) \\
&= \frac{3P}{4} \cdot L_m \cdot (I_{dr} I_{qs} - I_{qr} I_{ds}) \\
&= \frac{3P}{4} \cdot (\lambda_{ds} I_{qs} - \lambda_{qs} I_{ds})
\end{aligned} \tag{3.42}$$

3.5.1 Induction Machine Model Using Natural Variables

The variables of the natural variable model of the induction machine are chosen as the developed electromagnetic torque T_e , the developed reactive torque T_r , the rotor speed ω_r , and the square of the magnitude of the rotor flux linkage λ_{rr} . These variables are the same in all reference frames or independent of the selected reference frame. These natural variables are expressed in terms of the axis currents and flux linkages as:

$$\begin{aligned}
T_e &= k_t (\lambda_{dr} I_{qs} - \lambda_{qr} I_{ds}) \\
T_r &= k_t (\lambda_{dr} I_{ds} + \lambda_{qr} I_{qs}) \\
\lambda_{rr} &= \lambda_{qr}^2 + \lambda_{dr}^2
\end{aligned} \tag{3.49}$$

where $k_t = \frac{3PL_m}{4L_r}$ and P is the poles of the machine.

The stator and rotor voltage equations can be rewritten in terms of stator currents and rotor flux linkages as

$$\begin{aligned}
V_{qs} &= rI_{qs} - c\lambda_{qr} + \frac{\omega_r L_m}{L_r} \lambda_{dr} + L_\sigma pI_{qs} \\
V_{ds} &= rI_{ds} - c\lambda_{dr} - \frac{\omega_r L_m}{L_r} \lambda_{qr} + L_\sigma pI_{ds} \\
0 &= r_r I_{qr} + p\lambda_{qr} + (\omega - \omega_r) \lambda_{dr} \\
0 &= r_r I_{dr} + p\lambda_{dr} - (\omega - \omega_r) \lambda_{qr}
\end{aligned} \tag{3.50}$$

where $r = \frac{r_s}{k} + \frac{r_r L_m^2}{L_r^2}$, $c = \frac{r_r L_m}{L_r^2}$.

To obtain the desired model, equations (3.49) are differentiated and then expressed in terms of the defined natural variables as follows.

$$pT_e = -\left(\frac{r_s}{L_\sigma k} + \frac{r_r L_s}{L_\sigma L_r}\right)T_e - \omega_r T_r - \frac{k_t L_m}{L_\sigma L_r} \omega_r \lambda_{rr} + \frac{k_t}{L_\sigma k} m_1 \quad (3.51)$$

$$p\omega_r = \frac{P}{2J}(T_e - T_L) \quad (3.52)$$

$$pT_r = -\left(\frac{r_s}{L_\sigma k} + \frac{r_r L_s}{L_\sigma L_r}\right)T_r + \frac{r_r L_m}{L_r k_t} \frac{T_e^2 + T_r^2}{\lambda_{rr}} + \omega_r T_e + \frac{k_t r_r L_m}{L_\sigma L_r^2} \lambda_{rr} + \frac{k_t}{L_\sigma k} m_2 \quad (3.53)$$

$$p\lambda_{rr} = -\frac{2r_r}{L_r} \lambda_{rr} + \frac{2r_r L_m}{k_t L_r} T_r \quad (3.54)$$

where

$$\begin{aligned} m_1 &= \lambda_{dr} V_{qs} - \lambda_{qr} V_{ds} \\ m_2 &= \lambda_{qr} V_{qs} + \lambda_{dr} V_{ds} \end{aligned} \quad (3.55)$$

The quantities m_1 and m_2 are calculated using the outputs of the controllers for T_e and T_r . Then the voltages commands are calculated by solving (3.55).

$$\begin{aligned} V_{qs} &= \frac{m_1 \lambda_{dr} + m_2 \lambda_{qr}}{\lambda_{rr}} \\ V_{ds} &= \frac{m_2 \lambda_{dr} - m_1 \lambda_{qr}}{\lambda_{rr}} \end{aligned} \quad (3.56)$$

The natural variables model of the induction machine can also be expressed in terms of the stator flux in place of the rotor flux. The model equations are derived as

below. The method used in the derivation is the same as that used for the model of the natural variables in terms of the rotor flux. The natural variables are defined as follows.

$$\begin{aligned} T_e &= k(\lambda_{ds}I_{qs} - \lambda_{qs}I_{ds}) \\ T_r &= -k(\lambda_{qs}I_{qs} + \lambda_{ds}I_{ds}) \\ \lambda_{ss} &= \lambda_{qs}^2 + \lambda_{ds}^2 \end{aligned} \quad (3.57)$$

where $k_t = \frac{3P}{4}$.

To obtain the desired model, equations (3.57) are differentiated and then expressed in terms of the defined natural variables as follows.

$$pT_e = k \left[m_3 - \frac{1}{L_\sigma} \left(r_s + \frac{r_r L_s}{L_r} \right) T_e - \omega_r T_r - \frac{k\omega_r}{L_\sigma} \lambda_{ss} \right] \quad (3.58)$$

$$pT_r = k \left(m_4 - \frac{r_r}{L_\sigma L_r} \lambda_{ss} \right) - \frac{1}{L_\sigma} \left(r_s + \frac{r_r L_s}{L_r} \right) T_r + \omega_r T_e + \frac{r_s}{k\lambda_{ss}} (T_e^2 + T_r^2) \quad (3.59)$$

$$p\lambda_{ss} = 2(\lambda_{qs}V_{qs} + \lambda_{ds}V_{ds}) - \frac{2r_s}{k} T_r \quad (3.60)$$

where

$$\begin{aligned} m_3 &= \left(\frac{\lambda_{ds} - L_\sigma I_{ds}}{L_\sigma} \right) V_{qs} - \left(\frac{\lambda_{qs} - L_\sigma I_{qs}}{L_\sigma} \right) V_{ds} \\ m_4 &= - \left(\frac{\lambda_{qs} + L_\sigma I_{qs}}{L_\sigma} \right) V_{qs} - \left(\frac{\lambda_{ds} + L_\sigma I_{ds}}{L_\sigma} \right) V_{ds} . \end{aligned}$$

Equations (3.58) to (3.60) are the model equations for the induction machine in terms of the natural variables T_e , T_r and λ_{ss} .

3.5.2 Induction Machine Model Using Flux Linkages

The voltage equations of the induction machine can be expressed in terms of the stator and rotor flux linkages, which find the applications in the flux observers. In the arbitrary reference frame, the complex form is adopted for all quantities in q-d axis to simplify the analysis as follows.

$$V_{qds} = V_{qs} + jV_{ds} \ , \ V_{qdr} = V_{qr} + jV_{dr}$$

$$I_{qds} = I_{qs} + jI_{ds} \ , \ I_{qdr} = I_{qr} + jI_{dr}$$

$$\lambda_{qds} = \lambda_{qs} + j\lambda_{ds} \ , \ \lambda_{qdr} = \lambda_{qr} + j\lambda_{dr}$$

The stator and rotor voltage equations of an induction machine are

$$V_{qds} = r_s I_{qds} + p\lambda_{qds} - j\omega_e \lambda_{qds} \quad (3.61)$$

$$V_{qdr} = r_r I_{qdr} + p\lambda_{qdr} - j(\omega_e - \omega_r) \lambda_{qdr} \quad (3.62)$$

The currents in the equations are substituted with the flux linkages to generate the state equations in terms of the flux linkages using

$$\lambda_{qds} = L_s I_{qds} + L_m I_{qdr}$$

$$\lambda_{qdr} = L_r I_{qdr} + L_m I_{qds}$$

Define $L_\sigma = L_s - \frac{L_m^2}{L_r}$ and express the currents in terms of the flux linkages as

$$I_{qds} = \frac{1}{L_\sigma} \lambda_{qds} - \frac{L_m}{L_\sigma L_r} \lambda_{qdr} \quad (3.63)$$

$$I_{qdr} = -\frac{L_m}{L_\sigma L_r} \lambda_{qds} + \frac{L_s}{L_\sigma L_r} \lambda_{qdr} \quad (3.64)$$

The stator and rotor voltage equations can be rewritten as

$$V_{qds} = \frac{r_s}{L_\sigma} \lambda_{qds} - \frac{r_s L_m}{L_\sigma L_r} \lambda_{qdr} + p \lambda_{qds} - j \omega_e \lambda_{qds} \quad (3.65)$$

$$V_{qdr} = -\frac{r_r L_m}{L_\sigma L_r} \lambda_{qds} + -\frac{r_r L_s}{L_\sigma L_r} \lambda_{qdr} + p \lambda_{qdr} - j(\omega_e - \omega_r) \lambda_{qdr} \quad (3.66)$$

3.6 Parameters of Induction Machines

The parameters of the induction machine are very important for the analysis and especially for the implementation of control system. The determination of the parameters involves three different tests, the dc test, no-load test and blocked rotor test. The phase model shown in Figure 3.5 is used to determine the phase parameters of the machine assuming that three phases are symmetrical. The stator core loss is represented by the core loss resistance in parallel with the mutual inductance. And the slip is defined as

$$s = \frac{\omega_e - \omega_r}{\omega_e} \quad (3.67)$$

The stator resistances of the testing induction motor are calculated by measuring the phase current when a DC voltage is applied between two phases (The DC voltage is applied to the phase to neutral when the neutral point is accessible). The average value of the three measurements is then divided by two to calculate the phase resistance.

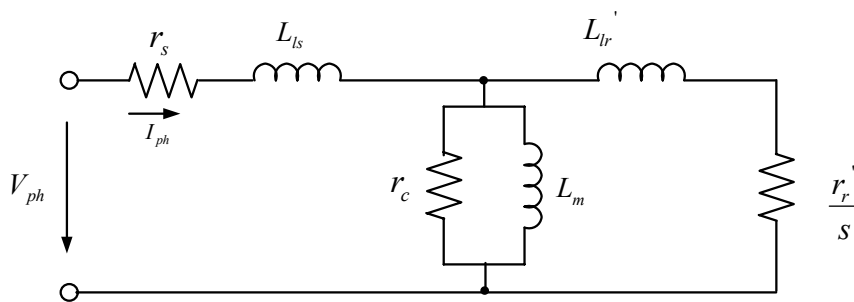


Figure 3.5 The phase model of the induction machine.

$$r_s = \frac{\bar{V}_{dc}}{2\bar{I}_{dc}} \quad (3.68)$$

The second test performed is the no-load test, which is used to calculate the magnetizing inductance and the core loss resistance. The three-phase balanced voltage with normal frequency is applied to the induction machine that is disconnected from the load and then the phase currents and the total active power are measured. In this case, the slip is nearly zero. The assumption is made for the calculations that the core loss resistance is big compared with the impedance due to the mutual inductance and the voltage drop on the stator resistance is small. The equations in (3.69) are used to calculate the relationship between the mutual inductance and phase voltage and the relationship between the core loss resistance and phase voltage.

$$\begin{aligned} |r_s + j\omega(L_{ls} + L_m)| &= \frac{V_{ph}}{I_{ph}} \\ 3r_s I_{ph}^2 + 3\frac{V_{ph}^2}{r_c} &= P \end{aligned} \quad (3.69)$$

The third test performed is the blocked rotor test, which is used to calculate the leakage inductances and the rotor resistance. The three-phase balanced voltage is applied to the induction machine, the rotor of which is held stationary. Then the phase currents and the total active power are measured. In this case, the slip is nearly unity. The impedance of the core loss resistance and the mutual inductance is big compared with the impedance of the rotor leakage inductance and rotor resistance. So the equations in (3.70) are applied to calculate the leakage inductances by assuming the stator leakage inductance is equal to the rotor leakage inductance.

$$\left| (r_s + r_r') + j\omega(L_{ls} + L_{lr}') \right| = \frac{V_{ph}}{I_{ph}} \quad (3.70)$$

$$3(r_s + r_r') I_{ph}^2 = P$$

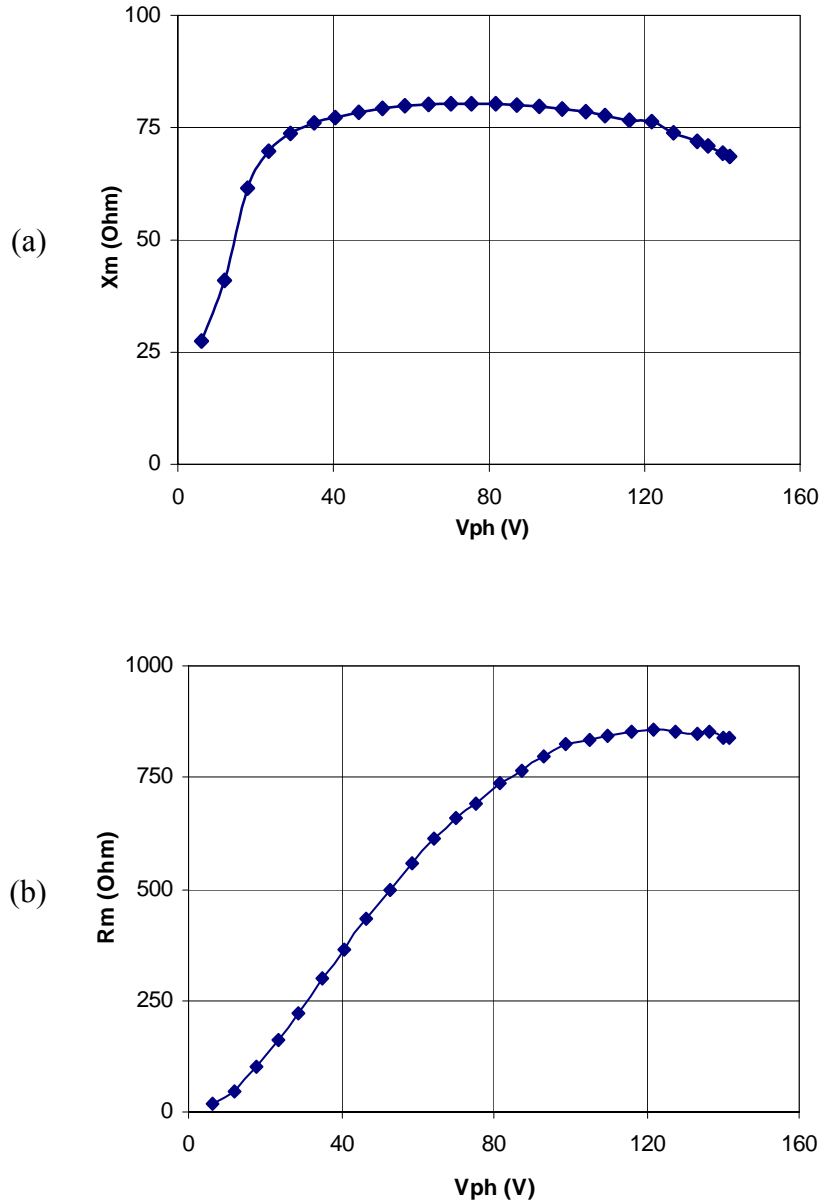


Figure 3.6 No-load test: (a) Mutual impedance vs phase voltage, (b) equivalent core loss resistance vs phase voltage.

It is shown that the equivalent core loss resistance is much greater than the corresponding mutual impedance in the no-load test, which means that the core loss can be ignored in the analysis. All of these parameters are changing with respect to the phase voltages and/or currents. So the average values are used in the following analysis. The parameters of the experimental induction motor are shown in Table 3.1.

As it can be seen from Figure 3.6, the core loss is not negligible when the induction machine is running at low supply voltage. The stator core loss has to be considered especially when the total electrical loss is to be minimized. The stationary reference frame q-d equivalent circuit of the induction machine with consideration of stator core loss is shown in Figure 3.8, in which the core loss is represented by the power consumed by the core loss resistance.

In order to analyze the machine, the machine voltage equations are expressed in terms of the torque effective currents instead of the actual input currents. These currents are I'_{qs} and I'_{ds} in the stationary q-d reference frame. When the stator core loss is neglected, these two currents are identical to I_{qs} and I_{ds} , respectively. The voltage equations considering the stator core loss are given as

Table 3.1 Parameters of the experimental induction motor

$R_s = 1.9812 \ \Omega$	$L_{ls} = 0.0091 \ H$
$R_r = 1.85 \ \Omega$	$L_{lr} = 0.0091 \ H$
$L_m = 0.1986 \ H$	$P = 4$

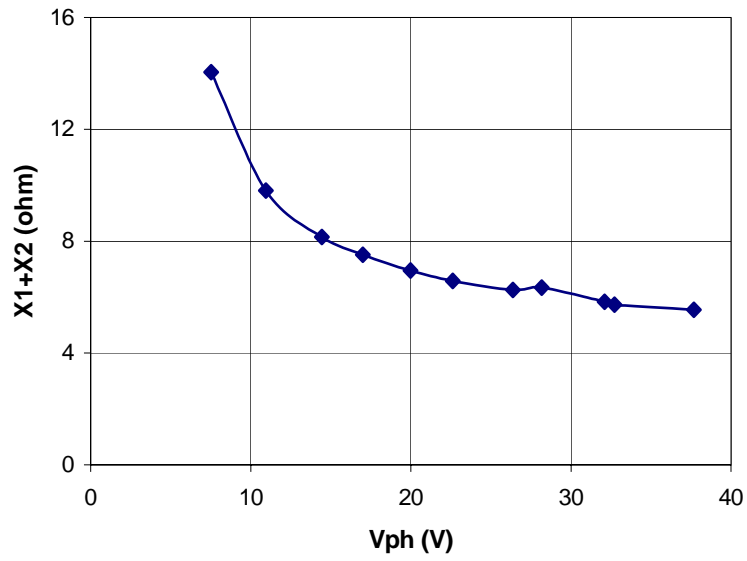


Figure 3.7 Blocked rotor test: leakage impedance vs phase voltage.

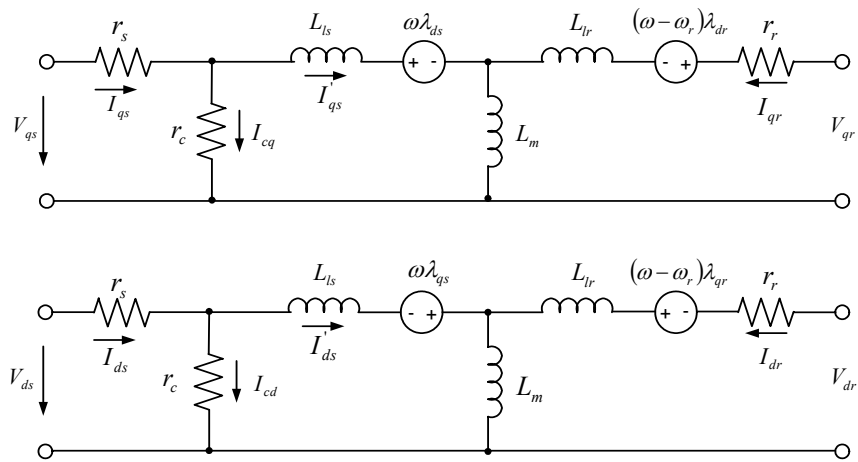


Figure 3.8 The q-d equivalent circuit model of the induction machine including core loss resistance.

$$\begin{aligned}
\frac{V_{qs}}{k} &= rI'_{qs} - c\lambda_{qr} + \frac{\omega_r L_m}{L_r} \lambda_{dr} + L_\sigma pI'_{qs} \\
\frac{V_{ds}}{k} &= rI'_{ds} - c\lambda_{dr} - \frac{\omega_r L_m}{L_r} \lambda_{qr} + L_\sigma pI'_{ds} \\
0 &= r_r I_{qr} + p\lambda_{qr} - \omega_r \lambda_{dr} \\
0 &= r_r I_{dr} + p\lambda_{dr} + \omega_r \lambda_{qr}
\end{aligned} \tag{3.45}$$

where $r = \frac{r_s}{k} + \frac{r_r L_m^2}{L_r^2}$, $c = \frac{r_r L_m}{L_r^2}$.

3.7 Conclusion

This chapter presented the induction machine model in both stationary and the arbitrary reference frames. The general transformations between different reference frames are derived, which are used to get the voltage equations in the arbitrary reference frame. The procedure of determining induction machine parameters is illustrated through the test on the experimental machine.

CHAPTER 4

VECTOR CONTROL OF INDUCTION MACHINE

4.1 Introduction

Induction motors have been widely used in the industrial drive system as a means of converting electric power to mechanical power. With the development of the vector control technology, the induction machine drive systems offer high performance as well as independent control on torque and flux linkages, which is similar to that of the DC machine. Furthermore, it's possible to drive the induction machines above their rated speed through flux weakening, which also finds a lot of industrial applications. The major applications include pumps, fans, electric vehicles, machine tools, robotics, and many kinds of electric propulsions. The vector control is referred for controlling both amplitude and phase of the AC excitation. And the vector control of voltages and currents results in the control of spatial orientation of the electromagnetic fields in the machine, which leads to the field orientation. It is usually desired to have the 90° orientation between the MMF due to the armature current and the field.

The control schemes available for the induction motor drives are the scalar control, direct torque control, adaptive control, and vector or field oriented control. The vector control is mainly discussed in this chapter. In the case of induction machines, the rotor flux oriented control is usually employed although it is possible to implement stator flux oriented and also magnetizing flux oriented control. The stator/rotor flux linkages of the induction machines are necessary for the vector control. In terms of the methods of

obtaining the flux linkages, the field oriented induction machine drive systems are classified into two categories, the direct field oriented system with flux sensors and the indirect field oriented system. In the former case, the flux quantities (magnitude and angle) are directly measured by using Hall-effect sensors, search coils, tapped stator windings of the machine, or calculated from the so-called flux model. For the indirect field oriented control system, the magnitude and space angle of the flux linkages are obtained by utilizing the monitored stator currents and the rotor speed. The space angle of the flux linkage is then obtained as the sum of the monitored rotor angle (corresponding to the rotor speed) and the computed reference value of the slip angle (corresponding to the slip frequency). The latter one is still receiving wide attention although some sensorless control strategies have been proposed in the last few years [4.1-4.4]. The exact estimation of rotor position is one of the key issues in the vector control system and the installation of encoders/ revolvers seems to be the most reliable way. Every kind of estimation has to be compared with the output of the encoder to check the effectiveness.

4.2 Fundamentals of Vector Control

In general, an electric motor is used to generate the desired torque for the purpose of driving. And the electric torque is basically the result of interaction of two magnetic fields that are not aligned on the same direction. The source of magnetic field can be the winding current (either AC or DC) or permanent magnets. A simple case is the separately excited DC machine in which the armature and field currents can be controlled independently (in the case of permanent magnet machine, the field is introduced by the

permanent magnet instead of the field current). Once the magnetic field is selected, the magnitude of the armature current can be controlled in order to generate the desired torque.

The DC machine model can be simplified as shown in Figure 4.1. The electromagnetic interaction between the field flux and the armature MMF results in two basic outputs: an induced voltage proportional to the rotor speed and an electromagnetic torque proportional to the armature current.

$$E_a = \frac{P}{2} \cdot \lambda_{af} \omega_{rm} \tag{4.1}$$

$$T_e = \frac{P}{2} \cdot \lambda_{af} I_a$$

where ω_{rm} is the rotor speed in mechanical radians per second, P is the number of poles and λ_{af} is the flux produced by the field current that links the armature winding. The difference between the field flux and the flux linked with the armature winding is the leaked flux, which can be represented by the leakage inductance. The electric torque can be finally written as

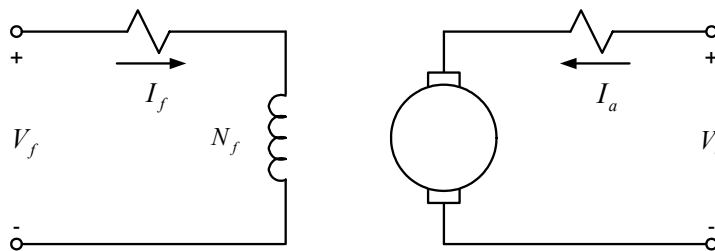


Figure 4.1 Idealized DC machine circuit diagram.

$$\lambda_{af} = \frac{L_{af}}{L_f} \cdot \lambda_f$$

$$T_e = \frac{P}{2} \cdot \frac{L_{af}}{L_f} \cdot \lambda_f I_a$$
(4.2)

From the above example of DC machine, some requirements need to be satisfied for the torque control. The armature current should be independently controlled in order to overcome the effects of armature winding resistance, leakage inductance, and induced voltage. The field flux should be independently controlled or kept constant. The spatial angle between the flux axis and the MMF axis due to the armature current should be independently controlled orthogonal in order to avoid interaction of the flux and MMF. If these three requirements are met at every instant of time, the torque will instantaneously follow the armature current and instantaneous torque control will result.

For the DC machine, most of the conditions are satisfied according to the structure itself and the operation principle. But in AC machines, these requirements have to be achieved through external control and the process is much more complex than that of DC machines.

4.3 Vector Control of Induction Machine

In general, the steady state torque control results when the requirements for the instantaneous torque control are met for steady state conditions. However, the steady state operation is the special case of the transient analysis by assuming the derivative terms to be zero. So it is useful to derive the vector control of induction machine using

the transient model, which has been derived in Chapter 3. The general phasor diagram of the stator voltages, currents and rotor flux is shown in Figure 4.2.

The rotor flux linkage λ_r is supposed to have q- and d-axis components as the voltages and currents have. But it is possible to align the whole phasor with the synchronous reference frame. By this way, the analysis becomes simple and the field is only represented by a scalar instead of a phasor. The electric torque equation for the induction machine is

$$\begin{aligned}
 T_e &= \frac{3P}{4} \cdot \frac{L_m}{L_r} \cdot (\lambda_{dr} I_{qs} - \lambda_{qr} I_{ds}) \\
 &= \frac{3P}{4} \cdot (\lambda_{ds} I_{qs} - \lambda_{qs} I_{ds}) \\
 &= \frac{3P}{4} \cdot L_m \cdot (I_{dr} I_{qs} - I_{qr} I_{ds})
 \end{aligned} \tag{4.3}$$

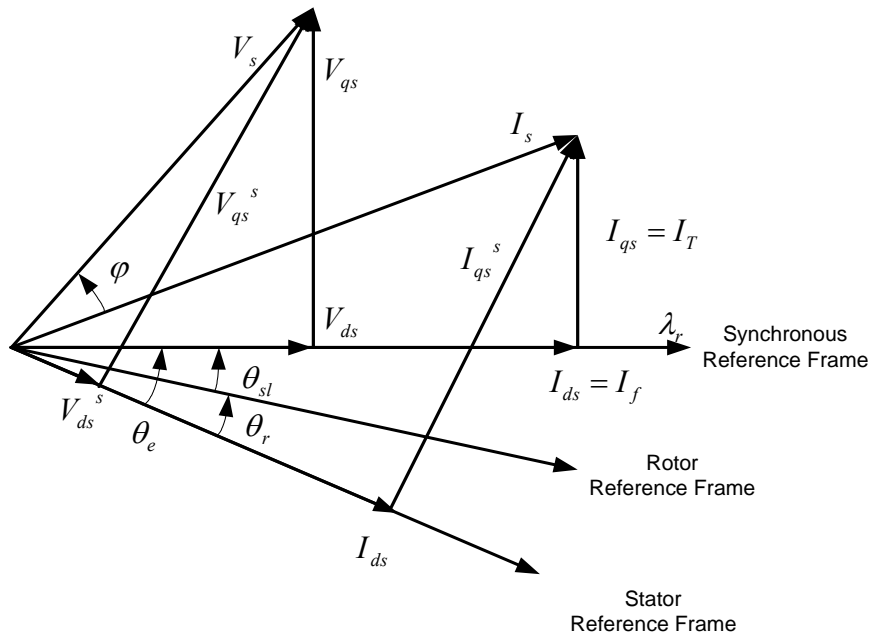


Figure 4.2 Phasor diagram of vector control of the induction machine.

in which all the flux linkages and currents can be represented in any reference frame since the electric torque is a scalar that is independent of any reference frame. There different forms are achieved by applying the relationship between the flux linkages and currents. They are used in different control schemes according to the selected state variables and the reference frame. If the rotor flux linkage is aligned with the synchronous reference frame, it means

$$\begin{aligned}\lambda_{qr} &= 0 \\ \lambda_r &= \lambda_{dr}\end{aligned}\tag{4.4}$$

And the torque equation changes to

$$T_e = \frac{3P}{4} \cdot \frac{L_m}{L_r} \cdot \lambda_{dr} I_{qs}\tag{4.5}$$

This form is similar to the torque equation of the DC machine. So if the rotor flux linkage λ_r is regulated or kept constant, the output torque will be proportional to the q-axis stator current ($I_{qs}^e = I_T$) in the synchronous reference frame.

Apparently the rotor flux linkage and the torque producing stator current are not independent. All stator and rotor flux linkages and the torque are coming from the AC voltages applied to the induction machine and the current generated. So instantaneous decoupling and independent control of the rotor flux linkages and stator currents are the two most important issues to deal with.

Since the control mentioned in the above is basically in the synchronous reference frame, the instant angle for the synchronous reference frame with respect to the stationary reference frame needs to be determined first. According to Figure 4.2, this angle is the position angle of the rotor flux linkage θ_e . If this angle is known, all variables can be

transformed into the synchronous reference frame, in which the quantities after transformation become DC quantities. Depending upon the measure of getting the position angle of the rotor flux linkages, the vector control schemes can be classified into two categories: direct and indirect vector control. In the direct vector control scheme, the angle is determined from the flux measurements using Hall sensors or flux sensing windings. While in the indirect vector control scheme, the angle is computed from the measured rotor position and the slip relation. The relationship between these angles is shown in (4.6).

$$\begin{aligned}\theta_e &= \theta_r + \theta_{sl} \\ &= \int (\omega_r + \omega_{sl}) dt = \int \omega_e dt\end{aligned}\tag{4.6}$$

In order to get the rotor flux angle for the direct vector control, the additional sensors or windings need to be installed inside the induction machine, which need special design for different type of machines and introduce a potential fault condition. So the more popular control scheme is the indirect vector control scheme, in which the rotor speed is measured using rotor position or speed sensors. The slip frequency is calculated from the voltage equations and then the position angle of the rotor flux is calculated using (4.6). In the normal operation, the rotor speed is always important and monitored, which means the indirect vector control scheme will not increase the cost at all. The indirect vector control for induction machine is derived in detail in the following section.

4.4 Derivation of Indirect Vector Control of Induction Machine

In the indirect vector control of induction machine, a voltage source inverter is supposed to drive the machine so that the slip frequency can be changing according to the particular requirement. Assuming the rotor speed is measured, then the slip frequency is derived from the rotor voltage equations. The rotor voltage equations in the synchronous reference frame are

$$\begin{aligned} 0 &= r_r I_{qr} + p\lambda_{qr} + (\omega_e - \omega_r)\lambda_{dr} \\ 0 &= r_r I_{dr} + p\lambda_{dr} - (\omega_e - \omega_r)\lambda_{qr} \end{aligned} \quad (4.7)$$

where

$$\begin{aligned} \omega_{sl} &= \omega_e - \omega_r \\ \lambda_{qr} &= L_r I_{qr} + L_m I_{qs} \\ \lambda_{dr} &= L_r I_{dr} + L_m I_{ds} \end{aligned} \quad (4.8)$$

When the rotor flux is aligned onto d-axis of the synchronous reference frame as shown in Figure 4.1, the following yields

$$\begin{aligned} \lambda_r &= \lambda_{dr} \\ \lambda_{qr} &= 0, \quad p\lambda_{qr} = 0 \end{aligned} \quad (4.9)$$

Substituting (4.9) in (4.7) results the simple rotor equations

$$\begin{aligned} 0 &= r_r I_{qr} + (\omega_e - \omega_r)\lambda_{dr} \\ 0 &= r_r I_{dr} + p\lambda_{dr} \end{aligned} \quad (4.10)$$

The currents flowing in the rotor windings of induction machine are generally not known. But they can be represented by the stator currents, which are normally monitored for the sake of control and purpose of protection. Considering (4.8 – 4.9) together,

$$\begin{aligned}
I_{qr} &= -\frac{L_m}{L_r} \cdot I_{qs} \\
I_{dr} &= \frac{\lambda_{dr} - L_m I_{ds}}{L_r}
\end{aligned} \tag{4.11}$$

Substituting (4.11) in (4.10) yields the slip calculation.

$$\begin{aligned}
\omega_{sl} &= \frac{r_r L_m}{L_r} \cdot \frac{I_{qs}}{\lambda_{dr}} \\
p\lambda_{dr} + \frac{r_r}{L_r} \cdot \lambda_{dr} &= \frac{r_r L_m}{L_r} \cdot I_{ds}
\end{aligned} \tag{4.12}$$

and

$$\begin{aligned}
\omega_{sl} &= \frac{r_r L_m}{L_r} \cdot \frac{I_{qs}}{\lambda_{dr}} \\
p\lambda_{dr} + \frac{r_r}{L_r} \cdot \lambda_{dr} &= \frac{r_r L_m}{L_r} \cdot I_{ds}
\end{aligned} \tag{4.13}$$

Since the stator windings of induction machines are generally star-connected and the neutral is not accessible, two phase currents are necessarily measured in the calculation of the slip and the third current can be substituted by these two currents. For example, when the stator currents for phase A and phase B are measured, these currents are then transformed from ABC stationary reference frame into q-d synchronous reference frame as follows.

$$I_c = -I_a - I_b \tag{4.14}$$

$$\begin{aligned}
I_{qs}^s &= I_a \\
I_{ds}^s &= -\frac{1}{\sqrt{3}} I_a - \frac{2}{\sqrt{3}} I_b
\end{aligned} \tag{4.15}$$

$$\begin{aligned}
I_{qs} &= I_{qs}^s \cos \theta_e - I_{ds}^s \sin \theta_e \\
I_{ds} &= I_{qs}^s \sin \theta_e + I_{ds}^s \cos \theta_e
\end{aligned} \tag{4.16}$$

The rotor flux linkage is then estimated from (4.13), which is essentially a low pass filter. And it is finally used to calculate the slip.

4.5 Input-output Feedback Linearization

It is seen that the dynamic equations of the induction machine are nonlinear, the control of which is difficult to design. However, with some transformations, the nonlinear system can be converted into the corresponding linear system. Feedback linearization is one of the approaches for the nonlinear control design [4.13, 4.14]. The fundamental idea is to apply linear control techniques for the nonlinear system through transforming a nonlinear system dynamics into a fully or partly linear one. It has been used to solve a lot of practical control problems in industry. The simplest form of feedback linearization is to cancel the nonlinearities in a nonlinear system so that the closed-loop dynamics is in a linear form. This idea can be simply applied to a class of nonlinear systems described by the so-called companion form or controllability canonical form. The nonlinear system to be considered has the following form.

$$\dot{x} = f(x) + g(x)u \quad x \in \mathfrak{R}^n, \quad u \in \mathfrak{R}^m \quad (4.17)$$

Some definitions are used in the analysis including the Lie derivative and relative order degree. Let $h : \mathfrak{R}^n \rightarrow \mathfrak{R}$ be a scalar function and $f : \mathfrak{R}^n \rightarrow \mathfrak{R}^n$ be a vector field. The notation ($L_f h : \mathfrak{R}^n \rightarrow \mathfrak{R}$) is used to denote the scalar function,

$$L_f h(x) = \frac{\partial h}{\partial x} f(x) \quad (4.18)$$

which is also called the directional derivative or the Lie derivative of h in the direction of the vector field $f(\cdot)$. Similarly, the higher order derivatives are defined as

$$(L_f^k h)(x) = (L_f^{k-1} h)(x) \quad (4.19)$$

for $k = 1, 2, 3, \dots$. If $\dot{x} = f(x)$, then $L_f h(x)$ is simply $\dot{h}(x)$ as $x(t)$ evolves according to the state dynamics. Similarly, $(L_f^2 h)(x) = \ddot{h}(x(t))$ etc.

Consider $y = h(x)$ as the scalar output of a nonlinear system. It has a relative degree r with respect to the input u at $x = 0$ if $(L_g L_f^{r-1} h)(x) \neq 0$ and $L_g h(x) = (L_g L_f h)(x) = (L_g L_f^2 h)(x) = \dots = (L_g L_f^{r-2} h)(x) = 0$. Essentially, the relative degree r is the number of times the output $y = h(x)$ has to be differentiated before any input appears in its expression. Since $f(x)$ and $h(x)$ are smooth functions, $L_g h(x=0) \neq 0$ implies that $L_g h(x) \neq 0$ in a neighborhood of $x = 0$.

Consider the single input case first and let $y = h(x) \in \mathfrak{R}$ be the output. Suppose that $y = h(x)$ has relative degree of n . Then

$$\begin{aligned} \dot{y} &= L_f h(x) + L_g h(x) \cdot u = L_f h(x) \\ \ddot{y} &= L_f^2 h(x) + L_g L_f h(x) \cdot u = L_f^2 h(x) \\ &\vdots \\ y^{(n-1)} &= L_f^{n-1} h(x) + L_g L_f^{n-2} h(x) \cdot u = L_f^{n-1} h(x) \\ y^{(n)} &= L_f^n h(x) + L_g L_f^{n-1} h(x) \cdot u \end{aligned} \quad (4.20)$$

Define now a nonlinear change of coordinates,

$$\begin{aligned}
\dot{z}_1 &= z_2 \\
\dot{z}_2 &= z_3 \\
&\vdots \\
\dot{z}_{n-1} &= z_n \\
\dot{z}_n &= L_f^n h(x) + L_g L_f^{n-1} \cdot u = a(x) + b(x)u
\end{aligned} \tag{4.21}$$

When represented in matrix form, it is

$$\begin{pmatrix} \dot{z}_1 \\ \dot{z}_2 \\ \vdots \\ \dot{z}_n \end{pmatrix} = \begin{pmatrix} h(x) \\ L_f h(x) \\ \vdots \\ L_f^{n-1} h(x) \end{pmatrix} =: \phi(x) \tag{4.22}$$

where $\phi(x): \mathfrak{R}^n \rightarrow \mathfrak{R}^n$ is smooth locally invertible function (diffeomorphism) in a neighborhood of $x = 0$. This is known as the controller canonical form and is the exact same form as the linear system. If the feedback of the form is defined as

$$u = \frac{1}{b(x)} [-a(x) + v] \tag{4.23}$$

where v is an exogenous control signal, then, the resulting system becomes

$$\frac{d^n z_1}{dt^n} = \dot{z}_n = v \tag{4.24}$$

which is simply a chain of integrators. $v(t)$ can be designed according to certain requirements. It can be designed for set point regulation and trajectory tracking.

A controller that ensure that $y = h(x)$ is regulated at a desired constant value can be easily designed. To ensure that $y = h(x) = y^*$, $v(t)$ can be designed as

$$v(t) = -a_0(z_1 - y^*) - a_1 z_2 - \dots - a_{n-1} z_n \tag{4.25}$$

so that $s^n + a_{n-1}s^{n-1} + a_{n-2}s^{n-2} + \dots + a_0$ has all the roots on the left half plane. For example, for $n = 3$, if the closed loop poles are desired to be at $-p < 0$, then the following polynomial can be chosen.

$$s^3 + a_2s^2 + a_1s + a_0 = (s + p)^3 = s^3 + 3ps^2 + 3p^2s + p^3 \quad (4.26)$$

so that $a_2 = 3p$, $a_1 = 3p^2$, $a_0 = p^3$.

Similarly, the tracking controller that allows $y(t)$ to track a smooth desired trajectory $y^*(t)$ can be designed by writing the error dynamics, $e(t) = y(t) - y^*(t)$. It can be seen easily that

$$\frac{d^n e}{dt^n} = \frac{d^n y}{dt^n} - y^{*(n)}(t) = \dot{z}_n - y^{*(n)}(t) = v - y^{*(n)}(t) \quad (4.27)$$

where $y^{*(n)}(t)$ is the n -th time derivative of $y^*(t)$. Therefore, a tracking controller can be designed to be

$$v(t) = y^{*(n)}(t) - a_0(z_1 - y^*) - a_1(z_2 - \dot{y}^*) - \dots - a_{n-1}(z_n - y^{*(n-1)}) \quad (4.28)$$

where $s^n + a_{n-1}s^{n-1} + a_{n-2}s^{n-2} + \dots + a_0$ has all the roots on the left half plane.

The above algorithm requires that the output function $y = h(x)$ with a relative degree of $r = n$. If $r < n$, then the procedure can be only proceeded up to r steps, i.e.

$$\begin{aligned} \dot{y} &= L_f h(x) + L_g h(x) \cdot u = L_f h(x) =: z_1 \\ \ddot{y} &= L_f^2 h(x) + L_g L_f h(x) \cdot u = L_f^2 h(x) =: z_2 \\ &\vdots \\ y^{(r-1)} &= L_f^{r-1} h(x) + L_g L_f^{r-2} h(x) \cdot u = L_f^{r-1} h(x) =: z_r \\ y^{(r)} &= L_f^r h(x) + L_g L_f^{r-1} h(x) \cdot u = a(x) + b(x)u \end{aligned} \quad (4.29)$$

As far as the input-output relationship is concerned, the linear system $y^{(r)} = v(t)$ is obtained, from which additional feedback control can be implemented.

$$u = \frac{1}{b(x)} [-a(x) + v(t)] \quad (4.30)$$

A tracking controller can be designed as

$$v(t) = y^{*(r)}(t) - a_0(z_1 - y^*) - a_1(z_2 - \dot{y}^*) - \dots - a_{r-1}(z_r - y^{*(r-1)}) \quad (4.31)$$

with $s^r + a_{r-1}s^{r-1} + a_{r-2}s^{r-2} + \dots + a_0$ being a polynomial with stable roots to achieve tracking. The issue of internal stability becomes important. Specially, $x(t)$ cannot be guaranteed to be bounded.

The described feedback linearization technique for the nonlinear system can be applied to the induction machine control. Selecting the stator currents and rotor flux linkages as the states, the dynamic equations of the induction motor are

$$L_\sigma pI_{qs} = V_{qs} - rI_{qs} - \omega_e L_\sigma I_{ds} + \frac{r_r L_m}{L_r^2} \lambda_{qr} - \omega_r \frac{L_m}{L_r} \lambda_{dr} \quad (4.32)$$

$$L_\sigma pI_{ds} = V_{ds} - rI_{ds} + \omega_e L_\sigma I_{qs} + \frac{r_r L_m}{L_r^2} \lambda_{dr} + \omega_r \frac{L_m}{L_r} \lambda_{qr} \quad (4.33)$$

$$p\lambda_{qr} = -\frac{r_r}{L_r} \lambda_{qr} + \frac{r_r L_m}{L_r} I_{qs} - (\omega_e - \omega_r) \lambda_{dr} \quad (4.34)$$

$$p\lambda_{dr} = -\frac{r_r}{L_r} \lambda_{dr} + \frac{r_r L_m}{L_r} I_{ds} + (\omega_e - \omega_r) \lambda_{qr} \quad (4.35)$$

$$T_e = \frac{3PL_m}{4L_r} \cdot (\lambda_{dr} I_{qs} - \lambda_{qr} I_{ds}) \quad (4.36)$$

where $L_\sigma = L_s - \frac{L_m^2}{L_r}$ is the stator leakage inductance, $r = r_s + \frac{r_r L_m^2}{L_r}$.

Under field oriented assumption, the rotor flux must be aligned with the d -axis ($\lambda_{qr} = 0$) and the dynamic equations are simplified as

$$L_{\sigma} p I_{qs} = V_{qs} - r I_{qs} - \omega_e L_{\sigma} I_{ds} - \omega_r \frac{L_m}{L_r} \lambda_{dr} \quad (4.37)$$

$$L_{\sigma} p I_{ds} = V_{ds} - r I_{ds} + \omega_e L_{\sigma} I_{qs} + \frac{r L_m}{L_r^2} \lambda_{dr} \quad (4.38)$$

$$p \lambda_{dr} = -\frac{r_r}{L_r} \lambda_{dr} + \frac{r_r L_m}{L_r} I_{ds} \quad (4.39)$$

$$(\omega_e - \omega_r) = \frac{r_r L_m}{L_r} \cdot \frac{I_{qs}}{\lambda_{dr}} \quad (4.40)$$

$$T_e = \frac{3 P L_m}{4 L_r} \cdot \lambda_{dr} I_{qs} \quad (4.41)$$

The objective of the control design is to make torque and rotor flux tracks the desired trajectories. Consider the following choice of the control input

$$\sigma_{dr} = -\frac{r_r}{L_r} \lambda_{dr} + \frac{r_r L_m}{L_r} I_{ds} \quad (4.42)$$

where σ_{dr} is a new input to be determined. With this choice, a simple linear integrator relationship between λ_{dr} and the new input σ_{dr} results.

$$\dot{\lambda}_{dr} = \sigma_{dr} \quad (4.43)$$

The design of a tracking controller for this integrator relationship is simple. The tracking error can be defined by $e_1 = \lambda_{dr} - \lambda_{dr}^*$ and σ_{dr} is chosen as

$$\sigma_{dr} = \dot{\lambda}_{dr}^* - k_1 e_1 \quad (4.44)$$

with k_1 being a positive constant, the tracking error of the closed loop system is given by

$$\dot{e}_1 + k_1 e_1 = 0 \quad (4.45)$$

which represents the exponentially stable error dynamics.

To generate a direct relationship between the output T_e and the input, differentiate the torque equation

$$\dot{T}_e = \frac{3PL_m}{4L_r} \cdot (\dot{\lambda}_{dr} I_{qs} + \lambda_{dr} \dot{I}_{qs}) \quad (4.46)$$

Now choose \dot{I}_{qs} to satisfy

$$\dot{I}_{qs} = \frac{1}{\lambda_{dr}} (-\sigma_{dr} I_{qs} + \sigma_T) \quad (4.47)$$

where $\dot{\lambda}_{dr}$ has been replaced by σ_{dr} and σ_T is designed to place the poles of the equivalent linear dynamics. The nonlinearity is cancelled and the equivalent dynamics is expressed as

$$\dot{T}_e = \frac{3PL_m}{4L_r} \cdot \sigma_T \quad (4.48)$$

A possible design for σ_T is $\sigma_T = \dot{T}_e^* - k_2 e_2$ and e_2 is defined as $e_2 = T_e - T_e^*$. This leads to a convergent tracking error, e_2 with positive k_2

$$\dot{e}_2 + k_2 e_2 = 0 \quad (4.49)$$

Similar controller design can be applied to the stator currents. The control design strategy shown in the above example is referred to as the input-output linearization approach through generating a linear input-output relation and then formulating a controller based on the linear control. In the above example, the closed-loop dynamics has been represented by the error dynamics since the order of the error dynamic equation is the same as the order of the whole system. However, this is not the general case. Frequently, part of the system dynamics described by the state components is rendered "unobservable" in the input-output linearization. This part of dynamics is called the

internal dynamics because it cannot be seen from the external input-output relationship. The tracking control design is completely solved only if this internal dynamics is stable, which means that all the states remain bounded during tracking.

For the linear system, the internal dynamics is simply determined by the locations of the zeros. The internal dynamics is stable if all zeros are in the left-half plane, which means that the system is "minimum-phase". However, this cannot be directly used for the nonlinear system. The so-called zero-dynamics is then defined in order to determine the stability of the internal dynamics. It is defined to be the internal dynamics of the nonlinear system when the system output is kept at zero by the input. The study of the internal dynamics stability can be simplified locally by studying that of the zero-dynamics instead. Different control strategies have to be applied if the zero dynamics is unstable. The control design based on the input-output linearization can be summarized in three steps:

- Differentiate the output y until the input u appears;
- Choose u to cancel the nonlinearities and guarantee tracking convergence;
- Study the stability of the internal dynamics.

4.6 Formulation of Indirect Vector Control Scheme of Induction Machine

Based on the above analysis, the indirect vector control scheme can be formulated from the voltage equations and the motion equation of the induction machine. These equations are

$$V_{qs} = r_s I_{qs} + p \lambda_{qs} + \omega_e \lambda_{ds} \quad (4.50)$$

$$V_{ds} = r_s I_{ds} + p\lambda_{ds} - \omega_e \lambda_{qs} \quad (4.51)$$

$$0 = r_r I_{qr} + p\lambda_{qr} + (\omega_e - \omega_r)\lambda_{dr} \quad (4.52)$$

$$0 = r_r I_{dr} + p\lambda_{dr} - (\omega_e - \omega_r)\lambda_{qr} \quad (4.53)$$

$$T_e = \frac{3P}{4} \cdot \frac{L_m}{L_r} \cdot (\lambda_{dr} I_{qs} - \lambda_{qr} I_{ds}) \quad (4.54)$$

$$p\omega_r = \frac{P}{2J} (T_e - T_L) \quad (4.55)$$

As discussed in the above section, the rotor currents are not known and they can be substituted using the stator currents and rotor flux linkages since

$$\begin{aligned} \lambda_{dr} &= L_r I_{dr} + L_m I_{ds} \\ \lambda_{qr} &= L_r I_{qr} + L_m I_{qs} \end{aligned} \quad (4.56)$$

Depending on the state variables that are used for the control, variables in the voltage equations can be further reduced. Here the stator currents and rotor flux linkages are chosen as the state variables in the indirect vector control of induction machine. The stator flux linkages are replaced by the rotor flux linkages and stator currents using

$$\begin{aligned} \lambda_{ds} &= L_s I_{ds} + L_m I_{dr} \\ \lambda_{qs} &= L_s I_{qs} + L_m I_{qr} \end{aligned} \quad (4.57)$$

Then the stator and rotor voltage equations are rewritten as

$$V_{qs} = L_\sigma p I_{qs} + r I_{qs} + \omega_e L_\sigma I_{ds} - \frac{r_r L_m}{L_r^2} \lambda_{qr} + \omega_r \frac{L_m}{L_r} \lambda_{dr} \quad (4.58)$$

$$V_{ds} = L_\sigma p I_{ds} + r I_{ds} - \omega_e L_\sigma I_{qs} - \frac{r_r L_m}{L_r^2} \lambda_{dr} - \omega_r \frac{L_m}{L_r} \lambda_{qr} \quad (4.59)$$

$$0 = p\lambda_{qr} + \frac{r_r}{L_r} \lambda_{qr} - \frac{r_r L_m}{L_r} I_{qs} + (\omega_e - \omega_r)\lambda_{dr} \quad (4.60)$$

$$0 = p\lambda_{dr} + \frac{r_r}{L_r}\lambda_{dr} - \frac{r_r L_m}{L_r} I_{ds} - (\omega_e - \omega_r)\lambda_{qr} \quad (4.61)$$

The number of equations is reduced to four when $\lambda_{qr} = 0$ for the rotor flux oriented control. All terms including λ_{qr} are zero and the simplified equations are

$$L_\sigma pI_{qs} + rI_{qs} = V_{qs} - \omega_e L_\sigma I_{ds} - \omega_r \frac{L_m}{L_r} \lambda_{dr} \quad (4.62)$$

$$L_\sigma pI_{ds} + rI_{ds} = V_{ds} + \omega_e L_\sigma I_{qs} + \frac{r_r L_m}{L_r^2} \lambda_{dr} \quad (4.63)$$

$$p\lambda_{dr} + \frac{r_r}{L_r}\lambda_{dr} = \frac{r_r L_m}{L_r} I_{ds} \quad (4.64)$$

$$p\omega_r = \frac{P}{2J} \cdot (K_e \lambda_{dr} I_{qs} - T_L) \quad (4.65)$$

The control scheme is then designed based on the system of differential equations derived above. Define

$$\sigma_{qs} = L_\sigma pI_{qs} + rI_{qs} = K_{qs} (I_{qs}^* - I_{qs}) \quad (4.66)$$

$$\sigma_{ds} = L_\sigma pI_{ds} + rI_{ds} = K_{ds} (I_{ds}^* - I_{ds}) \quad (4.67)$$

where K_{ds}, K_{qs} can be any kind of controller (PI controller, etc). σ_{ds} and σ_{qs} are the outputs of the controllers. I_{qs}^* and I_{ds}^* are the desired q- and d-axis stator currents. Then desired q- and d-axis stator voltages V_{qs}^* and V_{ds}^* are calculated based on the input-output linearization by

$$V_{qs}^* = \sigma_{qs} + \omega_e L_\sigma I_{ds} + \omega_r \frac{L_m}{L_r} \lambda_{dr} \quad (4.68)$$

$$V_{ds}^* = \sigma_{ds} - \omega_e L_\sigma I_{qs} - \frac{r_r L_m}{L_r^2} \lambda_{dr} \quad (4.69)$$

In the process of linearization, the dynamics from the other state λ_{dr} is coming into play. It makes the cascaded control design more complicated. However, the time constant of the rotor flux linkage is much bigger than that of the stator currents. It is seen from (4.64) that the time constant for the d-axis rotor flux linkage is $L_r / r_r = 0.2077 / 1.85 = 0.11227 \text{ s}$. The time constant for the stator currents is $L_\sigma / r = 0.0178 / 3.6272 = 0.0048 \text{ s}$. Apparently the response of the stator currents is much faster than that of the rotor flux linkage. Thus in the analysis of the dynamics in the stator currents, the rotor flux linkage can be seen as constant. Then the feedback linearization control technique can be applied.

Similarly, define $I_{qs}^* = K_w \cdot (\omega_r^* - \omega_r)$ and $I_{ds}^* = K_{dr} \cdot (\lambda_{dr}^* - \lambda_{dr})$, then

$$p^2 \omega_r = K \cdot p \cdot [K_w \cdot (\omega_r^* - \omega_r)] \quad (4.70)$$

$$T_r p \lambda_{dr} + \lambda_{dr} = L_m \cdot K_{dr} (\lambda_{dr}^* - \lambda_{dr}) \quad (4.71)$$

where $K = \frac{PK_e}{2J} \lambda_{dr}$. K_{dr}, K_w can be any kind of controller (PI controller, etc). λ_{dr}^* and ω_r^* are the rotor flux command and speed command, respectively.

In the formulation of the control scheme, to regulate the rotor flux linkage and the rotor speed to desired values are the two objectives. Apparently the stator voltages that are needed to generate the desired rotor flux linkage and rotor speed are not directly related to these variables. So the alternative way is to regulate the rotor flux linkage and rotor speed through some controllers and the outputs of these two controllers give out the reference values for the q- and d-axis stator currents in synchronous reference frame. Then the actual q- and d-axis stator currents are regulated to these two reference currents to get the stator voltages. The proposed control scheme is shown in Figure 4.3.

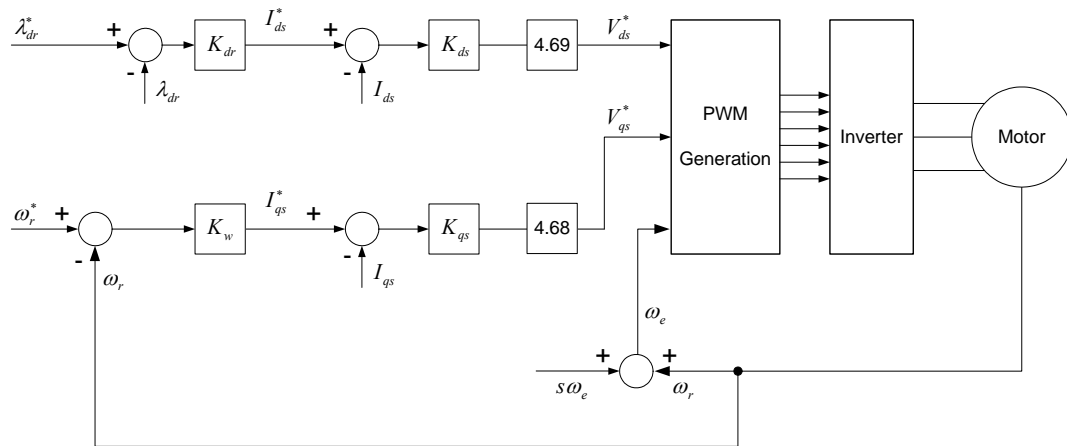


Figure 4.3 Proposed indirect vector control scheme for the induction motor.

Four controllers are used in the proposed control scheme. The parameters of these controllers need to be determined appropriately according to the specific type. PI type controllers are quite popular for the control and hence used in the above scheme.

4.7 Control Design for Indirect Vector Control Scheme of Induction Machine

Based on the above analysis, the indirect vector control scheme can be formulated from the voltage equations and the motion equation of the induction machine. The control objective is to regulate the actual quantities to the command values. In the case of indirect vector control of induction machine, both the d-axis rotor flux linkage and rotor speed need to be regulated to the desired values, which can be changing for the d-axis rotor flux linkage to achieve minimum electric loss (stator and rotor copper loss and stator core loss) operation and for the rotor speed in order to achieve variable speed operation. Apparently the equations used for the formulation of control scheme are not linear between the inputs and outputs. So one of the nonlinear control methods, the so-called

input-output linearization technique is applied such that the relationship between the input variables and output variables is linear after some feedback compensation and then the linear controller such as PI, PD, IP or PID can be used. For examples, the stator voltage equations are repeated below

$$V_{qs} = L_{\sigma} pI_{qs} + rI_{qs} + \omega_e L_{\sigma} I_{ds} + \omega_r \frac{L_m}{L_r} \lambda_{dr} \quad (4.72)$$

$$V_{ds} = L_{\sigma} pI_{ds} + rI_{ds} - \omega_e L_{\sigma} I_{qs} - \frac{r_r L_m}{L_r^2} \lambda_{dr} \quad (4.73)$$

There is the term including I_{ds} in the q-axis equation and there is the term including I_{qs} in the d-axis equation. So these two equations are coupled and the traditional linear controllers cannot be used. Also there are some other terms included such that the required voltages cannot be achieved from the current control directly. However, through the exact linearization method, these equations can be linearized by putting the terms other than the currents control to one side.

$$L_{\sigma} pI_{qs} + rI_{qs} = V_{qs} - \omega_e L_{\sigma} I_{ds} - \omega_r \frac{L_m}{L_r} \lambda_{dr} \quad (4.74)$$

$$L_{\sigma} pI_{ds} + rI_{ds} = V_{ds} + \omega_e L_{\sigma} I_{qs} + \frac{r_r L_m}{L_r^2} \lambda_{dr} \quad (4.75)$$

And then the linear controllers are used to regulate the currents as shown in Figure 4.4, in which

$$\sigma_{qs} = L_{\sigma} pI_{qs} + rI_{qs} \quad (4.76)$$

$$\sigma_{ds} = L_{\sigma} pI_{ds} + rI_{ds} \quad (4.77)$$

The idea behind is to use the linear controllers that include integrations to calculate the derivative terms. And the nonlinear equations become linear when all the nonlinear

terms are moved to the other side of the equations. Then the q- and d-axis voltages are calculated as shown in Figure 4.4.

$$V_{qs}^* = \sigma_{qs} + \omega_e L_\sigma I_{ds} + \omega_r \frac{L_m}{L_r} \lambda_{dr} \quad (4.78)$$

$$V_{ds}^* = \sigma_{ds} - \omega_e L_\sigma I_{qs} - \frac{r_r L_m}{L_r^2} \lambda_{dr} \quad (4.79)$$

The transfer functions between the reference and actual currents can be derived as

$$\frac{I_{qs}}{I_{qs}^*} = \frac{K_{qs}}{L_\sigma \cdot p + r + K_{qs}} \quad (4.80)$$

$$\frac{I_{ds}}{I_{ds}^*} = \frac{K_{ds}}{L_\sigma \cdot p + r + K_{ds}} \quad (4.81)$$

Since the general PI controllers are widely used and proved to be effective, they are also applied in the following analysis. The transfer functions for the two controllers in the above diagrams are

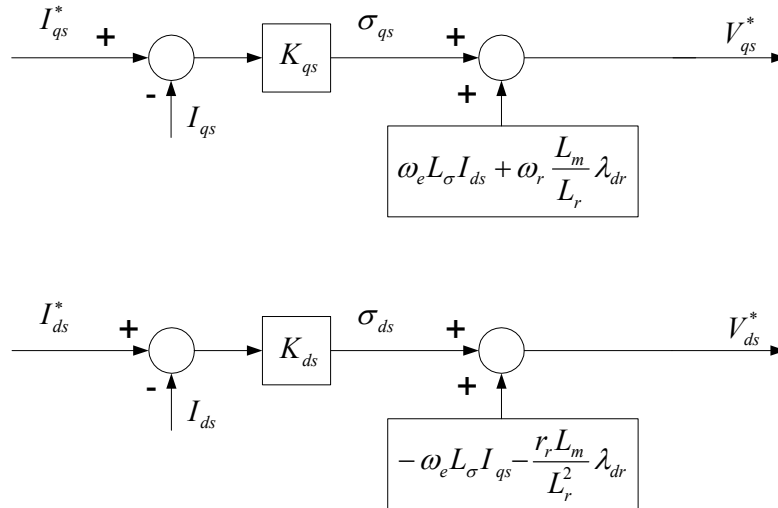


Figure 4.4 Linearization diagram for current control.

$$K_{qs} = K_{qsP} + \frac{K_{qsl}}{p}$$

$$K_{ds} = K_{dsP} + \frac{K_{dsl}}{p}$$

Then the transfer functions between the reference and actual currents are changed to the following.

$$\frac{I_{qs}}{I_{qs}^*} = \frac{K_{qsP} \cdot p + K_{qsl}}{L_{\sigma} \cdot p^2 + (r + K_{qsP}) \cdot p + K_{qsl}} \quad (4.82)$$

$$\frac{I_{ds}}{I_{ds}^*} = \frac{K_{dsP} \cdot p + K_{dsl}}{L_{\sigma} \cdot p^2 + (r + K_{dsP}) \cdot p + K_{dsl}} \quad (4.83)$$

Choosing the appropriate control parameters is very critical to gain good performance although the whole system might be able to work for a wide range of parameters. Many researchers select the gains based on the experience or just by trying. This is not good especially when they are designed for a new system. The most important objective is to maintain the system stable by selecting appropriate parameters. And then those parameters can be tuned up corresponding to the specified performance requirement. It is noted that there are some methods that can be used to determine the parameters in the stable region.

One of the approaches is using Butterworth polynomial to optimize the closed-loop eigenvalue locations. The Butterworth method locates the eigenvalues uniformly in the left-half S-plane on a circle with radius ω_0 , with its center at the origin as shown in Figure 4.5. The Butterworth polynomials for a transfer function with a second order denominator is given as

$$p^2 + \sqrt{2}p\omega_0 + \omega_0^2 = 0 \quad (4.84)$$

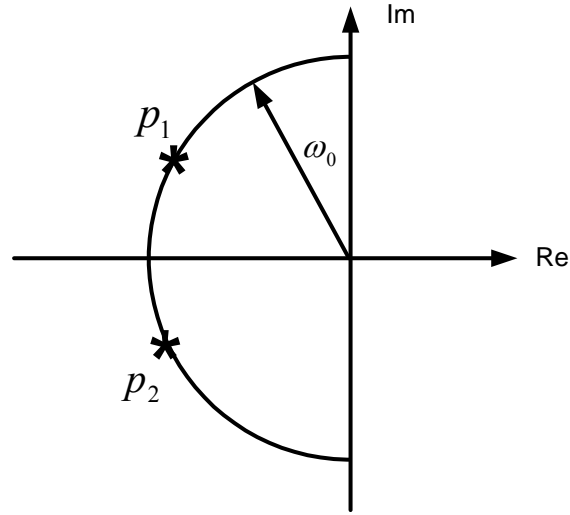


Figure 4.5 Poles location for 2nd Butterworth polynomial.

The PI parameters are determined through comparing the coefficients in (4.84) with the denominators of the corresponding transfer functions and choosing appropriate ω_0 .

$$\sqrt{2}\omega_0 = \frac{r + K_{qsP}}{L_\sigma} \quad (4.85)$$

$$\omega_0^2 = \frac{K_{qsI}}{L_\sigma}$$

$$\sqrt{2}\omega_0 = \frac{r + K_{dsP}}{L_\sigma} \quad (4.86)$$

$$\omega_0^2 = \frac{K_{dsI}}{L_\sigma}$$

The idea behind is to use the linear controllers that include integrations to calculate the derivative terms. And the nonlinear equations become linear when all the nonlinear terms are moved to the other side of the equations. Then the q- and d-axis voltages are calculated as shown in Figure 4.4.

Similarly the q- and d-axis stator current references in the synchronous reference frame are calculated from the controller outputs from the rotor flux linkage and rotor speed. From the rotor voltage equation corresponding to the flux orientation ($\lambda_{qr} = 0$) and the motion equation,

$$p\lambda_{dr} + \frac{r_r}{L_r}\lambda_{dr} = \frac{r_r L_m}{L_r} I_{ds} \quad (4.87)$$

$$p\omega_r = \frac{P}{2J} \cdot (K_e \lambda_{dr} I_{qs} - T_L) \quad (4.88)$$

Define $I_{ds}^* = K_{dr} \cdot (\lambda_{dr}^* - \lambda_{dr})$ and $I_{qs}^* = K_w \cdot (\omega_r^* - \omega_r)$, then

$$\frac{L_r}{r_r} p\lambda_{dr} + \lambda_{dr} = L_m \cdot K_{dr} (\lambda_{dr}^* - \lambda_{dr}) \quad (4.89)$$

$$p^2 \omega_r = K \cdot p \cdot [K_w \cdot (\omega_r^* - \omega_r)] \quad (4.90)$$

where $K = \frac{PK_e}{2J} \lambda_{dr} \cdot K_{dr}$, K_w can be any kind of linear controllers (PI controller, etc).

λ_{dr}^* and ω_r^* are the rotor flux command and speed command, respectively.

The transfer function between the reference and actual rotor flux linkages and the one between the reference and actual rotor speeds can be derived as

$$\frac{\lambda_{dr}}{\lambda_{dr}^*} = \frac{L_m K_{dr}}{\frac{L_r}{r_r} \cdot p + 1 + L_m K_{dr}} \quad (4.91)$$

$$\frac{\omega_r}{\omega_r^*} = \frac{KK_w}{p + KK_w} \quad (4.92)$$

When PI controllers are used for the regulation of rotor flux and rotor speed,

$$K_{dr} = K_{drP} + \frac{K_{drI}}{s}$$

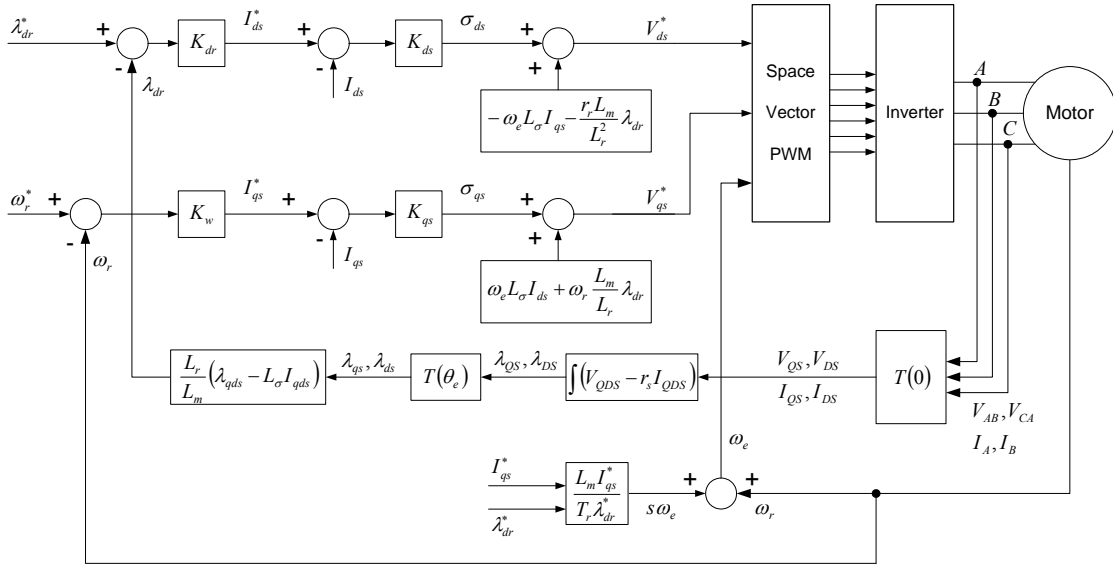


Figure 4.6 Indirect vector control diagram for induction machines.

$$K_w = K_{wP} + \frac{K_{wI}}{s}$$

Then these two transfer functions are changed to

$$\frac{\lambda_{dr}}{\lambda_{dr}^*} = \frac{L_m K_{drP} \cdot p + L_m K_{drI}}{\frac{L_r}{r_r} \cdot p^2 + (1 + L_m K_{drP}) \cdot p + L_m K_{drI}} \quad (4.93)$$

$$\frac{\omega_r}{\omega_r^*} = \frac{KK_{wP} \cdot p + KK_{wI}}{p^2 + KK_{wP} \cdot p + KK_{wI}} \quad (4.94)$$

4.8 Simulation Results

The proposed control scheme is simulated using Simulink. The flux command λ_{dr} is assumed to be constant, which might be changeable during efficiency optimization. The speed command is ramped up to make sure that the actual speed can follow the

command very well such that the outputs from the controllers are within the limits most of the time. Some limits have been set up to the output of the controllers especially the commands for I_{ds} and I_{qs} are limited within two times the rated current. The starting current is greatly decreased by this mean. The rotor flux command is used in the slip calculation instead of the actual rotor flux such that the slip does not change significantly during the transience. It can be seen from Figure 4.7 that the starting process is very smooth and the overshoot is very small.

When the motor reaches steady state, a constant load (2 Nm) is applied to the motor at 2 second and then released at 3 second. The transient process is shown in Figure 4.8. The actual speed follows the speed command very well although there are small disturbances at the time when the load is applied and released. The stator current increases to some extent due to the applied load. Once the load is disconnected, all variables go back to the states before the application of the load. The simulation results show that the controllers are designed properly to give the desired responses.

Figure 4.9 shows the motor speed and electric torque when the reference speed changes after the motor reaches steady state. The speed change between rated speed and half of the rated speed is shown in Figure 4.9(a) and the change between positive and negative half of the rated speed is shown in Figure 4.9(b). It is seen that the actual speed tracks the reference speed very well and the control scheme is robust to the speed changes.

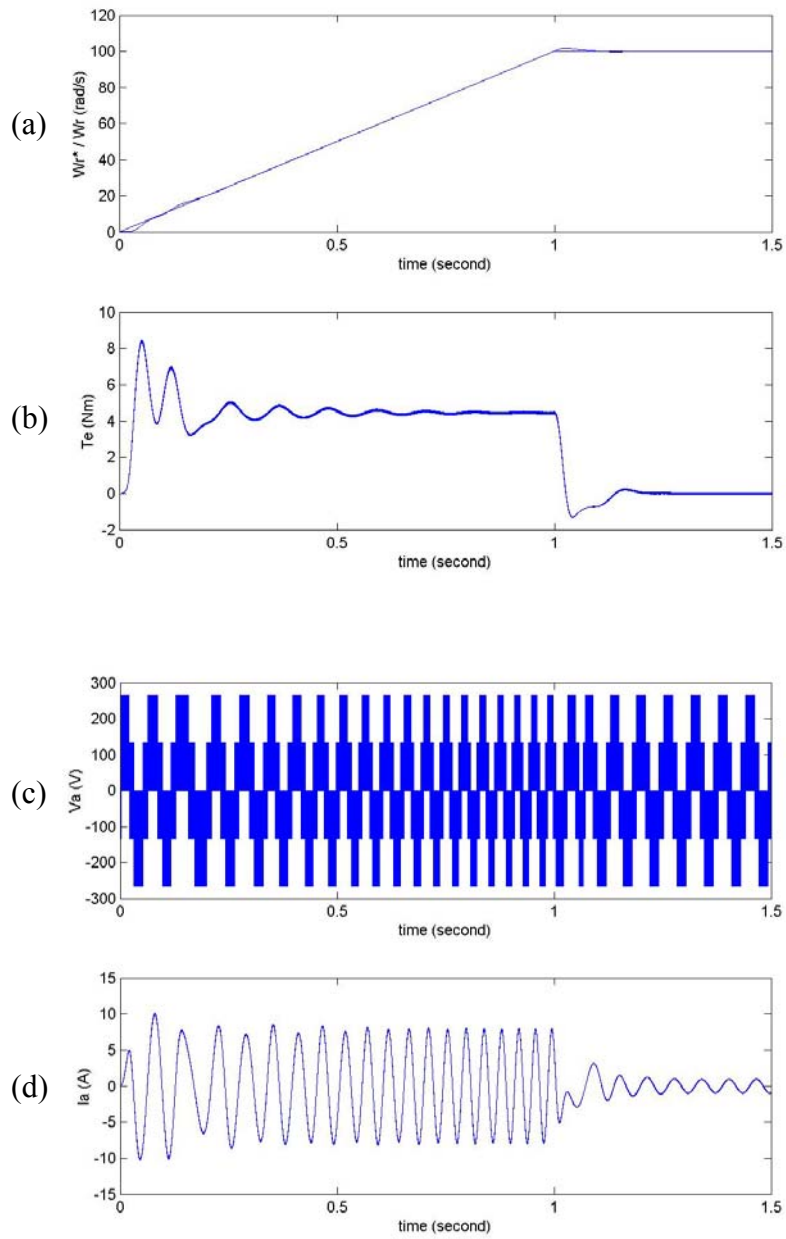


Figure 4.7 Starting transients at no-load. (a) Speed command and actual speed; (b) electrical torque; (c) phase A voltage; (d) phase A current.

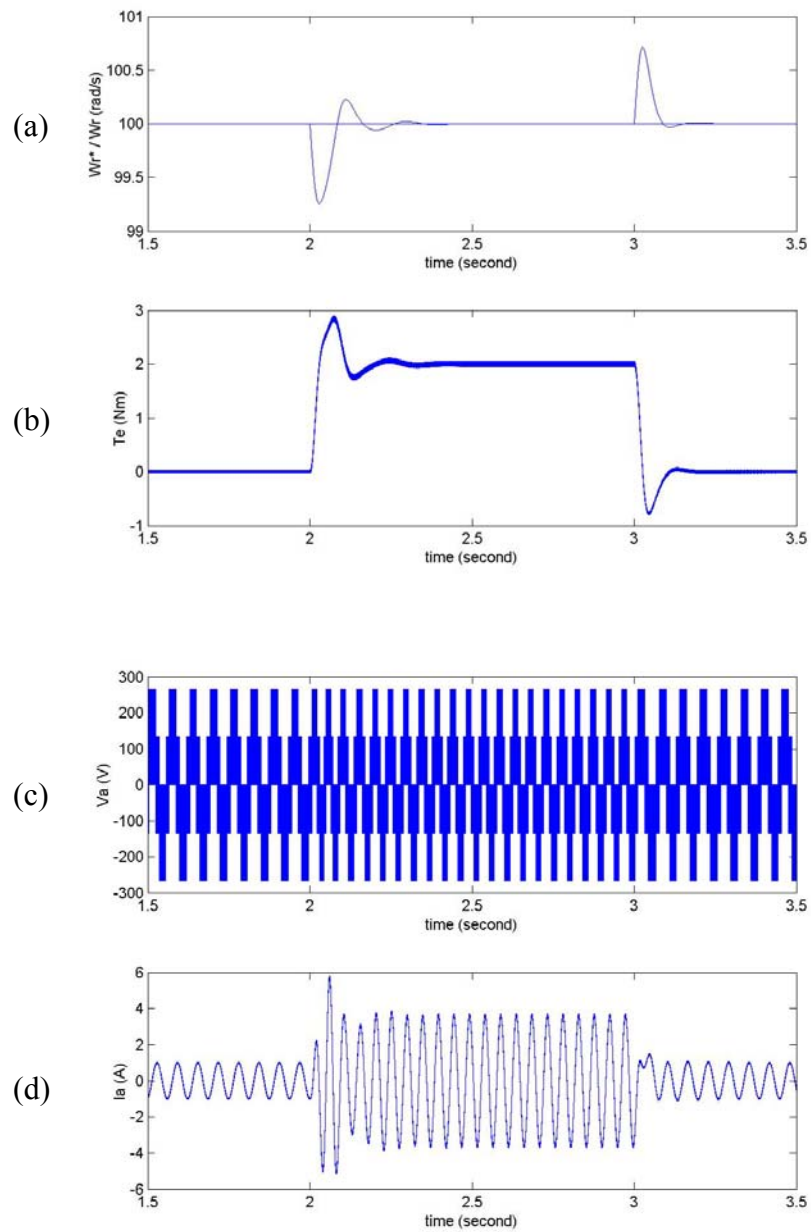


Figure 4.8 Response to the load change at steady state. (a) Speed command and actual speed; (b) electrical torque; (c) phase A voltage; (d) phase A current.

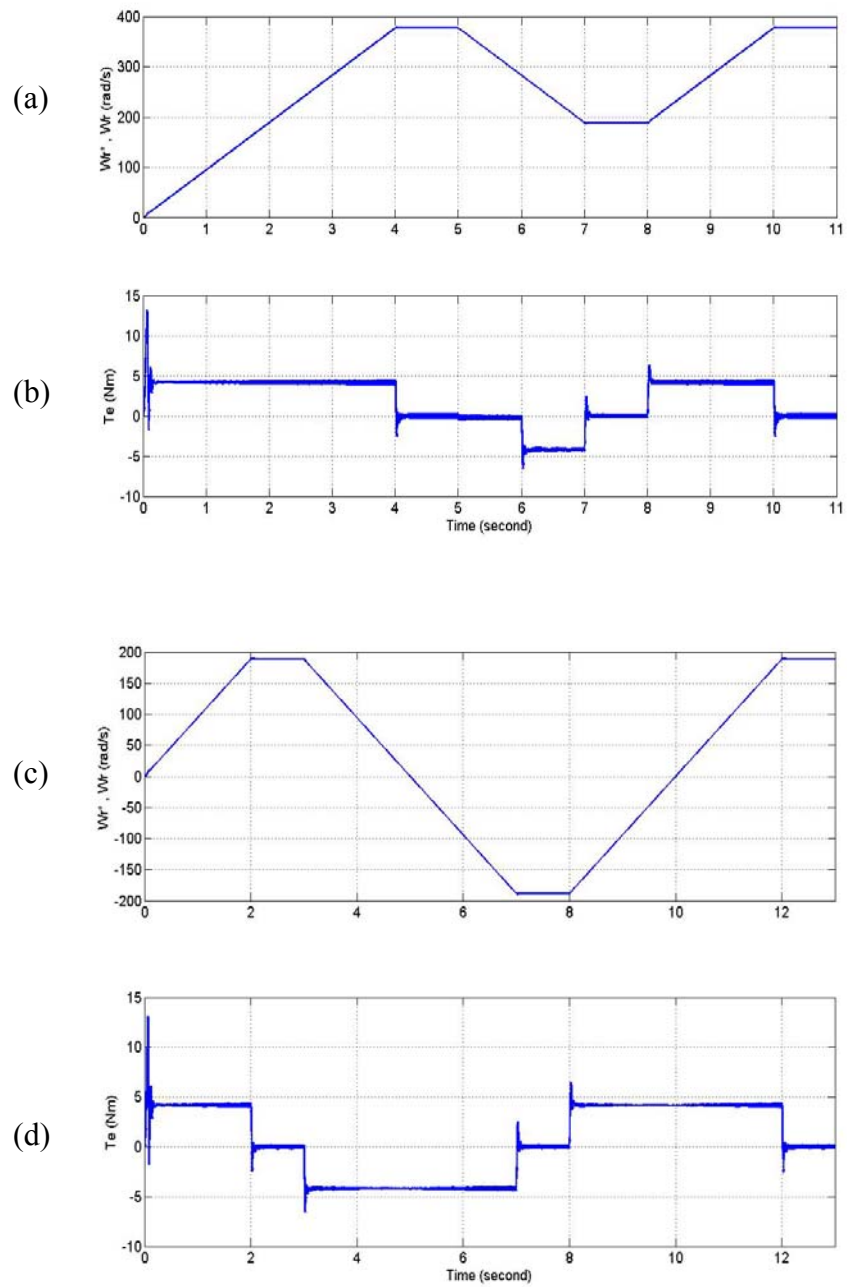


Figure 4.9 Response to the speed change after steady state. (a) Speed command and actual speed; (b) electrical torque; (c) speed command and actual speed; (d) electrical torque.

4.9 DSP Implementation and Experimental Results

The proposed control scheme has been implemented by the software written in assembly language through TI DSP TMS320LF2407. The space vector (SV) PWM is used because the SV PWM technique utilizes DC bus voltage more efficiently and generates less harmonic distortion in a three-phase voltage source inverter (VSI). There are several important issues regarding the implementation and the first one is the calculation of the rotor flux linkages.

4.9.1 Calculation of Rotor Flux Linkages

The calculation of rotor flux linkages is a big problem in the actual implementation since it is difficult to estimate. Generally, the measured quantities are the stator voltages and currents, which can be easily measured using voltage and current sensors. Although there are some observers or other methods that can be used to estimate the rotor flux, the direct approach is to integrate the back-EMF in the stationary q-d reference frame. Since the signals to be integrated are AC signals, the drift and saturation problems cannot be avoided if the pure integration is applied. This is natural because of the following reasons:

- (a) It is not realistic to start the integration when the integrated signal is exactly at zero. This is called the initial condition problem and it results in a DC component after integration.

- (b) The signal itself is not pure AC signal and it has DC component. The average value of the integrated signal is not zero due to the distortion of the signal itself and the resolution of the sensors. The existing DC offset will drift the integration result to saturation.
- (c) The frequency of the integrated signal is not high enough especially during the starting. This will make integration result to saturation even if the magnitude of the signal to be integrated is very small.

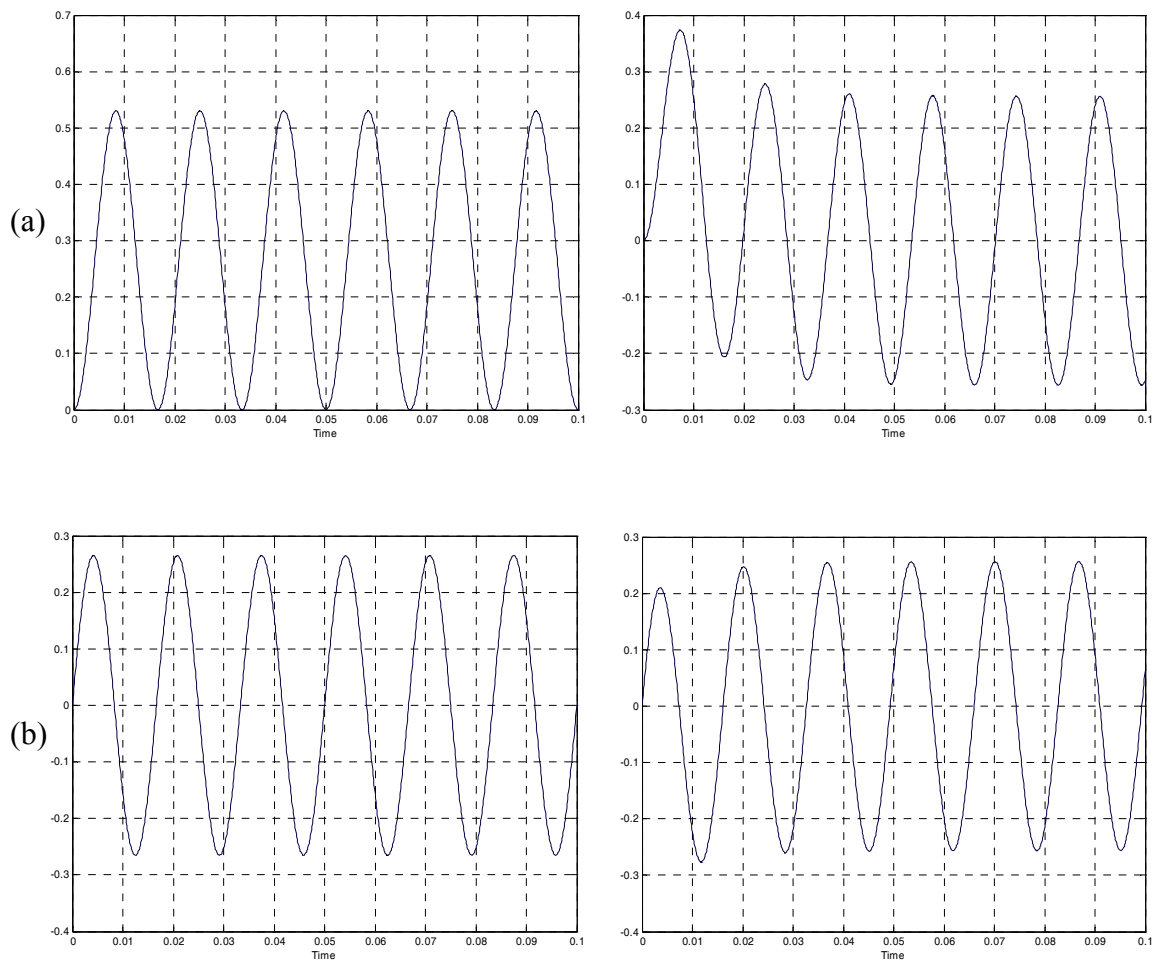
The stator fluxes are generally estimated from the stator voltage equations in the stationary reference frame by integrating back-EMF as

$$\begin{aligned}\lambda_{ds} &= \int (V_{ds} - r_s I_{ds}) dt \\ \lambda_{qs} &= \int (V_{qs} - r_s I_{qs}) dt\end{aligned}\tag{4.95}$$

where q_s and d_s represent the stator q-d components in the stationary reference frame. The integration of (4.58) by pure integrator involves the drift and saturation problems. To solve the problems, the pure integrator is replaced by a Low Pass Filter (LPF). The transfer function of a LPF is $\frac{1}{s+a}$ compared with that of a pure integrator $\frac{1}{s}$.

The described problem can be easily verified through simulation. In the simulation, the signal to be integrated is assume to take the form $100 \cdot \sin(377t + \alpha_0) + A_0$, where α_0 is the initial angle of the signal to be integrated and A_0 is the DC offset. For the comparison, the parameter a used in the LPF is selected as 100. The output waveforms after the integration using a pure integrator and a LPF are shown in Figure 4.10 under different conditions. The first simulation shows the effects of different initial angles (0 , $\pi/2$ and π) when the DC offset is assumed to be zero. It is seen that the integration

using a pure integrator is correct only when the initial angle is 90 degrees. However, this angle is not equal to 90 degrees in general. The second simulation shows the effect of DC offset. Although the selected DC offset is very small compared with the AC component, it still shifts the output continuously. But the outputs at the steady state are always correct when the LPF is used. The only problem it has is that the outputs during the first few cycles are not correct.

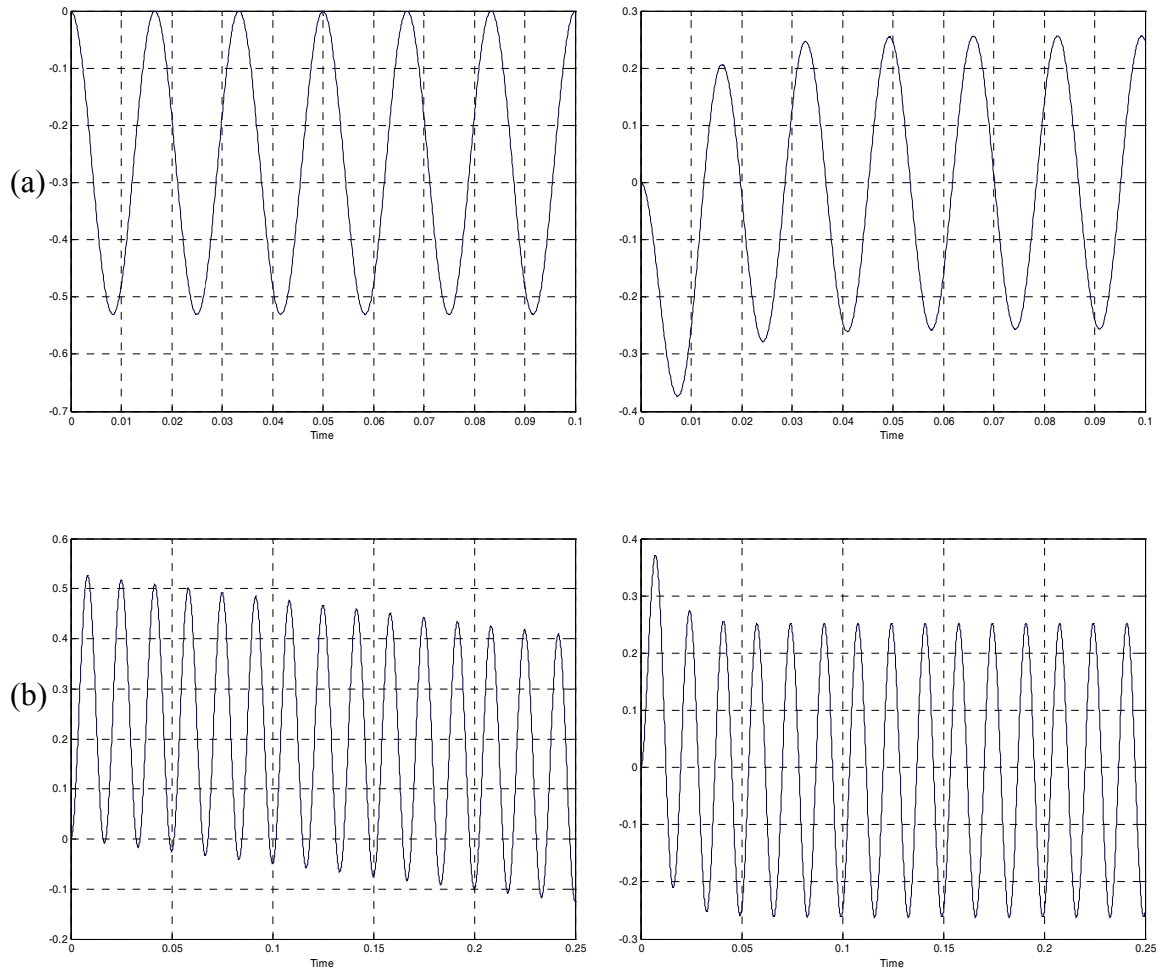


Using a pure integrator

Using a low pass filter

Figure 4.10a Comparison of simulations of integration using a pure integrator and a LPF.

(a) $\alpha_0 = 0, A_0 = 0$; (b) $\alpha_0 = \frac{\pi}{2}, A_0 = 0$.



Using a pure integrator

Using a low pass filter

Figure 4.10b Comparison of simulations of integration using a pure integrator and a LPF.

(a) $\alpha_0 = \pi, A_0 = 0$; (b) $\alpha_0 = 0, A_0 = -0.5$.

The integrations using the pure integrator and low pass filter are verified through experiments by estimating the stator flux linkages λ_{qs} and λ_{ds} . As shown in Figure 4.11, the drift problem with the pure integrator can be seen clearly. However, using low pass filter give the stable results and the stator flux linkages after transformed into the synchronous reference frame are good DC quantities.

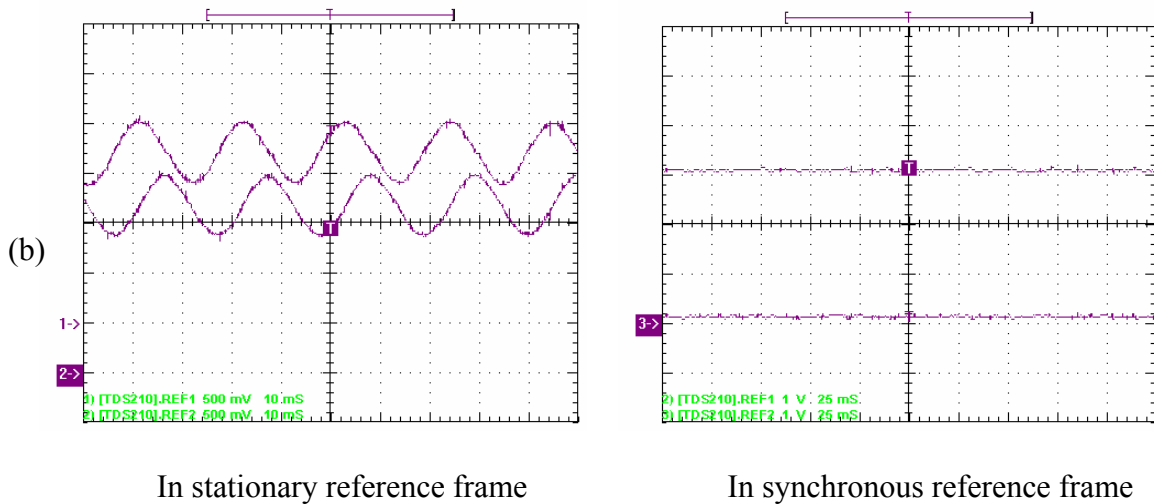
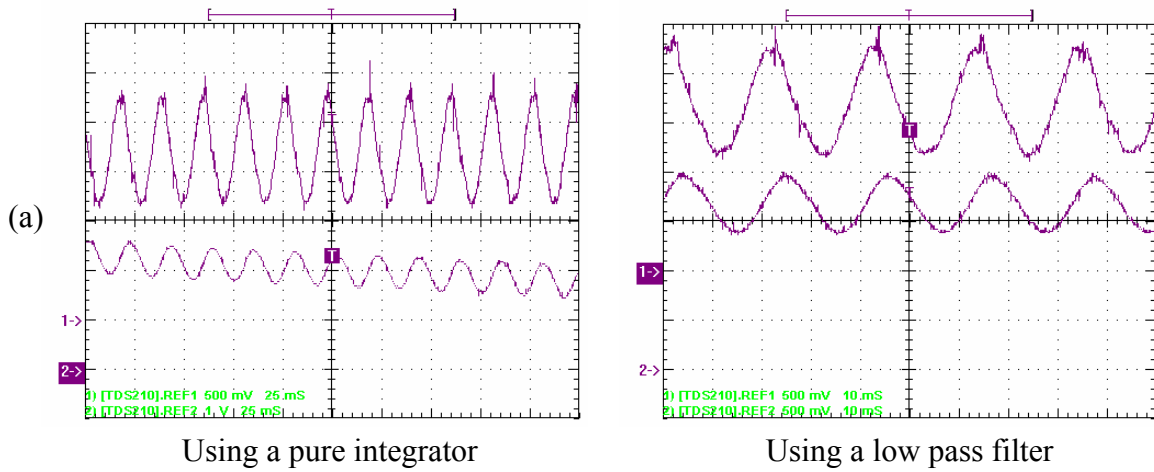


Figure 4.11 Comparison of experimental results of integration using a pure integrator and a LPF.

(a) Estimation of λ_{qs} from $(V_{qs} - r_s I_{qs})$, Ch1: $(V_{qs} - r_s I_{qs})$, Ch2: λ_{qs} ; (b)

estimation of λ_{qs} and λ_{ds} using low pass filters, Ch1: λ_{qs} , Ch2: λ_{ds} .

By using the low pass filter, the small DC offset in the integrated signals cannot cause saturation although the estimated values are not correct at the very beginning. The DC offset in the outputs introduced by the initial values is also mitigated. But there still exists the magnitude and phase errors due to the introduction of a (cut-off frequency)

especially when a is relatively big, which is generally the case to get a good performance for the LPF. The gain and phase compensations are

$$G = \frac{\sqrt{\omega_e^2 + a^2}}{\omega_e} \quad (4.96)$$

$$P = \exp(-j \cdot \phi_1)$$

where $\phi_1 = \tan^{-1}\left(\frac{a}{\omega_e}\right)$.

These two compensations can be simplified through combination.

$$G \cdot P = \frac{1}{\omega_e} (\omega_e - j \cdot a) \quad (4.97)$$

If the pole of LPF is varied proportionally to the synchronous motor speed, the proportion of the motor frequency to the cutoff frequency is constant. The compensation is then converted to a q-d transformation with constant coefficients. Assuming k is a constant such that $k = \frac{a}{\omega_e}$. The compensation becomes

$$\lambda_{qs} + j\lambda_{ds} = (\lambda_{qsl} + j\lambda_{dsl}) \cdot (1 - jk)$$

$$\lambda_{qs} = \lambda_{qsl} + k \cdot \lambda_{dsl} \quad (4.98)$$

$$\lambda_{ds} = \lambda_{dsl} - k \cdot \lambda_{qsl}$$

where λ_{dsl} , λ_{qsl} are the estimated flux using LPF and λ_{ds} , λ_{qs} are the flux after compensation. Then the rotor fluxes can be estimated using the stator and rotor flux linkages expressions

$$\lambda_{qds} = L_s I_{qds} + L_m I_{qdr} \quad (4.99)$$

$$\lambda_{qdr} = L_r I_{qdr} + L_m I_{qds}$$

Define $L_\sigma = L_s - \frac{L_m^2}{L_r}$, then the rotor fluxes are expressed in terms of stator fluxes

and stator currents by eliminating the rotor currents.

$$\lambda_{qdr} = \frac{L_r}{L_m} \cdot (\lambda_{qds} - L_\sigma I_{qds}) \quad (4.100)$$

4.9.2 Per Unit Model and Base Values

Since the TMS320LF2407 is a fixed point DSP, the Per Unit model of the motor has been used with the consideration of the flexibility and precision together. In this model, all quantities refer to the base values. Theoretically, the base values can be chosen as any number. But they are more meaningful if the nominal values are used to determine the base values. When the voltages and currents are sampled through DSP, the instantaneous data points are read. So the base values for the voltages and currents are chosen as the corresponding magnitudes instead of RMS values. Following equations are applied in calculating these values.

$$\begin{aligned} V_{base} &= \sqrt{2} \cdot V_n = \sqrt{2} \cdot \frac{220}{\sqrt{3}} = 179.63 \quad V \\ I_{base} &= \sqrt{2} \cdot I_n = \sqrt{2} \cdot 3.8 = 5.374 \quad A \\ \omega_{base} &= 2\pi f_n = 2\pi \cdot 60 = 377 \quad rad/sec \end{aligned} \quad (4.101)$$

$$\begin{aligned} \Psi_{base} &= \frac{V_{base}}{\omega_{base}} = \frac{179.63}{377} = 0.4765 \quad Wb \\ Z_{base} &= \frac{V_{base}}{I_{base}} = \frac{179.63}{5.374} = 33.426 \quad \Omega \end{aligned}$$

where V_{base} and I_{base} are the maximum values of the phase nominal voltage and current;

ω_{base} is the electrical nominal rotor flux speed; Ψ_{base} is the base flux.

The real quantities are implemented in the control are defined as follows.

$$\begin{aligned}
v &= \frac{V}{V_{base}} \\
i &= \frac{I}{I_{base}} \\
\psi &= \frac{\Psi}{\Psi_{base}} \\
f &= \frac{\text{rotor flux speed}}{\omega_{base}} \\
n &= \text{pole pairs} * f
\end{aligned}
\tag{4.102}$$

where v, i, ψ, f, n are per unit voltage, current, rotor flux speed, and electrical rotor speed, respectively. V_{base} and I_{base} are the maximum values of the phase nominal voltage and current; ω_{base} is the electrical nominal rotor flux speed; Ψ_{base} is the base flux.

By this way, the software representation of voltage, current, speed and flux is equal to one when the drive reaches its nominal speed under nominal load. But the actual quantities might reach higher values than the nominal, especially for the current. During the starting transient, it generally exceeds the nominal current. So appropriate numerical format needs to be considered, which is quite important for the fixed-point DSP. The numeric format used in this application is mainly Q₁₂ for 16-bit DSP, which means that four highest bits are dedicated to the integer part and twelve lowest bits are dedicated to the fractional part. Then representation range of this data format is from -8 to 8 and the resolution is 0.00024414 (1/2¹²).

4.9.3 Voltage / Current Sensing and Scaling

The proposed control scheme requires two line-line voltages and two phase currents as input. In this application, two LEM type voltage and current transducers sense these quantities. Therefore the outputs need to be rearranged and scaled so that they can be used in the control software as Q₁₂ format values. The complete process of acquiring the voltage and current are depicted in Figure 4.12 and Figure 4.13.

Basically the process of sensing voltage is the same as that of sensing current. In this application, the LEM output signals can be either positive or negative, the fundamental component of which should be sinusoidal. This signal must be translated by the analogue interface into the range of 0~3.3V in order to allow the ADC module on DSP to read both positive and negative values. The steps of the implemented voltage / current sensing are also shown in the figures.

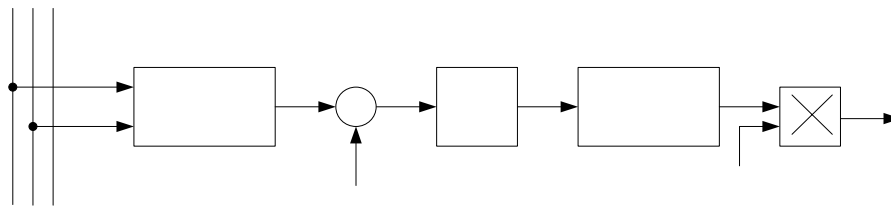


Figure 4.12 Voltage sensing and scaling block diagram (V_{ab}).

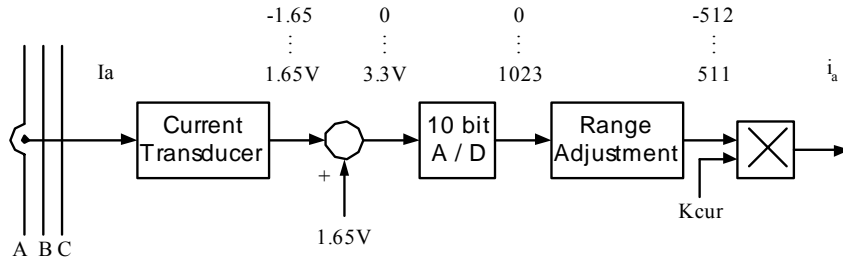


Figure 4.13 Current sensing and scaling block diagram (I_a).

The same procedures are applied on V_{ca} and I_b to calculate d-q quantities. The maximum outputs from the transducers represent the maximum measurable voltage / current, which might not necessarily equal to the maximum phase current. The ADC input voltage is converted into a ten bits digital value. The 1.65V analogue offset is digitally subtracted from the conversion result, thereby giving a signed integer value of the sensed voltage / current corresponding to the actual one.

The actual voltage and current with respect to 1.65V are denoted as V_{max} and I_{max} , respectively. Then the sensed voltages and currents must be expressed with the per unit model and be converted into the Q₁₂ format. The maximum voltage / current handled by the hardware is represented by 512 while the output 4096 or 1000h represents the base values V_{base} and I_{base} . The per unit voltage / current conversion into Q₁₂ format is achieved by multiplying the sensed voltage / current by the following constants.

$$K_{vol} = \frac{4096}{512 \cdot \frac{V_{base}}{V_{max}}} \quad K_{cur} = \frac{4096}{512 \cdot \frac{I_{base}}{I_{max}}}$$

In one single multiplication, this constant performs not only the per unit modeling but also the numerical conversion into Q₁₂ format. When nominal voltage is applied on a motor running at nominal speed and the current is nominal, the voltage and current

sensing and scaling block output is 1000h, which is equivalent to 1 in per unit. In this implementation, the maximum measurable voltage and current are $V_{\max} = 153.86$ V and $I_{\max} = 16.5$ A. So the constant values are

$$K_{vol} = \frac{4096}{512 \cdot \frac{179.63}{153.86}} = 6.8523 \Leftrightarrow 06DAh \quad Q_8$$

$$K_{cur} = \frac{4096}{512 \cdot \frac{16.5}{5.374}} = 24.5627 \Leftrightarrow 1890h \quad Q_8$$

Apparently K_{cur} is outside of the Q_{12} format range. The appropriate format to accommodate this constant is Q_8 format, which means that eight highest bits are dedicated to the integer part and eight lowest bits are dedicated to the fractional part. The corresponding resolution of Q_8 is 0.00390625. The same data format is applied for K_{vol} .

4.9.4 Speed Sensing and Scaling

A 4096 pulse absolute encoder is used to measure the rotor speed in this induction motor drive. Twelve digital I/O ports of the DSP TMS320LF2407 are occupied for reading the output of the encoder. Generally, the mechanical time constant is much lower than the electrical one. The speed regulation loop frequency might be lower than the current loop frequency and it can be achieved by means of a software counter. This counter takes the clock of PWM interrupt as the input and the speed is calculated every 250 PWM cycles.

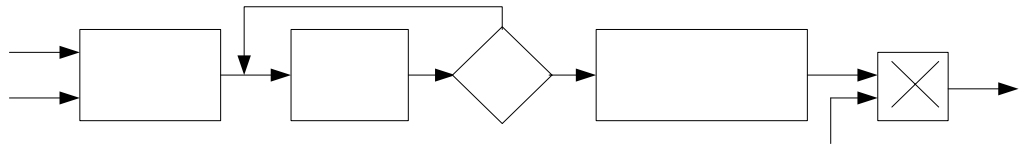


Figure 4.14 Speed sensing and scaling block diagram.

Assuming that n_p is the number of encoder pulses in 250 periods when the motor runs at the nominal speed, a software constant K_{speed} should be chosen as follows to let the speed feedback be transformed into the Q₁₂ format, which can be used directly in the control scheme.

$$K_{speed} \cdot n_p = 1000h$$

The nominal speed of current motor drive is 1800 rpm and the switching frequency of PWM is 10kHz. Then n_p and K_{speed} can be calculated as follows.

$$n_p = \frac{1800}{60} \cdot 4096 \cdot 250 \cdot 10^{-4} = 3072$$

$$K_{speed} = \frac{4096}{3072} = 1.3334 \Leftrightarrow 14Ah \quad Q_8$$

4.9.5 Slip Estimation

The slip calculation is shown in (4.12), in which I_{qs} can be directly calculated from the measured currents. The dynamic equation for λ_{dr} can be achieved by considering (4.11) and (4.13) simultaneously and eliminating I_{dr} .

$$\begin{aligned}
(T_r p + 1) \cdot \lambda_{dr} &= L_m I_{ds} \\
\omega_{slip} &= \frac{L_m I_{qs}}{T_r \lambda_{dr}}
\end{aligned} \tag{4.103}$$

And the rotor flux speed in per unit is just the sum of n and ω_{slip} .

$$f_s = n + \omega_{slip} \cdot \frac{1}{\omega_{base}} = n + \frac{L_m I_{qs}}{T_r \lambda_{dr}} \cdot \frac{1}{\omega_{base}} \tag{4.104}$$

The integration of this speed gives the rotor flux position. The above equations can be discretized as follows.

$$\begin{aligned}
\lambda_{dr_{k+1}} &= \lambda_{dr_k} + \frac{T}{T_r} (L_m I_{ds_k} - \lambda_{dr_k}) \\
f_{s_{k+1}} &= n_{k+1} + \frac{1}{T_r \omega_{base}} \cdot \frac{L_m I_{qs_k}}{\lambda_{dr_{k+1}}}
\end{aligned} \tag{4.105}$$

The rotor flux is calculated during the slip estimation, which provides the alternative way different with the application of LPF. Once the rotor flux speed has been calculated, the necessary rotor flux position is computed by the integration formula.

$$\theta_{k+1} = \theta_k + f_{s_k} \cdot \omega_{base} T \tag{4.106}$$

As the rotor flux position rang is $0 \sim 2\pi$, 16 bits integer values have been used to achieve the maximum resolution. The latter part of (4.103) is the angle variation within one sample period. At nominal operation ($f_s = 1000h$), the angle variation $\omega_{base} T$ is equal to 0.0377 rad. In one electrical revolution performed at nominal speed, there are 166.66 increments of the rotor flux position. Let K be the constant that converts the $0 \sim 2\pi$ range into the $0 \sim 65535$ range. Then K is calculated as follows.

$$\begin{aligned}
K &= \frac{65536}{166.66} = 393.22 \\
\theta_{k+1} &= \theta_k + K \cdot f_s
\end{aligned} \tag{4.107}$$

4.9.6 Program Flowchart

The program flowchart of DSP implementation is shown in Figure 4.15.

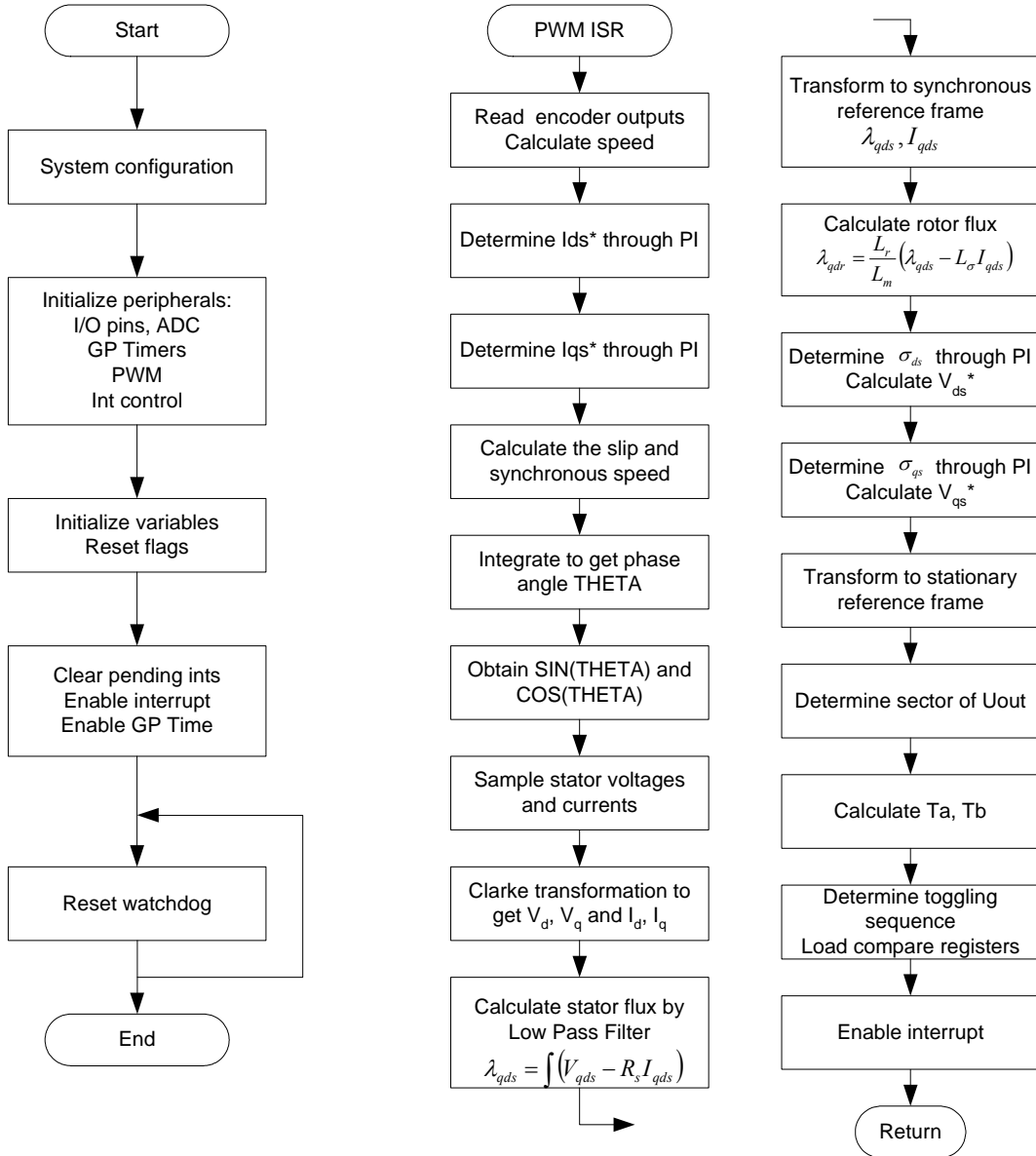


Figure 4.15 Program flowchart.

4.10 Experimental Results

The above program flow has been implemented and Figures 4.16 and 4.17 below shows the experimental result using the indirect field oriented speed control for 1 hp induction motor drive with the parameters determined in the former section. In Figure 4.16, it shows that the actual speed tracks the reference speed closely (they are separated in order to show the response clearly). Figure 4.17 shows the steady-state waveforms, in which the rotor flux linkage, both q- and d-axis stator currents are regulated in synchronous reference frame. The q- and d-axis stator currents and voltages are also shown.

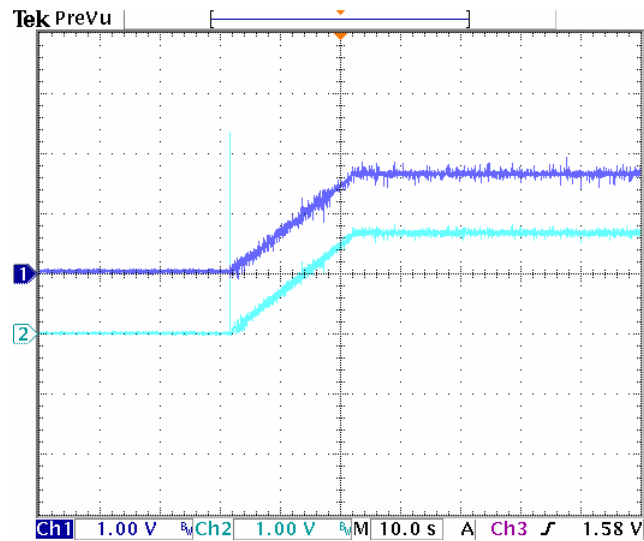


Figure 4.16 Experimental results: the reference speed and actual speed when the reference speed is ramped up from 0 to 900rpm. Ch1: reference speed (545rpm/div); Ch2: actual speed (545rpm/div).

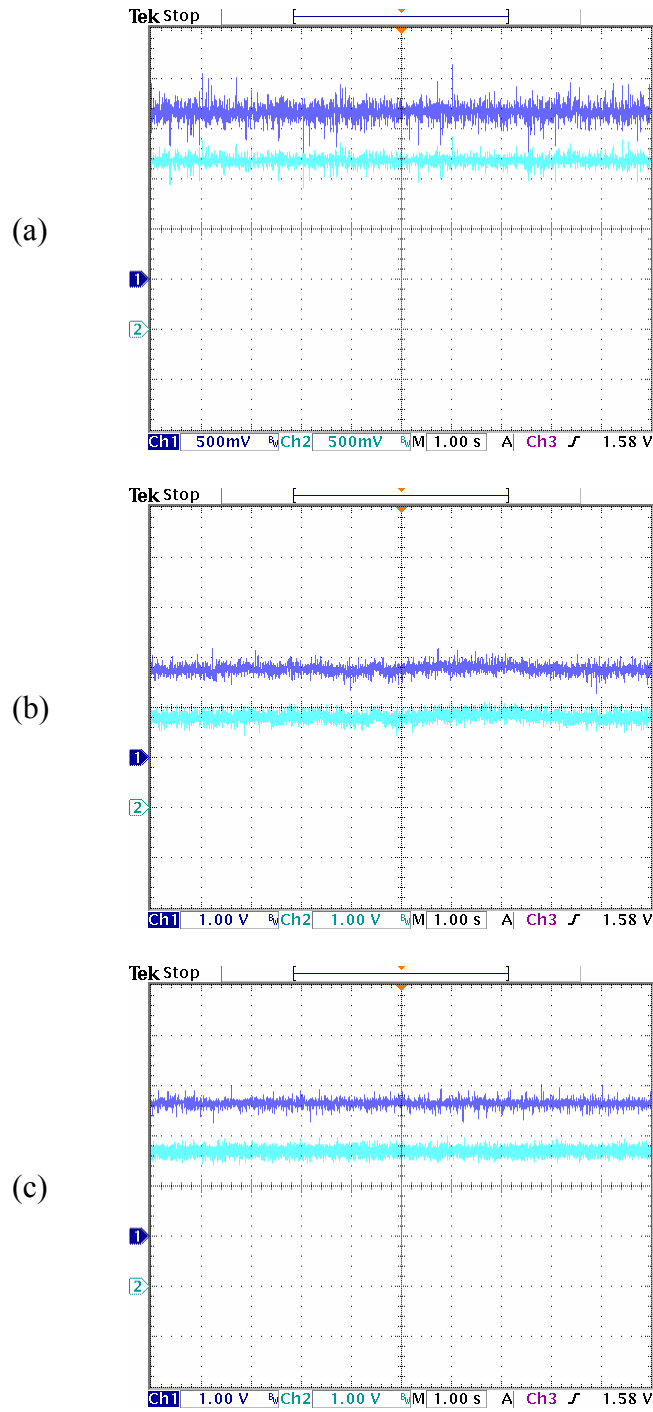


Figure 4.17a Experimental results at steady state. (a) Reference and actual d-axis rotor flux linkages (0.6Wb/div); (b) reference q-axis stator currents (-1.65V, 3A/div); (c) reference d-axis stator current (-1.65V, 3A/div).

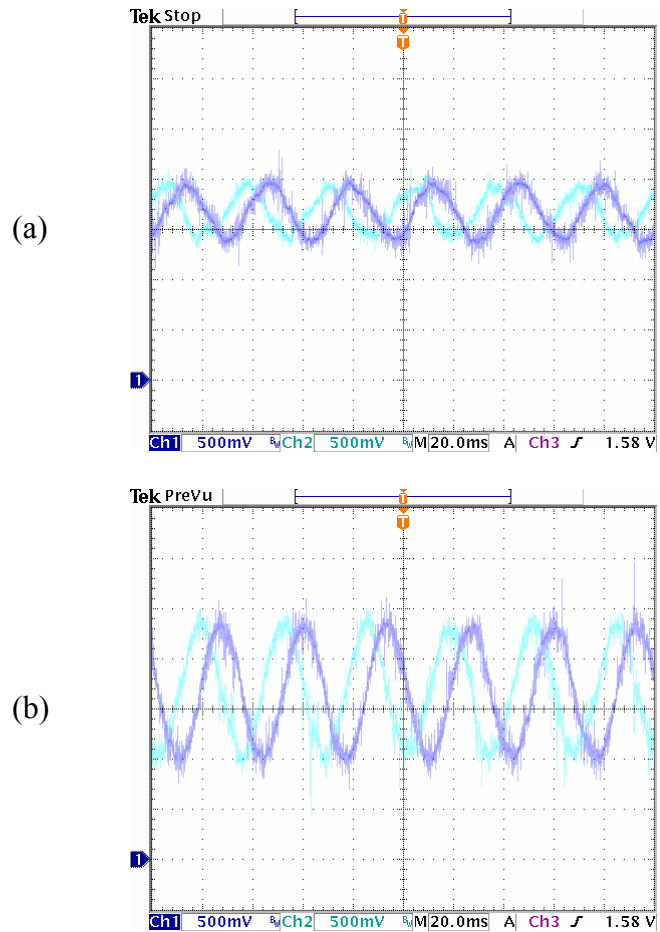


Figure 4.17b Experimental results at steady state. (a) Q- and d-axis stator current in stationary reference frame (6A/div); (b) q- and d-axis stator voltages in stationary reference frame (50V/div).

Sometimes the induction machine is required to operate in both rotating directions, clockwise and counter-clockwise. Such kind of operation has been verified through experiments by changing the reference speed between -300rpm and 300rpm as shown in Figure 4.18. The actual speed tracks the reference speed very well all the time.

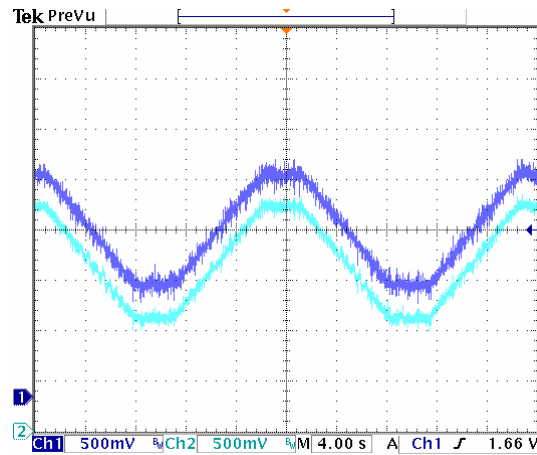


Figure 4.18 Experimental results for speed regulation between -300rpm and 300rpm.

Ch1: reference speed (273rpm/div); Ch2: actual speed (273rpm/div).

4.11 Conclusion

This chapter illustrates the rotor flux oriented control of the induction machine. The principles of rotor flux orientation are presented and then applied in the design of the speed control using linearization method. The Butterworth polynomial is used to select the appropriate controller parameters and the scheme is verified through simulation and also implemented using DSP. The implementation procedures are presented in detail including the measurements of speed, stator voltages and currents, the normalization of equations and corresponding representation in DSP programming. These procedures are also used in the implementation of other different schemes.

CHAPTER 5
EFFICIENCY OPTIMIZING CONTROL OF INDUCTION MOTOR USING
NATURAL VARIABLES

5.1 Introduction

As mentioned in Chapter 1, the efficiency improvement of induction machines is receiving more and more attentions since they are the greatest consumer of electric power. A lot of energy will be saved even if the total efficiency of the induction machine can be improved for just a little bit. Once the induction machine is manufactured, some of the losses are not controllable including the some mechanical, electrical and stray losses. However, the overall system losses of the induction machine can be minimized since the resistive and core losses are depending upon the operating conditions. For example, the induction machine can be operated at different flux level while the net output power is maintained the same. Apparently the sum of the resistive and core losses is different under the operation at different flux level. The study of the copper and core loss components reveals that their trends conflict – when the core loss increases, the copper loss tends to decrease. However, for a given load torque, there is an air-gap flux density at which the total loss is minimized. Hence, electrical loss minimization process ultimately comes down to the selection of the appropriate air-gap flux density. Since the air-gap flux density must be variable when the load is changing, control schemes in which the (rotor, air-gap) flux linkage is constant will yield sub-optimal efficiency operation especially when the load is light.

This chapter presents an approach of simultaneously optimizing the efficiency of induction motor drives and selecting flux linkage reference through the minimization of the copper and core losses while ensuring high dynamic performance. The induction machine model which accounts for the varying core loss resistance and saturation dependent magnetizing inductance, uses natural variables, which are reference frame independent quantities, as state variables – square of total rotor flux, active torque, reactive torques, which is corresponding to the reactive power and rotor speed. The inverter driving the motor is under pulse-width modulation and is voltage controlled. Utilization of the nonlinear geometric control methodology of input-output linearization with decoupling facility permits the implementation of the control in the stationary reference frame. This approach eliminates the need of synchronous reference transformation and flux alignment required in classical vector control schemes. The efficiency optimizing formulation yields a reference rotor flux which ensures minimum loss resulting in an improved efficiency of the drive system. The proposed scheme and its advantages are demonstrated both by computer simulations and some experimental results for induction motor speed control.

5.2 Induction Motor Model with Core Loss

The stationary reference frame q-d equivalent circuit of the induction machine is shown in Figure 5.1 in which the core loss is represented by a core loss resistance. The voltage equations for the induction motor in the arbitrary reference frame rotating at the speed ω are given as:

$$\begin{aligned}
V_{qs} &= r_s I_{qs} + p\lambda_{qs} + \omega\lambda_{ds} \\
V_{ds} &= r_s I_{ds} + p\lambda_{ds} - \omega\lambda_{qs} \\
0 &= r_r I_{qr} + p\lambda_{qr} + (\omega - \omega_r)\lambda_{dr} \\
0 &= r_r I_{dr} + p\lambda_{dr} - (\omega - \omega_r)\lambda_{qr}
\end{aligned} \tag{5.1}$$

where

$$\begin{aligned}
\lambda_{qs} &= L_s I'_{qs} + L_m I_{qr} & \lambda_{qr} &= L_r I_{qr} + L_m I'_{qs} \\
\lambda_{ds} &= L_s I'_{ds} + L_m I_{dr} & \lambda_{dr} &= L_r I_{dr} + L_m I'_{ds}
\end{aligned}$$

Define $L_\sigma = L_s - \frac{L_m^2}{L_r}$ and $k = 1 + \frac{r_s}{r_c}$, the stator voltage equations can be expressed

in terms of I'_{qs}, I'_{ds} and $\lambda_{qr}, \lambda_{dr}$ as follows.

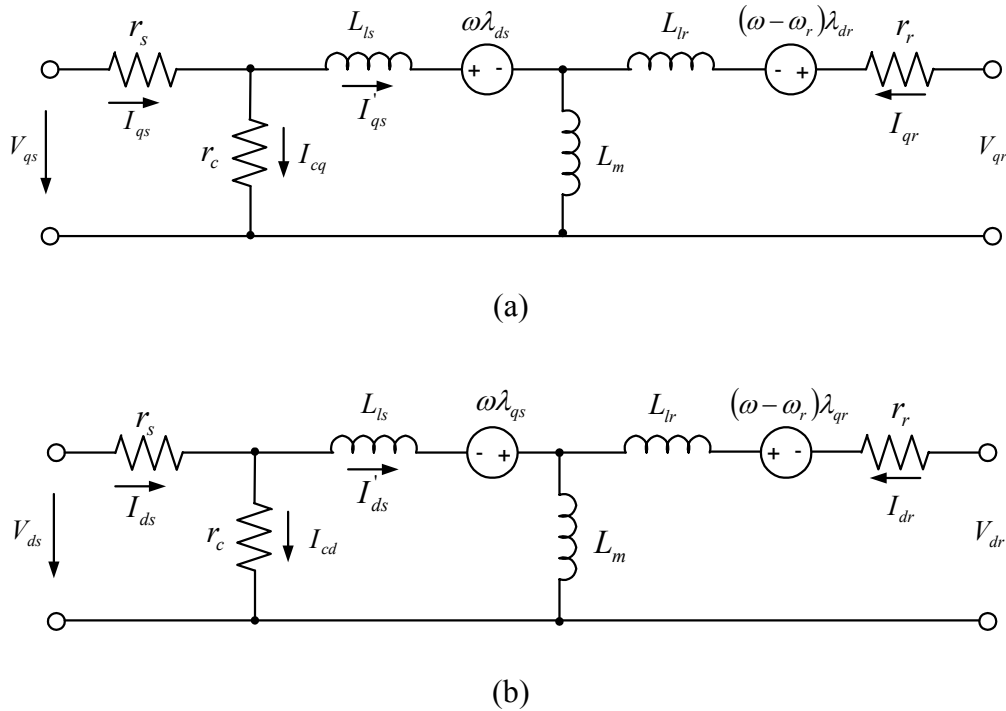


Figure 5.1 The q-d equivalent circuit model of the induction machine including core loss resistance. (a) Q-axis; (b) d-axis.

$$\begin{aligned}
\frac{V_{qs}}{k} &= rI_{qs}' - c\lambda_{qr} + \frac{\omega_r L_m}{L_r} \lambda_{dr} + L_\sigma pI_{qs}' \\
\frac{V_{ds}}{k} &= rI_{ds}' - c\lambda_{dr} - \frac{\omega_r L_m}{L_r} \lambda_{qr} + L_\sigma pI_{ds}' \\
0 &= r_r I_{qr} + p\lambda_{qr} - \omega_r \lambda_{dr} \\
0 &= r_r I_{dr} + p\lambda_{dr} + \omega_r \lambda_{qr}
\end{aligned} \tag{5.2}$$

where

$$r = \frac{r_s}{k} + \frac{r_r L_m^2}{L_r^2}, \quad c = \frac{r_r L_m}{L_r^2}.$$

V_{qs} and V_{ds} are the stator qd-axis voltages. I_{qs}' and I_{ds}' are the q- and d-axis torque effective currents. I_{qr} and I_{dr} are the q- and d-axis rotor currents. λ_{qr} and λ_{dr} are the rotor flux linkages. r_s , r_r , and r_c are the stator, rotor resistance and stator core loss resistance, which accounts for the stator core loss. L_s , L_r , and L_m are stator self-inductance, rotor self-inductance, and mutual inductance. ω_r is the electrical rotor speed and p represents the derivative.

Equations (5.1-2) contain the mutual inductance and the core loss resistance that are changing with the flux linkage. These changes are accounted for in both computer simulations and experimental implementation of the controllers by updating them as the stator flux linkage varies. These parameter changes for a 1 hp machine are shown in Figure 3.6, in which the measured mutual inductance and core resistance are plotted as a function of the stator flux linkage.

5.3 Natural Variable Model and Total Loss Minimization

The variables of the natural variable model of the induction machine are chosen as the developed electromagnetic torque T_e , the developed reactive torque T_r , the rotor speed ω_r , and the square of the magnitude of the rotor flux linkage λ_{rr} . These variables are the same in all reference frames or independent of the selected reference frame. Then these natural variables are expressed in terms of the axis currents and flux linkages as:

$$\begin{aligned} T_e &= k_t (\lambda_{dr} I'_{qs} - \lambda_{qr} I'_{ds}) \\ T_r &= k_t (\lambda_{dr} I'_{ds} + \lambda_{qr} I'_{qs}) \\ \lambda_{rr} &= \lambda_{qr}^2 + \lambda_{dr}^2 \end{aligned} \quad (5.3)$$

where $k_t = \frac{3PL_m}{4L_r}$ and P is the poles of the machine.

The losses existing in the induction machine include many different kinds such as the stator and rotor copper losses, stator and rotor core losses, mechanical loss, and stray loss. Generally these losses vary under different operating conditions. However, under the certain operating condition, most of the losses are not controllable except the stator and rotor copper and core losses. The stator and rotor copper losses are essentially determined by the corresponding resistances and currents while the stator core loss can be calculated from the core loss resistance and the currents flowing through.

$$P_L = \frac{3}{2} r_s (I_{qs}^2 + I_{ds}^2) + \frac{3}{2} r_r (I_{qr}^2 + I_{dr}^2) + \frac{3}{2} r_c (I_{cq}^2 + I_{cd}^2) \quad (5.4)$$

Since now the effective torque currents are used, the stator and rotor currents and the currents flowing through the core loss resistance can be expressed in terms of I_{qs}' , I_{ds}' , λ_{qr} , and λ_{dr} . And eventually the total loss can be rewritten using the natural variables defined in (5.3) as

$$P_L = \frac{3}{2k_t^2} \left[r + \frac{k(r^2 + \omega_e^2 L_\sigma^2)}{r_c} \right] \frac{T_e^2 + T_r^2}{\lambda_{rr}} + \frac{3}{2} \left(\frac{kc^2}{r_c} + \frac{r_r}{L_r^2} + \frac{kL_m^2}{r_c L_r^2} \omega_r^2 \right) \lambda_{rr} \quad (5.5)$$

$$+ \frac{3}{k_t} \left(\frac{kL_\sigma L_m}{r_c L_r} \omega_e \omega_r - \frac{kr_c}{r_c} - c \right) T_r + \frac{3k}{k_t r_c} \left(c \omega_e L_\sigma + r \omega_r \frac{L_m}{L_r} \right) T_e$$

where $r = \frac{r_s}{k} + \frac{r_r L_m^2}{L_r^2}$, $c = \frac{r_r L_m}{L_r^2}$.

The total electrical loss is to be minimized when the motor is subject to an operating load torque, $T_e = T_e^*$. Either λ_{rr} or T_r can be chosen as the control variable to form the loss minimization function γ . Both λ_{rr} and T_r cannot be used as the control variables at the same time for the loss minimization. This can be examined from the derivative of the magnitude square of the rotor flux linkages. Apparently the derivative of λ_{rr} is zero at steady state, which means that λ_{rr} and T_r are dependent if all the machine parameters are assumed constants.

$$p\lambda_{rr} = -\frac{2r_r}{L_r} \lambda_{rr} + \frac{2r_r L_m}{k_t L_r} T_r \quad (5.6)$$

The electric loss is minimized when any of the two determinants in (5.7-8) is identically equal to zero. These two determinants are not zero in general while they are supposed to be zero when the total electrical loss is minimized.

$$\gamma = \frac{\left| \frac{\partial T_e}{\partial P_L} \quad \frac{\partial T_e}{\partial \lambda_{rr}} \right|}{\left| \frac{\partial T_e}{\partial T_e} \quad \frac{\partial T_e}{\partial \lambda_{rr}} \right|} = \frac{\partial P_L}{\partial \lambda_{rr}} = 0 \quad \Rightarrow \quad \gamma = f_1(T_e, \lambda_{rr}, \omega_e, \omega_r) \quad (5.7)$$

$$\gamma = \frac{\left| \frac{\partial T_e}{\partial P_L} \quad \frac{\partial T_e}{\partial T_r} \right|}{\left| \frac{\partial T_e}{\partial T_e} \quad \frac{\partial T_e}{\partial T_r} \right|} = \frac{\partial P_L}{\partial T_r} = 0 \quad \Rightarrow \quad \gamma_2 = f(T_e, T_r, \omega_e, \omega_r) \quad (5.8)$$

Based on the above analysis, these two formulations give out the same results at the steady state. In the case of (5.7), it can be expressed in terms of the natural variables as

$$\begin{aligned} \gamma = & \frac{3}{2k_t^2} \left[r + \frac{k(r^2 + \omega_e^2 L_\sigma^2)}{r_c} \right] \left(\frac{2T_r}{\lambda_{rr} L_m} \frac{k_t}{L_m} - \frac{T_e^2 + T_r^2}{\lambda_{rr}^2} \right) \\ & + \frac{3}{2} \left(\frac{kc^2}{r_c} + \frac{r_r}{L_r^2} + \frac{kL_m^2}{r_c L_r^2} \omega_r^2 \right) + \frac{3}{L_m} \left(\frac{kL_\sigma L_m}{r_c L_r} \omega_e \omega_r - \frac{krc}{r_c} - c \right) \end{aligned} \quad (5.9)$$

The total electric loss is minimized when $\gamma = 0$ under steady-state operation. Then the corresponding optimum rotor flux is calculated as

$$\lambda_{rr} = \sqrt{\frac{\frac{3}{2k_t^2} R(T_e^2 + T_r^2)}{\frac{3}{2} \left(\frac{kc^2}{r_c} + \frac{r_r}{L_r^2} + \frac{kL_m^2}{r_c L_r^2} \omega_r^2 \right) + \frac{3}{L_m} \left(\frac{kL_\sigma L_m}{r_c L_r} \omega_e \omega_r - \frac{krc}{r_c} - c \right) + \frac{3}{L_m} R}} \quad (5.10)$$

where

$$R = r + \frac{k(r^2 + \omega_e^2 L_\sigma^2)}{r_c}.$$

5.4 Formulation of Control Scheme

The total loss minimization is achieved through appropriate command of the q-d axis machine voltages by closed-loop controllers using a voltage controlled voltage source inverter. Since the model of the machine is nonlinear and coupled, the principles of nonlinear control of the input-output linearization with decoupling are used to remove the nonlinearity and coupled terms thereby enabling classical linear system control methodology to be used to determine both the constant gain parameters and the structure of the controllers [5.11-5.12]. This is possible since the input-output linearization and decoupling strategy ensures linear relationships between the input control variables and the controlled variables with each output-input pair decoupled from each other.

Input-output linearization is a three-step process: (a) differentiate a controlled variable until an input variable appears, (b) choose the input variable to cancel nonlinear terms and guarantee tracking convergence, and (c) study the stability of the internal dynamics. The total number of differentiations for all controlled variables is called the relative order r , while the internal dynamics are composed of $n-r$ states (n is the total number of the system dynamic states). When operations (a-c) are performed on the motor model equations (5.3), the resulting equations are linearized, decoupled with no internal dynamics and input-output linearizable. Hence any realistic dynamics can be imposed by means of linear controllers.

$$pT_e = -\left(\frac{r_s}{L_\sigma k} + \frac{r_r L_s}{L_\sigma L_r}\right)T_e - \omega_r T_r - \frac{k_t L_m}{L_\sigma L_r} \omega_r \lambda_{rr} + \frac{k_t}{L_\sigma k} m_1 \quad (5.11)$$

$$p\omega_r = \frac{P}{2J}(T_e - T_L) \quad (5.12)$$

$$pT_r = -\left(\frac{r_s}{L_\sigma k} + \frac{r_r L_s}{L_\sigma L_r}\right)T_r + \frac{r_r L_m}{L_r k_t} \frac{T_e^2 + T_r^2}{\lambda_{rr}} + \omega_r T_e + \frac{k_t r_r L_m}{L_\sigma L_r^2} \lambda_{rr} + \frac{k_t}{L_\sigma k} m_2 \quad (5.13)$$

$$p\lambda_{rr} = -\frac{2r_r}{L_r} \lambda_{rr} + \frac{2r_r L_m}{k_t L_r} T_r \quad (5.14)$$

where

$$\begin{aligned} m_1 &= \lambda_{dr} V_{qs} - \lambda_{qr} V_{ds} \\ m_2 &= \lambda_{qr} V_{qs} + \lambda_{dr} V_{ds} \end{aligned} \quad (5.15)$$

The quantities m_1 and m_2 are calculated using the outputs of the controllers for T_e and T_r . Then the voltages commands are calculated by solving (5.15).

$$\begin{aligned} V_{qs} &= \frac{m_1 \lambda_{dr} + m_2 \lambda_{qr}}{\lambda_{rr}} \\ V_{ds} &= \frac{m_2 \lambda_{dr} - m_1 \lambda_{qr}}{\lambda_{rr}} \end{aligned} \quad (5.16)$$

Popular PI controllers are applied for the control of λ_{rr} , T_e , T_r , and ω_r .

$$K_\lambda = K_{p\lambda} + \frac{K_{i\lambda}}{p}, \quad K_{T_r} = K_{pT_r} + \frac{K_{iT_r}}{p},$$

$$K_\omega = K_{p\omega} + \frac{K_{i\omega}}{p}, \quad K_{T_e} = K_{pT_e} + \frac{K_{iT_e}}{p}$$

Their corresponding transfer functions are derived as follows.

$$\begin{aligned} \sigma_\lambda &= p\lambda_{rr} + \frac{2r_r}{L_r} \lambda_{rr} = K_\lambda (\lambda_{rr}^* - \lambda_{rr}) \\ \sigma_{T_r} &= pT_r + \left(\frac{r_s}{L_\sigma k} + \frac{r_r L_s}{L_\sigma L_r}\right)T_r = K_{T_r} (T_r^* - T_r) \end{aligned} \quad (5.17)$$

$$p^2 \omega_r = \frac{P}{2J} \cdot p[K_\omega (\omega_r^* - \omega_r)], \quad T_e = K_\omega (\omega_r^* - \omega_r)$$

$$\sigma_{T_e} = pT_e + \left(\frac{r_s}{L_\sigma k} + \frac{r_r L_s}{L_\sigma L_r} \right) T_e = K_{T_e} (T_e^* - T_e)$$

The controller parameters are determined from the transfer functions by tuning the denominators to be Butterworth polynomial compliant, which is to optimize the closed-loop eigen-values to be uniformly located in the left half plane on the circle of the resonant frequency. Butterworth polynomial for a transfer function with a second order polynomial is given by

$$p^2 + \sqrt{2}p\omega_0 + \omega_0^2 = 0 \quad (5.18)$$

Comparing the coefficients of the denominators of the transfer functions obtained from (5.17) and (5.18) gives the controllers' gains for a chosen resonant frequency ω_0 . The selection of the resonant frequency is such as to ensure the closed-loop transfer functions of the controlled variables have minimum-phase characteristics [5.13]. The controller structure for the motor speed control is shown in Figure 5.2.

The rotor position, motor phase currents and phase voltages are measured to estimate the natural variables and the rotor flux linkages which are required for the control implementation. Only the stationary reference frame transformation is required in the estimation of the natural variables.

$$\omega_{slip} = \frac{r_r L_m}{L_r K_t} \cdot \frac{T_e}{\lambda_{rr}} \quad (5.20)$$

Then the rotor speed can be estimated using (5.19-20) as

$$\omega_r = \frac{-\frac{2}{3}Q - \frac{r_r L_m}{L_r K_t} \cdot \frac{T_e}{\lambda_{rr}} \cdot L_\sigma \cdot \frac{T_e^2 + T_r^2}{K_t^2 \lambda_{rr}} - \frac{r_r L_m}{K_t L_r^2} \cdot T_e}{L_\sigma \cdot \frac{T_e^2 + T_r^2}{K_t^2 \lambda_{rr}} + \frac{r_r L_m}{K_t L_r} \cdot T_r} \quad (5.21)$$

This method is simulated and the procedures of sensorless scheme for both simulation and implementation are similar. First of all, the control scheme with speed regulation using speed sensor should work properly. Then the speed is estimated while the motor is still running using the speed from the speed sensor as feedback. Once the estimated speed is getting very close to the actual speed, it can then be used as feedback to see if it works. Of course, the simulation has to be done first and then it can be implemented after the simulation works. In this simulation, the reference rotor speed is ramped up from 0 to 150 rad/s. The rotor speed is estimated very well when the actual rotor speed is used as the feedback. However, there are big oscillations in the actual rotor speed while the estimated rotor speed is used as the feedback. And the developed electric torque also has big oscillations, which is not desirable.

5.5.2 Using Rotor Voltage Equations

It is known that the rotor speed information can be extracted from the rotor voltage equations, which can be classified into category of using the motor back EMF. The two rotor voltage equations are

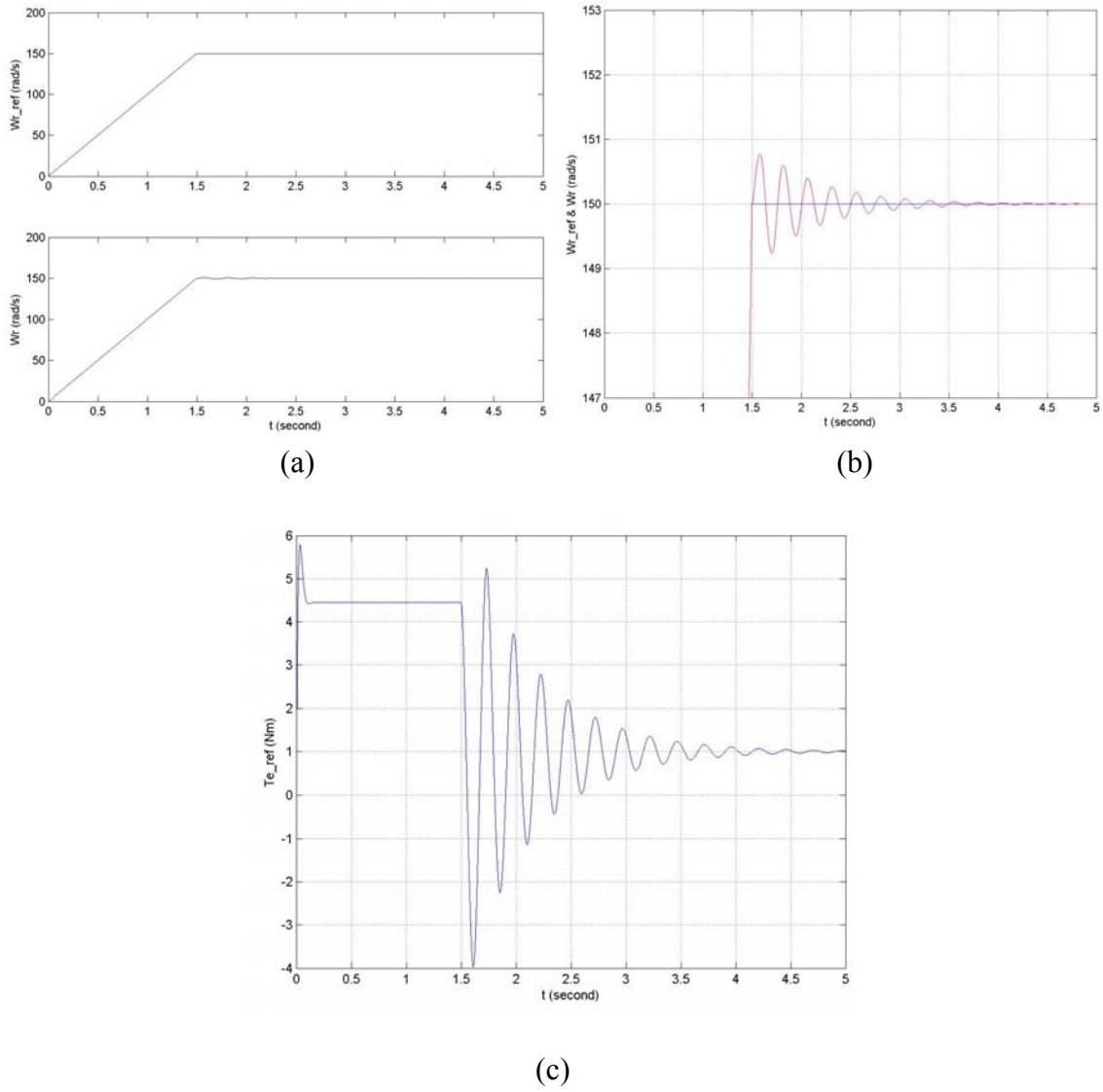


Figure 5.3 Simulation of the rotor speed estimation including reactive power. (a) Reference and actual rotor speeds; (b) Reference and actual rotor speeds; (c) Developed electric torque.

$$\begin{aligned}
 0 &= r_r I_{qr} + p \lambda_{qr} + j(\omega_e - \omega_r) \lambda_{dr} \\
 0 &= r_r I_{dr} + p \lambda_{dr} - j(\omega_e - \omega_r) \lambda_{qr}
 \end{aligned} \tag{5.22}$$

The rotor currents are not directly measurable and can be expressed in terms of the rotor flux linkages and stator currents as

$$\begin{aligned}
I_{qr} &= \frac{1}{L_r} \cdot (\lambda_{qr} - L_m I_{qs}) \\
I_{dr} &= \frac{1}{L_r} \cdot (\lambda_{dr} - L_m I_{ds})
\end{aligned} \tag{5.23}$$

The rotor voltage equations change to

$$\begin{aligned}
0 &= \frac{r_r}{L_r} \lambda_{qr} - \frac{r_r L_m}{L_r} I_{qs} + p \lambda_{qr} + (\omega_e - \omega_r) \lambda_{dr} \\
0 &= \frac{r_r}{L_r} \lambda_{dr} - \frac{r_r L_m}{L_r} I_{ds} + p \lambda_{dr} - (\omega_e - \omega_r) \lambda_{qr}
\end{aligned} \tag{5.24}$$

When $\omega_e = 0$, there equations are simplified in the stationary reference frame as

$$\begin{aligned}
0 &= \frac{r_r}{L_r} \lambda_{qr} - \frac{r_r L_m}{L_r} I_{qs} + p \lambda_{qr} - \omega_r \lambda_{dr} \\
0 &= \frac{r_r}{L_r} \lambda_{dr} - \frac{r_r L_m}{L_r} I_{ds} + p \lambda_{dr} + \omega_r \lambda_{qr}
\end{aligned} \tag{5.25}$$

Either one of these two equations can be used to estimate the rotor speed when the rotor flux linkages are known. Since both λ_{qr} and λ_{dr} are AC signals, the estimation will not work properly when the flux linkage as the coefficient of ω_r is zero. One of the solutions is to use both equations alternatively by finding the bigger rotor flux linkage.

That is

$$\text{If } |\lambda_{dr}| > |\lambda_{qr}|$$

$$\hat{\omega}_r = \left(p \lambda_{qr} + \frac{r_r}{L_r} \lambda_{qr} - \frac{r_r L_m}{L_r} I_{qs} \right) / \lambda_{dr} = X / \lambda_{dr} \tag{5.26}$$

Else

$$\hat{\omega}_r = \left(-p \lambda_{dr} - \frac{r_r}{L_r} \lambda_{dr} + \frac{r_r L_m}{L_r} I_{ds} \right) / \lambda_{qr} = Y / \lambda_{qr} \tag{5.27}$$

The simulation results are shown in Figure 5.4. It is seen that the rotor speed is regulated when the estimated speed is used as the feedback. The only problem is that the estimated rotor speed is oscillating around the actual speed. This kind of oscillation exists all the time such that it is not a good estimation.

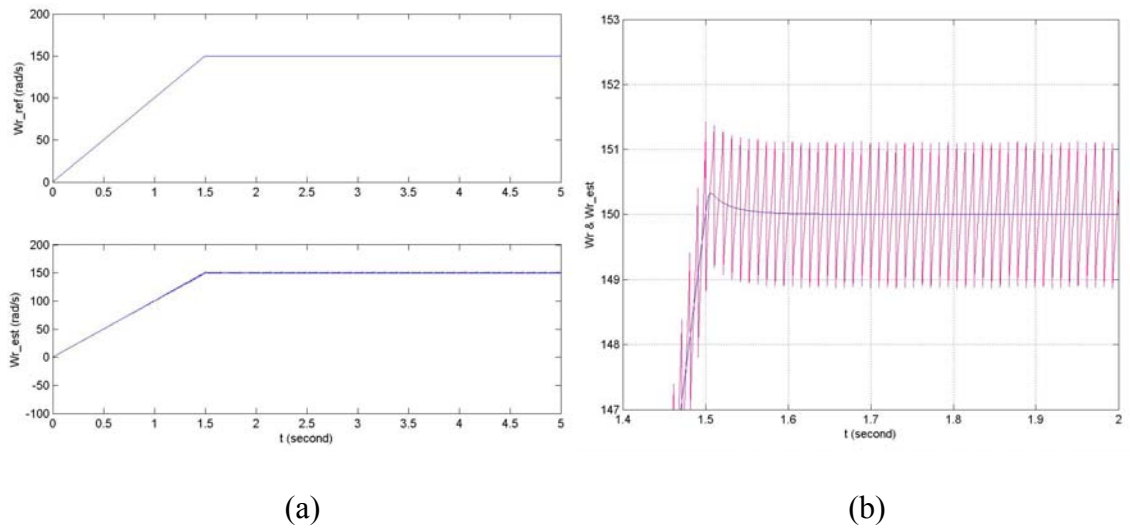


Figure 5.4 Simulation of the rotor speed estimation using rotor voltage equations. (a) Reference and estimated rotor speeds; (b) reference and estimated rotor speeds.

5.5.3 Using Rotor Voltage Equations (modified)

Instead of using only one of the two rotor voltage equations at a time, it is possible to use both of them at the same time in order to eliminate the oscillations. That is using the square root of the sum of squares of the estimated speed from these two equations.

The rotor speed can be estimated from

$$\begin{aligned}\hat{\omega}_r &= \left(p\lambda_{qr} + \frac{r_r}{L_r} \lambda_{qr} - \frac{r_r L_m}{L_r} I_{qs} \right) / \lambda_{dr} = X / \lambda_{dr} \\ \hat{\omega}_r &= \left(-p\lambda_{dr} - \frac{r_r}{L_r} \lambda_{dr} + \frac{r_r L_m}{L_r} I_{ds} \right) / \lambda_{qr} = Y / \lambda_{qr}\end{aligned}\tag{5.28}$$

And the final rotor speed is re-calculated from (5.28) as

$$\omega_r = \sqrt{\frac{X^2 + Y^2}{\lambda_{dr}^2 + \lambda_{qr}^2}}\tag{5.29}$$

The simulation results are shown in Figure 5.5. It is seen that the rotor speed is regulated very well when the estimated speed is used as the feedback. The steady state error between the actual rotor speed and the estimated rotor speed is very small. And the estimated rotor speed is constant at the steady state, which is good characteristic. It means that the error for the estimation can be compensated even if this error is big.

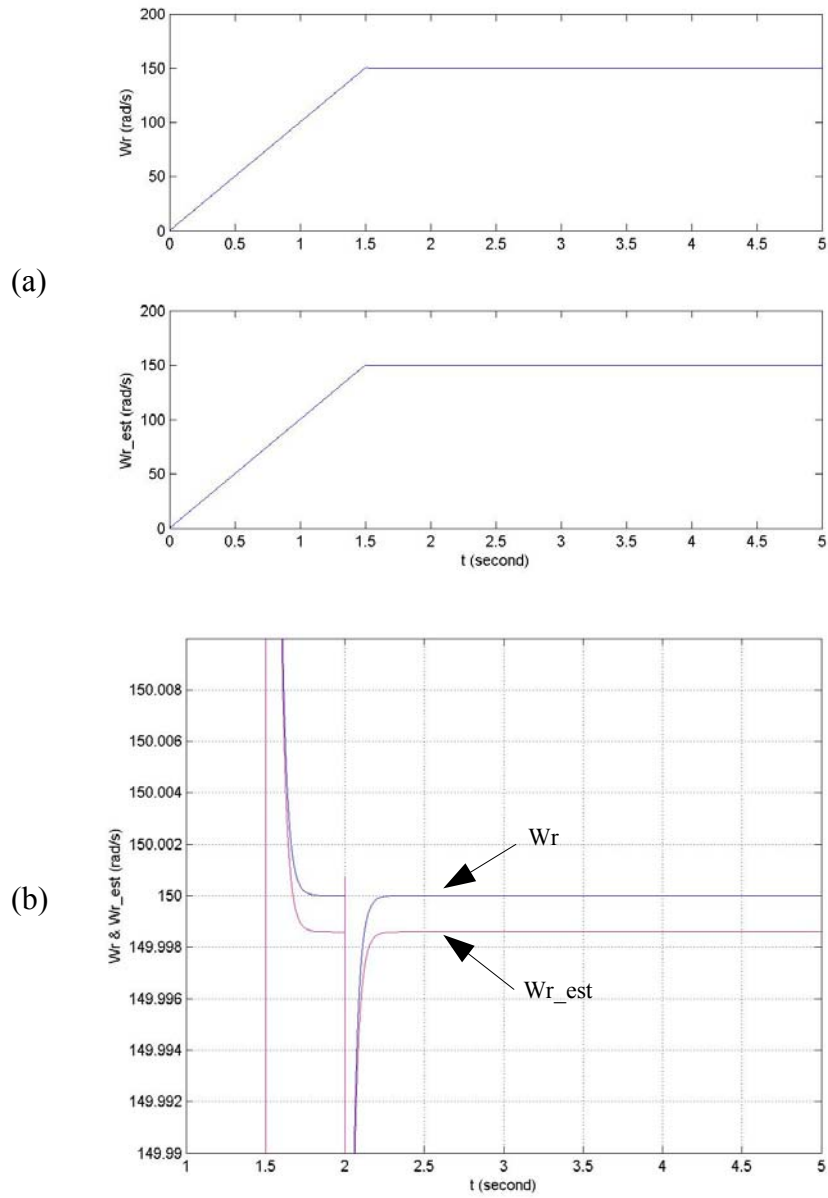


Figure 5.5 Simulation of the rotor speed estimation using rotor voltage equations. (a) Reference and estimated rotor speeds; (b) reference and estimated rotor speeds.

5.6 Simulation Results

Figure 5.6 gives the no-load starting transient of an experimental 1 hp induction machine whose parameters are shown in Figure 3.6 and Table 3.1. The reference speed is ramped from zero to 300 rad/sec while seeking to minimize the total electrical loss. The simulation results show that the rotor flux linkage quickly builds up and maintains an almost constant rated value and becomes small at steady-state. The total loss reduces as the developed torque becomes zero, in which case the ideal stator current is zero and hence the copper loss is zero.

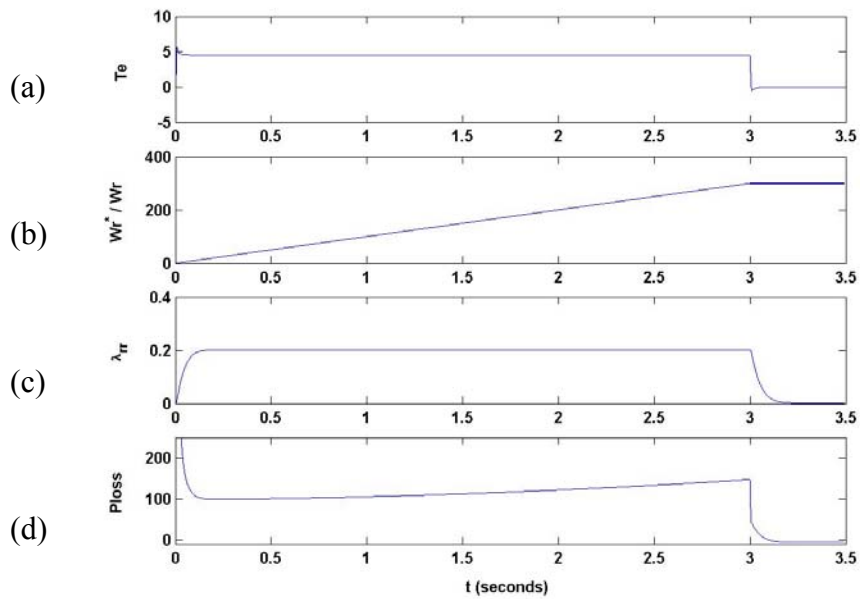


Figure 5.6 Speed regulation and loss minimization for motor starting from zero speed to 300 rad/sec. (a) Developed torque; (b) reference and actual rotor speeds; (c) rotor flux linkage; (d) total electric loss.

In Figure 5.7, the speed is maintained at 300 rad/sec, but the load torque is changing. As expected, the rotor flux responds to the changing load demand resulting in the minimization of the losses. As the load demand decreases, the optimum rotor flux linkage also decreases resulting in a lower loss. In Figure 5.8, the rotor speed is changed with time and it is seen that both the rotor flux linkage and the loss seeks the minimum level. The speed change with constant slope is basically working as putting a constant load to the induction motor. In these simulations, the rotor flux linkage is limited below the rated value, the square of which is about 0.2 wb^2 .

Figures 5.6-8 demonstrate the possibilities that this control scheme presents – changing load or reference speed commands appropriate flux linkage to minimize the electric loss while giving high performance speed control. Figure 5.9 shows the changing speed between both positive and negative directions. It appears that the motor speed is still regulated very well under such operating condition.

The proposed speed estimation method has already been simulated for the speed control in the above section. Figure 5.10 shows the speed response for a constant flux reference when the load is under step change. It is seen that the estimated speed is almost identical to the actual speed. It verifies the effectiveness of the proposed sensorless approach.

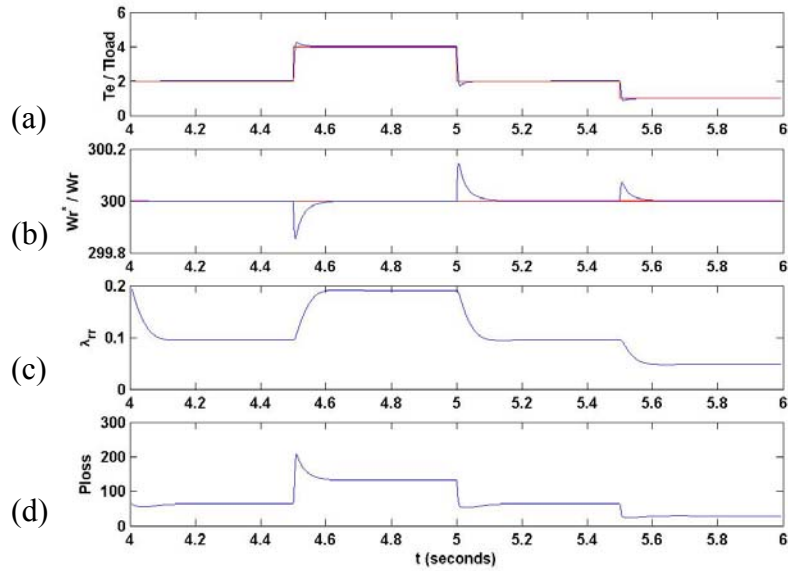


Figure 5.7 Speed regulation and loss minimization for changing load torque. (a) Developed torque; (b) actual and command rotor speed; (c) square of rotor flux linkage; (d) total electric loss.

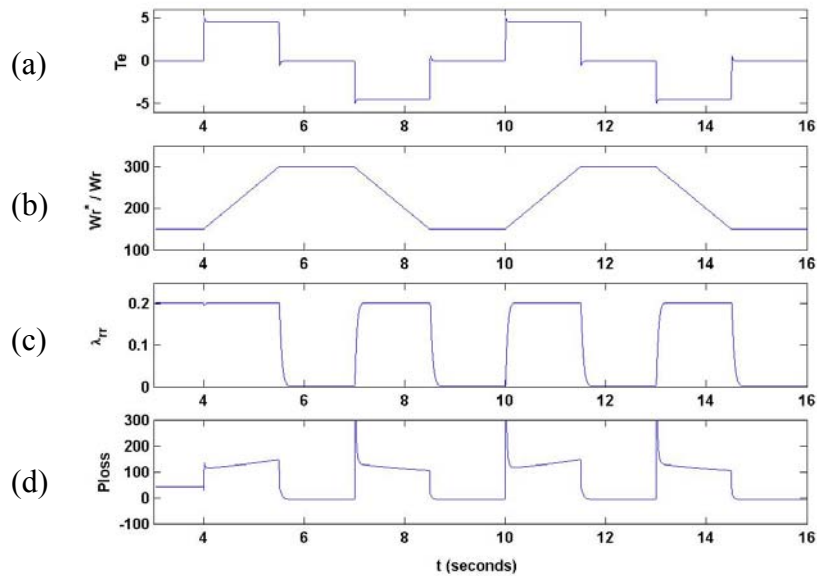


Figure 5.8 Speed regulation and loss minimization for changing rotor speed. (a) Developed torque; (b) actual and command rotor speed; (c) square of rotor flux linkage; (d) total electric loss.

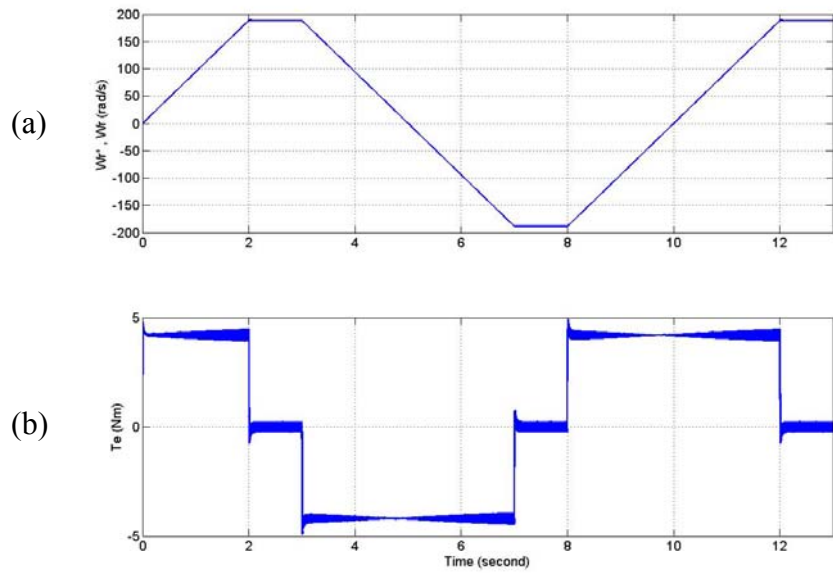


Figure 5.9 Response to the speed change after steady state. (a) Reference speed and actual speeds; (b) electrical torque.

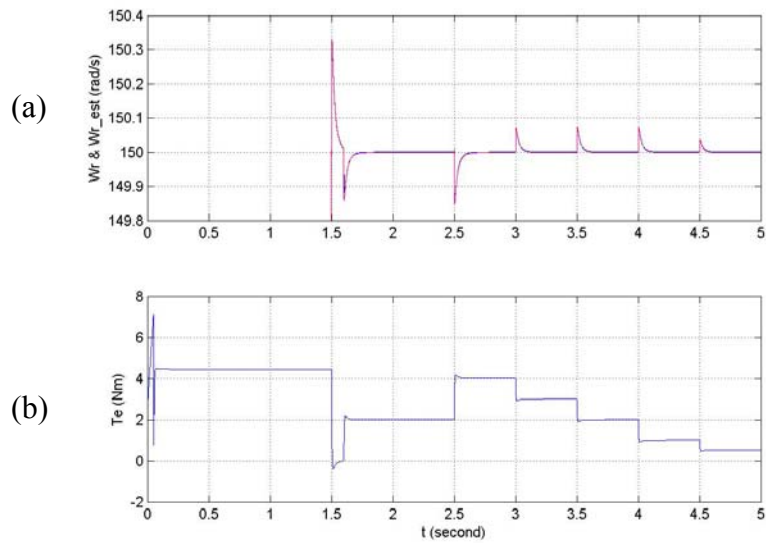


Figure 5.10 Actual / estimated rotor speed corresponding to load change. (a) Reference and estimated speeds; (b) electric torque.

5.7 Experimental Results

The proposed control scheme using natural variables and the modified rotor speed estimation have been implemented using TI DSP TMS320LF2407 EVM board. Figure 5.11 below shows the no-load speed response of the motor when it is ramped from zero speed to 820 rpm. While the reference speed tracks the actual closely, it is observed that the flux linkage is also changing and reducing as the steady-state no-load speed is approached which is what is observed in the simulation results. In Figure 5.12, reference speed is decreased and increased and the actual speed tracks it very well. Also observed is the fact that the rotor flux linkage changes with a change in the reference speed.

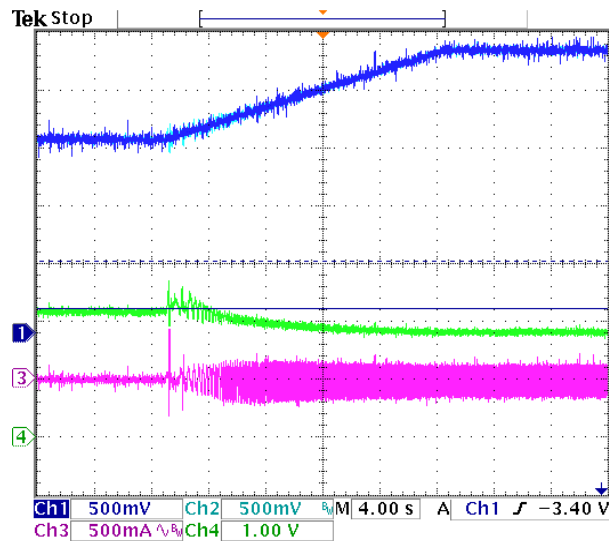


Figure 5.11 Speed regulation from zero to 900 rpm. Ch1: reference rotor speed (545rpm/div); Ch2: actual rotor speed (545rpm/div); Ch3: square of rotor flux linkage (0.1Wb²/div); Ch4: phase A current (6A/div).

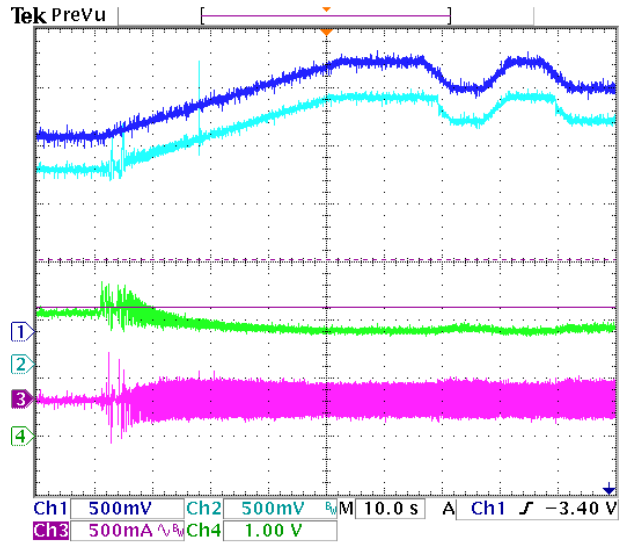


Figure 5.12 Speed regulation and loss minimization for changing rotor speed from zero to 900-600 rpm. Ch1: reference rotor speed (545rpm/div); Ch2: actual rotor speed (545rpm/div); Ch3: square of rotor flux linkage (0.1Wb²/div); Ch4: phase A current (6A/div).

In the experiments, the rotor speed is estimated using both rotor voltage equations and the actual speed measured from the absolute encoder is used as the feedback first to check whether the estimated rotor speed is close to the actual value. If they are very close, the estimated speed is then used as the feedback. The stator and rotor flux linkages are estimated using low pass filters with magnitude and phase error compensations illustrated in Chapter 4.

In the estimation of rotor flux linkages, the derivatives of the rotor flux linkages need to be calculated first. Generally the digital calculation of derivatives is not desired especially when the signals are AC signals. Since the rotor flux linkages are calculated from the stator flux linkages and the stator currents, one of the ways of getting better results is to use the measured quantities directly. Hence the derivatives of rotor flux

linkages can be expressed in terms of the stator voltages, stator currents and the derivatives of stator currents, which are expected to give better results since the stator currents are measured directly while the rotor fluxes are the estimated quantities using stator currents.

$$\begin{aligned} X &= \frac{L_r}{L_m} \cdot (V_{qs} - r_s I_{qs} - L_\sigma p I_{qs}) + \frac{r_r}{L_r} \lambda_{qr} - \frac{r_r L_m}{L_r} I_{qs} \\ Y &= -\frac{L_r}{L_m} \cdot (V_{ds} - r_s I_{ds} - L_\sigma p I_{ds}) - \frac{r_r}{L_r} \lambda_{dr} + \frac{r_r L_m}{L_r} I_{ds} \end{aligned} \quad (5.30)$$

And the derivatives of stator currents are calculated as

$$\begin{aligned} p I_{qs} &= \frac{I_{qs}(k+1) - I_{qs}(k)}{T_s} \\ p I_{ds} &= \frac{I_{ds}(k+1) - I_{ds}(k)}{T_s} \end{aligned} \quad (5.31)$$

where T_s is the sampling period, which is also the switching period in the DSP code. This method of calculating the derivatives of the stator currents is tested first by using the actual rotor speed measured from the absolute encoder. The actual rotor speed tracks the reference speed very well. But there are big spikes in the estimated rotor speed as shown in Figure 5.13 when the reference rotor speed is ramped up from 0 to 600rpm. This is the normal case when the derivatives are calculated using (5.31).

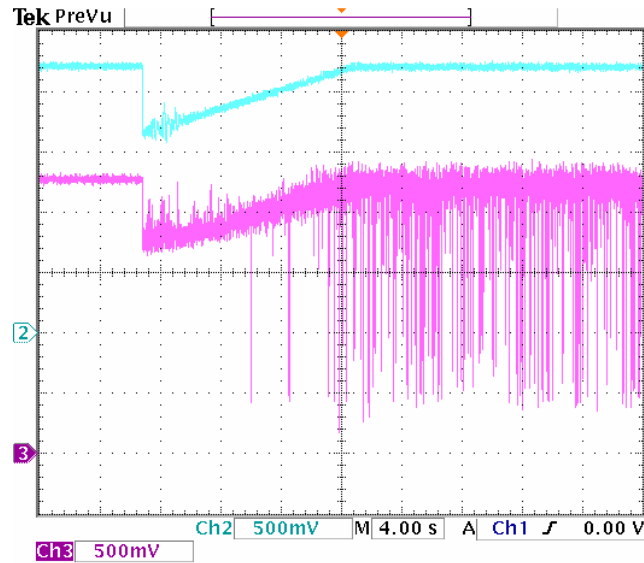


Figure 5.13 Actual rotor speed and estimated rotor speed (using actual speed as feedback). Ch2: actual rotor speed (545rpm/div); Ch3: estimated rotor speed (545rpm/div).

Then the estimation of the rotor speed without calculating the derivatives of the stator currents is tested to check if those spikes come from the calculation of derivatives. The speed waveforms are shown in Figure 5.14 when the actual rotor speed is used as the feedback also. It is seen that the estimated rotor speed has a much better waveform than the previous case. However, the steady state value is much lower than the reference rotor speed. In this particular case, the reference rotor speed is 600rpm and the actual rotor speed is 597rpm. But the estimated rotor speed is only 548 rpm, which means that the calculation of the derivatives of the stator currents cannot be neglected.

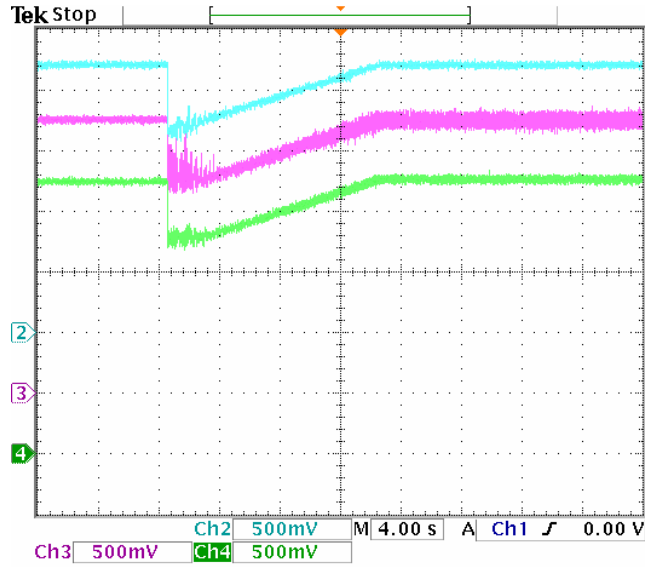


Figure 5.14 Actual rotor speed, estimated rotor speed and filtered estimated rotor speed (without calculating the derivatives, using actual speed as feedback). Ch2: actual rotor speed (545rpm/div); Ch3: estimated rotor speed (545rpm/div); Ch4: filtered estimated rotor speed (545rpm/div).

In order to avoid the spikes in the estimated rotor speed due the calculations of the derivatives of the stator currents, these derivatives are calculated every four sampling periods. By this way, the noise introduced by (5.30) can greatly reduced.

$$\begin{aligned}
 pI_{qs} &= \frac{I_{qs}(k) - I_{qs}(k-4)}{4 * T_s} \\
 pI_{ds} &= \frac{I_{ds}(k) - I_{ds}(k-4)}{4 * T_s}
 \end{aligned}
 \tag{5.32}$$

The speed waveforms are shown in Figure 5.15, in which the estimated speed is very close to the actual speed. At the steady state, the actual speed is 597rpm and the estimated one is 591rpm while the reference speed is 600rpm and the actual speed is used as the feedback.

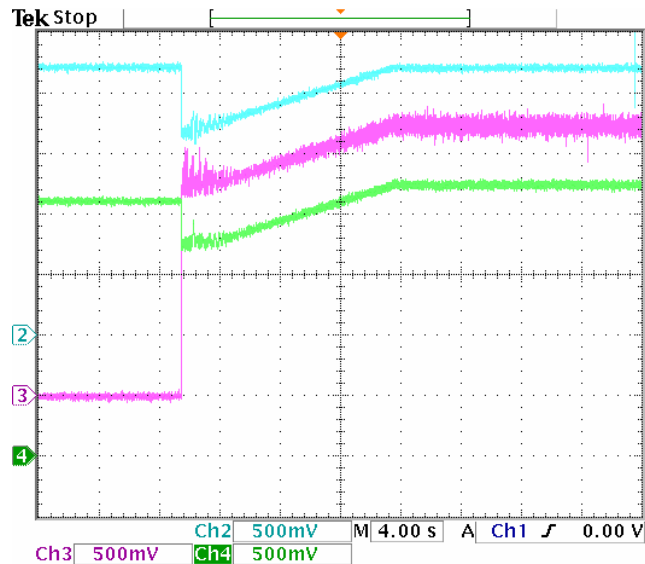


Figure 5.15 Actual rotor speed, estimated rotor speed and filtered estimated rotor speed (calculating the derivatives every 4 sampling period, using actual speed as feedback).

Ch2: actual rotor speed (545rpm/div); Ch3: estimated rotor speed (545rpm/div); Ch4: filtered estimated rotor speed (545rpm/div).

The next step is to use the estimated speed as the feedback signal. The speed waveforms are shown in Figure 5.16 for a constant speed reference and in Figure 5.17 for changing speed reference. It is seen that the estimated rotor speed is very close to the actual speed, which means that the rotor speed is estimated successfully. The only problem is that there are some oscillations in the estimated rotor speed and also in the actual rotor speed. This test is done at almost no-load condition. The waveforms are greatly improved when a light load is applied, as shown in Figure 5.18.

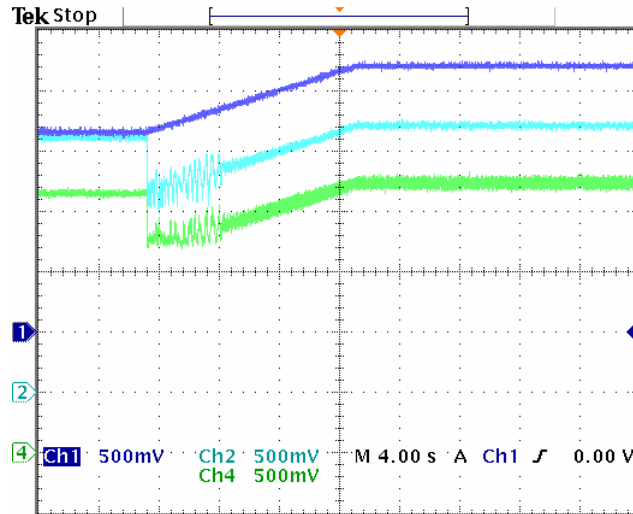


Figure 5.16 Reference rotor speed, actual rotor speed and estimated rotor speed (calculating the derivatives every 4 sampling period, using actual speed as feedback).
 Ch1: reference speed (545rpm/div); Ch2: measured speed (545rpm/div); Ch4: estimated speed (545rpm/div).

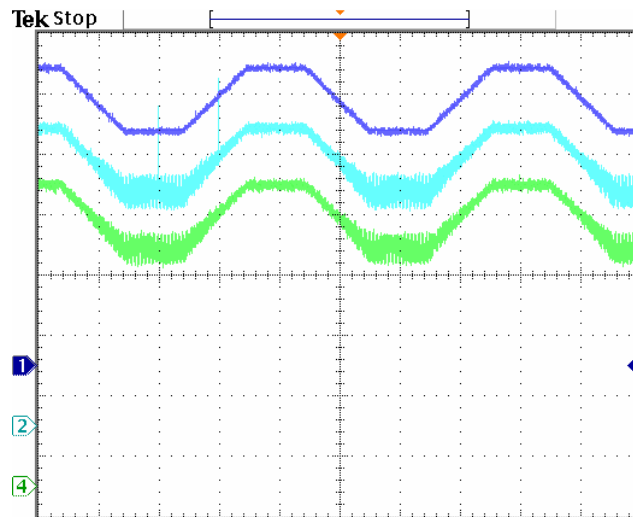


Figure 5.17 Reference rotor speed, actual rotor speed and estimated rotor speed (calculating the derivatives every 4 sampling period, using actual speed as feedback).
 Ch1: reference speed (545rpm/div); Ch2: measured speed (545rpm/div); Ch4: estimated speed (545rpm/div).

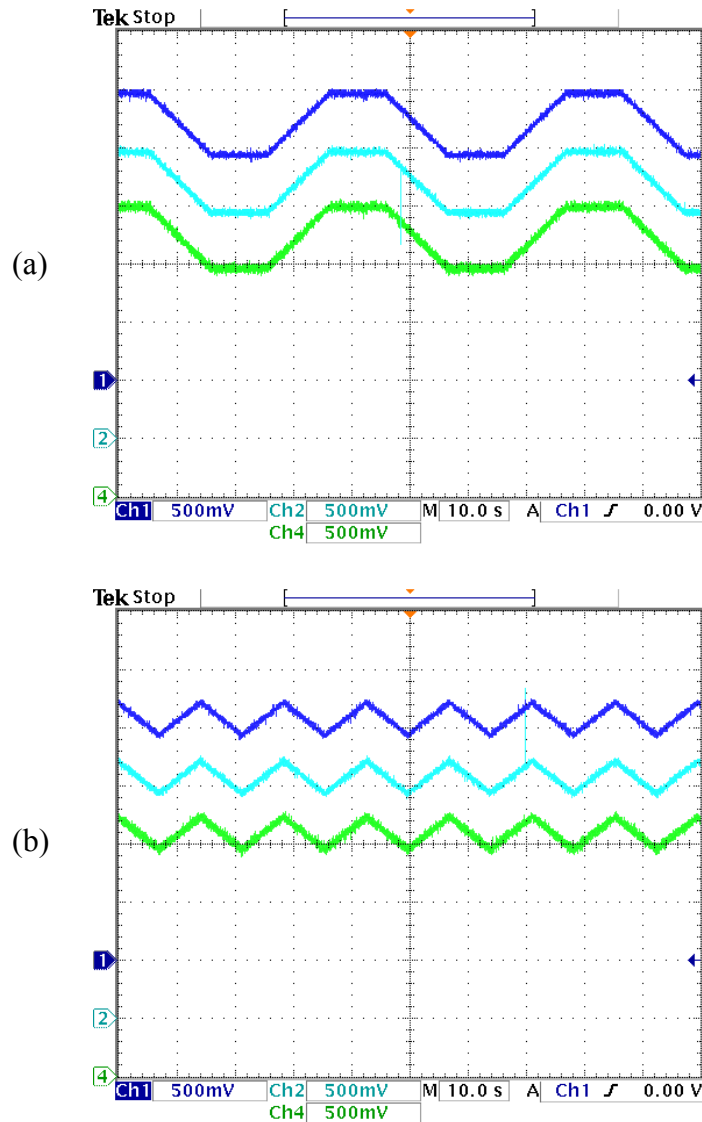


Figure 5.18 Experimental results for sensorless speed control. (a) 300 - 900rpm; (b) 300 - 600rpm. Ch1: reference speed (545rpm/div); Ch2: measured speed (545rpm/div); Ch4: estimated speed (545rpm/div).

Then the motor is driven to 600 rpm using the same speed estimation method. From the starting condition to steady-state speed, the rotor flux is set at rated condition after which the loss minimization algorithm is applied, which is shown in Figure 5.19. The reference speed tracks the actual speed closely and the magnitude square of flux linkage

reduces after the loss minimization algorithm kicks in. There is however an initial divergence between the actual and estimated speed at the starting condition when the rotor flux linkage is kept constant. Finally, Figure 5.20 displays the changing rotor flux linkage profile for the loaded motor under changing rotor speed condition. This graph succinctly demonstrates how the optimum rotor flux linkage command is changing which should consequently affect the loss in the machine – improving overall motor efficiency.

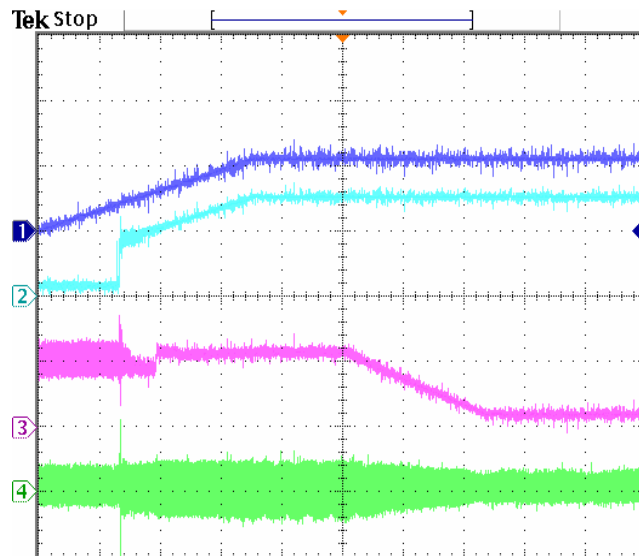


Figure 5.19 Speed regulation from zero to 600 rpm. Ch1: reference rotor speed (545rpm/div); Ch2: actual rotor speed (545rpm/div); Ch3: square of rotor flux linkage (0.1Wb²/div); Ch4: phase A current (6A/div).

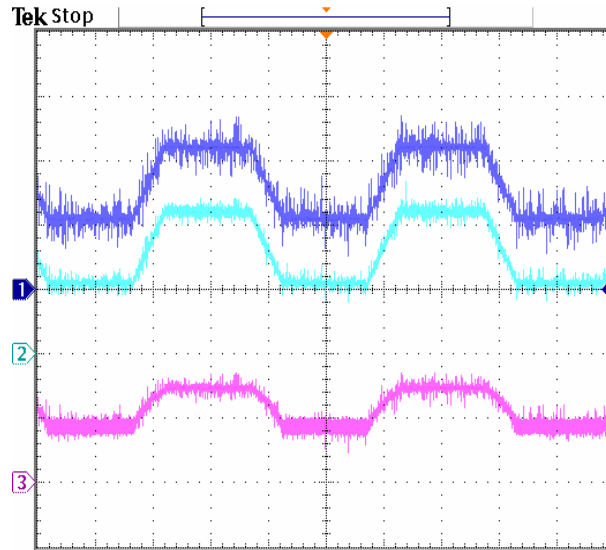


Figure 5.20 Speed regulation (300 – 600 rpm) showing rotor flux variation. Ch1: reference speed (273rpm/div); Ch2: estimated speed (273rpm/div); Ch3: rotor flux linkage (0.1Wb²/div).

5.8 Loss Minimization Using a Controller for the Loss Minimization Function

In the above analysis, the optimum rotor flux is calculated from the loss minimization function and then used in the control scheme. However, it is possible to regulate the loss minimization function directly and the loss is minimized when the function is regulated to be zero. The derivative of the loss minimization function is calculated as

$$p\gamma = -\frac{3}{2k_t^2} \frac{1}{\lambda_{rr}^2} \cdot (A + B) + C = \sigma_\gamma \quad (5.33)$$

where

$$\begin{aligned}
A &= \left[-\frac{r_s}{L_\sigma} + \left(2 - \frac{L_s}{L_\sigma} \right) \frac{r_r}{L_r} - \frac{r_r L_m}{k_t L_r} \frac{T_r}{\lambda_{rr}} \right] (T_e^2 + T_r^2) \\
B &= -\frac{k_t L_m}{L_\sigma L_r} \lambda_{rr} \left(\omega_r T_e - \frac{r_r}{L_r} T_r \right) + \frac{k_t}{k L_\sigma} (m_1 T_e + m_2 T_r) \\
C &= \frac{6kL_\sigma^2}{r_c L_m^2} \omega_e p \omega_r + \frac{3kL_m^2}{r_c L_r^2} \omega_r p \omega_r + \frac{3kL_\sigma}{r_c L_r} (\omega_e p \omega_r + \omega_r p \omega_e)
\end{aligned}$$

Differentiating (5.9) and substituting (5.6), the rotor speed dynamics is given as

$$p^2 \omega_r = K_\omega (\omega_r^* - \omega_r) = p T_e \quad (5.34)$$

A general controller K_ω such as the IP controller is assumed in (5.12) for the speed control loop and the corresponding transfer function is expressed in (5.35). The application of IP controller ensures that the denominator is Butterworth polynomial compliant and there is no zero in the numerator.

$$\frac{\omega_r}{\omega_r^*} = \frac{K_1}{p^2 + pK_1 + K_2} \quad (5.35)$$

Similarly, for the loss function loop, a controller K_γ such as the PI controller is used in (5.33) resulting in the following dynamics.

$$p\gamma = K_\gamma \cdot (\gamma - \gamma^*) = \sigma_\gamma \quad (5.36)$$

The corresponding transfer function is given as

$$\frac{\gamma}{\gamma^*} = \frac{K_3}{p^2 + pK_3 + K_4} \quad (5.37)$$

The schemes for the speed and loss minimization controllers are shown in shown in Figure 5.21.

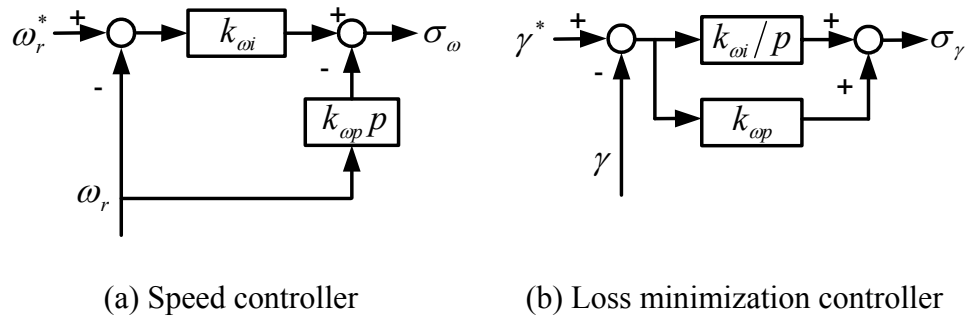


Figure 5.21 The structures of controllers.

The starred terms in (5.34-37) are the reference values which for γ^* is set to zero. The gain parameters of the PI and IP controllers are selected such that the denominator of the transfer functions of control variables are tuned to be Butterworth polynomial compliant also. Comparison of the coefficients of the denominators of the transfer function (5.35, 5.37) with (5.18) gives the gain parameters for the controllers for a chosen resonant frequency ω_0 .

Substituting (5.36) into (5.33) and (5.11) into (5.34), the resulting linear equations when solved gives m_1 and m_2 . From (5.16), the reference q-d voltages are determined and become the inputs to the space-vector implementation algorithm for the three-phase voltage source inverter driving the induction machine. Figure 5.22 schematically shows the overall block diagram for the drive system. The beauty of this control scheme is its simplicity. Only two controllers are necessary for the speed control and electrical loss minimization at the same time. However, the simulation of this control scheme is not successful. The reduction of controllers might be the reason, in which case the state variables are not regulated directly.

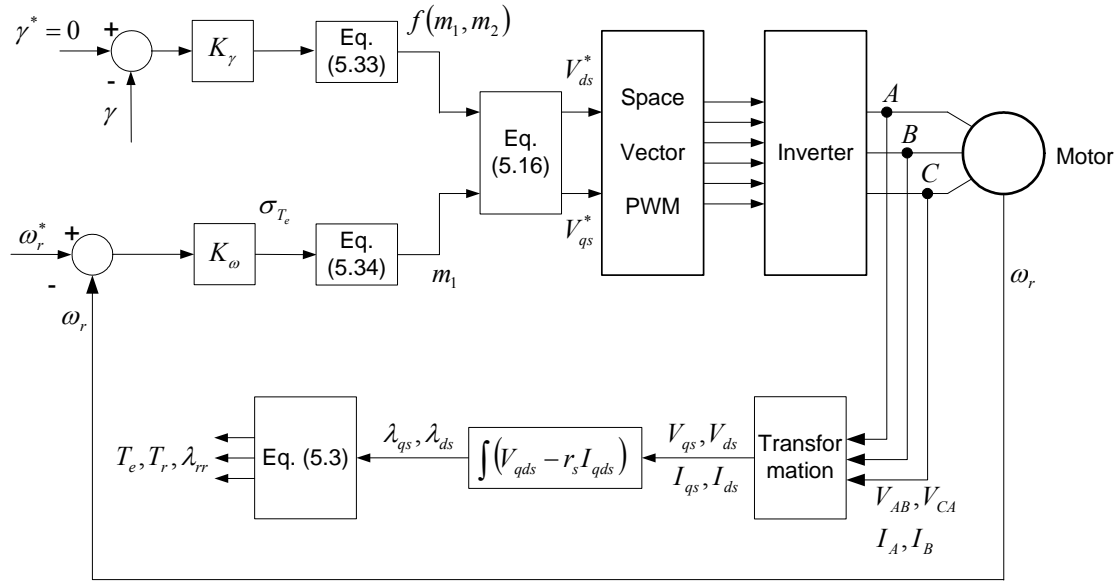


Figure 5.22 Schematic diagram of the control algorithm.

5.9 Conclusion

This chapter presents an approach of optimizing the efficiency of induction motor drives through minimizing the copper and core losses using geometric nonlinear control. This is made possible by a definition of a loss function which when regulated delivers minimum loss operation. The induction machine model accounts for the varying core loss resistance and saturation dependent magnetizing inductance by updating them as the stator flux linkage varies. In problem formulation, the model machine model uses natural and reference frame independent quantities as state variables. Utilization of the nonlinear geometric control methodology of input-output linearization with decoupling, permits the implementation of the control in the stationary reference frame. This approach eliminates the need of synchronous reference transformation and flux alignment required in classical vector control schemes. The new efficiency optimizing formulation yields a reference

rotor flux which ensures minimum loss and yields an improved efficiency of the drive system especially when driving part-load. The proposed control is validated by computer simulation and some experimental results on a 1 hp induction machine.

CHAPTER 6
SPEED ESTIMATION FOR INDUCTION MOTORS USING FULL-ORDER
FLUX OBSERVERS

6.1 Introduction

Induction motors have been studied for a long time since they were widely used in the industry. Speed control is quite common in most induction motor applications. Traditionally the speed information of an induction motor is measured or calculated using a rotor position or speed sensor. The research on the speed control of induction motors has been moving to the sensorless control, which eliminates the need of installing speed sensor in order to reduce the cost, or operate in special conditions.

Speed sensorless control is basically the algorithm of speed estimation that can infer the required measurement from other more easily available measurements like voltages and currents. The techniques that have been developed can be classified into three categories, which have been described in Chapter 1. The full-order observer system is an alternative method of the first category. It estimates the stator flux linkages or currents and rotor flux linkages using the voltages applied to the motor and measured currents. Then a particular error function can be chosen to estimate the rotor speed through some controllers. Since there are two sets of currents, one is the set of measured or actual currents and the other is the set of estimated currents, the torque equations corresponding to the active and reactive power are preferred. The adaptive mechanism is established when the rotor speed estimated from this error is used as the feedback. The estimated

rotor speed is equal to the actual speed when this error is minimized to be zero. Apparently this method is a closed-loop estimation, which is different from the flux estimation using the stator voltage equations.

From the review of the work on the full-order observers, some fundamental issues have not been adequately addressed including the selection of observer and the speed adaptation gains based on stability analysis. In this chapter, the full-order flux observer and the speed adaptive mechanism are defined. The model is used to estimate the flux linkages, stator currents and the rotor speed of an induction motor through an adaptive mechanism. The observer gains are chosen using Butterworth polynomials to ensure system stability. The transfer function between the estimated speed and actual speed is derived in the synchronous reference frame based on the error analysis, which are used to select appropriate PI controller parameters for the speed estimation that ensures operation in the stable region. The D-decomposition method is applied to determine the stable and unstable regions from the transfer function. The rotor flux oriented control including the observer and adaptive speed estimation are designed to examine the proposed methods. The controller parameters are determined from the corresponding transfer functions. The whole system is simulated in both motoring and regenerating modes. It is shown that all the controllers work properly and the rotor speed is regulated very well under different load conditions, which validate the proposed method of designing full-order flux observer and speed estimator.

6.2 Induction Machine Model

The analysis is based on the synchronous reference frame, the complex form is adopted for all quantities in q-d axis to simplify the analysis as

$$V_{qds} = V_{qs} + jV_{ds} \ , \ V_{qdr} = V_{qr} + jV_{dr}$$

$$I_{qds} = I_{qs} + jI_{ds} \ , \ I_{qdr} = I_{qr} + jI_{dr}$$

$$\lambda_{qds} = \lambda_{qs} + j\lambda_{ds} \ , \ \lambda_{qdr} = \lambda_{qr} + j\lambda_{dr}$$

The stator and rotor voltage equations of an induction machine are

$$V_{qds} = r_s I_{qds} + p\lambda_{qds} - j\omega_e \lambda_{qds} \tag{6.1}$$

$$V_{qdr} = r_r I_{qdr} + p\lambda_{qdr} - j(\omega_e - \omega_r)\lambda_{qdr} \tag{6.2}$$

The currents in the equations are substituted with the flux linkages to get the state equations in terms of the flux linkages using

$$\lambda_{qds} = L_s I_{qds} + L_m I_{qdr}$$

$$\lambda_{qdr} = L_r I_{qdr} + L_m I_{qds}$$

Define $L_\sigma = L_s - \frac{L_m^2}{L_r}$ and express the currents in terms of the flux linkages as

$$I_{qds} = \frac{1}{L_\sigma} \lambda_{qds} - \frac{L_m}{L_\sigma L_r} \lambda_{qdr} \tag{6.3}$$

$$I_{qdr} = -\frac{L_m}{L_\sigma L_r} \lambda_{qds} + \frac{L_s}{L_\sigma L_r} \lambda_{qdr} \tag{6.4}$$

Then the stator and rotor voltage equations can be rewritten as

$$V_{qds} = \frac{r_s}{L_\sigma} \lambda_{qds} - \frac{r_s L_m}{L_\sigma L_r} \lambda_{qdr} + p\lambda_{qds} - j\omega_e \lambda_{qds} \tag{6.5}$$

$$V_{qdr} = -\frac{r_r L_m}{L_\sigma L_r} \lambda_{qds} + -\frac{r_r L_s}{L_\sigma L_r} \lambda_{qdr} + p \lambda_{qdr} - j(\omega_e - \omega_r) \lambda_{qdr} \quad (6.6)$$

Rewrite these two equations in matrix form as ($V_{qdr} = 0$)

$$\begin{bmatrix} p \lambda_{qds} \\ p \lambda_{qdr} \end{bmatrix} = \begin{bmatrix} -\frac{r_s}{L_\sigma} + j\omega_e & \frac{r_s L_m}{L_\sigma L_r} \\ \frac{r_r L_m}{L_\sigma L_r} & -\frac{r_r L_s}{L_\sigma L_r} + j(\omega_e - \omega_r) \end{bmatrix} \begin{bmatrix} \lambda_{qds} \\ \lambda_{qdr} \end{bmatrix} + \begin{bmatrix} V_{qds} \\ 0 \end{bmatrix} \quad (6.7)$$

Using the stator and rotor flux linkages as the state variables,

$$X = \begin{bmatrix} \lambda_{qds} \\ \lambda_{qdr} \end{bmatrix}, \quad B = \begin{bmatrix} 1 & 0 \\ 0 & 1 \end{bmatrix}, \quad U = \begin{bmatrix} V_{qds} \\ 0 \end{bmatrix}$$

The state equations become

$$\dot{X} = A \cdot X + B \cdot U \quad (6.8)$$

where

$$A = \begin{bmatrix} -\frac{r_s}{L_\sigma} + j\omega_e & \frac{r_s L_m}{L_\sigma L_r} \\ \frac{r_r L_m}{L_\sigma L_r} & -\frac{r_r L_s}{L_\sigma L_r} + j(\omega_e - \omega_r) \end{bmatrix}. \quad (6.9)$$

The measured quantities are I_{qds} and the output equation is (6.3)

$$Y = C \cdot X \quad (6.10)$$

where,

$$C = \begin{bmatrix} 1 & -\frac{L_m}{L_\sigma L_r} \end{bmatrix}. \quad (6.11)$$

6.3 Full-order Flux Observer and Speed Estimation

The full-order flux observer is defined by (^ represents the estimated quantities).

$$\begin{aligned}\dot{\hat{X}} &= \hat{A} \cdot \hat{X} + B \cdot U + K \cdot (I_{qds} - \hat{I}_{qds}) \\ \hat{I}_{qds} &= \hat{C} \cdot \hat{X}\end{aligned}\quad (6.12)$$

Assuming all parameters are changing,

$$\hat{A} = \begin{bmatrix} -\frac{\hat{r}_s}{\hat{L}_\sigma} + j\omega_e & \frac{\hat{r}_s \hat{L}_m}{\hat{L}_\sigma \hat{L}_r} \\ \frac{\hat{r}_r \hat{L}_m}{\hat{L}_\sigma \hat{L}_r} & -\frac{\hat{r}_r \hat{L}_s}{\hat{L}_\sigma \hat{L}_r} + j(\omega_e - \hat{\omega}_r) \end{bmatrix}\quad (6.13)$$

$$\hat{C} = \begin{bmatrix} 1 & -\frac{\hat{L}_m}{\hat{L}_\sigma \hat{L}_r} \end{bmatrix}\quad (6.14)$$

The adaptation mechanism for the speed estimator is based on an error function chosen as (* represents the complex conjugate and $0 \leq k \leq 1$.)

$$\varepsilon = k \cdot \text{Im} \left[\hat{\lambda}_{qdr}^* \cdot (I_{qds} - \hat{I}_{qds}) \right] + (1-k) \cdot \text{Re} \left[\hat{\lambda}_{qdr}^* \cdot (I_{qds} - \hat{I}_{qds}) \right]\quad (6.15)$$

The former term of the error function is the change in the active torque and the second term is the change in the reactive torque. The variable k allows the weighting of the active and reactive torque changes in the error function.

When a general PI (Proportional-integration) controller is chosen to generate the speed estimation, the speed can be estimated from

$$\begin{aligned}\hat{\omega}_r &= K_\omega \cdot \varepsilon \\ &= K_{op} \cdot \varepsilon + K_{oi} \cdot \int \varepsilon dt\end{aligned}\quad (6.16)$$

6.4 Theory of MRAS (Model Reference Adaptive System)

MRAS has been shown to be very effective in estimating motor speed. Two independent observers need to be constructed to estimate the components of the rotor flux linkages in the stationary reference frame. One is from the stator voltage equations and the other one is from the rotor voltage equations. Since the stator voltage equations do not involve the rotor speed, this observer may be regarded as a reference model of the induction motor. The rotor voltage equations, which involve the rotor speed, may be regarded as an adjustable model. The errors between the states of these two models are then used to drive a suitable adaptation mechanism that generates the estimation of the rotor speed. It is shown that a successful MRAS design can yield the desired values with less computational error than an open-loop calculation and is often simpler to implement. The general structure of MRAS is shown in Figure 6.1.

In the paper by Colin Schauder [6.7], the speed identification using MRAS techniques is illustrated as an alternate way of calculating the motor speed. Two independent observers are constructed to estimate the components of the rotor flux vector: one based on the stator voltage equations and the other based on the rotor voltage equations. Since the stator voltage equations does not involve the quantity of rotor speed, this observer may be regarded as a reference model of the induction motor, and the rotor voltage equation, which does involve the rotor speed, may be regarded as an adjustable model. The error between the states of these two models is then used to drive a suitable adaptation mechanism that generates the estimated rotor speed for the adjustable model.

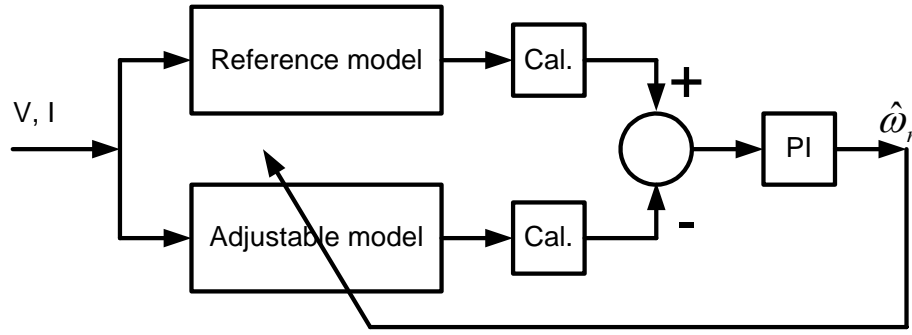


Figure 6.1 Structure of MRAS for speed estimation.

The design of an adaptation mechanism is analyzed by taking account of the overall stability of the system. The error function for the speed estimation is chosen based on Popov's criterion, which is the error between the products of q- and d-axis flux linkages from those two models. A general PI regulator is used for the speed adaptation mechanism. The dynamic response is studied through the system equations, linearized about a selected operating point in the synchronous reference frame. In general, the rotor speed is a variable and the models are linear time-varying systems. For the purpose of deriving an adaptation mechanism, however, it is valid to initially treat the rotor speed as a constant parameter of the reference model. Through the analysis of Popov's criterion for hyperstability, a candidate adaptation mechanism is chosen to satisfy it as

$$\hat{\omega}_r = \Phi_2([\varepsilon]) + \int_0^t \Phi_1([\varepsilon])d\tau \quad (6.17)$$

$$\Phi_1 = K_2(\varepsilon_q \hat{\lambda}_d - \varepsilon_d \hat{\lambda}_q) = K_2(\lambda_q \hat{\lambda}_d - \lambda_d \hat{\lambda}_q)$$

$$\Phi_2 = K_1(\varepsilon_q \hat{\lambda}_d - \varepsilon_d \hat{\lambda}_q) = K_1(\lambda_q \hat{\lambda}_d - \lambda_d \hat{\lambda}_q)$$

where ε_q and ε_d are the state (rotor flux linkage) errors.

The dynamic response of MRAS speed identification is analyzed through linearizing the equations for small deviations about a particular steady state solution. This is done after transforming the equations to a reference frame rotating synchronously with the stator current vector. Some extensions have been made by the use of auxiliary variables since the model outputs need not be the actual motor flux components but can be auxiliary variables related to them. In the former method, the rotor flux observer is difficult to implement due to the pure integration of sensed variables and this leads to problems with initial conditions and drift. The pure integration is then replaced by low pass filters, through insertion of an identical linear transfer matrix into both the reference and adjustable model.

In the paper by Fangzhen Peng, an MRAS scheme is proposed that does not require any integrator based on the defined quantity representing the instantaneous reactive power of the rotor flux linkages [6.2]. The counter-electromotive force (EMF) is used instead of the rotor flux vector, which was used in the conventional MRAS system. Two independent observers are configured to estimate the components of the counter-EMF vector, one based on the stator voltage equations and the other based on the rotor voltage equations. The observer model from the stator voltage equations is regarded as the reference model of the induction motor since the rotor speed is not involved explicitly and the observer model from the rotor voltage equations is regarded as the adjustable model. The error between the outputs of these two observers is then used to drive a suitable adaptation mechanism that generates the estimated rotor speed for the adjustable model.

For the adaptation mechanism of an MRAS, it is important to ensure that the system is stable and the estimated quantity converges to the actual value. The stability is analyzed using Popov's criterion by treating the rotor speed as a constant parameter. It is shown that the Popov's criterion is satisfied when a PI controller is applied to the difference between the cross product of estimated back-EMF and the difference between the actual and estimated back-EMF. The speed estimation is further simplified as the output of a PI controller into the cross product between the actual and estimated back-EMF. Since the reference model does not require pure integration, this system can achieve good performance even at low speed, as long as the value of the stator resistance is known precisely and instantaneously. Since the stator resistance varies with the temperature and the stator resistance, thermal variations affect the performance and stability of the MRAS speed estimator especially at low speeds. A speed identification scheme with a low sensitivity to the stator resistance variations is necessary for applications of low-speed drives. The cross product of the counter-EMF vector and the stator current vector, whose magnitude represents the instantaneous reactive power maintaining the magnetizing current is defined. Two such products are found from the counter-EMF and the difference between these two products is fed to a PI controller to estimate the rotor speed. It is evident that the speed estimation system is completely robust to the stator resistance other than requiring no integral calculation.

$$\hat{\omega}_r = \left(K_p + \frac{K_I}{p} \right) (\hat{e}_m \otimes e_m) \quad (6.18)$$

where \hat{e}_m and e_m are the counter-EMF vectors calculated from the adjustable and reference models.

In M. Rashed's paper [6.13], a stable back-EMF MRAS-based speed estimator is proposed, in which the error signal is equal to the sum of two component error signals. The first component error signal is the modulus of the cross product of the estimated rotor flux vector and the error in the estimated back-EMF voltage vector, while the second component error signal is the dot product of the same quantities. The error signal is given by (6.19), in which Δe_s is the back-EMF error vector.

$$\begin{aligned}\varepsilon_{\omega_r} &= |\lambda_r \times \Delta e_s| + k_{\omega_r} \lambda_r \cdot \Delta e_s \\ \hat{\omega}_r &= k_{p\omega} \varepsilon_{\omega_r} + \int k_{i\omega} \varepsilon_{\omega_r} dt\end{aligned}\tag{6.19}$$

The motivation for including both the cross and scalar products of the back-EMF error vector and the estimated rotor flux vector is that the error signal ε_{ω_r} may become zero irrespective to the magnitude of the back-EMF error vector if only the cross product is used. This condition can arise when the back-EMF error vector is aligned with the rotor flux vector. However, under such conditions the scalar product of back-EMF error vector and the rotor flux vector is nonzero. By incorporating both the cross and scalar products a nonzero error signal can be obtained in all operating modes. The design gain k_{ω_r} is introduced to ensure stable operation. The stable MRAS stator resistance estimator is also proposed as in (6.13). The cross product term represents the difference between the measured and the estimated airgap reactive power and the dot-product term represents the difference in the airgap active power.

$$\begin{aligned}\varepsilon_{R_s} &= i_s \cdot \Delta e_s + k_{R_s} |i_s \times \Delta e_s| \\ \hat{R}_s &= k_{pR_s} \varepsilon_{R_s} + \int k_{iR_s} \varepsilon_{R_s} dt\end{aligned}\tag{6.20}$$

6.5 State Error Analysis and Transfer Function for Speed Estimation

The error between the measured and estimated states is needed to obtain the transfer function for the speed estimation. The error is defined as

$$e = X - \hat{X} \quad (6.21)$$

$$\begin{aligned} \dot{e} &= \dot{X} - \dot{\hat{X}} \\ &= (A - K \cdot C) \cdot X - (\hat{A} - K \cdot \hat{C}) \cdot \hat{X} \\ &= (A - K \cdot C) \cdot e - (\Delta A - K \cdot \Delta C) \cdot \hat{X} \end{aligned} \quad (6.22)$$

where

$$\Delta A = A - \hat{A}, \quad \Delta C = C - \hat{C},$$

$$\Delta A = \underbrace{\begin{bmatrix} -\frac{r_s}{L_\sigma} - \left(-\frac{\hat{r}_s}{\hat{L}_\sigma} \right) & \frac{r_s L_m}{L_\sigma L_r} - \frac{\hat{r}_s \hat{L}_m}{\hat{L}_\sigma \hat{L}_r} \\ \frac{r_r L_m}{L_\sigma L_r} - \frac{\hat{r}_r \hat{L}_m}{\hat{L}_\sigma \hat{L}_r} & -\frac{r_r L_s}{L_\sigma L_r} - \left(-\frac{\hat{r}_r \hat{L}_s}{\hat{L}_\sigma \hat{L}_r} \right) \end{bmatrix}}_{\gamma_1} - \begin{bmatrix} 0 & 0 \\ 0 & j(\omega_r - \hat{\omega}_r) \end{bmatrix},$$

$$\Delta C = \begin{bmatrix} \frac{1}{L_\sigma} - \frac{1}{\hat{L}_\sigma} & -\frac{L_m}{L_\sigma L_r} - \left(-\frac{\hat{L}_m}{\hat{L}_\sigma \hat{L}_r} \right) \end{bmatrix}.$$

The derivative of the state error can be expressed in the form of two components: one without speed information and the other with speed information.

$$\dot{e} = (A - K \cdot C) \cdot e + \underbrace{\gamma \cdot \hat{X}}_{\underbrace{\begin{bmatrix} 0 \\ j\lambda_{qdr} \end{bmatrix}}_Z} - (\Delta A - K \cdot \Delta C) \cdot \hat{X} \quad (6.23)$$

where $\gamma = \gamma_1 - K \cdot \Delta C$.

The state error is solved as

$$e = [p \cdot I - A + K \cdot C]^{-1} \cdot [\gamma \cdot \hat{X} - Z \cdot (\omega_r - \hat{\omega}_r)] \quad (6.24)$$

Then the output error can be expressed in terms of speed information and states.

$$\begin{aligned} Y - \hat{Y} &= I_{qds} - \hat{I}_{qds} \\ &= C \cdot X - \hat{C} \cdot \hat{X} \\ &= (C - \Delta C) \cdot e + \Delta C \cdot X \\ &= (C - \Delta C) \cdot [p \cdot I - A + K \cdot C]^{-1} [\gamma \cdot \hat{X} - Z \cdot (\omega_r - \hat{\omega}_r)] + \Delta C \cdot X \end{aligned} \quad (6.25)$$

The speed is estimated using (6.16) and (6.25).

$$\begin{aligned} \hat{\omega}_r &= K_\omega \cdot \left\{ k \cdot \text{Im} \left[\hat{\lambda}_{qdr}^* \cdot (I_{qds} - \hat{I}_{qds}) \right] + (1-k) \cdot \text{Re} \left[\hat{\lambda}_{qdr}^* \cdot (I_{qds} - \hat{I}_{qds}) \right] \right\} \\ &= K_\omega \cdot k \cdot \text{Im} \left\{ \hat{\lambda}_{qdr}^* \cdot (C - \Delta C) \cdot [p \cdot I - A + K \cdot C]^{-1} [\gamma \cdot \hat{X} - Z \cdot (\omega_r - \hat{\omega}_r)] + \hat{\lambda}_{qdr}^* \cdot \Delta C \cdot X \right\} \\ &\quad + K_\omega \cdot (1-k) \cdot \text{Re} \left\{ \hat{\lambda}_{qdr}^* \cdot (C - \Delta C) \cdot [p \cdot I - A + K \cdot C]^{-1} [\gamma \cdot \hat{X} - Z \cdot (\omega_r - \hat{\omega}_r)] + \hat{\lambda}_{qdr}^* \cdot \Delta C \cdot X \right\} \end{aligned} \quad (6.26)$$

To simplify the analysis, assume the parameters are constant, which means $\Delta C = 0$ and $\gamma = 0$. Then the speed estimation is simplified as

$$\begin{aligned} \hat{\omega}_r &= -K_\omega \cdot \left\{ k \cdot \text{Im} \left[\hat{\lambda}_{qdr}^* \cdot (I_{qds} - \hat{I}_{qds}) \right] + (1-k) \cdot \text{Re} \left[\hat{\lambda}_{qdr}^* \cdot (I_{qds} - \hat{I}_{qds}) \right] \right\} \\ &= -K_\omega \cdot k \cdot \text{Im} \left\{ \hat{\lambda}_{qdr}^* \cdot C \cdot [p \cdot I - A + K \cdot C]^{-1} Z \cdot (\omega_r - \hat{\omega}_r) \right\} \\ &\quad - K_\omega \cdot (1-k) \cdot \text{Re} \left\{ \hat{\lambda}_{qdr}^* \cdot C \cdot [p \cdot I - A + K \cdot C]^{-1} Z \cdot (\omega_r - \hat{\omega}_r) \right\} \end{aligned} \quad (6.27)$$

Assuming $[p \cdot I - A + K \cdot C]$ has the form

$$[p \cdot I - A + K \cdot C] = \begin{bmatrix} P_{11} & P_{12} \\ P_{21} & P_{22} \end{bmatrix}$$

Then

$$T = -\left|\hat{\lambda}_{qdr}\right|^2 \cdot (\omega_r - \hat{\omega}_r) \cdot \frac{L_m}{L_\sigma L_r} \cdot j \cdot \frac{p - j\omega}{P_{11}P_{22} - P_{12}P_{21}}$$

Define $K = \begin{bmatrix} K_{11} + jK_{12} \\ K_{21} + jK_{22} \end{bmatrix}$ and $T_1 = P_{11}P_{22} - P_{12}P_{21} = t_1 + jt_2$. Then

$$\begin{aligned} t_1 &= -\frac{r_s r_r L_m^2}{L_\sigma^2 L_r^2} - \omega_e^2 - \frac{K_{11} r_r L_m^2}{L_\sigma^2 L_r^2} + p^2 + \frac{r_s}{L_\sigma} p + \frac{K_{11}}{L_\sigma} p + \frac{r_s r_r L_s}{L_\sigma^2 L_r} + \frac{K_{11} r_r L_s}{L_\sigma^2 L_r} + \\ &\quad \omega_e \omega_r + \frac{K_{12} \omega_e}{L_\sigma} - \frac{K_{12} \omega_r}{L_\sigma} + \frac{r_r L_s}{L_\sigma L_r} p - \frac{K_{21} L_m}{L_\sigma L_r} p - \frac{K_{22} \omega_e L_m}{L_\sigma L_r} \quad , \\ &= p^2 + t_{12} p + t_{13} \end{aligned}$$

$$\begin{aligned} t_2 &= -2\omega_e p + \omega_r p + \frac{K_{12}}{L_\sigma} p - \frac{r_s \omega_e}{L_\sigma} + \frac{r_s \omega_r}{L_\sigma} - \frac{K_{11} \omega_e}{L_\sigma} + \frac{K_{11} \omega_r}{L_\sigma} + \frac{K_{12} r_r L_s}{L_\sigma^2 L_r} - \\ &\quad \frac{K_{22} L_m}{L_\sigma L_r} p - \frac{r_r \omega_e L_s}{L_\sigma L_r} + \frac{K_{21} \omega_e L_m}{L_\sigma L_r} - \frac{K_{12} r_r L_m^2}{L_\sigma^2 L_r^2} \quad , \\ &= t_{22} p + t_{23} \end{aligned}$$

and

$$T = -\left|\hat{\lambda}_{qdr}\right|^2 \cdot (\omega_r - \hat{\omega}_r) \cdot \frac{L_m}{L_\sigma L_r} \cdot \frac{(\omega_e t_1 + p t_2) + j(p t_1 - \omega_e t_2)}{t_1^2 + t_2^2}.$$

So

$$\text{Im}(T) = -\left|\hat{\lambda}_{qdr}\right|^2 \cdot (\omega_r - \hat{\omega}_r) \cdot \frac{L_m}{L_\sigma L_r} \cdot \frac{p t_1 - \omega_e t_2}{t_1^2 + t_2^2}$$

$$\text{Re}(T) = -\left|\hat{\lambda}_{qdr}\right|^2 \cdot (\omega_r - \hat{\omega}_r) \cdot \frac{L_m}{L_\sigma L_r} \cdot \frac{p t_2 + \omega_e t_1}{t_1^2 + t_2^2}$$

Define

$$G_1(p) = \left|\hat{\lambda}_{qdr}\right|^2 \cdot (\omega_r - \hat{\omega}_r) \cdot \frac{L_m}{L_\sigma L_r} \cdot \frac{p t_1 - \omega_e t_2}{t_1^2 + t_2^2}$$

$$G_2(p) = \left| \hat{\lambda}_{qdr} \right|^2 \cdot (\omega_r - \hat{\omega}_r) \cdot \frac{L_m}{L_\sigma L_r} \cdot \frac{pt_2 + \omega_e t_1}{t_1^2 + t_2^2}$$

Then

$$\hat{\omega}_r = -K_\omega \cdot [k \cdot G_1(p) + (1-k) \cdot G_2(p)] \cdot (\omega_r - \hat{\omega}_r) \quad (6.28)$$

Define $G(p) = k \cdot G_1(p) + (1-k) \cdot G_2(p)$, then the transfer function between the estimated speed and the actual speed is

$$\frac{\hat{\omega}_r}{\omega_r} = \frac{K_\omega \cdot G(p)}{1 + K_\omega \cdot G(p)} \quad (6.29)$$

where

$$G(p) = K_G \cdot \frac{a_3 p^3 + a_2 p^2 + a_1 p + a_0}{p^4 + b_3 p^3 + b_2 p^2 + b_1 p + b_0} \quad (6.30)$$

$$\begin{aligned} a_3 &= k, & b_3 &= 2t_{12}, \\ a_2 &= kt_{12} + (1-k)(t_{22} + \omega_e), & b_2 &= t_{12}^2 + 2t_{13} + t_{22}^2, \\ a_1 &= k(t_{13} - \omega_e t_{22}) + (1-k)(t_{23} + \omega_e t_{12}), & b_1 &= 2t_{12}t_{13} + 2t_{22}t_{23}, \\ a_0 &= -k\omega_e t_{23} + (1-k)\omega_e t_{13}, & b_0 &= t_{13}^2 + t_{23}^2, \end{aligned}$$

$$K_G = \left| \hat{\lambda}_{qdr} \right|^2 \cdot \frac{L_m}{L_\sigma L_r}.$$

Assuming the controller is a general PI controller, the transfer function is

$$\frac{\hat{\omega}_r}{\omega_r} = \frac{\left(K_{op} + \frac{K_{oi}}{p} \right) \cdot G(p)}{1 + \left(K_{op} + \frac{K_{oi}}{p} \right) \cdot G(p)} = \frac{A_4 p^4 + A_3 p^3 + A_2 p^2 + A_1 p + A_0}{p^5 + B_4 p^4 + B_3 p^3 + B_2 p^2 + B_1 p + B_0} \quad (6.31)$$

where,

$$\begin{aligned}
A_4 &= a_3 K_{op} \cdot K_G & B_4 &= b_3 + a_3 K_{op} \cdot K_G \\
A_3 &= (a_3 K_{oi} + a_2 K_{op}) \cdot K_G & B_3 &= b_2 + (a_3 K_{oi} + a_2 K_{op}) \cdot K_G \\
A_2 &= (a_2 K_{oi} + a_1 K_{op}) \cdot K_G & \text{and } B_2 &= b_1 + (a_2 K_{oi} + a_1 K_{op}) \cdot K_G \quad . \quad (6.32) \\
A_1 &= (a_1 K_{oi} + a_0 K_{op}) \cdot K_G & B_1 &= b_0 + (a_1 K_{oi} + a_0 K_{op}) \cdot K_G \\
A_0 &= a_0 K_{oi} \cdot K_G & B_0 &= a_0 K_{oi} \cdot K_G
\end{aligned}$$

When $k = 1$, the analysis can be simplified as follows.

$$\hat{\omega}_r = K_\omega \cdot \text{Im} \left[\hat{\lambda}_{qdr}^* \cdot (I_{qds} - \hat{I}_{qds}) \right] \quad (6.33)$$

The speed estimation is simplified assuming the parameters are constant, i.e.

$\Delta C = 0$ and $\gamma = 0$.

$$\hat{\omega}_r = -K_\omega \cdot \text{Im} \left\{ \hat{\lambda}_{qdr}^* \cdot C \cdot [p \cdot I - A + K \cdot C]^{-1} Z \cdot (\omega_r - \hat{\omega}_r) \right\} \quad (6.34)$$

And

$$\hat{\omega}_r = -K_\omega \cdot G_1(p) \cdot (\omega_r - \hat{\omega}_r)$$

where $G_1(p) = K_G \cdot \frac{p^3 + a_2 p^2 + a_1 p + a_0}{p^4 + b_3 p^3 + b_2 p^2 + b_1 p + b_0}$, and the transfer function between the

estimated speed and the actual speed is

$$\frac{\hat{\omega}_r}{\omega_r} = \frac{K_\omega \cdot G_1(p)}{1 + K_\omega \cdot G_1(p)} \quad (6.35)$$

Assuming the controller is a general PI controller, the transfer function is

$$\frac{\hat{\omega}_r}{\omega_r} = \frac{\left(K_{op} + \frac{K_{oi}}{p} \right) \cdot G_1(p)}{1 + \left(K_{op} + \frac{K_{oi}}{p} \right) \cdot G_1(p)} = \frac{A(p)}{B(p)} \quad (6.36)$$

where,

$$A(p) = A_4 p^4 + A_3 p^3 + A_2 p^2 + A_1 p + A_0,$$

$$B(p) = p^5 + B_4 p^4 + B_3 p^3 + B_2 p^2 + B_1 p + B_0,$$

$$\begin{aligned}
A_4 &= K_{op} \cdot K_G & B_4 &= b_3 + K_{op} \cdot K_G \\
A_3 &= (K_{oi} + a_2 K_{op}) \cdot K_G & B_3 &= b_2 + (K_{oi} + a_2 K_{op}) \cdot K_G \\
A_2 &= (a_2 K_{oi} + a_1 K_{op}) \cdot K_G & \text{and } B_2 &= b_1 + (a_2 K_{oi} + a_1 K_{op}) \cdot K_G \quad . \quad (6.37) \\
A_1 &= (a_1 K_{oi} + a_0 K_{op}) \cdot K_G & B_1 &= b_0 + (a_1 K_{oi} + a_0 K_{op}) \cdot K_G \\
A_0 &= a_0 K_{oi} \cdot K_G & B_0 &= a_0 K_{oi} \cdot K_G
\end{aligned}$$

The above analysis is based on the assumption that the estimated speed is almost identical to the actual speed. However, this is not always true. The transfer function between the actual speed and the reference speed can be derived depending on the speed controller. The dynamics of the speed controller is given by

$$p^2 \omega_r = \sigma_\omega = K_\omega \cdot (\omega_r^* - \hat{\omega}_r) \quad (6.38)$$

Substituting for $\hat{\omega}_r$ from (6.34), (6.37) results.

$$\frac{\omega_r}{\omega_r^*} = \frac{K_\omega B(p)}{p^2 B(p) + K_\omega A(p)} \quad (6.39)$$

6.6 Observer Gain Selection

There are multiple choices for the observer gain (K_{11} , K_{12} , K_{21} , and K_{22}). Here, the 4th order Butterworth polynomial is applied. The idea of using the Butterworth polynomial is to locate the poles of the transfer function evenly in the left half s-plane. The locations of poles are shown in Figure 6.2. Since the complex form is used in the formulation, only two solutions can be found. However the complex conjugates of these two solutions yield the remaining two poles according to Figure 6.2 [6.9]. The four poles are given as

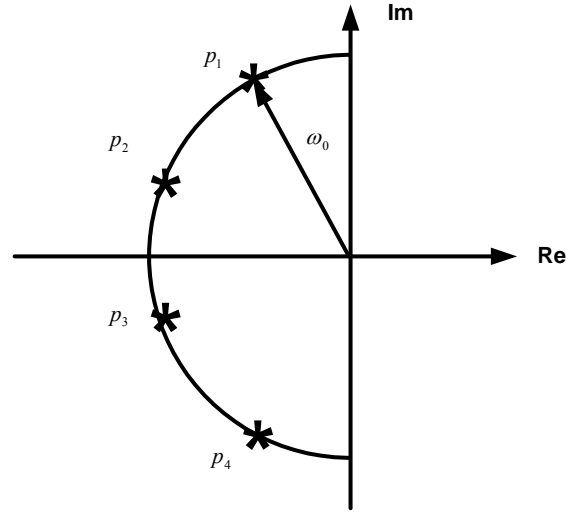


Figure 6.2 Poles location for 4th Butterworth polynomial.

$$p_1 = \omega_0 \cdot e^{j\frac{5\pi}{8}}, p_2 = \omega_0 \cdot e^{j\frac{7\pi}{8}}, p_3 = \omega_0 \cdot e^{j\frac{9\pi}{8}}, p_4 = \omega_0 \cdot e^{j\frac{11\pi}{8}}. \quad (6.40)$$

The first two poles are used to construct the quadratic form, which is compared with the characteristic equations of the observer model.

$$(p - p_1)(p - p_2) = p^2 + \omega_0(1.3066 - j1.3066) \cdot p - j \cdot \omega_0^2 \quad (6.41)$$

The poles of the observer system can be calculated from the state equations.

$$|p \cdot I - A + K \cdot C| = p^2 + b \cdot p + c = 0 \quad (6.42)$$

$$p_{1,2} = \frac{-b \pm \sqrt{b^2 - 4c}}{2}$$

where

$$b = \frac{r_s}{L_\sigma} + \frac{r_r L_s}{L_\sigma L_r} - j(2\omega_e - \omega_r) + \frac{1}{L_\sigma} (K_{11} + jK_{12}) - \frac{L_m}{L_\sigma L_r} (K_{21} + jK_{22}),$$

$$c = \frac{r_s r_r}{L_\sigma L_r} + \frac{r_r (K_{11} + jK_{12})}{L_\sigma L_r} - j(\omega_e - \omega_r) \frac{r_s}{L_\sigma} - j\omega_e \frac{r_r L_s}{L_\sigma L_r} - \omega_e (\omega_e - \omega_r) + j\omega_e \frac{L_m (K_{21} + jK_{22})}{L_\sigma L_r} - j(\omega_e - \omega_r) \frac{K_{11} + jK_{12}}{L_\sigma}$$

To ensure that the poles of the observer model are located according to the Butterworth polynomial, the coefficients from (6.38) and (6.39) should be the same, i.e.

$$\begin{aligned} \frac{r_s}{L_\sigma} + \frac{r_r L_s}{L_\sigma L_r} + \frac{K_{11}}{L_\sigma} - \frac{L_m K_{21}}{L_\sigma L_r} &= 1.3066 \cdot \omega_0 \\ (2\omega_e - \omega_r) + \frac{K_{12}}{L_\sigma} - \frac{L_m K_{22}}{L_\sigma L_r} &= 1.3066 \cdot \omega_0 \end{aligned} \quad (6.43)$$

$$\begin{aligned} \frac{r_s r_r}{L_\sigma L_r} + \frac{r_r K_{11}}{L_\sigma L_r} - \omega_e (\omega_e - \omega_r) - \frac{\omega_e L_m K_{22}}{L_\sigma L_r} + \frac{(\omega_e - \omega_r) K_{12}}{L_\sigma} &= 0 \\ -\frac{r_r K_{12}}{L_\sigma L_r} + \frac{(\omega_e - \omega_r) r_s}{L_\sigma} + \frac{\omega_e r_r L_s}{L_\sigma L_r} - \frac{\omega_e L_m K_{21}}{L_\sigma L_r} + \frac{(\omega_e - \omega_r) K_{11}}{L_\sigma} &= \omega_0^2 \end{aligned} \quad (6.44)$$

Thus the four observer gains can be determined by choosing appropriate ω_0 as follows.

$$K_{11} = \frac{1}{\frac{r_r^2}{L_r^2} + \omega_r^2} \cdot \left[\left(\frac{r_r}{L_r} + \omega_r \right) \cdot 1.3066 \cdot \omega_e L_\sigma \omega_0 - \omega_e^2 \frac{r_r L_\sigma}{L_r} - \omega_r L_\sigma \omega_0^2 \right] - r_s \quad (6.45)$$

$$K_{12} = \frac{1}{\frac{r_r^2}{L_r^2} + \omega_r^2} \cdot \left[\left(\frac{r_r}{L_r} - \omega_r \right) \cdot 1.3066 \cdot \omega_e L_\sigma \omega_0 + \omega_e^2 \omega_r L_\sigma - \frac{r_r L_\sigma}{L_r} \omega_0^2 \right] \quad (6.46)$$

$$\begin{aligned} K_{21} &= \frac{L_r}{L_m} \cdot \frac{1}{\frac{r_r^2}{L_r^2} + \omega_r^2} \cdot \left[\left(\frac{r_r}{L_r} + \omega_r \right) \cdot 1.3066 \cdot \omega_e L_\sigma \omega_0 - \omega_e^2 \frac{r_r L_\sigma}{L_r} - \omega_r L_\sigma \omega_0^2 \right] \\ &\quad - 1.3066 \cdot \frac{L_\sigma L_r}{L_m} \omega_0 + \frac{L_s}{L_m} r_r \end{aligned} \quad (6.47)$$

$$\begin{aligned}
K_{22} = & \frac{\frac{L_r}{L_m}}{\frac{r_r^2}{L_r^2} + \omega_r^2} \cdot \left[\left(\frac{r_r}{L_r} - \omega_r \right) \cdot 1.3066 \cdot \omega_e L_\sigma \omega_0 + \omega_e^2 \omega_r L_\sigma - \frac{r_r L_\sigma}{L_r} \omega_0^2 \right] \\
& + 1.3066 \cdot \frac{L_\sigma L_r}{L_m} \omega_0 - (2\omega_e - \omega_r) \frac{L_\sigma L_r}{L_m}
\end{aligned} \tag{6.48}$$

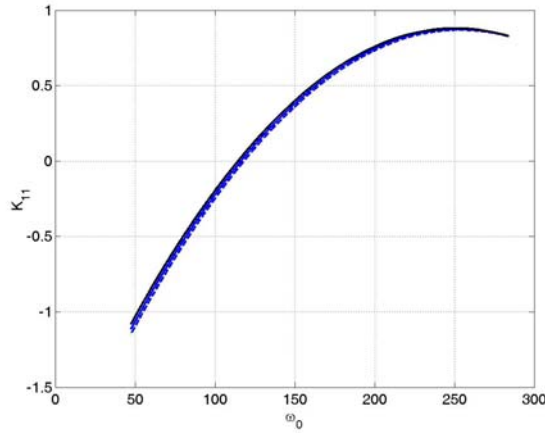
Theoretically a bigger value of ω_0 will give better system response. In this case, the value of ω_0 is determined from the poles of the open-loop machine model. Those poles can be calculated from the characteristic equation (6.49). The poles are given in [6.15]. When ω_0 is taken as the sum of the imaginary parts of the poles, the expression for ω_0 is shown in (6.50).

$$\begin{aligned}
p^2 + \left[\frac{r_s}{L_\sigma} + \frac{r_r L_s}{L_\sigma L_r} - j(2\omega_e - \omega_r) \right] \cdot p \\
+ \left[\frac{r_s r_r}{L_\sigma L_r} - \omega_e (\omega_e - \omega_r) - j(\omega_e - \omega_r) \frac{r_s}{L_\sigma} - j\omega_e \frac{r_r L_s}{L_\sigma L_r} \right] = 0
\end{aligned} \tag{6.49}$$

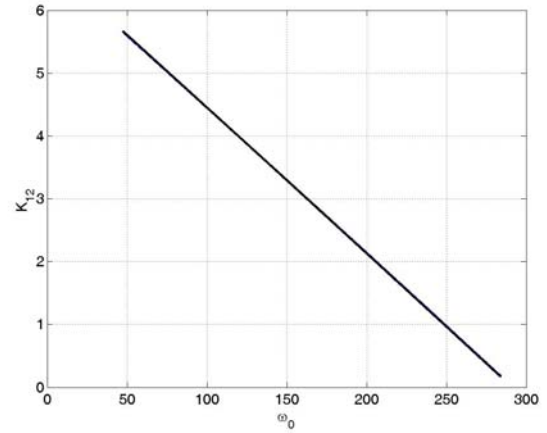
$$p_1 + p_2 = - \left(\frac{r_s}{L_\sigma} + \frac{r_r L_s}{L_\sigma L_r} \right) + j(2\omega_e - \omega_r)$$

$$\hat{\omega}_{00} = \frac{1}{2} \cdot \text{Im}(p_1 + p_2) = \frac{1}{2} \cdot (2\omega_e - \omega_r) \tag{6.50}$$

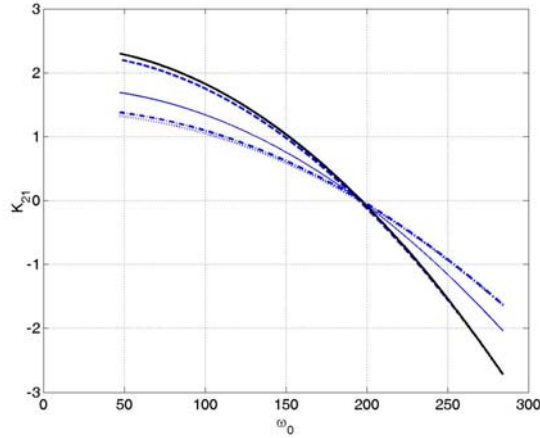
The relationship between the observer gains and ω_0 is shown in Figure 6.3 for the motoring mode and Figure 6.4 for the generating mode. The range of changing ω_0 is between $\hat{\omega}_{00}/4$ and $6\hat{\omega}_{00}/4$ while L_m and r_r change. It is seen that the parameters change does not have much effect on K_{11} and K_{12} . However, K_{21} and K_{22} are more likely to be affected.



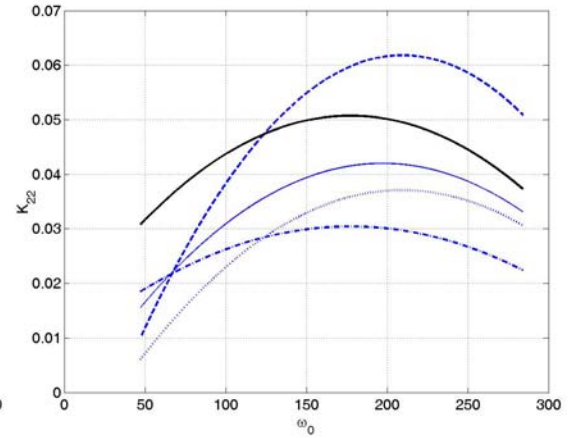
(a)



(b)



(c)



(d)

Figure 6.3 $K_{11}, K_{12}, K_{21}, K_{22}$ with respect to ω_0 when L_m and r_r changes

($\omega_e = 377$ rad/s, $\omega_r = 375$ rad/s in motoring mode). (a) K_{11} ; (b) K_{12} ; (c) K_{21} ; (d) K_{22} .

Solid line: $L_m = L_m^*$, $r_r = r_r^*$; Dotted line: $L_m = 1.25 L_m^*$, $r_r = 1.25 r_r^*$; Dashdot line:

$L_m = 1.25 L_m^*$, $r_r = 0.75 r_r^*$; Dashed: $L_m = 0.75 L_m^*$, $r_r = 1.25 r_r^*$; Solid line (light):

$$L_m = 0.75 L_m^*, r_r = 0.75 r_r^* .$$

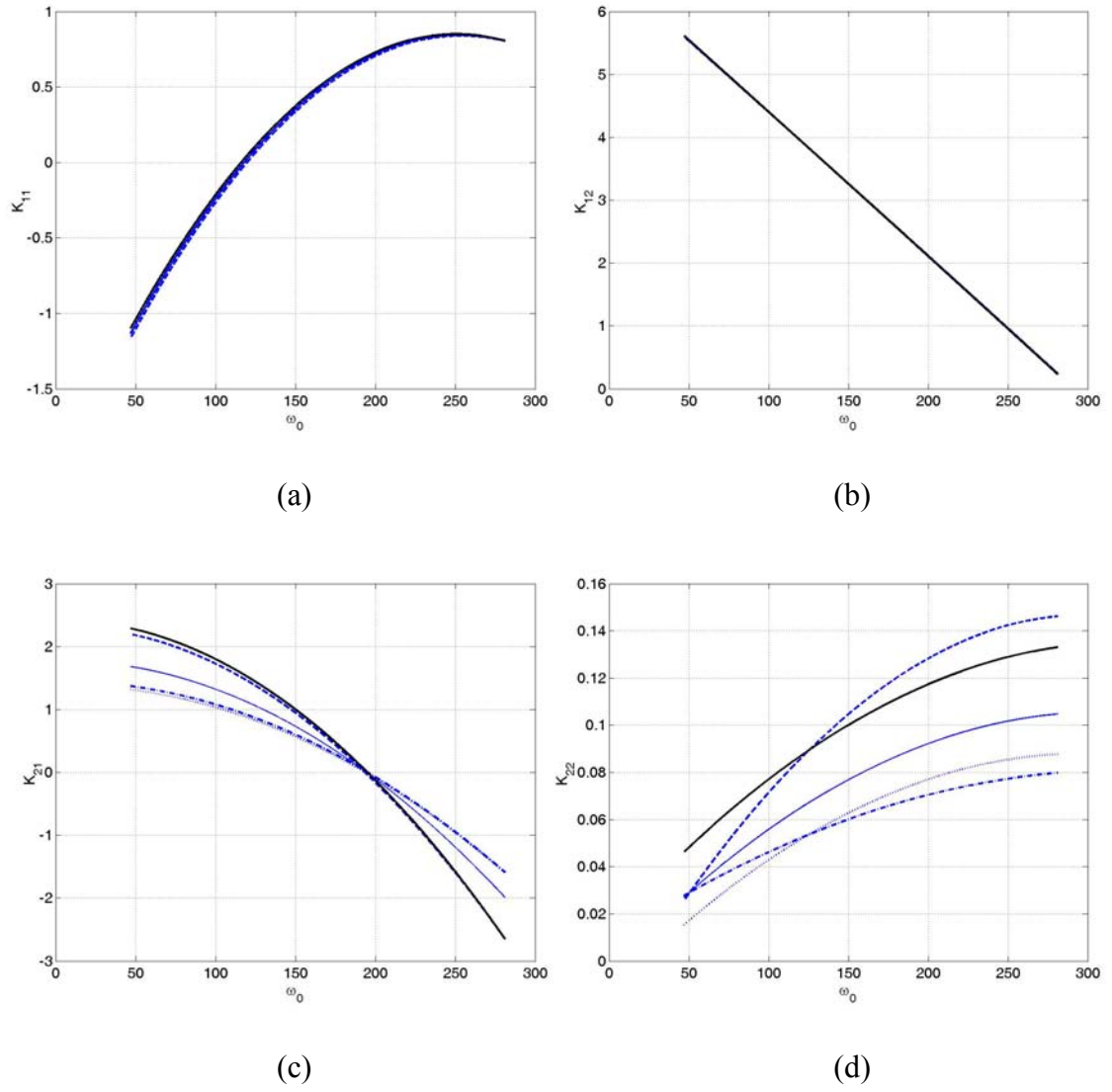


Figure 6.4 $K_{11}, K_{12}, K_{21}, K_{22}$ with respect to ω_0 when L_m and r_r changes

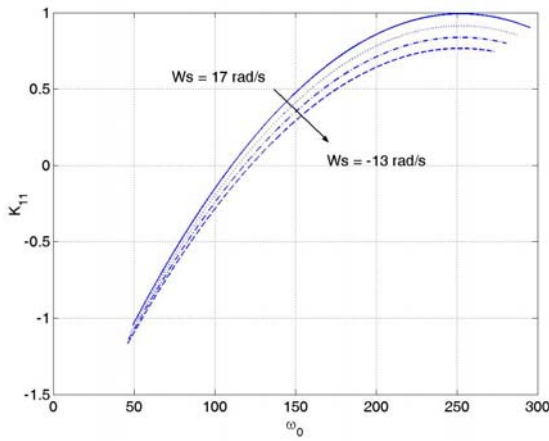
($\omega_e = 377$ rad/s, $\omega_r = 379$ rad/s in generating mode). (a) K_{11} ; (b) K_{12} ; (c) K_{21} ; (d) K_{22} .

Solid line: $L_m = L_m^*$, $r_r = r_r^*$; Dotted line: $L_m = 1.25 L_m^*$, $r_r = 1.25 r_r^*$; Dashdot line:

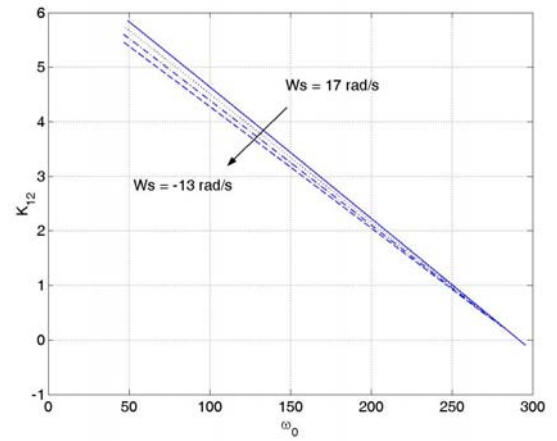
$L_m = 1.25 L_m^*$, $r_r = 0.75 r_r^*$; Dashed: $L_m = 0.75 L_m^*$, $r_r = 1.25 r_r^*$; Solid line (light):

$$L_m = 0.75 L_m^*, r_r = 0.75 r_r^* .$$

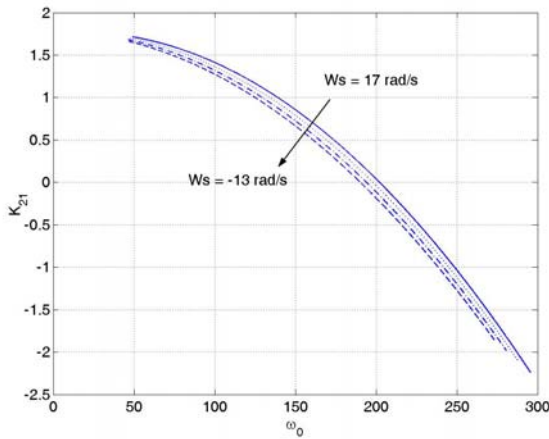
Figures 6.5 and 6.6 show that the observer gains change with ω_0 under different operating conditions. The gains K_{11} , K_{12} , and K_{21} tend to decrease when the machine enters the generating operation mode. But K_{22} tends to increase.



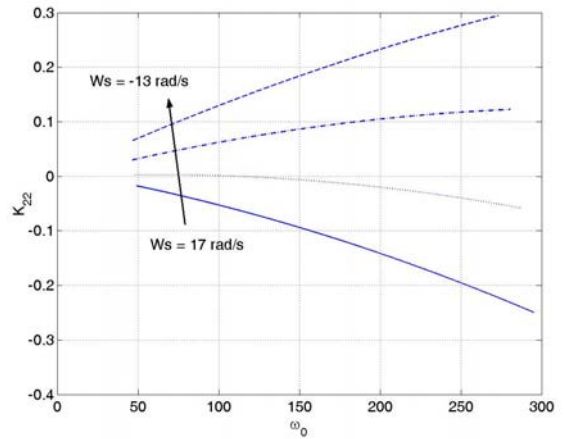
(a)



(b)



(c)

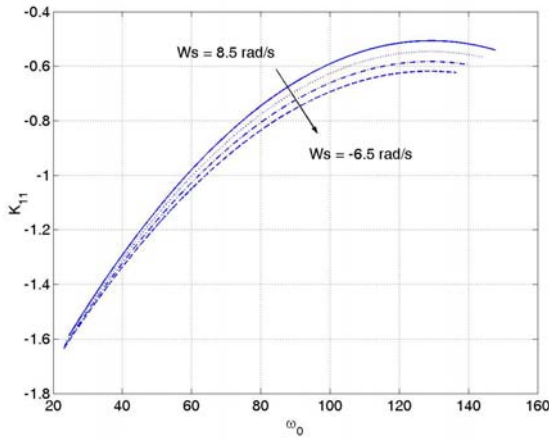


(d)

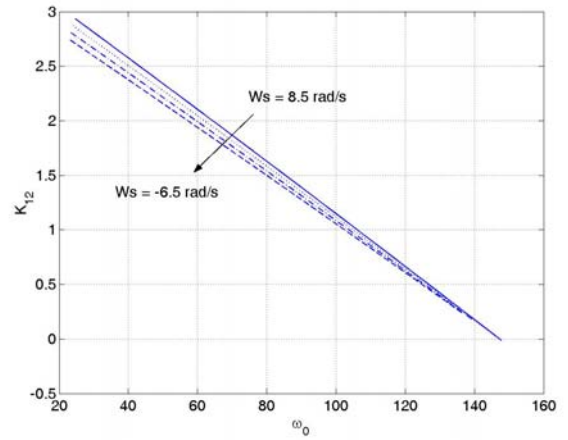
Figure 6.5 $K_{11}, K_{12}, K_{21}, K_{22}$ with respect to ω_0 under different operating conditions

($L_m = L_m^*$, $r_r = r_r^*$, $\omega_e = 377$ rad/s, 360 rad/s $\leq \omega_r \leq 390$ rad/s). (a) K_{11} ; (b) K_{12} ; (c)

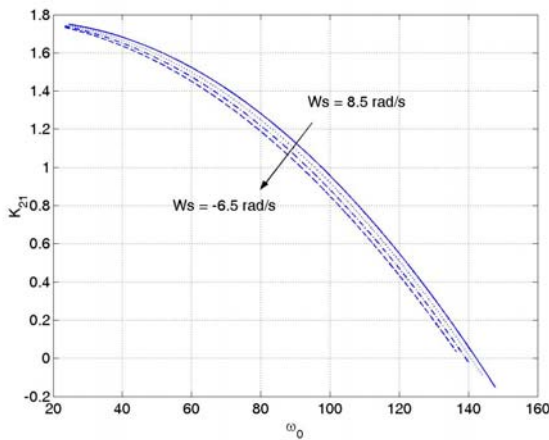
K_{21} ; (d) K_{22} .



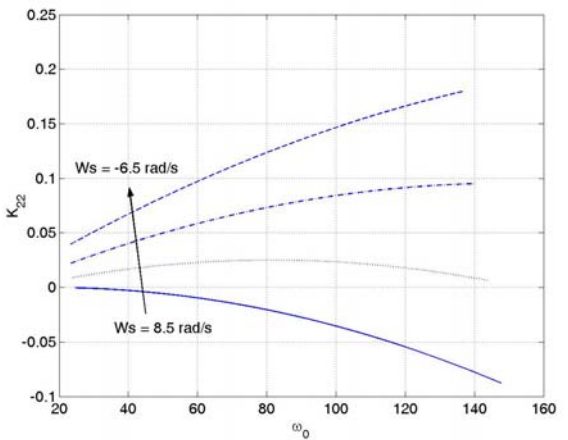
(a)



(b)



(c)



(d)

Figure 6.6 $K_{11}, K_{12}, K_{21}, K_{22}$ with respect to ω_0 under different operating conditions

($L_m = L_m^*$, $r_r = r_r^*$, $\omega_e = 188.5$ rad/s, 180 rad/s $\leq \omega_r \leq 195$ rad/s). (a) K_{11} ; (b) K_{12} ; (c)

K_{21} ; (d) K_{22} .

The observer gains are traditionally selected based on different considerations. In [6.5 - 6.6, 6.17], the observer gains are determined by choosing the poles of the observer model to be proportional to the poles of the machine model. In [6.16], the observer gains

are selected as $K_{11} = K_{12} = 0$, $K_{21} = K_{22} = -0.25 \cdot r_s$ to ensure stability during regenerating operation.

In [6.8], the observer gains are chosen as complex values in (6.51) to give enough damping at high speeds.

$$K = \lambda \begin{bmatrix} 1 + j \cdot \text{sign}(\hat{\omega}_m) \\ -1 + j \cdot \text{sign}(\hat{\omega}_m) \end{bmatrix} \quad (6.51)$$

and

$$\lambda = \begin{cases} \lambda' \cdot \frac{|\hat{\omega}_m|}{\omega_\lambda}, & \text{if } |\hat{\omega}_m| < \omega_\lambda \\ \lambda', & \text{if } |\hat{\omega}_m| \geq \omega_\lambda \end{cases} \quad (6.52)$$

where $\hat{\omega}_m$ is the estimated rotor speed and ω_λ is the base speed. λ' and ω_λ are selected based on the linearized model of the observer. It also shows that by choosing the observer gain as

$$K = \begin{bmatrix} -r_s \\ r_r \end{bmatrix} \quad (6.53)$$

the error function in (6.15) for the speed estimation can be rewritten as (when $k = 1$)

$$\begin{aligned} \varepsilon &= \text{Im} \left[\hat{\lambda}_{qdr}^* \cdot (I_{qds} - \hat{I}_{qds}) \right] \\ &= -\frac{1}{L_\sigma} \cdot \text{Im} \left[\hat{\lambda}_{qdr}^* \cdot (\hat{\lambda}_{qds} - L_\sigma I_{qds}) \right] \end{aligned} \quad (6.54)$$

The structure of the conventional MRAS for speed estimation is shown in Figure 6.1, in which the stator voltage equations are referred as the reference model and the rotor voltage equations are referred as the adjustable model. The rotor flux linkages are estimated in the stationary reference frame from the stator voltage equation (6.1) and rotor voltage equation (6.2), respectively. The error function is defined as

$$\varepsilon = -\text{Im} \left[\hat{\lambda}_{qdr}^* \cdot (\hat{\lambda}_{qds} - L_\sigma I_{qds}) \right] \quad (6.55)$$

The difference between (6.54) and (6.55) is the adaptation gain ($1/L_\sigma$). Hence, the conventional MRAS can be seen as a special case of the general speed-adaptive flux observer defined in (6.12), (6.15) and (6.16). The operation when all the observer gains are zero is discussed in [6.5 - 6.6, 6.8], which is an open-loop estimation. The proposed method of determining the observer gains, however, could give good system response, which is different from the original open-loop machine system.

6.7 D-decomposition Method

The denominator of the transfer function for the rotor speed in (6.36) is of 5th order. It is therefore difficult to obtain an analytical solution to the eigenvalues. The D-decomposition is then applied to determine the stability boundary (between the stable and unstable regions) from the characteristic equation [6.10 - 6.12].

The idea of interpreting the stability conditions for linear systems in the parameter plane has been generalized by Neimark in his D-decomposition method for consideration of multiparameter problems. Consider a real polynomial, which is corresponding to the characteristic equation of a transfer function,

$$F(s) = \sum_{k=0}^n a_k s^k \quad (6.56)$$

where the coefficients a_k are continuous functions of r system parameters p_i , that is $a_k = a_k(p_1, p_2, \dots, p_r)$. $s = \sigma + j\omega$ is the complex variable in general. Now the r -dimensional vector space, of which p_i are coordinates, can be decomposed into sets denoted by $D(m, n-m)$, which correspond to the polynomial having m zeros with

negative and $n-m$ zeros with positive real parts. Such a decomposition of the parameter space into sets is called the D-decomposition.

The boundary of the sets $D(m, n-m)$ consists of those points for which the polynomial $F(s)$ has finite zeros with vanishing real parts. The boundaries consist of surfaces determined by

$$a_0 = 0, a_n = 0 \quad (6.57)$$

and a surface determined by

$$\begin{aligned} R &= \sum_{k=0}^n a_k X_k(0, \omega) \\ I &= \sum_{k=0}^n a_k Y_k(0, \omega) \end{aligned} \quad (6.58)$$

where function $X_k(0, \omega)$ and $Y_k(0, \omega)$ are given by the recurrence formulas

$$\begin{aligned} X_{k+2} + \omega^2 X_k &= 0 \\ Y_{k+2} + \omega^2 Y_k &= 0 \end{aligned} \quad (6.59)$$

with $X_0 = 1, X_1 = 0, Y_0 = 0, Y_1 = \omega$.

The surface $a_0 = 0$ corresponds to a zero at the origin of the s plane and the surface $a_n = 0$ corresponds to a zero at infinity of the s plane. The surface (6.58) corresponds to a pair of pure imaginary zeros of the polynomial $F(s)$.

Eliminating ω^2 from (6.58), the following determinant is obtained.

$$\Delta_{n-1} = \begin{vmatrix} a_{n-1} & a_n & 0 & 0 & \cdots & 0 \\ a_{n-3} & a_{n-2} & a_{n-2} & a_{n-2} & \cdots & 0 \\ \vdots & \vdots & \vdots & \vdots & & \vdots \\ \vdots & \vdots & \vdots & \vdots & & \vdots \\ \vdots & \vdots & \vdots & \vdots & & \vdots \\ 0 & 0 & a_0 & a_1 & \cdots & a_n \end{vmatrix} = 0 \quad (6.60)$$

where Δ_{n-1} is the next-to-the-last Hurwitz determinant Δ_n of $F(s)$. Thus the necessary and sufficient condition for the polynomial $F(s)$ to have finite zeros with vanishing real part is $a_0 a_1 \Delta_{n-1} = 0$.

The stability of a linear system with characteristic polynomial $F(s)$ is assured if a point in the space is chosen from the set $D(n,0)$. Points on the boundary of the set $D(n,0)$ apparently satisfy the condition.

Although the D-decomposition is defined in a parameter space, it is convenient to apply only to two-parameter problems. The common conditions for determining the boundary of $D(n,0)$ provide two equations relating r parameters. In the case of two parameters, the boundary of the stable and unstable regions can be determined from (6.57) and (6.58). The conditions for (6.58) are equivalent to the $F(s)$ with substituting $s = j\omega$. By changing ω , certain curve (D-decomposition curve) can be drawn using the two unknowns as the axis, which separate the stable and unstable regions. The stable region is determined through a certain shading rule [6.10]. For the stability analysis, the shading area is on the left half plane in the s -plane and the corresponding shading area in the parameter plane is determined by calculating the determinant of Jacobian matrix. In the case of the two parameters (α and β) problem, the Jacobian matrix is defined as

$$J = \begin{bmatrix} \frac{\partial R}{\partial \alpha} & \frac{\partial R}{\partial \beta} \\ \frac{\partial I}{\partial \alpha} & \frac{\partial I}{\partial \beta} \end{bmatrix} \quad (6.61)$$

where R and I are the real and imaginary parts of the characteristic equation when $s = j\omega$ is substituted. If determinant of J ($\det(J)$) is greater than 0, the shading area in the parameter plane will be on the left hand side of the D-decomposition curve when ω is

increasing. If $\det(J) < 0$, then the shading area in the parameter plane will be on the right hand side of the D-decomposition curve when ω is increasing. The stable and unstable regions can be determined through examining the real part of the roots of the characteristic equation.

6.8 PI Control Parameters Selection

Choosing appropriate PI control parameters to regulate the error function of the model reference adaptive mechanism is an important issue related to the stability of the motor system. Some constraints have to be applied to the transfer function between the estimated and actual speeds once it is known. First of all, all of the poles should be in the left half s-plane, which implies that all poles have negative real parts. All of the zeros of the transfer function also should have negative real parts such that the system is minimum phase. The best way of checking the stability of a transfer function is using Routh table, from which the conditions for the system to be stable can be found. However, those coefficients in (6.37) are so complicated that it is difficult to find the explicit conditions. The D-decomposition method is then applied to select the PI controller parameters, which ensure that all the eigenvalues of the transfer function and zeros have negative real parts. Two critical conditions need to be examined in this case. The first is that there is one zero, and the other is that there is a purely imaginary pair for the eigenvalues. These conditions are

$$\begin{aligned}\lambda &= 0 \\ \lambda &= \pm j\omega_0\end{aligned}\tag{6.62}$$

Given in (6.36), the transfer function for the speed is

$$\frac{\hat{\omega}_r}{\omega_r} = \frac{A_4 p^4 + A_3 p^3 + A_2 p^2 + A_1 p + A_0}{p^5 + B_4 p^4 + B_3 p^3 + B_2 p^2 + B_1 p + B_0}$$

To satisfy the first condition,

$$\lambda = 0 \Rightarrow B_0 = 0 \text{ or } t_{23} = 0 \quad (6.63)$$

which gives a certain constraint for choosing the observer gains under different operating conditions. t_{23} is depending on the machine parameters and the observer gains. For this case of study, it can be easily checked from computer simulation since the observer gains are determined using the Butterworth polynomial method previously. Figure 6.7 shows the relationship between t_{23} and ω_o , in which t_{23} is always less than zero. It means that there is no pole at zero.

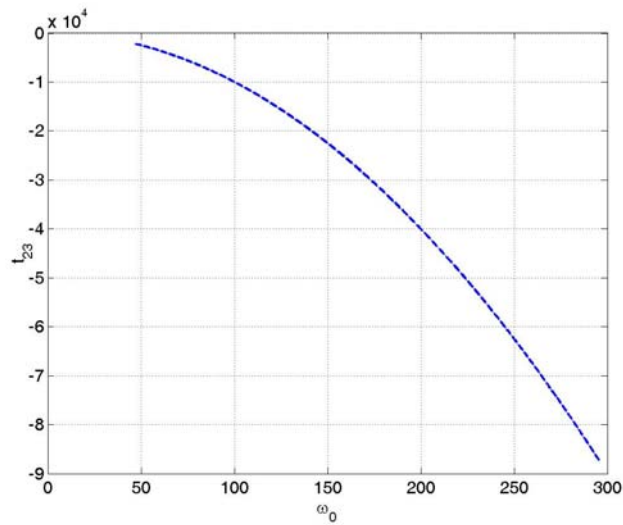


Figure 6.7 t_{23} with respect to ω_o under different operating conditions ($L_m = L_m^*$,

$$r_r = r_r^*, \omega_e = 377 \text{ rad/s}, 360 \text{ rad/s} \leq \omega_r \leq 390 \text{ rad/s}).$$

To satisfy the second condition,

$$\lambda = \pm j\omega_0 \Rightarrow \begin{cases} \omega_0^4 - B_3 \cdot \omega_0^2 + B_1 = 0 \\ B_4 \cdot \omega_0^4 - B_2 \cdot \omega_0^2 + B_0 = 0 \end{cases} \quad (6.64)$$

Since all the B coefficients in (6.37) are the linear functions of K_{op} and K_{oi} , the relationship between K_{op} and K_{oi} can be drawn when ω_0 is changing. Figure 6.8 shows the relationship under a particular operating condition when slip frequency is changing from positive (motoring mode) to negative (generating mode). One basic condition for choosing K_{op} and K_{oi} is that both of them should be positive. By choosing two points on the two sides of the curve, the eigenvalues and zeros can be calculated. From the calculation, the region on the upper side is the stable region while the inner side is the unstable region. This verifies that the PI controller parameters can be chosen arbitrary large. However, noise will cause some problems when large values are used in the DSP hardware implementation.

The above D-decomposition curve is corresponding to the condition when $0 \neq \omega < \infty$. However, there is another constraint when $\omega = 0$, which forms a straight line (singular line) in the parameter plane [6.14]. The number of stable roots in each region defined by this decomposition changes at two with crossing the curve and at one with crossing a singular line. In the above case, the singular line is corresponding to the condition when $K_{oi} = 0$ from (6.37). This condition is automatically satisfied when $K_{oi} > 0$ is chosen.

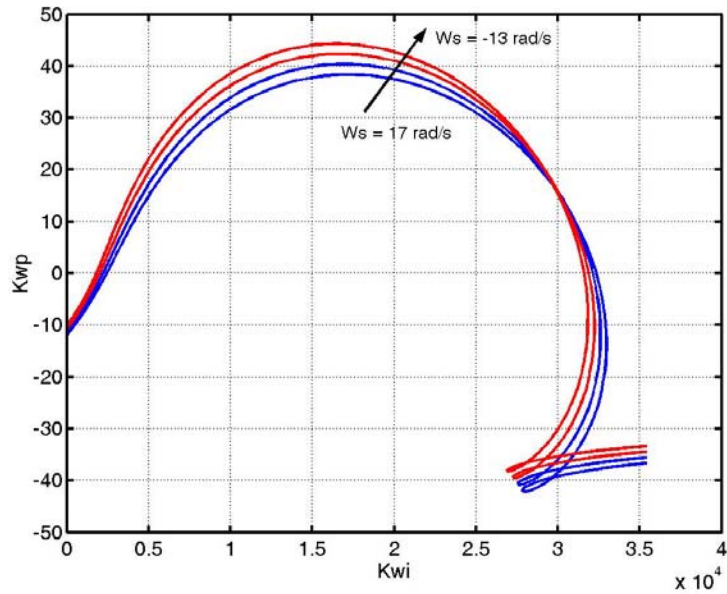


Figure 6.8 Relationship between K_{wp} and K_{wi} at different slip frequencies.

$$(\omega_e = 377 \text{ rad/s and } -13 \text{ rad/s} \leq \omega_s \leq 17 \text{ rad/s})$$

Only the active power is used as the error function in Figure 6.8. The drawback of only using the active power as the error function is that the estimation at low speed range is very bad. The performance of the observer system in the low speed region can be improved by including the reactive power as part of the error function. The coefficient k is defined as the partition factor between the active power and reactive power. The D-decomposition curves change when k is changing between 0 and 1.

Figure 6.9 shows the D-decomposition curves for different k values. For different k values, the stable region is always on the left side of the curves when ω_0 is increasing according to the shading rules. The similar trend can be observed that the stable region of the controller parameters for the motoring operation is larger. Under the same operation condition, the stable region corresponding to bigger k is also larger.

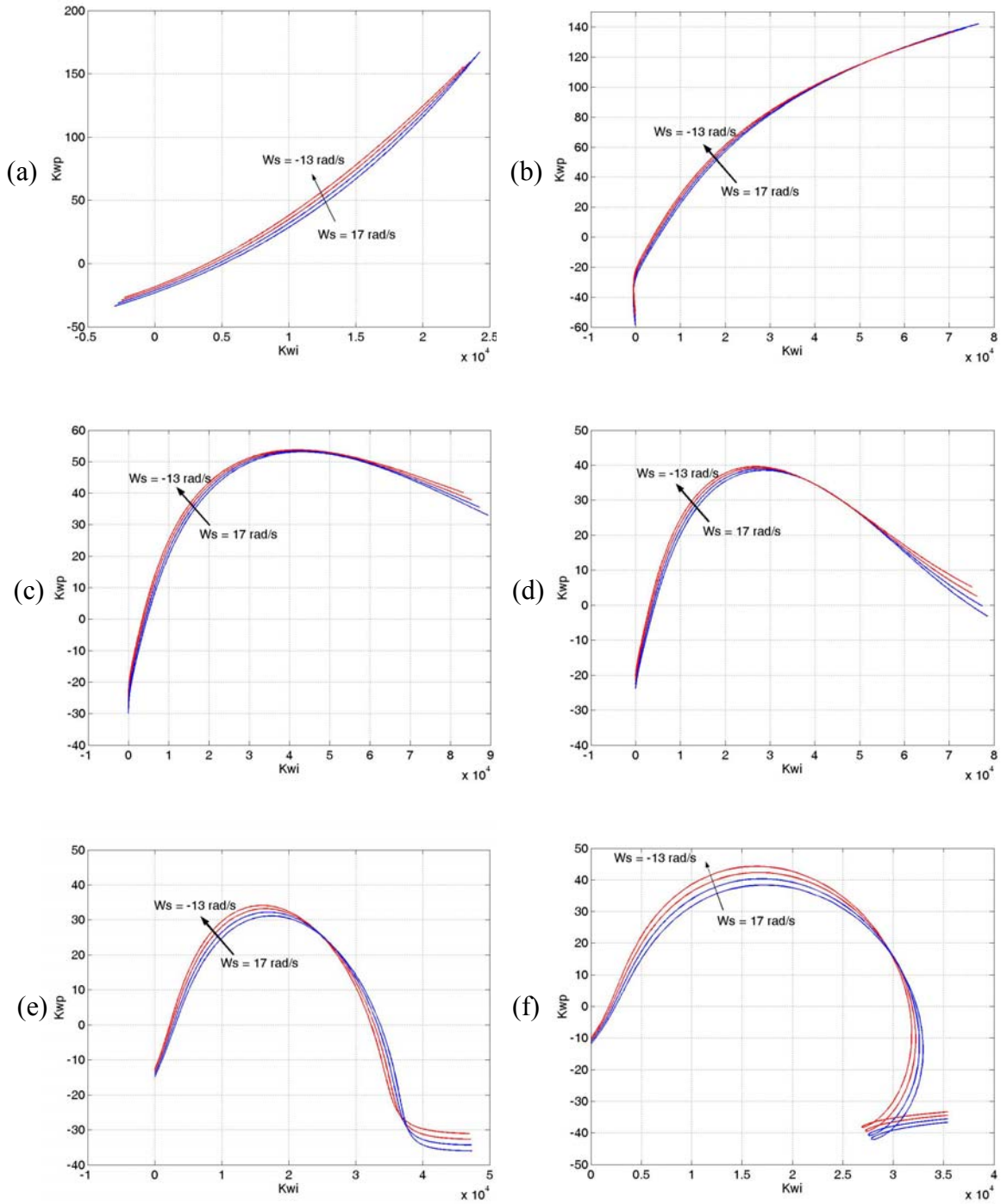


Figure 6.9 Relationship between K_{wp} and K_{wi} at different slip frequency. (a) $k = 0.0$; (b) $k = 0.2$; (c) $k = 0.4$; (d) $k = 0.5$; (e) $k = 0.8$; (f) $k = 1.0$.
 $(\omega_e = 377 \text{ rad/s and } -13 \text{ rad/s} \leq \omega_s \leq 17 \text{ rad/s})$.

The extreme cases for the parameter changes are now considered for the fixed k ($k = 0.5$). The changes in L_m and r_r are considered within -50 percent and $+50$ percent. Then the four extremes cases are (* represent the nominal value)

$$1: r_r = 0.5r_r^*, L_m = 0.5L_m^* ;$$

$$2: r_r = 0.5r_r^*, L_m = 1.5L_m^* ;$$

$$3: r_r = 1.5r_r^*, L_m = 0.5L_m^* ;$$

$$4: r_r = 1.5r_r^*, L_m = 1.5L_m^* .$$

Figures 10 and 11 show the D-decomposition curves under the above extreme cases in both motoring and generating modes. In the motoring operation mode, it is seen that the stable region for the controller parameters is larger when L_m is fixed and r_r has positive error. The similar trend can also be observed when r_r is fixed and L_m has positive error. The stable region enlarges with the increasing r_r and L_m . Also r_r has more influence on the stable region than L_m . However, in the generating operation mode, the stable region for the controller parameters reduces when r_r is fixed and L_m has positive error although the stable region increases when L_m is fixed and r_r has positive error. The differences between the curves are much more significant in the generating mode than in the motoring operation mode.

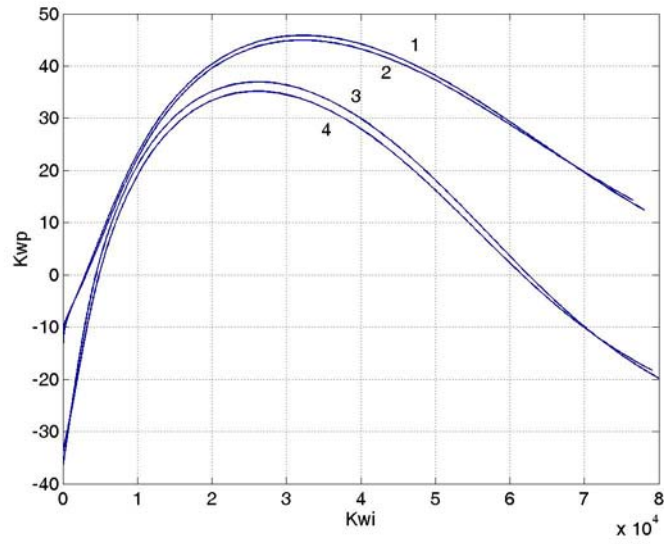


Figure 6.10 Relationship between K_{wp} and K_{wi} under parameter changes in motoring

mode ($k = 0.5$, $\omega_e = 377$ rad/s and $\omega_s = 17$ rad/s). 1: $r_r = 0.5r_r^*$, $L_m = 0.5L_m^*$; 2:
 $r_r = 0.5r_r^*$, $L_m = 1.5L_m^*$; 3: $r_r = 1.5r_r^*$, $L_m = 0.5L_m^*$; 4: $r_r = 1.5r_r^*$, $L_m = 1.5L_m^*$.

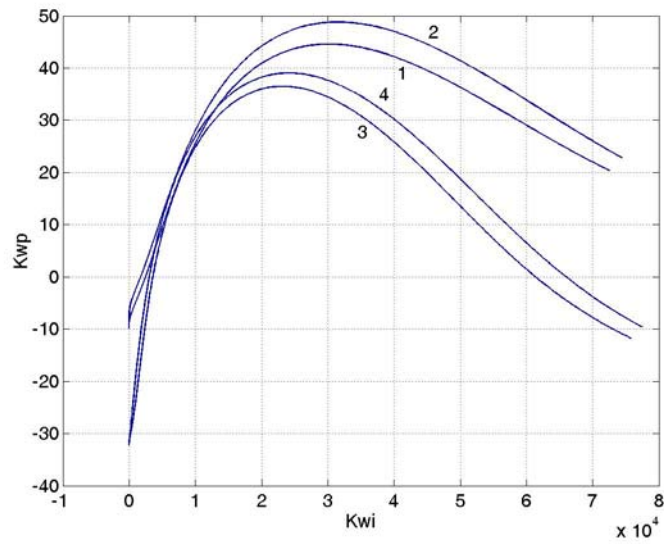


Figure 6.11 Relationship between K_{wp} and K_{wi} under parameter changes in generating

mode ($k = 0.5$, $\omega_e = 377$ rad/s and $\omega_s = -13$ rad/s). 1: $r_r = 0.5r_r^*$, $L_m = 0.5L_m^*$; 2:
 $r_r = 0.5r_r^*$, $L_m = 1.5L_m^*$; 3: $r_r = 1.5r_r^*$, $L_m = 0.5L_m^*$; 4: $r_r = 1.5r_r^*$, $L_m = 1.5L_m^*$.

The above analysis shows the effects of the changing machine parameters on the stable region of controller parameters. Those curves are useful for the selection of controller parameters for the adaptive speed estimation. From the above analysis, the speed estimation has to be considered in the design of the speed regulator. The transfer function between the actual and reference speeds is also of a higher order. The D-decomposition method can be applied to choose appropriate control parameters for the speed regulation. The controller used to generate the second derivative of the rotor speed is chosen as PD (proportion-differential) controller. The structure of the PD controller is shown in Figure 6.12 and the transfer function between the actual and reference speeds is derived below.

$$\begin{aligned}
 p^2 \omega_r &= K_{orp} (\omega_r^* - \hat{\omega}_r) - K_{ord} \cdot p \omega_r \\
 &= K_{orp} \left(\omega_r^* - \frac{A(p)}{B(p)} \cdot \omega_r \right) - K_{ord} \cdot \frac{A(p)}{B(p)} \cdot p \omega_r \\
 \frac{\omega_r}{\omega_r^*} &= \frac{K_{orp} \cdot B(p)}{B(p) \cdot p^2 + K_{orp} \cdot A(p) + K_{ord} \cdot A(p) \cdot p} = \frac{C(p)}{D(p)} \quad (6.65)
 \end{aligned}$$

$$\begin{aligned}
 D(p) &= p^7 + B_4 \cdot p^6 + (B_3 + A_4 K_{ord}) \cdot p^5 + (B_2 + A_4 K_{orp} + A_3 K_{ord}) \cdot p^4 \\
 &\quad + (B_1 + A_3 K_{orp} + A_2 K_{ord}) \cdot p^3 + (B_0 + A_2 K_{orp} + A_1 K_{ord}) \cdot p^2 \\
 &\quad + (A_1 K_{orp} + A_0 K_{ord}) \cdot p + A_0 K_{orp}
 \end{aligned}$$

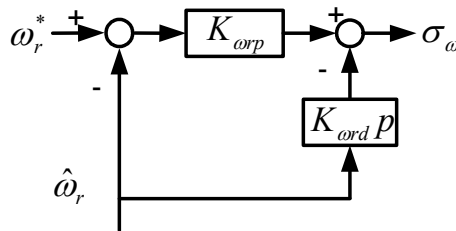


Figure 6.12 Structure of PD controller used for speed regulation.

Similar analysis has been done on the control design for the speed regulation. First, the particular set of the controller parameters for the speed estimation is chosen such that the system is stable for all of the operation conditions. This parameter set is then used to generate the transfer function between the actual and reference speeds. From Figure 6.8, the controller parameters for the speed estimation are chosen as $K_{op} = 50$, $K_{oi} = 10000$. The curves shown in Figure 13 corresponding to the generating operation mode are located on the left side when ω_0 is increasing. The stable region of the controller parameters for the speed regulation increases with the increasing k since the stable region is on the left side of the curves when ω_0 is increasing according to the shading rules.

Figures 6.14 and 6.15 show the influence of parameter changes on the controller parameters for the speed regulation. Similar trend can be observed as the D-decomposition curves for the speed estimation. In the motoring operation mode, the stable region for the controller parameters increases when L_m is fixed and r_r has positive error. The same trend is also observed when r_r is fixed and L_m has positive error. However, in the generating operation mode, the stable region for the controller parameters reduces when r_r is fixed and L_m has positive error although the stable region increases when L_m is fixed and r_r has positive error. The differences between the curves are much more significant in the generating mode than in the motoring operation mode.

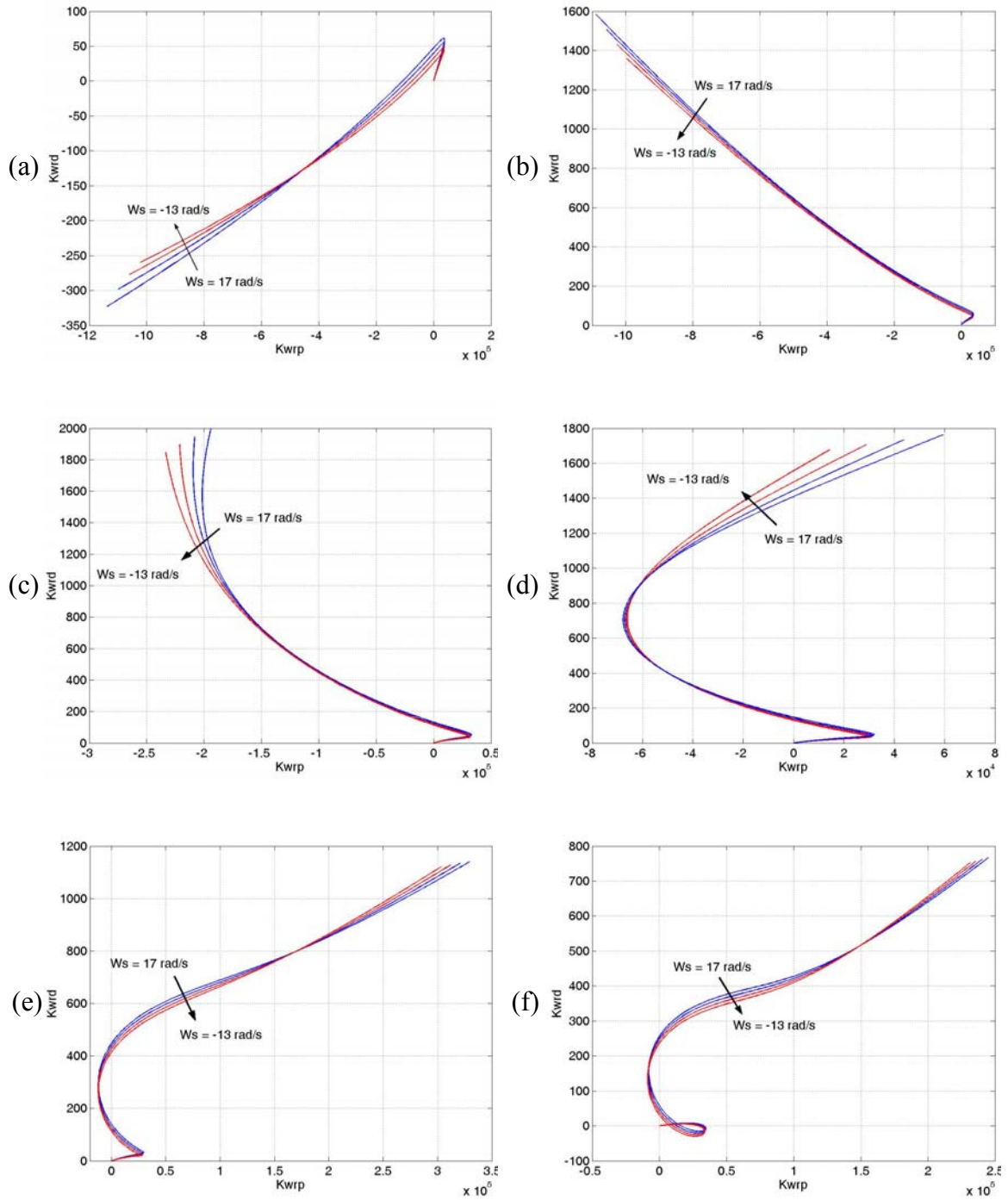


Figure 6.13 Relationship between K_{wrd} and K_{wrp} at different slip frequency. (a) $k = 0.0$;

(b) $k = 0.2$; (c) $k = 0.4$; (d) $k = 0.5$ (e) $k = 0.8$; (f) $k = 1.0$.

($\omega_e = 377$ rad/s and -13 rad/s $\leq \omega_s \leq 17$ rad/s).

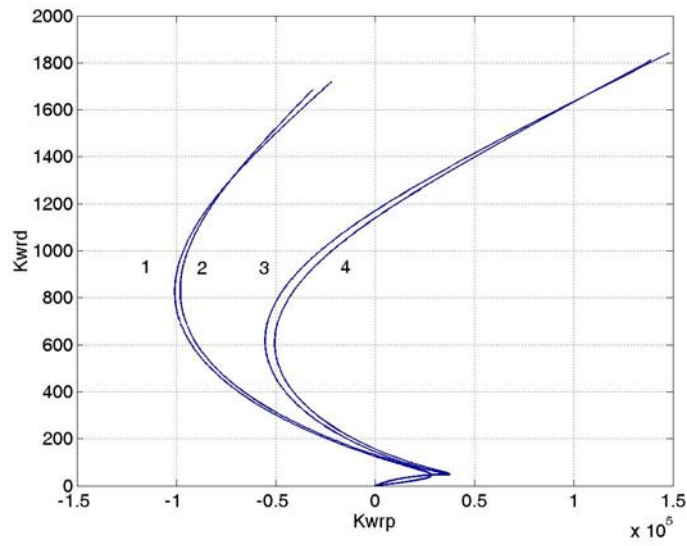


Figure 6.14 Relationship between K_{wrd} and K_{wrp} under parameter changes in motoring

mode ($k = 0.5$, $\omega_e = 377$ rad/s and $\omega_s = 17$ rad/s). 1: $r_r = 0.5r_r^*$, $L_m = 0.5L_m^*$; 2:
 $r_r = 0.5r_r^*$, $L_m = 1.5L_m^*$; 3: $r_r = 1.5r_r^*$, $L_m = 0.5L_m^*$; 4: $r_r = 1.5r_r^*$, $L_m = 1.5L_m^*$.

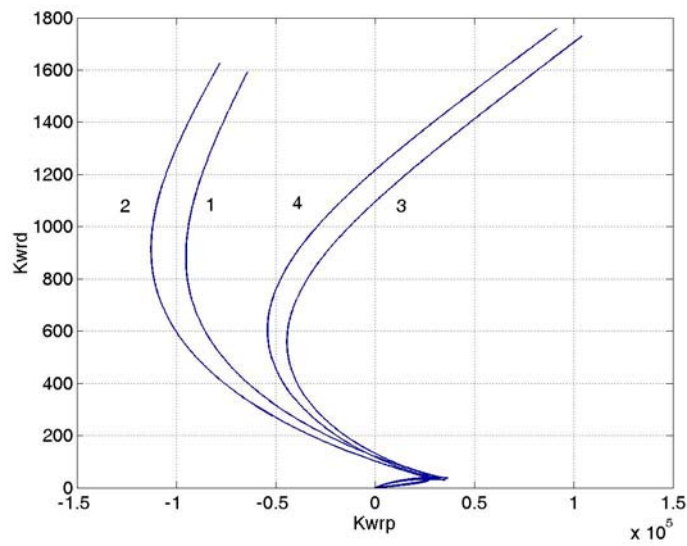


Figure 6.15 Relationship between K_{wrd} and K_{wrp} under parameter changes in generating

mode ($k = 0.5$, $\omega_e = 377$ rad/s and $\omega_s = -13$ rad/s). 1: $r_r = 0.5r_r^*$, $L_m = 0.5L_m^*$; 2:
 $r_r = 0.5r_r^*$, $L_m = 1.5L_m^*$; 3: $r_r = 1.5r_r^*$, $L_m = 0.5L_m^*$; 4: $r_r = 1.5r_r^*$, $L_m = 1.5L_m^*$.

6.9 Formulation of Control Scheme

The rotor flux oriented control is used for testing the proposed full-order flux observer and adaptive speed estimation. The stator and rotor voltage equations are used again to formulate the whole control scheme. The objectives of the control are to regulate the rotor speed and operate the induction motor under the specified rotor flux linkages (λ_{dr} is constant and $\lambda_{qr} = 0$). The stator and rotor voltage equations are rewritten as

$$L_{\sigma} p I_{qs} + r I_{qs} = \sigma_{qs} = V_{qs} - \omega_e L_{\sigma} I_{ds} + \frac{r_r L_m}{L_r^2} \lambda_{qr} - \omega_r \frac{L_m}{L_r} \lambda_{dr} \quad (6.66)$$

$$L_{\sigma} p I_{ds} + r I_{ds} = \sigma_{ds} = V_{ds} + \omega_e L_{\sigma} I_{qs} + \frac{r_r L_m}{L_r^2} \lambda_{dr} + \omega_r \frac{L_m}{L_r} \lambda_{qr} \quad (6.67)$$

$$p \lambda_{qr} + \frac{r_r}{L_r} \lambda_{qr} = \sigma_{qr} = \frac{r_r L_m}{L_r} I_{qs} - (\omega_e - \omega_r) \lambda_{dr} \quad (6.68)$$

$$p \lambda_{dr} + \frac{r_r}{L_r} \lambda_{dr} = \sigma_{dr} = \frac{r_r L_m}{L_r} I_{ds} + (\omega_e - \omega_r) \lambda_{qr} \quad (6.69)$$

$$p \omega_r = K_e (\lambda_{dr} I_{qs} - \lambda_{qr} I_{ds}) - T_L \frac{P}{2J} \quad (6.70)$$

In the control scheme, the PI controller parameters for the adaptive speed estimation are chosen based on the analysis in section 6.8. For all the other controllers, the transfer functions are found first and then the parameters are determined using the Butterworth polynomial by choosing appropriate ω_0 . Two controllers are used to maintain $\lambda_{dr}, \lambda_{qr}$ as the desired values. The corresponding transfer functions can be derived as follows.

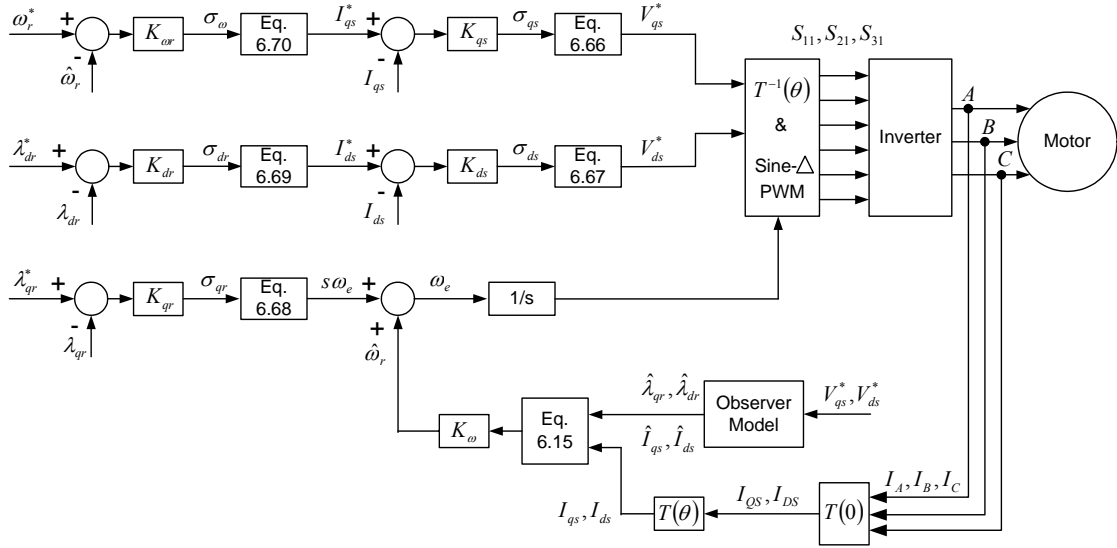


Figure 6.16 Rotor flux oriented control including full-order flux observer and adaptive speed estimation.

From (6.69),

$$p\lambda_{dr} + \frac{r_r}{L_r}\lambda_{dr} = K_{dr} \cdot (\lambda_{dr}^* - \lambda_{dr})$$

$$\frac{\lambda_{dr}}{\lambda_{dr}^*} = \frac{K_{dr}}{K_{dr} + p + \frac{r_r}{L_r}} \quad (6.71)$$

From (6.68),

$$p\lambda_{qr} + \frac{r_r}{L_r}\lambda_{qr} = K_{qr} \cdot (\lambda_{qr}^* - \lambda_{qr})$$

$$\frac{\lambda_{qr}}{\lambda_{qr}^*} = \frac{K_{qr}}{K_{qr} + p + \frac{r_r}{L_r}} \quad (6.72)$$

The other two controllers are used to maintain I_{ds}, I_{qs} at the desired values. The corresponding transfer functions can be derived from (6.66) and (6.67) as follows.

$$L_{\sigma} p I_{qs} + r I_{qs} = K_{qs} \cdot (I_{qs}^* - I_{qs})$$

$$\frac{I_{qs}}{I_{qs}^*} = \frac{K_{qs}}{K_{qs} + L_{\sigma} p + r} \quad (6.73)$$

$$L_{\sigma} p I_{ds} + r I_{ds} = K_{ds} \cdot (I_{ds}^* - I_{ds})$$

$$\frac{I_{ds}}{I_{ds}^*} = \frac{K_{ds}}{K_{ds} + L_{\sigma} p + r} \quad (6.74)$$

The transfer function between the actual and reference speeds is given in (6.65).

In the simulation, general PI controllers are used and the parameters are calculated by assuming particular ω_0 from the transfer functions when compared with the second order Butterworth polynomial. The machine parameters are

$$r_s = 1.9812 \, \Omega, \quad r_r = 1.85 \, \Omega,$$

$$L_s = 0.2077 \, \text{H}, \quad L_r = 0.2077 \, \text{H}, \quad L_m = 0.1986 \, \text{H},$$

$$\omega_e = 377 \, \text{rad/s}, \quad \omega_r = 375 \, \text{rad/s}, \quad |\lambda_{qdr}| = 0.4.$$

When ω_0 is chosen 300 rad/s,

The PI controller parameters for λ_{dr} (K_{dr}) are $K_p = 125$ and $K_i = 46517$.

The PI controller parameters for λ_{qr} (K_{qr}) are $K_p = 415$ and $K_i = 90000$.

The PI controller parameters for I_{qs} (K_{qs}) are $K_p = 3.9$ and $K_i = 1602$.

The PI controller parameters for I_{ds} (K_{ds}) are $K_p = 3.9$ and $K_i = 1602$.

The PD controller parameters for $\hat{\omega}_r$ ($K_{\omega r}$) are $K_p = 50000$ and $K_d = 500$.

The PI controller parameters for $\hat{\omega}_r$ (K_{ω}) are $K_p = 50$ and $K_i = 10000$.

The estimator gains are chosen corresponding to the analysis as

$$K_{11} = 0.6887, \quad K_{12} = 2.3792, \quad K_{21} = 0.1175, \quad K_{22} = 0.0419.$$

6.10 Simulation Results

The actual induction motor model and the observer model are included in the computer simulation. The two sets of stator currents used for the speed estimation are coming from these two models respectively. The same q- and d-axis voltages are applied to these two models. The flux linkages are estimated from the voltage equations and then the currents are calculated from these flux linkages.

Simulations have been done based on the proposed control scheme, which includes the rotor flux oriented control, full-order flux observer, and adaptive speed estimation. The rotor speed is ramped up to the rated value (377 rad/s) during the starting period. The speed reference reaches the steady state at $t = 2$ seconds. A full load (4Nm) is applied to the motor at $t = 3$ seconds and then the load is removed at $t = 4$ seconds. A negative load (-4Nm) is applied to test the operation of the motor in the regenerating mode.

The reference, actual and estimated speeds are shown in Figure 6.17(a). It is seen that the feedback speed, which is the estimated speed, tracks the reference speed very well. The actual speed is almost the same as the estimated one, although small difference can be seen among these three speeds from Figure 6.18. The torque developed in the induction motor is shown in Figure 6.17(b), which is corresponding to the load torque except for some ripples due to the switching of the converter.

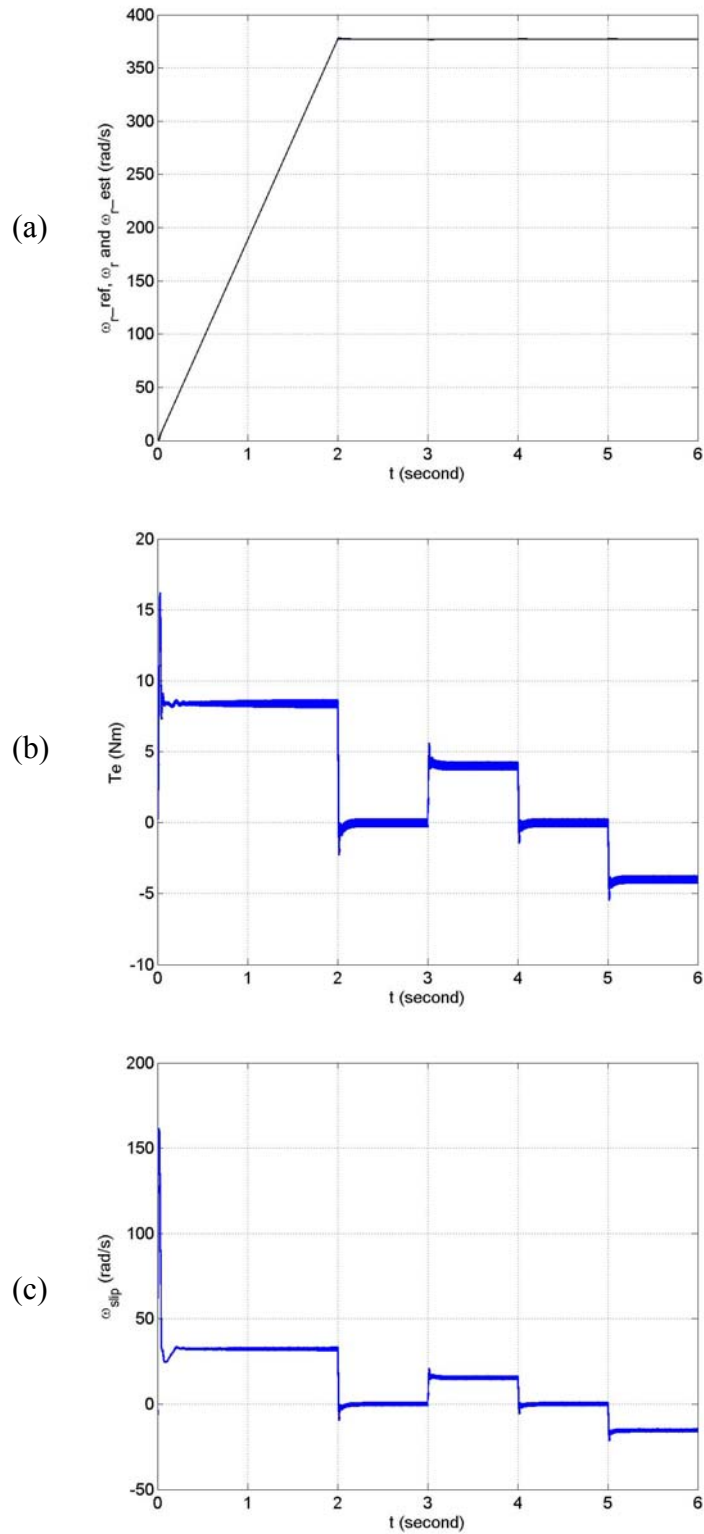
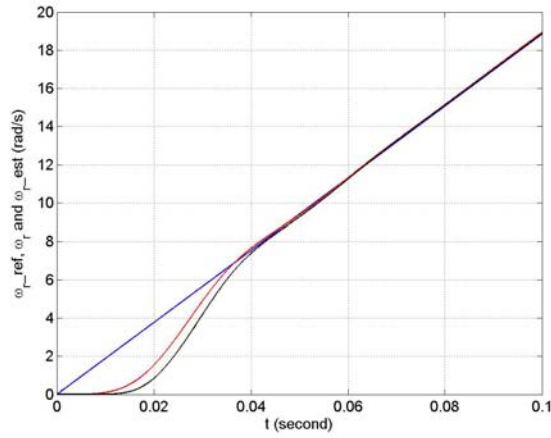


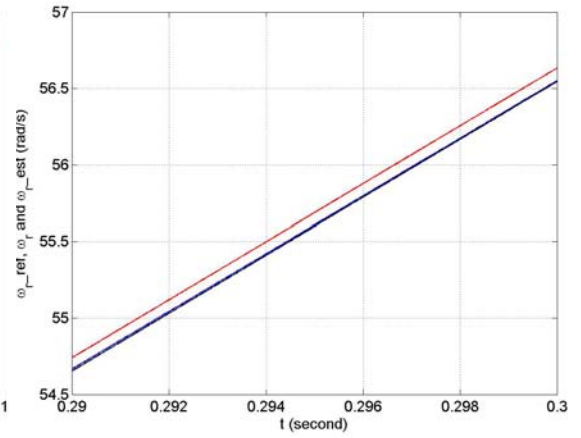
Figure 6.17 Starting transients and transients after change in load torque. (a) Reference, actual, estimated speed; (b) developed torque; (c) slip.

The differences between the actual and estimated q- and d-axis currents are shown in Figure 6.19. The differences are not zero during transience while they are zero at the steady state, which means that the estimated speed converges to the actual speed according to the adaptive speed mechanism. Figure 6.20 shows the regulations for the four controllers regulating the q- and d-axis rotor flux linkages and q- and d-axis stator currents. It is shown that both rotor flux linkages are regulated to the reference values except for small oscillations during the load change. The stator currents are also regulated although there are ripples in the estimated current, which are due to the switching of the converter. Figure 6.21 shows the actual and estimated rotor flux linkages in stationary reference frame. Figure 6.22 shows the actual and estimated stator and rotor flux linkages, which are almost identical.

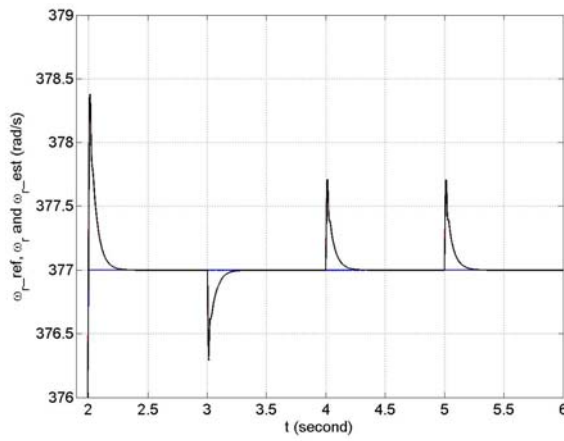
The speed changes after the motor speed gets to the steady state are made to check the capability of proposed design under no-load condition. The estimated speed tracks the reference very well and it is almost identical to the actual speed seen in Figure 6.23(a). The speed changes have the similar effects as load changes from Figure 6.23(b).



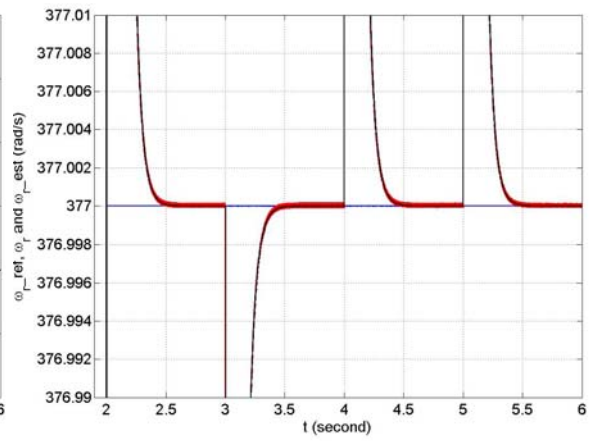
(a)



(b)



(c)



(d)

Figure 6.18 Starting transients and transients after change in load torque: reference, actual and estimated speeds (a) during starting; (b) after starting; (c) at the steady state; (d) zoomed around the reference speed.

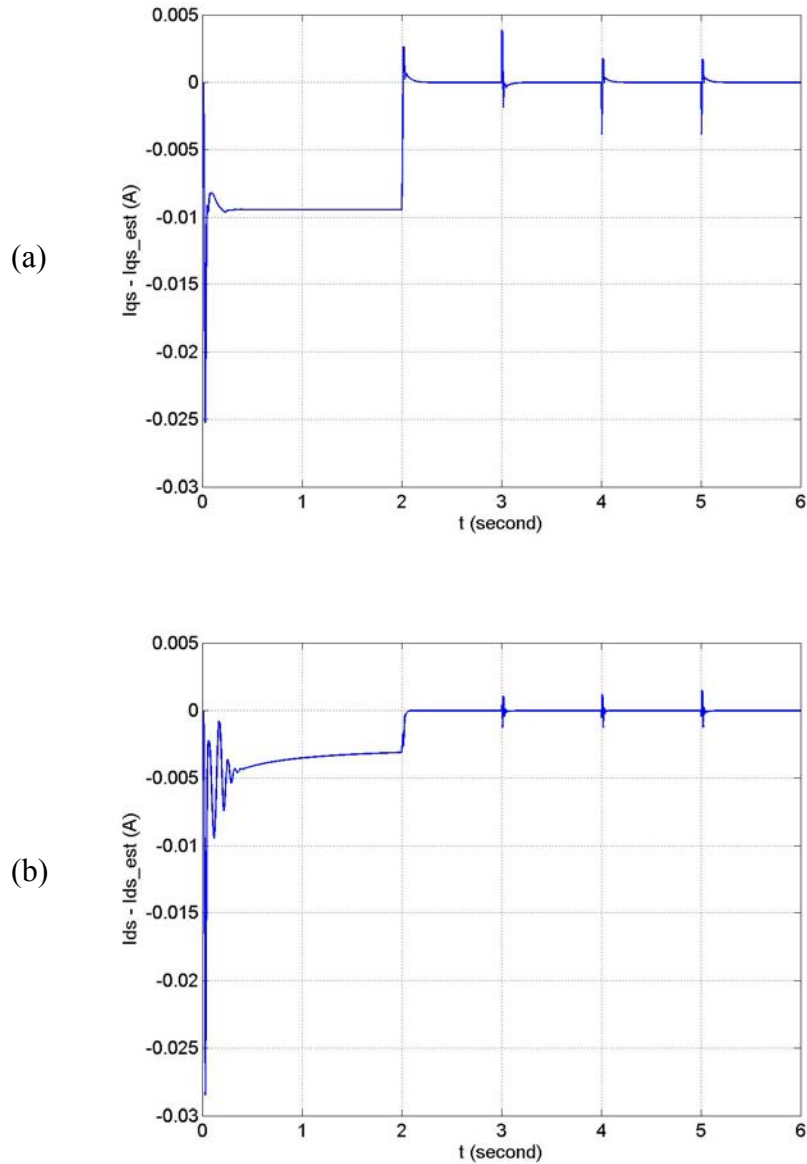


Figure 6.19 Starting transients and transients after change in load torque. (a) Difference between actual and estimated q-axis currents; (b) difference between actual and estimated d-axis currents.

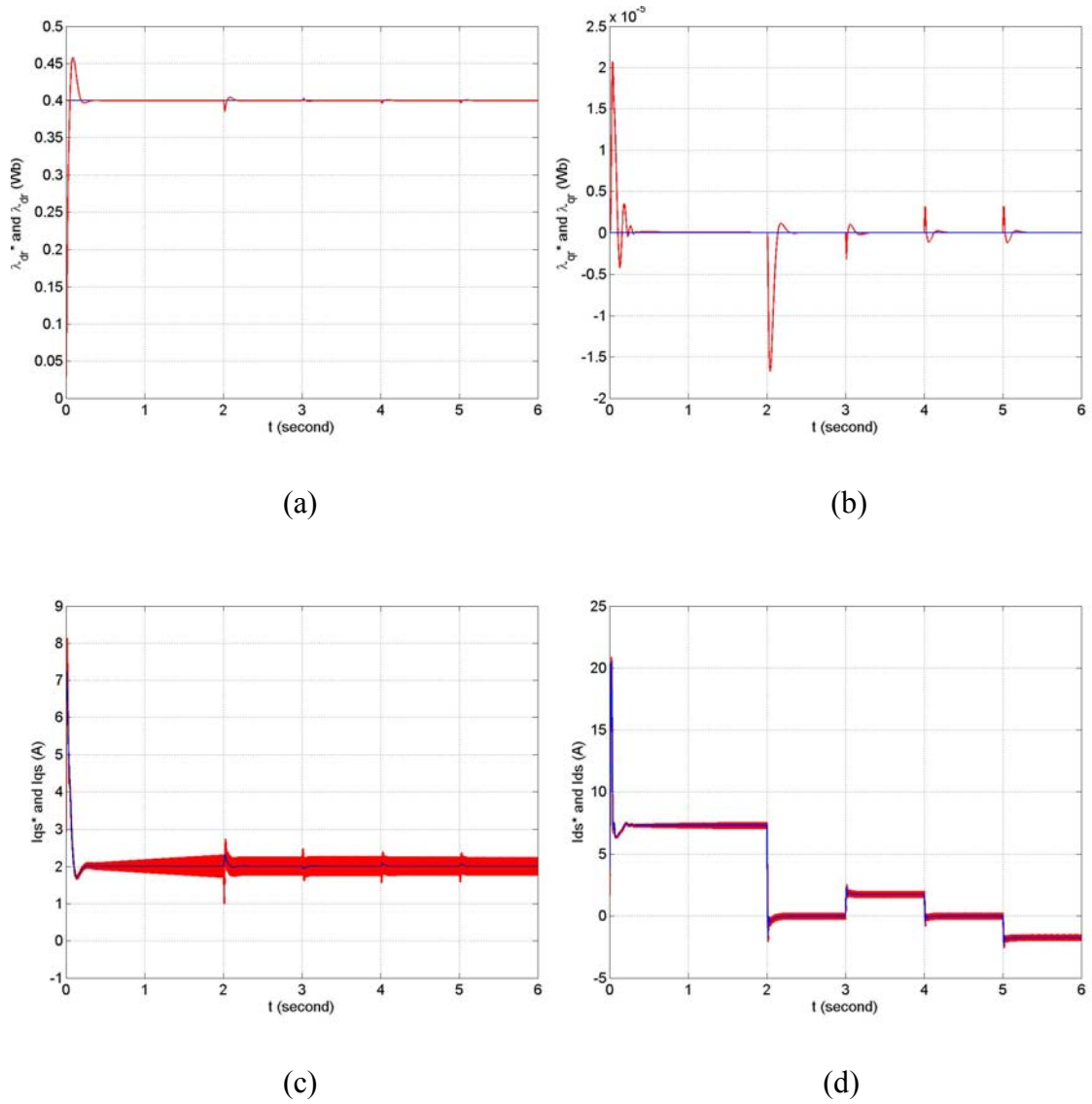


Figure 6.20 Starting transients and transients after change in load torque. (a) Regulation of λ_{dr} ; (b) regulation of λ_{qr} ; (c) regulation of I_{qs} ; (d) regulation of I_{ds} .

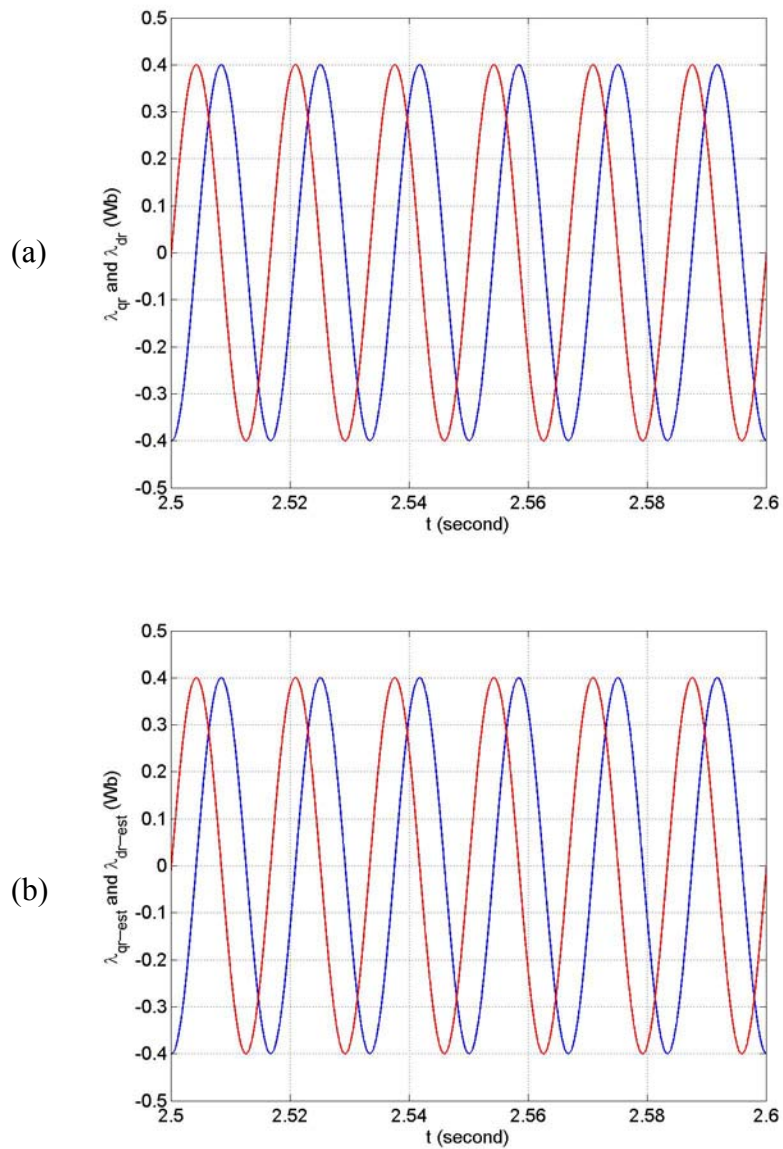
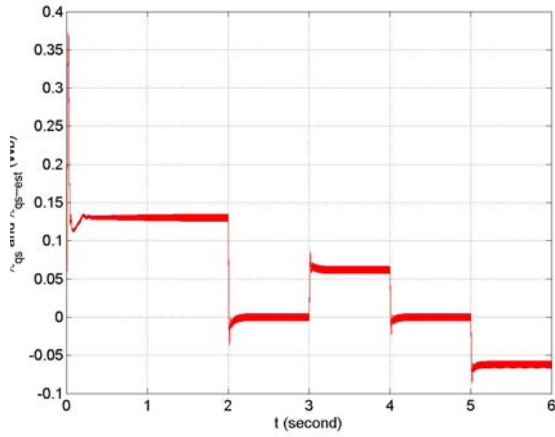
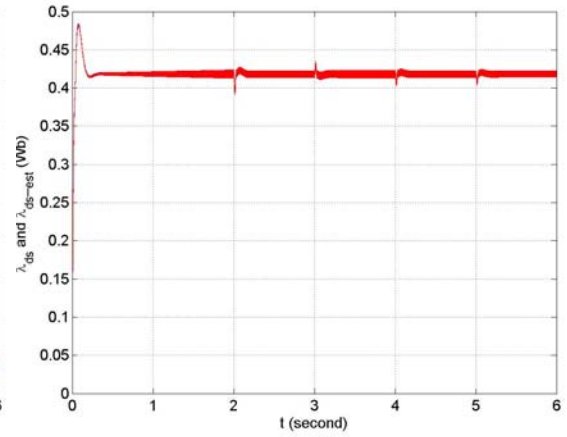


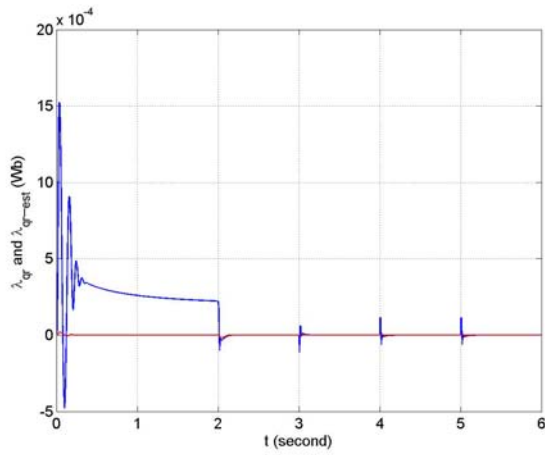
Figure 6.21 No-load flux linkages at steady state. (a) Actual q- and d-axis rotor flux linkages; (b) estimated q- and d-axis rotor flux linkages.



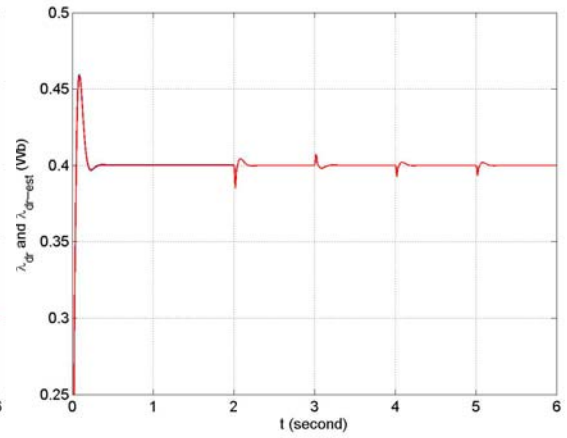
(a)



(b)



(c)



(d)

Figure 6.22 Starting transients and transients after change in load torque. (a) Actual and estimated λ_{qs} ; (b) actual and estimated λ_{ds} ; (c) actual and estimated λ_{qr} ; (d) actual and estimated λ_{dr} .

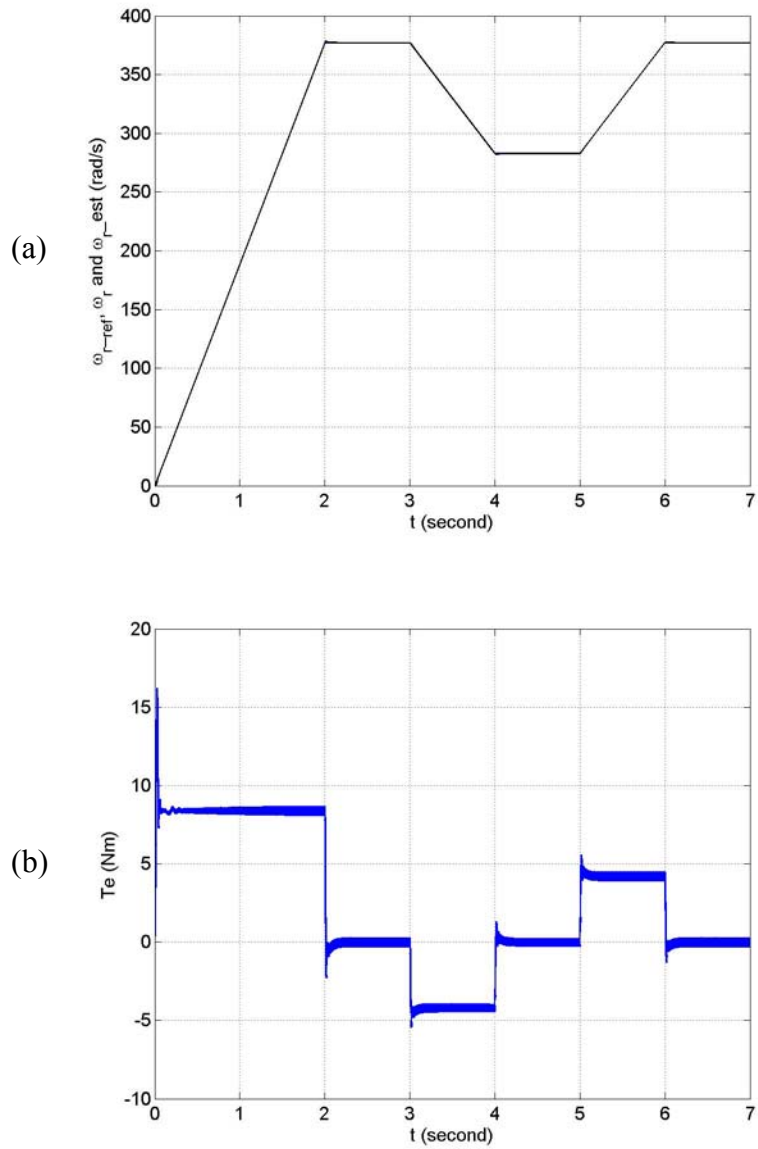


Figure 6.23 Response to the change in speed. (a) Reference, actual, estimated speed; (b) developed torque.

6.11 Conclusion

This chapter analyzes a full-order flux observer system. The model is used to estimate the rotor speed of an induction motor through the adaptive mechanism. The observer gains are chosen using 4th order Butterworth polynomial. The transfer function between the estimated and actual speeds is found based on the error analysis, which is used to determine the PI controller parameters for the speed estimation ensuring the operation in the stable region. The rotor flux oriented control including the observer and adaptive speed estimation is designed to examine the proposed methods. The controller parameters are determined from the corresponding transfer functions. The whole system is simulated in both motoring and regenerating modes. It is shown that all the controllers are working properly and the rotor speed is regulated very well under different load conditions, which validate the proposed method of designing full-order flux observer and speed estimation.

CHAPTER 7
GENERALIZED OVER-MODULATION METHODOLOGY FOR CURRENT
REGULATED THREE-PHASE VOLTAGE SOURCE CONVERTERS

7.1 Introduction

Operation of three-phase voltage source converters in the over-modulation regions could improve steady-state capabilities and dynamic system performance in the motor drive and utility applications. Both carrier-based PWM and space vector PWM operating in the linear modulation region have been discussed in Chapter 2, in which the equivalence between these two modulation schemes is found. However, their characteristics in the over-modulation region are quite different although some similarities are still there. In the case of carrier-based PWM, the modulation index has to be increased in the over-modulation region in order to generate the desired fundamental voltage since the modulation signal is clipped when it is out of the range between -1 and 1. For the space vector PWM, the sum of the calculated times spent on the two active states will be greater than 1, which is not realizable. The way of generating higher fundamental voltage is to adjust the trajectory of the voltage vector such that the voltage vector stays in the region in which the voltage is realizable for a longer time. Correspondingly the times spent on the active states will be adjusted to generate more fundamental voltage.

In this chapter, a more parsimonious equivalency/relationship between the two modulation schemes for converter operation in both linear and over-modulation regions

will be established using a partitioning parameter. A space vector algorithm is then proposed based the on-time for the top switching devices, which gives higher fundamental voltages than the scaling scheme. Both PWM schemes are applied in the current regulation using the linear controller and the fundamental current as the feedback through eliminating the load harmonic current. The mitigation control schemes based on load harmonic current estimation and use of anti-windup controllers are proposed to achieve high dynamic over-modulation performance. The confirmatory experimental results are given to demonstrate the effectiveness of the current control concept for all possible operating regions.

7.2 Linear PWM Modulation Schemes

In the direct digital PWM method, the complex plane stationary reference frame qd output voltage vector of the three-phase voltage source inverter is used to calculate the turn-on times of the inverter switching devices required to synthesize a reference three-phase balanced voltage set. In general, the three-phase balanced voltages expressed in the stationary reference frame; situated in the appropriate sector in Figure 7.1(b) are approximated by the time-average over a sampling period (converter switching period, T_s) of the two adjacent active qd voltage inverter vectors and the two zero states U_0 and U_7 . The switching turn-on times of the two active and two null states are utilized to determine the duty cycle information to program the active switch gate signals [7.3]. When the inverter is operating in the linear modulation region, the sum of the turn-on times of the two active switching modes is less than the switching period, in which case

the remaining time is occupied by using the two null vectors, U_0 and U_7 . If the normalized times for which the set of four voltage vectors V_{qda} , V_{qdb} , V_{qd0} , V_{qd7} are called into play are t_a , t_b , t_0 , t_7 , respectively, then the q and d components of the reference voltage V_{qd}^* are approximated as

$$\begin{aligned} V_{qd}^* &= V_q^* + jV_d^* = V_{qda}t_a + V_{qdb}t_b + V_{qd0}t_0 + V_{qd7}t_7, \\ t_c &= t_0 + t_7 = 1 - t_a - t_b, \quad \nabla = [V_{db} V_{qa} - V_{qb} V_{da}] \\ t_a &= [V_q^* V_{db} - V_d^* V_{qb}] / \nabla, \quad t_b = [V_d^* V_{qa} - V_q^* V_{da}] / \nabla \end{aligned} \quad (7.1)$$

Table 7.1 gives the total times the upper three top devices of the converter are turned on. The sum of these normalized times ($t_a + t_b$) is usually less than one for operation in the linear modulation region. Then the two null states can be appropriated for the remaining time, t_c , in which the normalized times for the null states are defined as $t_0 = \beta t_c$ and $t_7 = (1 - \beta)t_c$, respectively. For the classical space vector (SVPWM), $\beta = 0.5$ for which all the switches are switching all the time during the switching period. PWM schemes are known to reduce the effective converter switching frequency and switching loss when some of the devices are clamped either to the positive or/and negative rails during a switching cycle. This device clamping is realized in the space vector PWM when the total device turn-on time is equal to the switching period. Table 7.1 reveals that when $t_7 = t_c$ ($\beta = 0$), the normalized on-time of one of the three top devices is unity for all the sectors – a top device is always clamped to the positive rail. Similarly, when $t_c = t_0$ ($t_7 = 0$, $\beta = 1.0$), a top device will always be clamped to the negative rail. When the partition parameter is defined as in (7.2) in which a modulation phase angle δ is variable, a generalized space vector PWM (GSVPWM) results.

$$\beta = 0.5 \cdot [1 - \text{Sgn}(\text{Cos}(3\omega t + \delta))] \quad (7.2)$$

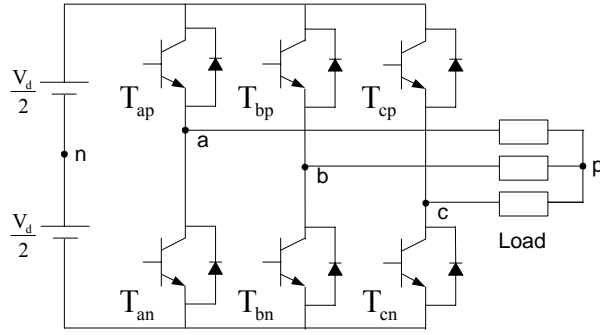
The relationship between the SVPWM and GDPWM is now set forth. Figure 7.1(a) shows a schematic diagram of a three-phase voltage source inverter in which the switching devices in the same leg are turned on complementarily. The phase voltage equations for star-connected, balanced three-phase loads expressed in terms of the existence functions (S_{ip}) of devices (T_{ip}) and input dc voltage V_d are given as

$$\begin{aligned}
 0.5 V_d (2S_{ap} - 1) &= 0.5 V_d M_{ap} = V_{ap} + V_{pn} \\
 0.5 V_d (2S_{bp} - 1) &= 0.5 V_d M_{bp} = V_{bp} + V_{pn} \\
 0.5 V_d (2S_{cp} - 1) &= 0.5 V_d M_{cp} = V_{cp} + V_{pn} \\
 S_{ip} &= 0.5 (1 + M_{ip}), \quad i = a, b, c
 \end{aligned} \tag{7.3}$$

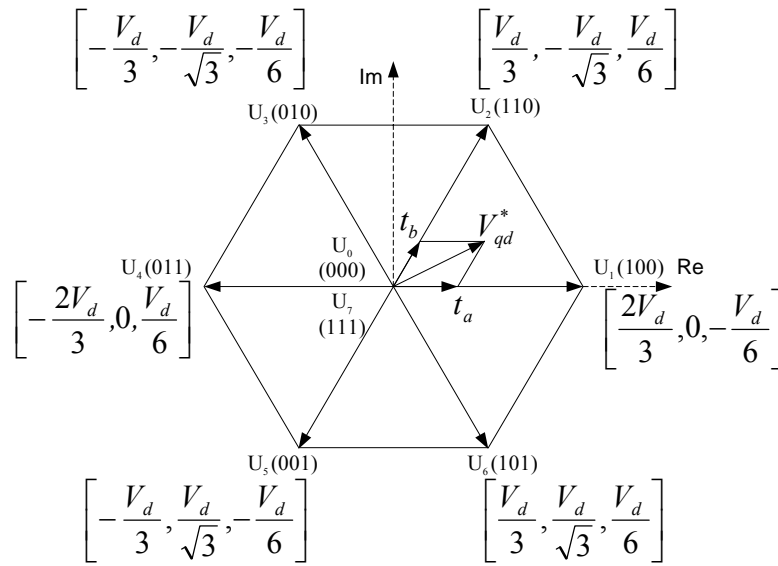
In equations in (7.1), V_{ap} , V_{bp} , V_{cp} are the phase voltages of the load while the voltage of the load neutral to inverter reference is V_{pn} . The modulation signals for the three top devices are M_{ap} , M_{bp} , M_{cp} . The equations for the generalized modulating signals of the top devices are expressed as [7.2]

Table 7.1 The turn-on normalized times for three top devices

Sector	1	2	3	4	5	6
τ_{ap}	$t_a+t_b+t_7$	t_a+t_7	t_7	T_7	t_b+t_7	$t_a+t_b+t_7$
τ_{bp}	t_b+t_7	$t_a+t_b+t_7$	$t_a+t_b+t_7$	t_a+t_7	t_7	t_7
τ_{cp}	t_7	t_7	t_b+t_7	$t_a+t_b+t_7$	$t_a+t_b+t_7$	t_a+t_7



(a)



(b)

Figure 7.1 (a) Schematic diagram of a voltage source inverter, (b) qdo voltages for the switching states.

$$M_{ip} = 2V_{ip}/V_d + 2V_{pn}/V_d, \quad i = a, b, c \quad (7.4)$$

$$V_{pn} = 0.5V_d(1-2\beta) - \beta V_{\min} - (1-\beta)V_{\max} \quad (7.5)$$

In (7.5) V_{\max} and V_{\min} are the instantaneous maximum and minimum magnitudes of the three reference balanced phase voltages, respectively. The carrier-based modulation signals which yield the same voltage waveforms as the classical space vector are obtained

when β in (7.5) is set equal to 0.5. However, other definitions of β in (7.2) with a variable modulation phase angle δ gives an infinite number of possibilities leading to the generalized discontinuous carrier-based triangle intersection PWM modulation method. Hence, the generalized space vector(GSVPWM) and the generalized discontinuous carrier-based triangle intersection(GDPWM) PWM, using the same value of β in (7.2) in the generation of the turn-on times or modulation signals yield fundamental output voltages with the same characteristics and hence are equivalent especially when operating in the linear modulation region.

7.3 Modulation in the Overmodulation Regions

Given the reference voltage as V_{qd}^* , the modulation magnitude index of a PWM inverter is defined as

$$M = \frac{|V_{qd}^*|}{\frac{2}{\pi} \cdot V_d}$$

Figure 7.2 shows the qd voltage trajectories of the inverter operating in the linear and over-modulation regions. When the inverter is operating in the linear region with the classical space vector modulation ($\beta = 0.5$), it generates sinusoidal three-phase voltages which follow the qd trajectory represented by the dark circle. The magnitude of the reference voltage lies within the inner circle of the hexagon and the magnitude modulation index ranges between zero and 0.907 ($0.0 \leq M \leq 0.907$). The inverter goes into the over-modulation region when part of the qd voltage vector is located outside the inner circle. The over-modulation region is further divided into two regions according to

the characteristics of the trajectory. In Figure 7.2(b) where $(0.907 \leq M \leq 0.95)$, corresponding to Region I over-modulation region, the inverter follows the trajectory of the dark line which generates the reference fundamental qd voltage represented by the inner dotted line. When the dark line reaches the vertices of the hexagon, the trajectory changes to that in Figure 7.2(c) representing the over-modulation region II $(0.95 \leq M \leq 1.0)$. In this case, the voltage vector stays at the vertices for enough time to generate the desired fundamental voltage [7.5].

In the space vector modulation scheme operating in the over-modulation region, the sum of the calculated times for the two adjacent active voltage states is greater than the switching period ($t_a + t_b > 1$) when the reference voltage vector is outside the hexagon. To satisfy the time constraint, times (t_a, t_b) are traditionally scaled down with respect to the switching period as shown in (7.6) to yield a new timing (t_a^*, t_b^*)

$$t_a^* = \frac{t_a}{t_a + t_b}, t_b^* = \frac{t_b}{t_a + t_b} \quad (7.6)$$

Under this scheme one of the top devices is clamped to the positive rail and another top device is clamped to the negative rail while the third one is switching under PWM. Another slightly different scheme based on Table I is proposed here which generates a higher fundamental voltage. For a device with a total normalized turn-on time greater than unity ($t_a + t_b + t_7 > 1$), the turn-on time is forced to be 1 (example: $\tau_{ap} = 1$ in sector 1). Also, since the normalized device turn-on times must be positive and less than unity, t_7 and $t_a + t_7$ or $t_b + t_7$ (depending on the sector) must satisfy these constraints: $t_7 \geq 0$, $t_a + t_7 \leq 1$ or $t_b + t_7 \leq 1$. Hence, if the new times are t_a^*, t_b^*, t_7^* , the algorithm becomes

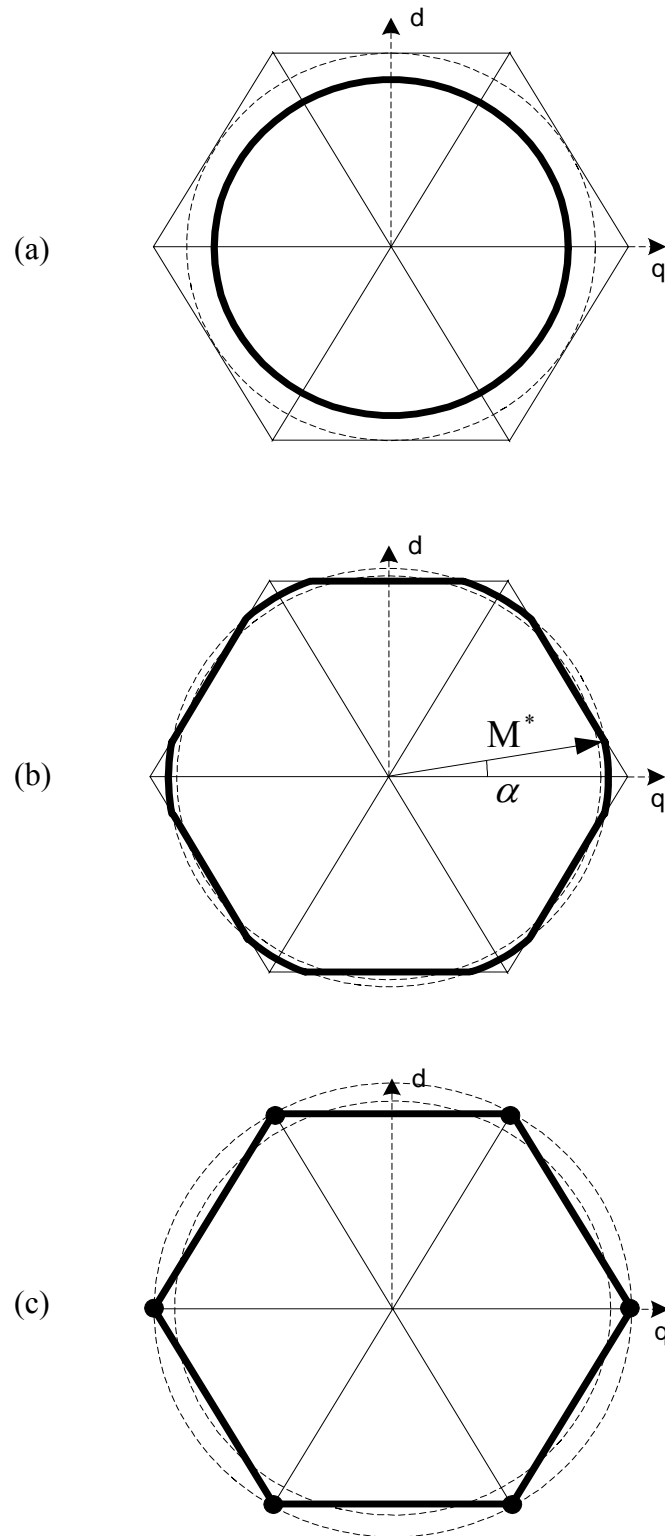


Figure 7.2 Voltage trajectories in the inverter. (a) Linear region; (b) over-modulation region I; (c) over-modulation region II.

$$\begin{aligned}
0 \leq t_a + t_b + t_7 \leq 1 & \Rightarrow t_a^* + t_b^* + t_7^* = 1 \\
0 \leq t_a + t_7, t_b + t_7 \leq 1 & \Rightarrow t_7^* \leq 1 - t_a, 1 - t_b \\
0 \leq t_7 \leq 1
\end{aligned} \tag{7.7}$$

In this formulation, t_7^* can be chosen as $t_7^* = \varepsilon (1 - t_a), \varepsilon (1 - t_b)$ while $0 \leq \varepsilon \leq 1$. Hence, in general, only one top device is clamped to the positive rail and the other two top devices are switching in the over-modulation region. Although an infinite possibilities exist, $\varepsilon = 0$ gives the highest fundamental voltage reference when two top devices are clamped (one to the positive rail and the other to the negative rail) as shown in Table 7.2. Note that in this case the time the switching top device is turned on is greater than the corresponding time for the traditional scaling solution.

For the inverter operating in the over-modulation regions, the generalized discontinuous carrier-based triangle intersection modulation scheme does not suffer the timing constraint of the generalized space vector; rather when the modulation signal is higher than the carrier signal, the device stays continually turned on – naturally limiting the fundamental component of the synthesized voltage.

Table 7.2 The turn-on normalized times for three top devices in the over-modulation region

Sector	1	2	3	4	5	6
τ_{ap}	1	t_a	0	0	t_b	1
τ_{bp}	t_b	1	1	t_a	0	0
τ_{cp}	0	0	t_b	1	1	t_a

7.4 Open-loop Voltage Generation

The classical space vector or generalized discontinuous triangle intersection PWM in which $\beta = 0.5$ can be used to generate the fundamental voltage in the linear region ($M \leq 0.907$). However, another space vector method and a generalized discontinuous triangle intersection PWM with α value of unity or zero have to be applied when the fundamental generated voltage is to be increased in the over-modulation region. The original voltage reference trajectory to be used as input to the modulator in the space vector PWM scheme needs to be changed in order to obtain the desired fundamental voltage since the reference voltage vector cannot be generated when it is out of the hexagon. The modification of the reference voltage vector introduces voltage harmonic components which are also reflected in the actual load voltage vector. In the over-modulation region I, the trajectory of reference voltage vector is changed from the inner circle to the dark line in Figure 7.2(b). When the voltage reference is within the hexagon, the classical space vector modulation is used and the suggested algorithm in Table II is implemented when the voltage trajectory lies on the hexagon. Analyzing q-axis voltage of the reference voltage trajectory gives the fundamental and harmonic components. As shown in Figure 7.2(b), particular crossover angle α or M^* (new modulation magnitude index, new voltage reference) can be found for a given reference voltage [7.5].

For a given voltage reference, the phase voltage waveform is divided into three segments for each sector. The voltage equations in each segment are expressed as (in sector 1)

$$V_q = \frac{V_{dc} \cdot \cos \theta}{\sqrt{3} \sin\left(\frac{2\pi}{3} - \alpha\right)}, \text{ for } 0 \leq \theta < \alpha \quad (7.8)$$

$$V_q = \frac{2}{3}V_{dc} - \frac{V_{dc} \cdot \sin \theta}{3 \sin\left(\frac{2\pi}{3} - \alpha\right)}, \text{ for } \alpha \leq \theta < \frac{\pi}{3} - \alpha \quad (7.9)$$

$$V_q = \frac{V_{dc} \cdot \cos \theta}{\sqrt{3} \sin\left(\frac{2\pi}{3} - \alpha\right)}, \text{ for } \frac{\pi}{3} - \alpha \leq \theta < \frac{\pi}{3} \quad (7.10)$$

where $\theta = \omega t$ and ω is the angular velocity of the fundamental voltage reference vector. Expanding the above equations in all of six sectors in a Fourier series and taking the fundamental component of it, the relationship between the crossover angle and modulation index can be found in Figure 7.3. The red one represents the relationship for the traditional scaling space vector modulation methods.

Similarly, the voltage trajectory in the over-modulation region II is modified from the inner circle to the dark line as shown in Figure 7.2(c). The major difference in this region is that the voltage vector stays at the vertices of the hexagon for some time (or corresponding holding angle α_h) and then moves along the edges. The voltage equations in each segment are expressed as (in sector 1)

$$V_q = \frac{2}{3}V_{dc}, \text{ for } 0 \leq \theta < \alpha_h \quad (7.11)$$

$$V_q = \frac{2}{3}V_{dc} - \frac{V_{dc} \cdot \sin \theta'}{3 \sin\left(\frac{2\pi}{3} - \theta'\right)}, \text{ for } \alpha_h \leq \theta < \frac{\pi}{3} - \alpha_h \quad (7.12)$$

$$V_q = \frac{1}{3}V_{dc}, \text{ for } \frac{\pi}{3} - \alpha_h \leq \theta < \frac{\pi}{3} \quad (7.13)$$

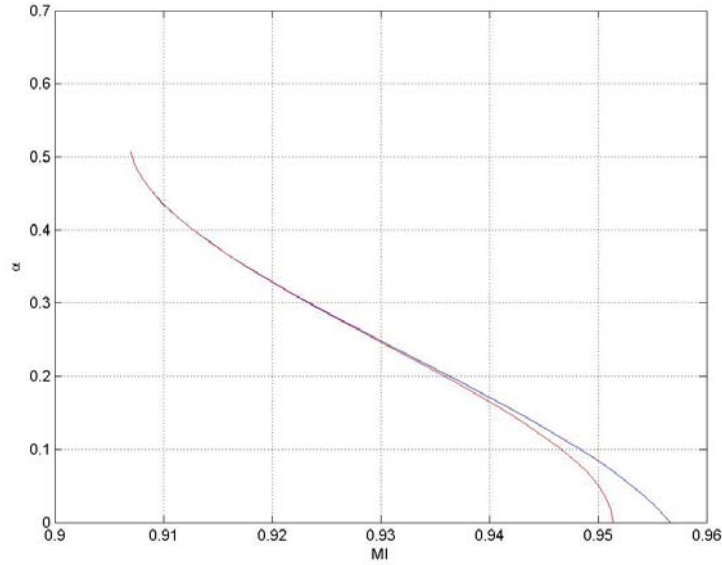


Figure 7.3 Relationship between crossover angle and modulation index in region I.

where

$$\theta' = \frac{\theta - \alpha_h}{\frac{\pi}{6} - \alpha_h} \cdot \frac{\pi}{6} \quad (7.14)$$

The relationship between the holding angle and modulation index can be found in Figure 7.4.

Figure 7.5 displays the comparison between the proposed turn-on time allocation and the classical scaling method after combining the above two figures. In over-modulation region I, for the same crossover angle, the new proposal yields higher modulation magnitude index (fundamental voltage) than that from the classical method. The same trend is seen in over-modulation region II until the two methods eventually yield the same fundamental voltage magnitude (modulation magnitude index) when the holding angle gets close to 0.524 radian (the six-step operation).

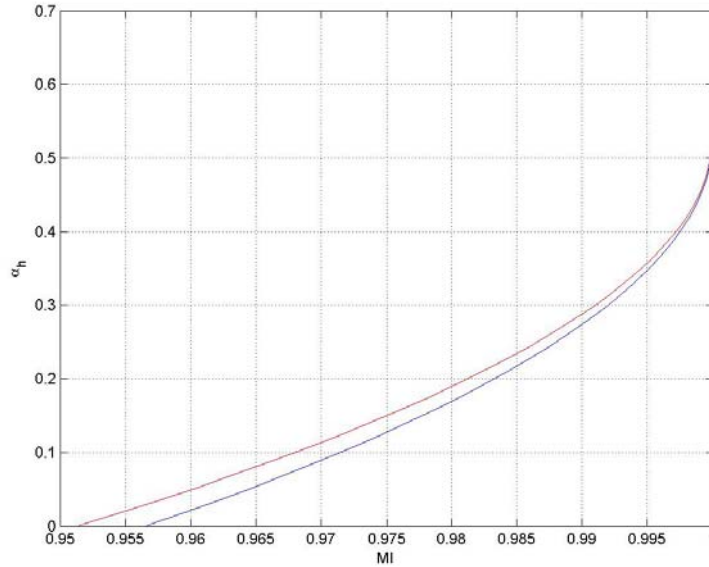


Figure 7.4 Relationship between holding angle and modulation index in region II.

Figure 7.6 also shows the plot of the new modulation magnitude index command (M^*) required to generate a desired voltage for the GDPWM scheme calculated from results in [7.3]. Similar to the approach of using space vector, the mapping curve showing the relationship between the reference and actual modulation signals needs to create first in the overmodulation region. It's also calculated through Fourier series method. The equations used for the three PWM methods are listed as following.

SVPWM, space vector PWM

$$\text{When } M^* \leq \frac{\pi}{3}, M = -\frac{1}{2}M^* + \frac{3}{\pi} \cdot M^* \cdot \arcsin\left(\frac{\pi}{2\sqrt{3}M^*}\right) + \frac{\sqrt{3}}{2} \sqrt{1 - \left(\frac{\pi}{2\sqrt{3}M^*}\right)^2};$$

$$\text{When } M^* > \frac{\pi}{3} M = \frac{3}{\pi} \cdot M^* \cdot \arcsin\left(\frac{\pi}{6M^*}\right) + \frac{1}{2} \sqrt{1 - \left(\frac{\pi}{6M^*}\right)^2}.$$

DPWM1, which is corresponding to the discontinuous PWM for $\delta = 0^\circ$.

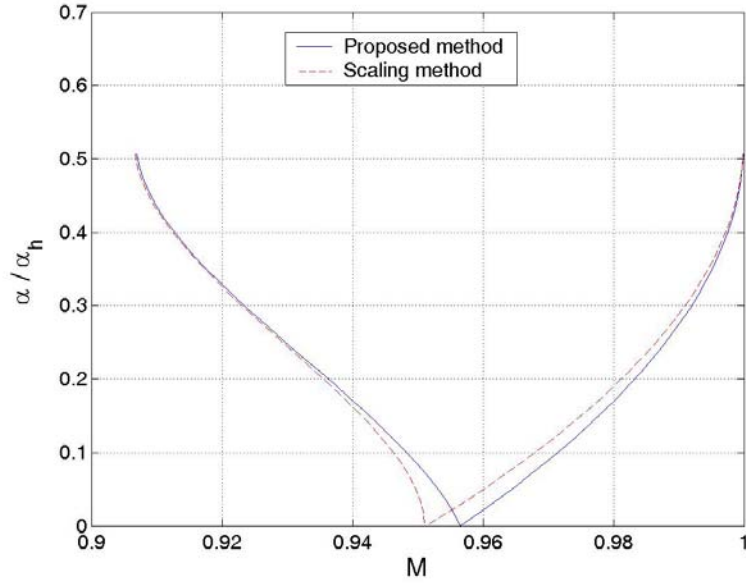


Figure 7.5 Relationship between the crossover / holding angle and modulation magnitude index.

$$M = -1 + \left(\frac{\sqrt{3}}{\pi} - \frac{1}{2} \right) M^* + \frac{\pi}{4\sqrt{3}} \cdot \frac{1}{M^*} + \frac{3}{\pi} \cdot M^* \cdot \arcsin\left(\frac{\pi}{2\sqrt{3}M^*} \right) + \frac{\sqrt{3}}{2} \sqrt{1 - \left(\frac{\pi}{2\sqrt{3}M^*} \right)^2}$$

DPWM2, which is corresponding to the discontinuous PWM for $\delta = -30^\circ$.

When $M^* \leq \frac{\pi}{3}$,

$$\begin{aligned} \psi &= -\frac{\pi}{3} + \arcsin\left(\frac{\pi}{2\sqrt{3}M_i^*} \right) \\ a_1 &= \frac{M^*}{4} - \frac{\sqrt{3}}{2} \sin\left(\psi - \frac{\pi}{6} \right) + \frac{3\psi}{2\pi} M^* - \frac{3}{4\pi} M^* \cos\left(2\psi + \frac{\pi}{6} \right); \\ b_1 &= -\frac{1}{2} \cos\left(\psi + \frac{\pi}{3} \right) + \frac{\sqrt{3}}{4\pi} M^* \times \left(\frac{\pi}{3} - 2\psi - \sin\left(2\psi - \frac{\pi}{3} \right) \right) \\ M &= 2\sqrt{a_1^2 + b_1^2} \end{aligned}$$

When $M^* > \frac{\pi}{3}$,

$$\alpha = \frac{2\pi}{3} - \arcsin\left(\frac{\pi}{2\sqrt{3}M^*}\right)$$

$$a_1 = \frac{\sin \alpha}{2} + \left(\frac{1}{2} - \frac{\sqrt{3}}{8\pi} - \frac{3\alpha}{4\pi}\right)M^* - \frac{\sqrt{3}}{4\pi}M^* \cos\left(2\alpha - \frac{2\pi}{3}\right);$$

$$b_1 = -\frac{\cos \alpha}{2} + \frac{\sqrt{3}}{2\pi}M^* \times \left(\frac{\sqrt{3}}{4} - \frac{1}{2}\sin\left(2\alpha - \frac{2\pi}{3}\right) + \frac{\pi}{3} - \frac{\alpha}{2}\right)$$

$$M = 2\sqrt{a_1^2 + b_1^2}$$

It is seen that in the overmodulation region, the actual modulation index M is calculated for the open-loop voltage generation when the desired modulation index is M^* . For the three cases displayed, the highest voltage gain (lowest M^*) is obtained when $\delta = 0^\circ$.

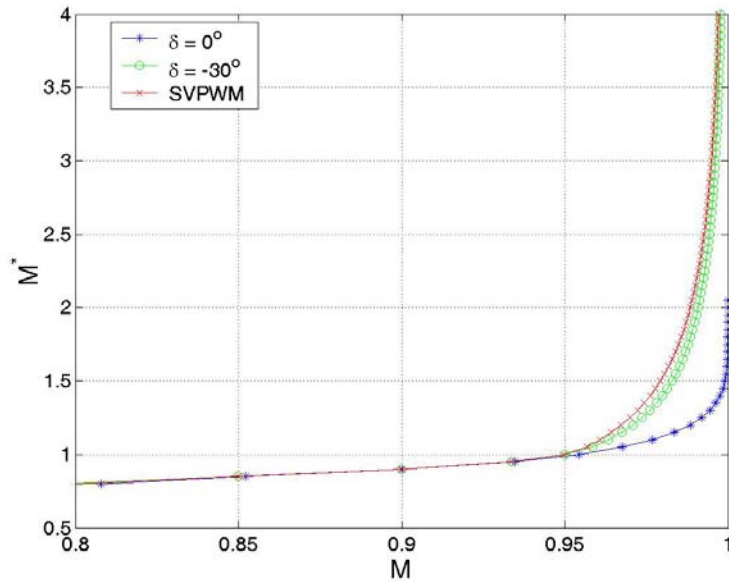


Figure 7.6 Mapping of the reference and actual modulation magnitude index for operation in the over-modulation region.

7.5 Current Regulation

Current regulation is generally required in most high performance motor drive applications in which the q and d axis stator currents are generally regulated to ensure torque or speed control. Standard proportional plus integral (PI) type controller implemented in the synchronous reference frame is usually adequate for most practical applications. However, when the modulator is required to operate in the over-modulation and six-step regions, the synchronous reference frame PI controller has been found to be inadequate due to its inability to regulate or reject the harmonic currents flowing in the load which are impressed by the added harmonic voltages. Although the harmonic current component of the load current can be filtered using a high pass filter, they lead to a slower system response requiring the current bandwidth to be reduced if the feasibility of control loop instability is to be minimized. An innovative solution for this problem which is applicable when the inverter is under space vector modulation is given in [7.6]. Instead of filtering the load current, the harmonic current is estimated and removed from the measured current, the balance of which is regulated using the classical synchronous reference frame PI controller. The actual reference voltage for the space vector calculation needed for the synthesis of the required fundamental load voltage vector is obtained from the off-line gain mapping shown in Figure 7.5. Through experimental results, it was shown that this scheme works well even up to the six-step operation.

In another development for an inverter using the discontinuous carrier-based triangle intersection PWM and operating in the over-modulation regions, because the

different modulation variants have different phase errors between the fundamental reference and actual fundamental voltages, it is shown that the standard synchronous reference frame PI current controller works poorly with varying degrees of success in executing motor speed or torque control. Dynamic over-modulation and steady-state over-modulation trends are different in so much as the modulation variant with the highest steady-state voltage gain does not give the best over-modulation dynamic current/torque response. This dynamic performance degradation is proposed to be diminished by using an anti-windup controller which bounds the integrator output of the synchronous reference PI controller with care taken to select the proper limit of the integrator [7.6].

In this section, a current regulation approach is presented that is similar in concept to the one set forth in [7.6] but differs in the open-loop load harmonic current estimation scheme. In [7.6], the estimated synchronous reference harmonic current is obtained by exciting a machine parameter dependent first-order estimator by the difference between the reference fundamental and actual voltages. In this chapter, the actual load harmonic model is used to estimate the harmonic current in the stationary reference frame. It is then subtracted from the stationary reference frame load current and the balance is transformed to the synchronous reference frame for current regulation. A converter feeding a passive load shown in Figure 7.5 illustrates the approach. The complex-variable model equation of the load in the stationary reference frame is given ($p = d/dt$) in (7.15). They are separated into the fundamental and harmonic components (f_{qdf} and f_{qdh} respectively). Transforming the fundamental component equations into the synchronous

reference frame rotating at ω_e , the model to be used for controller design for the fundamental load current component results in (7.17).

$$V_{qd} = r_s I_{qd} + L_s p I_{qd} + E_{qd} \quad (7.15)$$

$$V_{qd} = V_{qdf} + V_{qdh}, \quad I_{qd} = I_{qdf} + I_{qdh} \quad (7.16a)$$

$$V_{qdf} = r_s I_{qdf} + L_s p I_{qdf} + E_{qdf} \quad (7.16b)$$

$$V_{qdh} = r_s I_{qdh} + L_s p I_{qdh} \quad (7.16c)$$

$$V_{qde} = r_s I_{qde} + L_s p I_{qde} - j \omega_e I_{qde} + E_{qde} \quad (7.17)$$

In Figure 7.7, the harmonic load current in the stationary reference frame is estimated based on (7.16c). When the inverter is space vector modulated, the harmonic voltage is obtained from the difference between the actual space vector voltage trajectory shown in Figure 7.2 and the command fundamental voltage all expressed in the stationary reference frame. This current is subtracted from the measured current expressed in the stationary reference frame, the balance of which is the fundamental load current which expressed in the synchronous reference frame is used for the current regulation using the synchronous reference frame PI controllers. If the modulation method is the generalized discontinuous carrier-based triangle intersection PWM modulation, the harmonic voltage is obtained from the difference between the load voltage estimated using the converter switching functions and the reference fundamental voltage expressed in the stationary reference frame. Furthermore, in Figure 7.7, there is a gain-mapping block (G, which are Figures 7.5,6 for the space vector and carrier-based triangle intersection modulations, respectively) which maps the reference fundamental voltage (modulation magnitude index) to the actual modulation magnitude index (load fundamental voltage). In the carrier-based scheme the angle of the fundamental reference voltage is preserved in the

fundamental voltage mapping scheme. From (7.10) and Figure 7.7, the controller structure with a controller ($K_{qd} = \text{PI}$ or IP) is determined as follows.

$$V_{qde}^* = \sigma_{qde} - j \omega_e I_{qde} + E_{qde} \quad (7.18)$$

$$\sigma_{qde} = r_s I_{qde} + L_s p I_{qde} = K_{qd} (I_{qde}^* - I_{qde})$$

The transfer function of the current control (where $K_{qd} = K_p + K_i/p$) is

$$\frac{I_{qde}}{I_{qde}^*} = \frac{K_p p + K_i}{L_s p^2 + (r_s + K_p) p + K_i} \quad (7.19)$$

The controller parameters are appropriately selected to meet desired dynamic response specifications and system stability.

While the current control scheme (7.18) ensures current regulation when a converter operates in the over-modulation region, it may not give a good speed/torque control of a motor drive since torque pulsation producing harmonic currents are still present in the motor. A viable way to remedy this limitation is to use a modulation scheme which produces the least harmonic load voltage. Furthermore, a natural reference current regulator to eliminate or reduce the most important harmonic current component is added to the motor control algorithm, the output of which is added to the reference voltage generated by the synchronous reference frame PI controller to modulate the inverter to minimize the generated load harmonic voltage.

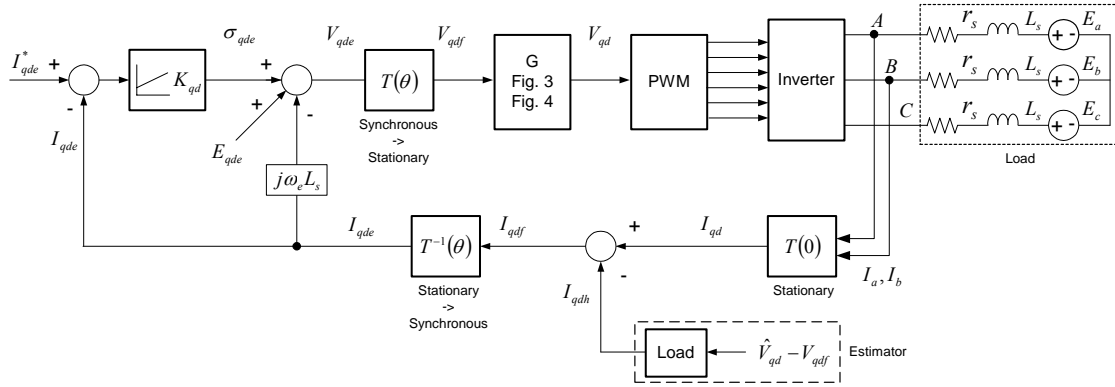


Figure 7.7 Diagram of current regulation in all modulation regions.

The current regulation in the overmodulation region is simulated through changing the reference currents. The reference currents are changed corresponding to Figure 7.8, in which the two currents are selected such that the operation is in the linear modulation region first. And then these two currents are ramped up to generate enough reference voltages and make the operation in the overmodulation region. It is seen that the two currents in the synchronous reference frame are regulated very well using the proposed method. The phase currents for the fundamental and harmonic components are shown in Figure 7.9. The harmonic component appears in the overmodulation region. But it has been eliminated effectively such that this component does not affect the regulation of fundamental q- and d-axis currents.

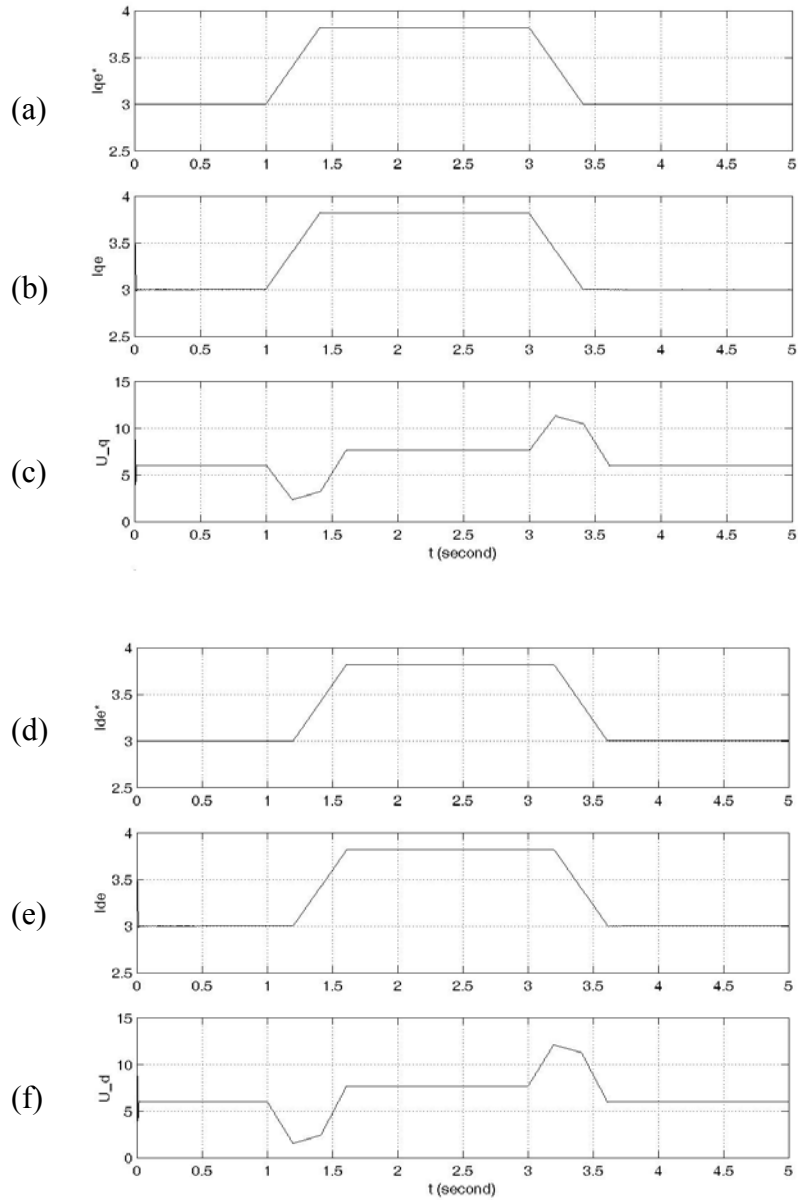


Figure 7.8 Simulation of current regulation for q- and d-axis currents. (a) Q-axis reference current; (b) q-axis actual current; (c) the output from the current controller for q-axis current; (d) d-axis reference current; (e) d-axis actual current; (f) the output from the current controller for d-axis current.

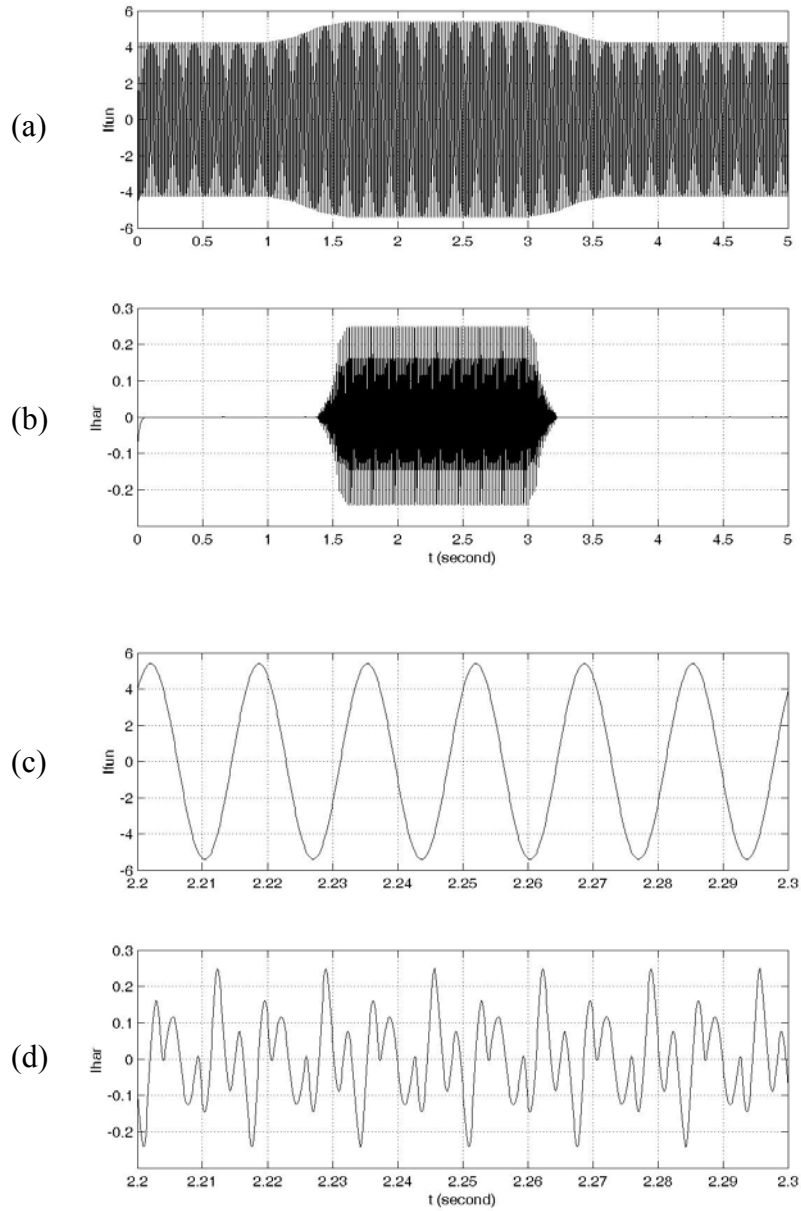
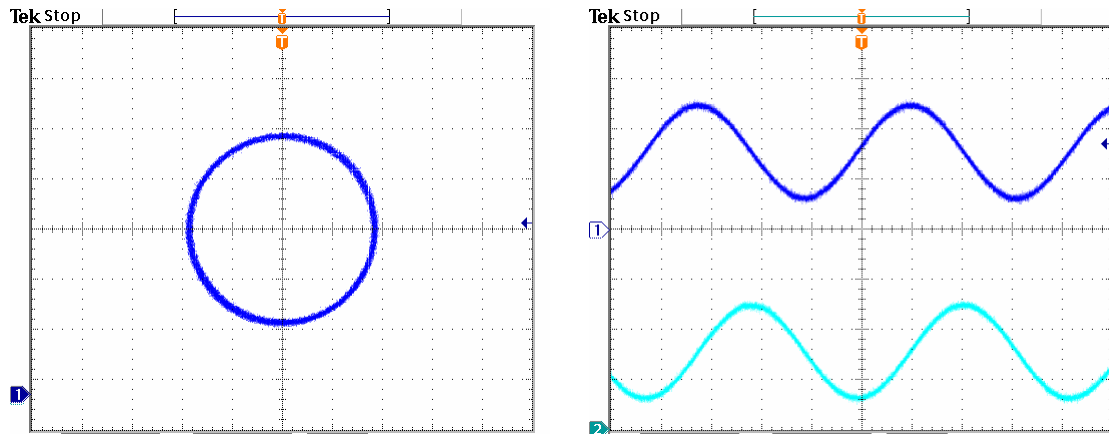


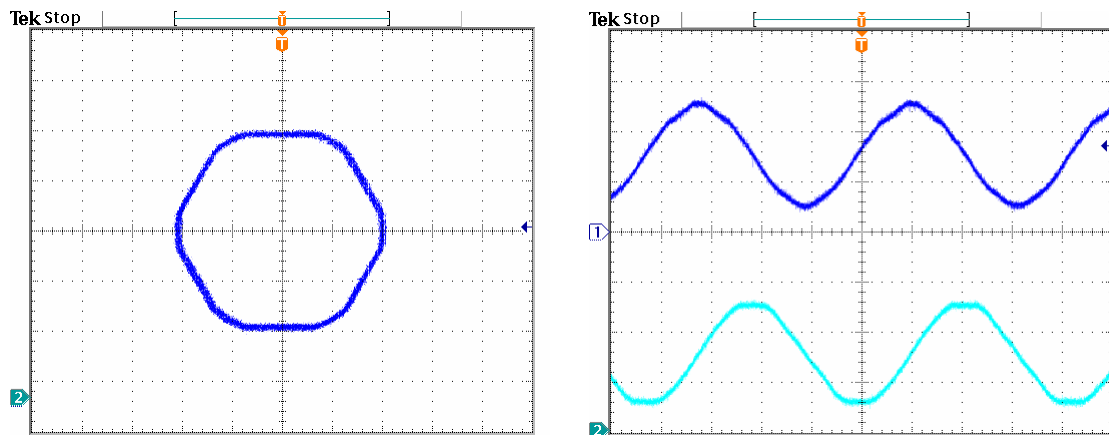
Figure 7.9 Simulation of current regulation. (a) Phase A fundamental current during the transient; (b) phase A harmonic current during the transient; (c) phase A fundamental current at steady state in the overmodulation region; (d) phase A harmonic current at steady state in the overmodulation region.

7.6 Experimental Results

The trajectories of V_q and V_d and the waveforms for V_q and V_d under four operation conditions are implemented using a TI TMS 320LF2407 DSP as shown in Figure 7.10.



(a)



(b)

Figure 7.10a Trajectory of V_q and V_d and the waveforms for V_q and V_d (0.6/div). (a)

Linear modulation region; (b) overmodulation region I.

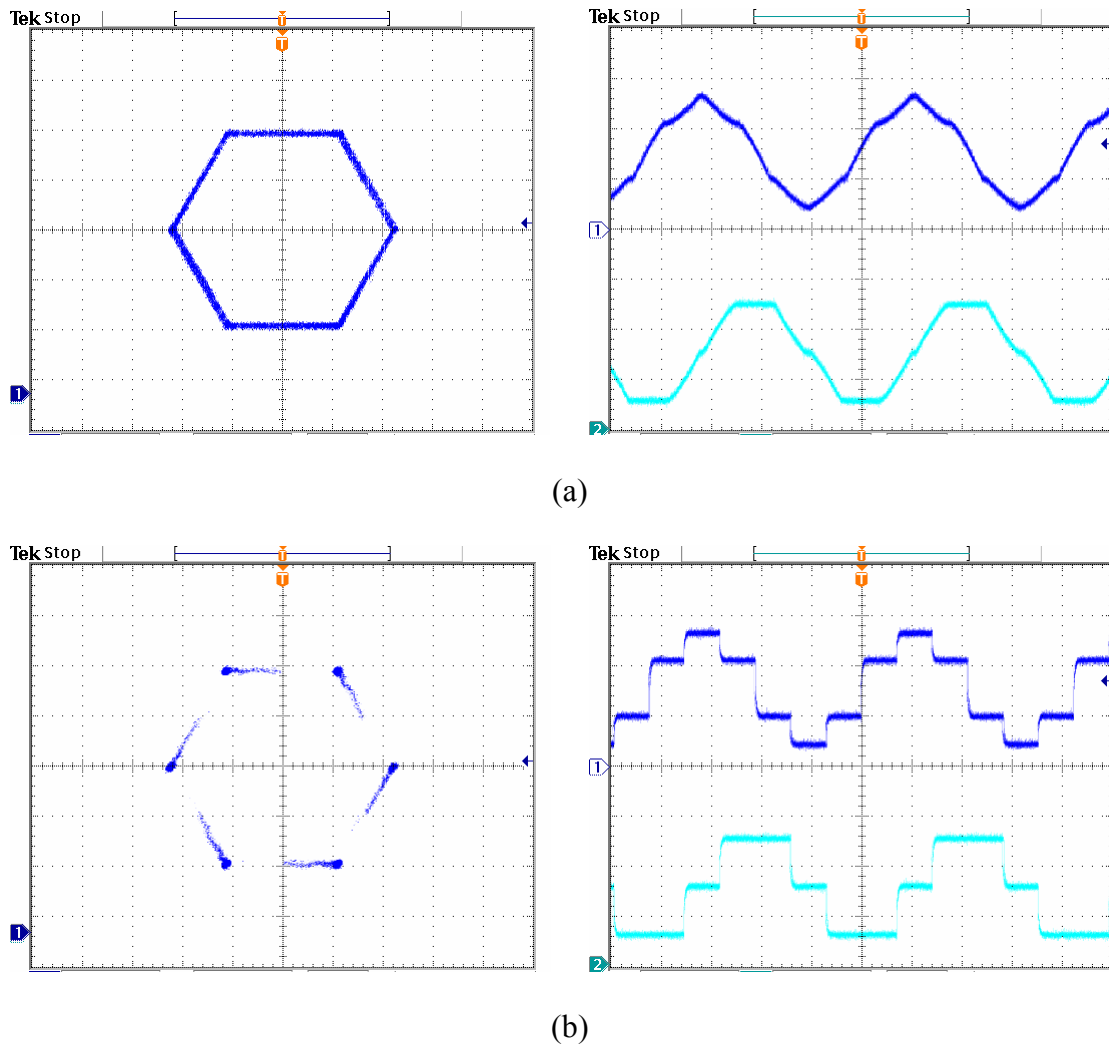


Figure 7.10b Trajectory of V_q and V_d and the waveforms for V_q and V_d (0.6/div). (a) Overmodulation region II; (b) six step operation.

The proposed current control technique and the modulation schemes have been implemented using the TMS 320LF2407 DSP. The experiments have been done by step changing the q and d -axis reference currents while the magnitudes of the current ensure transitions from one operation region to another. The three-phase wye-connected passive load has a per-phase resistance of 1.93 Ohms and a per-phase inductance of 56.65 mH.

The switching frequency of the converter is 10 kHz, load current frequency is 60 Hz and the DC input voltage is 150 V. The implementation procedure is as follows.

1. Determine the relationship between the crossover angle α / holding angle α_h and the magnitude of reference voltage using either linearization method or lookup table, which is corresponding to simulation results.
2. Check the region of current reference voltage and find the corresponding angle if it is in the overmodulation regions.

Linear modulation: use continuous / discontinuous method;

Overmodulation I: use curve for the crossover angle;

Overmodulation II: use curve for the holding angle.

3. In the overmodulation region I, for example in sector I,

When $0 < \theta < \alpha$, use linear modulation;

When $\alpha < \theta < 60^\circ - \alpha$, use the proposed method for the overmodulation: use

$$\frac{V_{dc}}{\sqrt{3} \cdot \sin(2\pi/3 - \alpha)}$$
 as the magnitude of reference voltage, θ as the

actual angle;

When $60^\circ - \alpha < \theta < 60^\circ$, use linear modulation again.

4. In the overmodulation region II, for example in sector I,

When $0 < \theta < \alpha_h$, hold the switching pattern at vertex 1;

When $\alpha_h < \theta < 60^\circ - \alpha_h$, calculate the actual angle to be used,

$$\theta' = \frac{\theta - \alpha_h}{\pi/6 - \alpha_h} \cdot \frac{\pi}{6}, \text{ use } \frac{2}{3}V_{dc} \text{ as the magnitude of reference voltage, } \theta'$$

as the actual angle and then use the proposed method for the overmodulation;

When $60^\circ - \alpha_h < \theta < 60^\circ$, hold the switching pattern at vertex 2.

In the implementation of the control scheme, the actual phase voltages are required in order to find the harmonic currents. There are two ways of doing this: either measuring the voltages using voltage sensors or using switching functions to reconstruct the phase voltages. The formulations are shown in (7.20).

$$\begin{aligned}
 V_{as} &= \frac{V_{dc}}{3T_s} \cdot (2\tau_{ap} - \tau_{bp} - \tau_{cp}) \\
 V_{bs} &= \frac{V_{dc}}{3T_s} \cdot (-\tau_{ap} + 2\tau_{bp} - \tau_{cp}) \\
 V_{cs} &= \frac{V_{dc}}{3T_s} \cdot (-\tau_{ap} - \tau_{bp} + 2\tau_{cp})
 \end{aligned} \tag{7.20}$$

where τ_{ap} , τ_{bp} and τ_{cp} are the on-durations for the three top devices calculated from symmetric sine-PWM and T_s is the switching period.

The control system using the space vector modulation scheme (with the mapping gain block) is implemented and Figure 7.11 shows the q and d-axis currents, line-line voltage and phase current when the reference currents are varied to make the inverter transition from one region to another. It can be seen that the axes currents are regulated appropriately for the three regional transitions. Figure 7.12 gives phase ‘a’ currents in the three operational regions. The synthesized fundamental load currents obtained by removing the harmonic load are also displayed. In the same figure, the voltage trajectories during transitions are shown.

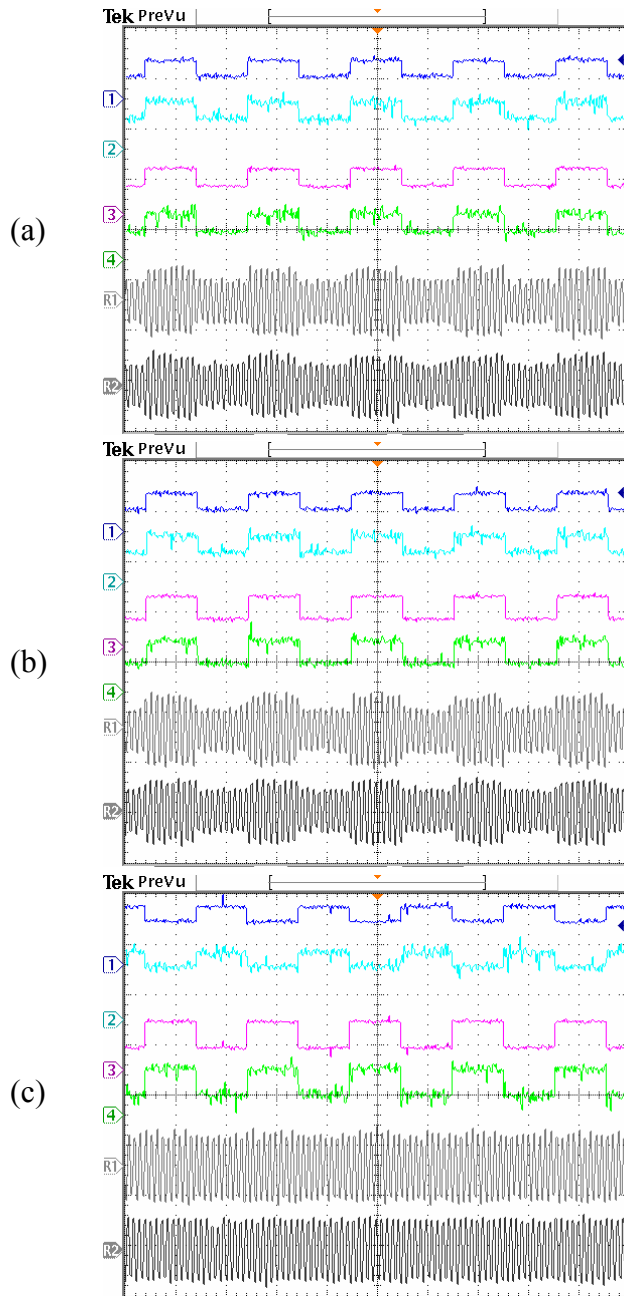


Figure 7.11 Current regulation using space vector modulation. (a) Linear – over-modulation region I; (b) linear–overmodulation region II; (c) overmodulation region I–II. (1) reference q-axis current (3A/div), (2) measured fundamental q-axis current (3A/div), (3) reference d-axis current (3A/div), (4) measured fundamental d-axis current (3A/div), (R1) line-line voltage (200V/div), (R2) phase A measured (raw) current (6A/div).

Figure 7.13 shows corresponding current regulation results when the inverter is modulated with the discontinuous carrier-based triangle intersection modulation (with the mapping gain accounted for) and $\delta = 0^\circ$. The current regulation is very good. Figure 7.14 shows the estimated harmonic currents (with converter operating in the linear and over-modulation regions) which when subtracted from the load currents make load current regulation possible. The fundamental currents feedback for current control is very clean even when the converter is operating in over-modulation region II.

Finally, one questions whether the mapping block G is really needed in the current control system to achieve good current regulation using discontinuous PWM. It would appear, based on limited computer simulation studies that the current regulation is achieved without accounting for mapping gain when the converter operates in the over-modulation region. The important consideration therefore to good current regulation using the decoupling control scheme shown in Figure 7.7 is not so much on the type of modulation scheme, but on the ability to remove the load harmonic current from the current control loop.

However, for speed and torque control, modulation schemes giving minimum harmonic voltage components with the current regulation in Figure 7.5 should be very effective. Figure 7.15 displays the current regulation using the discontinuous carrier-based triangle intersection modulation with $\delta = 0^\circ$ without including the non-linear mapping gain. The current regulator works well for all transitions from linear to the over-modulation regions of operation. Experimental results confirmed by simulation results do not show any increase of converter actuating reference voltages when compared to the case when the mapping gain is included in the control scheme. Apparently, the

decoupling terms in the expression of the reference voltage (7.18) ensures the appropriate matching of the reference and the fundamental component of the actual voltage – minimizing both the magnitude and phase errors.

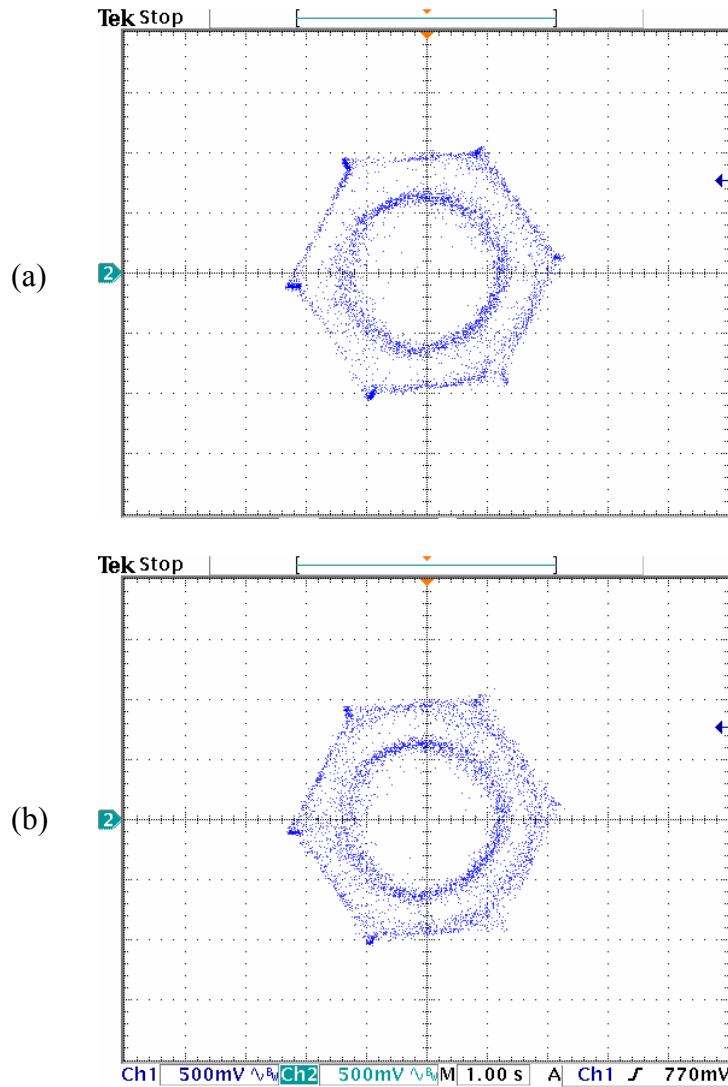


Figure 7.12a Voltage ($V_q - V_d$) trajectories using space vector modulation (25V/div). (a) Linear to over-modulation region I transition; (b) linear to over-modulation region II transition.

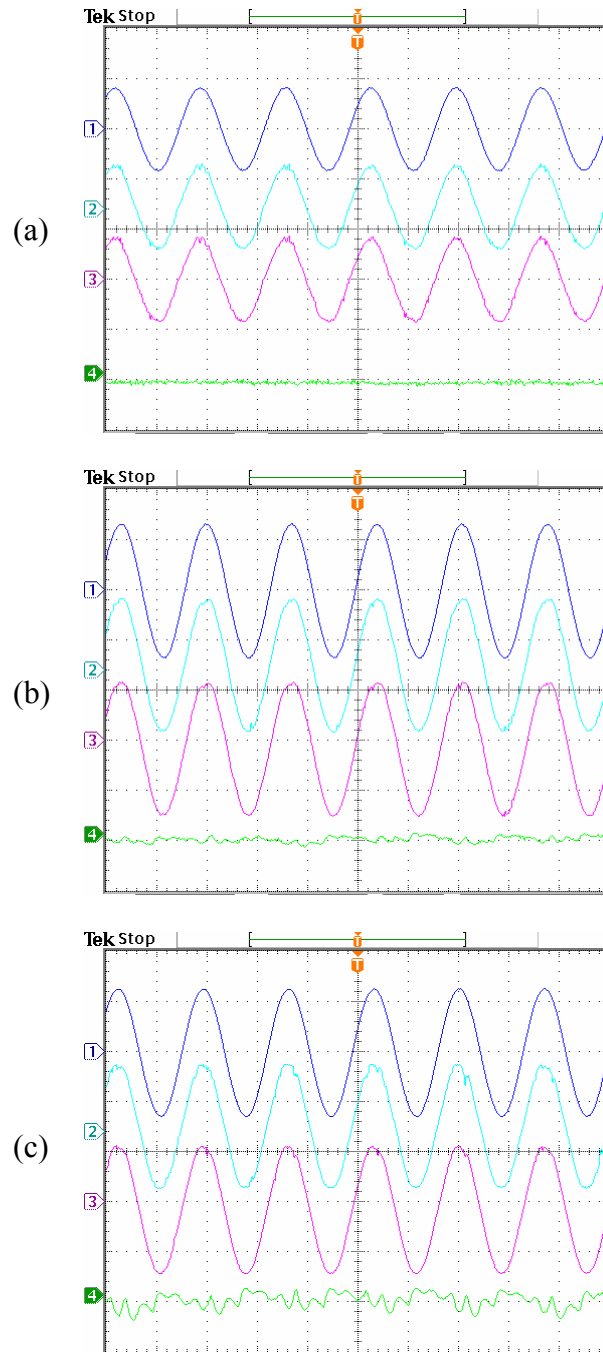


Figure 7.12b Current waveforms of phase A. (a) Linear modulation region; (b) over-modulation region I; (c) over-modulation region II. Ch1: reference current (1.5A/div), Ch2: measured current (1.5A/div); Ch3: fundamental frequency current (1.5A/div); Ch4: harmonic current (0.6A/div).

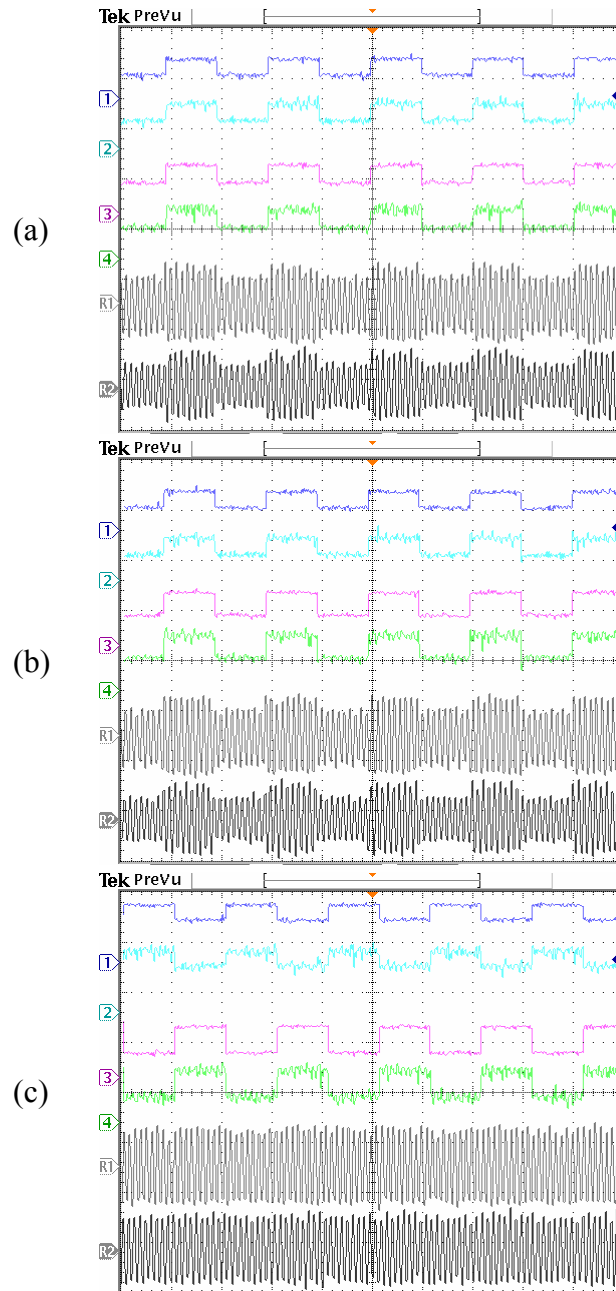


Figure 7.13 Current regulation using discontinuous carrier-based modulation with gain

G. (a) Linear – over-modulation region I; (b) linear–overmodulation region II; (c) overmodulation region I–II. Ch1: reference q-axis current (3A/div); Ch2: measured fundamental q-axis current (3A/div); Ch3: reference d-axis current (3A/div); Ch4: measured fundamental d-axis current (3A/div); ChR1: line-line voltage (200V/div), ChR2: phase A measured (raw) current (6A/div).

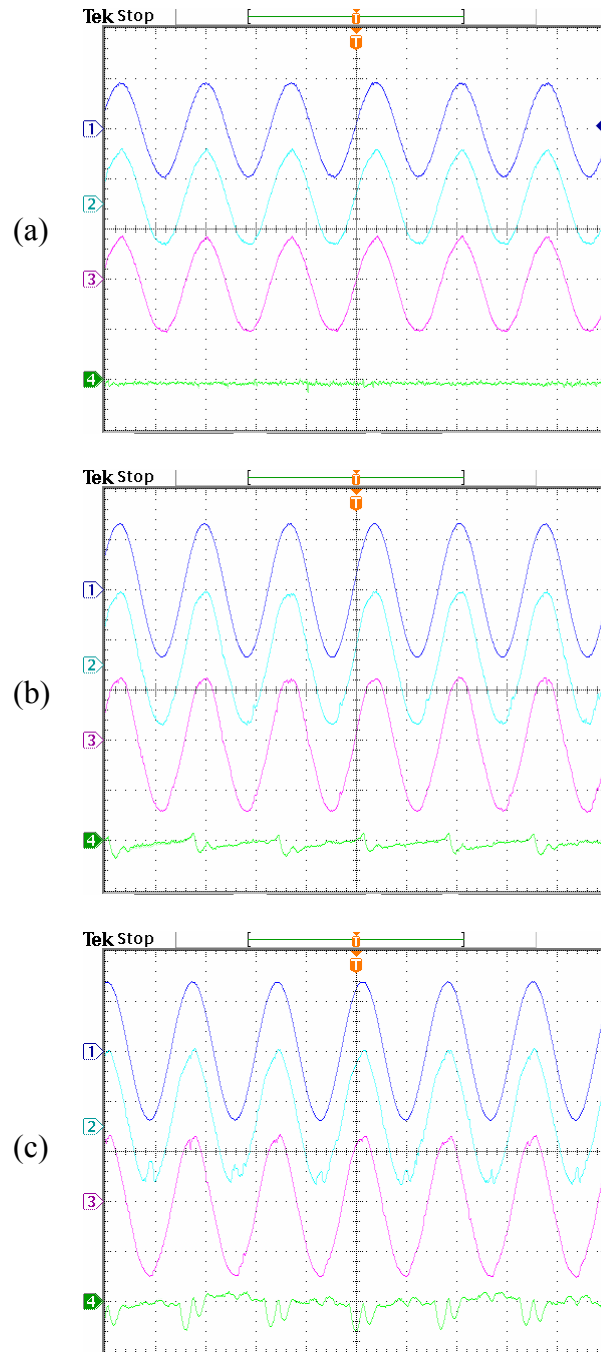


Figure 7.14 Current waveforms of phase A using discontinuous carrier-based modulation with gain G . (a) Linear modulation region; (b) over-modulation region II; (c) over-modulation region II. Ch1: reference current (1.5A/div); Ch2: measured current (1.5A/div); Ch3: fundamental frequency current (1.5A/div); Ch4: harmonic current (0.6A/div).

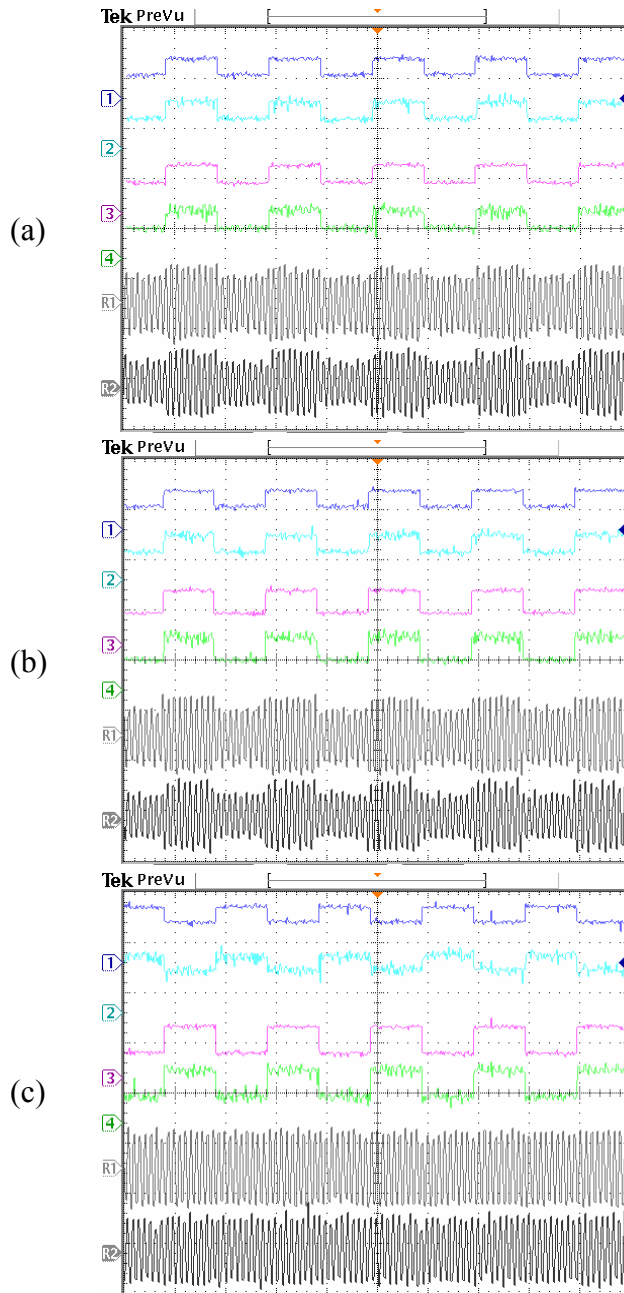


Figure 7.15 Current regulation using discontinuous carrier-based modulation without gain G . (a) Linear – over-modulation region I; (b) linear-overmodulation region II; (c) overmodulation region I–II. Ch1: reference q-axis current (3A/div); Ch2: measured fundamental q-axis current (3A/div); Ch3: reference d-axis current (3A/div); Ch4: measured fundamental d-axis current (3A/div); ChR1: line-line voltage (200V/div); ChR2: phase A measured (raw) current (6A/div).

7.7 Conclusion

This chapter developed and unified the generalized space vector (GSVPWM) and generalized discontinuous carrier-based (GDPWM) PWM methods in the linear and over-modulation regions. A time-varying partition factor β (which is time-varying in general and ranging between zero and unity) provides an equivalency link between the two schemes. An algorithm that provides a higher fundamental voltage than the time-scaling procedure traditionally used for space vector PWM modulator for voltage synthesis in the over-modulation region is also proposed.

Then the load current regulation of a current regulated voltage source inverter is explored accounting for the nonlinear converter gain introduced when operating in the over-modulation regions. A current decoupling and linearizing control scheme with the harmonic current estimation process is used to ensure good current regulation even when the converter operates in the over-modulation region for both the generalized space vector and the generalized discontinuous carrier based triangle intersection modulation schemes. Some experimental results have been provided to confirm the validity of the control and estimation schemes for the two modulation methods. It would appear that with a good load harmonic estimation algorithm and a decoupling linearizing control structure, any modulator scheme with a high open loop voltage gain characteristics will provide a high performance closed loop current characteristics with or without accounting for the converter gain nonlinearity. The modulation phase angle δ which gives different GDPWM and GSVPWM schemes can indeed be regulated on-line to ensure the

nulling of the phase angle between the reference and actual voltage vectors – a phase angle difference which has been proven to negatively influence the over-modulation response of the controlled drive systems.

CHAPTER 8

CONCLUSIONS AND FUTURE WORK

This chapter summarizes the contributions made by this dissertation. The contributions in different areas are described in separate paragraphs. The previous work done in these areas has been detailed in Chapter 1 to establish some background on the work carried out in this dissertation. The scope for future work is discussed and some suggestions are made based on the work developed.

8.1 Conclusions

The PWM modulation techniques for the three-phase voltage source inverter are presented including both carrier-based PWM and space vector PWM. The equivalence is set up between these two methods for the normal operation. The concept of space vector is extended to the multi-phase systems in the example of five and six phases. The space vector diagram is drawn using the generalized transformation and then used to synthesize the reference voltages. For the multi-phase system, the reference voltage other than the fundamental one can be generated, which can be third harmonic component when the single machine is running or other sequence component that can be used to drive the other motor in series. The calculation of zero sequence voltage expressions is done by choosing the appropriate active and null states and then these expressions are generalized and added to the reference voltage to generate the modulation signals. The switching

signals are generated using carrier-based PWM through the comparison between these modulation signals and the high frequency carrier signals. This method is easy to implement compared with the direct space vector approach and can be used for any multi-phase system.

The induction machine model in the arbitrary reference frame and the general transformations are presented explicitly, which are used for the control analysis of induction machines. The procedure of determining the machine parameters is presented and used to determine the parameters of the experimental induction machine. Then the rotor flux oriented control of the induction machine is illustrated and the cascaded speed control scheme is designed. The controller parameters are designed using Butterworth polynomial and the implementation procedures are presented in detail, which are useful for the design and implementation of any other control system. The proposed scheme has been verified through simulations and experiments.

The natural variables are defined for the induction machine and then used to formulate the speed control, which are all calculated in stationary reference frame and no reference frame transformation is necessary. The efficiency of the induction machine is improved through the minimum electrical loss strategy formulated using the same variables. The optimum rotor flux is resulted from the strategy and used as the reference one in the speed control. Also the rotor speed estimation using both rotor voltage equations is proposed and the simulation shows much better estimation result. The experiments are conducted to verify the proposed formulation and the sensorless method.

The closed-loop speed estimation using the full-order flux observer is explored and the design process is illustrated for the speed control. The consideration of including the

reactive power in the error function for the speed estimation improves the performance in the low speed range. The observer gains are determined using the 4th order Butterworth polynomial and the control parameters for the speed estimation are selected using the D-decomposition method to ensure the system stability. It is shown that the same set of parameters can be chosen from the proposed method to make the system stable under both motoring and regenerating modes. The characteristics of the full-order flux observer and the effectiveness of proposed method of selecting parameters have been shown in the simulation results.

The modulation characteristics for the carrier-based PWM and space vector PWM are found in over-modulation region. A new over-modulation scheme is proposed using the concept of space vector, which has a higher voltage gain compared with the traditional scaling method. The application for the current regulation is generalized for both modulation methods and the idea of eliminating the harmonic current in stationary reference frame is proposed in order to use the linear controller structure and generate higher fundamental voltages in the over-modulation region. Both PWM methods are implemented for the current regulation on the R-L load and the comparison is made on the analysis of advantages and disadvantages.

8.2 Future Work

There are several possible areas for future research based on the sensorless control of induction machines and associated PWM modulation schemes presented in this dissertation. Although the modulation technique for three-phase voltage source

converters has been extended to the multi-phase system including five and six phases, the effect of selecting the active states and zero sequence voltages on the real multi-phase machine are not verified through experiments yet. It is expected that the electric torque performance of the induction machine can be possibly improved by using different states and zero sequence voltages.

The proposed sensorless approach using the full-order flux observers can also be used for the rotor speed sensorless control for the permanent magnet machine. The other application of this full-order flux observer system is for the multi-phase machines combined with the modulation scheme proposed in this dissertation. The procedures of selecting the observer gain and controller parameters are applicable for motor control system designs ensuring system stability.

The control using natural variables can be extended to the control of the multi-phase machines, which could also be used for loss minimization. The over-modulation technique for three-phase system and the idea of eliminating harmonic currents are helpful to enhance the robustness of multi-phase machine systems under both normal and faulty operating conditions.

REFERENCES

- [2.1] A. Schonung and H Stemmler, "Static frequency changers with subharmonic control in conjunction with reversible speed ac drives," *Brown Boveri Rev.*, vol. 1, no. 51, nos. 8/9, pp. 555-557, Sept. 1964.
- [2.2] G. Pfaff, A. Weschta, and A Wick, " Design and experimental results of a brushless ac servo drive," *IEEE Transactions on Industry Applications*, IA-20, pp. 814-821, 1984.
- [2.3] J A Houldsworth and D. A. Grant, " The use of harmonic distortion to increase the output voltage of the three phase PWM," *IEEE Transactions on Industry Applications*, vol. 24 , pp. 142-150, 1988.
- [2.4] A. Hava, R. J. Kerkman and T. A. Lipo, "A High Performance Generalized Discontinuous PWM Algorithm," *IEEE Transactions on Industry Applications*, vol. 34, no. 5, pp. 1059-1071, September/October 1998.
- [2.5] L. Xu and W. N. Fu, "Evaluation of third harmonic component effects in five-phase synchronous reluctance motor drive using time-stepping finite element method," *IEEE Transactions on Industry Applications*, vol. 38, no. 3, pp. 638 – 644, May/June 2002.
- [2.6] R. O. Lyra and T. A. Lipo, "Torque density improvement in a six-phase induction motor with third harmonic current injection," *IEEE Transactions on Industry Applications*, vol. 38, no. 5, pp. 1351 – 1360, Sep./Oct. 2002.
- [2.7] E. Levi, M. Jones and S. N. Vukosavic, " Even-phase multi-motor vector controlled drive with single inverter supply and series connection of stator windings," *IEE Proceeding - Electric Power and Applications*, vol. 150, no. 5, pp. 580 – 590, September 2003.
- [2.8] E. Levi, M. Jones, N. Vukosavic and H. A. Toliyat, " A novel concept of a multiphase, multimotor vector controlled drive system supplied from a single voltage source inverter," *IEEE Transactions on Power Electronics*, vol. 19, no. 2, pp. 320 – 335, March 2004.
- [2.9] E. Levi, S. N. Vukosavic and M. Jones, "Vector control schemes for series-connected six-phase two-motor drive systems," *IEE Proceedings – Electric Power and Applications*, vol. 152, no. 2, pp. 226 – 238, April 2005.
- [2.10] O. Ojo, "The generalized discontinuous PWM scheme for three-phase voltage source inverters," *IEEE Transactions on Industrial Electronics*, vol. 51, no. 6, pp. 1280 – 1289, December 2004.
- [2.11] E. A. Klingshirn, "High power order induction motors, - Part I – Description and theoretical consideration," *IEEE Transactions on Power Systems and Apparatus*, vol. 102, no. 1, pp. 46 – 53, January 1983.

- [2.12] M. A. Abbas, R. Christen and T. M. Jahns, “ Six-phase voltage source inverter driven induction motor,” *IEEE Transactions on Industry Applications*, vol. 20, no. 5, pp. 1251 – 1259, September/October 1984.
- [2.13] H. A. Toliyat, S. Waikar and T. A. Lipo, “Analysis and simulation of five phase synchronous machines including third harmonic of airgap MMF,” *IEEE Transactions on Industry Applications*, vol. 34, no. 2, pp. 332 – 339, March/April 1998.
- [2.14] L. Parsa and H. A. Toliyat, “Five-phase permanent magnet motor drives,” *IEEE Transactions on Industry Applications*, vol. 41, no. 1, pp. 30 – 37, Jan./Feb. 2005.
- [2.15] L. Xu, “ Rotor structure selections of nonsine five-phase synchronous reluctance machines for improved torque capability,” *IEEE Transactions on Industry Applications*, vol. 36, no. 4, pp. 1111 – 1117, July/August 2000.
- [2.16] H. M. Ryu, J. W. Kim and S. K. Sul, “ Synchronous frame current control of multi-phase synchronous motor. Part I – Modeling and current control based on multiple d-q spaces concept under balanced condition,” Conference Record of the Annual Meeting of the *IEEE Industry Applications Society*, pp. 63 – 70, October 2004.
- [2.17] Y. Zhao and T. A. Lipo, “Space vector PWM control of dual three-phase induction machine using vector space decomposition,” *IEEE Transactions on Industry Applications*, vol. 31, no. 5, pp. 1177 – 1184, September/October 1995.
- [2.18] D. Hadiouche, L. Baghli and A. Rezzoug, “Space vector PWM techniques for dual three-phase ac machines: Analysis, performance evaluation and DSP implementation,” Conference Record of the annual meeting of the *IEEE Industry Applications Society*, pp. 648-655, October 2003.
- [2.19] C. B. Jacobina, R. S. Miranda, M. B. Correa, A. M. Lima and N. Rocha, “ Five phase converter dual-winding ac drive systems,” Conference Record of the *IEEE International Electric Machines and Drives Conference*, pp. 1345 – 1349, May 2005.
- [2.20] J. W. Kelly, E. G. Strangas and J. M. Miller, “Multi-phase space vector pulse width modulation,” *IEEE Transactions on Energy Conversion*, vol. 18, no. 2, pp. 259 – 264, June 2003.
- [2.21] H. M. Ryu, J. H. Kim and S. K. Sul, “Analysis of multi-phase space vector pulse-width modulation based on multiple d-q space concepts,” To appear in the *IEEE Transactions on Power Electronics*.

- [2.22] G. J. Retter, **Matrix and Space-Phasor Theory of Electrical Machines**, Akademiai Kiado, Budapest, Hungary, 1987.
- [2.23] P. J. Davis, **Circulant Matrices**, Chelsea Publishing Company, 1979.
- [2.24] A. Hava, R. J. Kerkman and T. A. Lipo, “A high performance generalized discontinuous PWM algorithm,” *IEEE Transactions on Industry Applications*, vol. 34, no. 5, pp. 1059 – 1071, September/October 1998.
- [4.1] Myoung-Ho Shin, Dong-Seok Hyun, Soon-Bong Cho and Song-Yul Choe, “An improved stator flux estimation for speed sensorless stator flux orientation control of induction motors”, *IEEE Transaction on Power Electronics*, vol. 15, no. 2, pp. 312-317, 2000.
- [4.2] X. Xu and D. W. Novontny, “Implementation of direct stator flux orientation control on a versatile DSP based system”, *IEEE Transaction on Industry Applications*, vol. 27, no. 4, pp. 694-700, 1991.
- [4.3] L. Harnefors, “Design and analysis of general rotor-flux oriented vector control systems,” *IEEE Transactions on Industrial Electronics*, vol. 48, pp. 383-389, April 2001.
- [4.4] B. K. Bose and N. R. Patel, “A programmable cascaded low-pass filter-based flux synthesis for a stator flux-oriented vector-controlled induction motor drive”, *IEEE Transaction on Industrial Electronics*, vol. 44, no. 1, pp. 140-143, 1997.
- [4.5] I. Kioskeridis and N. Margaris, “Loss minimization in scalar-controlled induction motor drives with search controllers,” *IEEE Transactions on Power Electronics*, vol. 11, no. 2, pp. 213-220, March 1996.
- [4.6] M. P. Kazmierkowski, R. Krishnan and F. Blaabjerg, **Control in Power Electronics : Selected Problems**, Academic Press, 2002.
- [4.7] Zhenyu Yu, “Space-vector PWM with TMS320C24x/F24x using hardware and software determined switching patterns”, Application Report, Texas Instruments, 1999.
- [4.8] Olorunfemi, Ojo, “Field orientation control of a doubly-fed synchronous reluctance machine”, Research Report 98-01, 1998.
- [4.9] Ahmet M. Hava, Russel J. Kerkman, and Thomas A. Lipo, “Simple analytical and graphical methods for carrier-based PWM-VSI drives”, *IEEE Transactions on Power Electronics*, vol. 14, no. 1, pp. 49-61, 1999.

- [4.10] Riccardo Marino, Sergei Peresada and Paolo Valigi, "Adaptive input-output linearizing control of induction motors", *IEEE Transactions on Automatic Control*, vol. 38, no. 2, pp. 208-221, 1993.
- [4.11] P. Vas, **Sensorless Vector and Direct Torque Control**, Oxford University Press, New York, 1998.
- [4.12] Paul C. Krause, Oleg Wasynczuk and Scott D. Sudhoff, **Analysis of Electric Machinery**, McGraw-Hill, New York, 1994.
- [4.13] R. Marino and P. Tomei, **Nonlinear Control Design, Geometric, Adaptive and Robust**, Prentice-Hall, New York, 1995.
- [4.14] Alberto Isidori, **Nonlinear Control Systems**, Third Edition, Springer-Verlag London, 1995.
- [4.15] G. Luckjiff, I. Wallace and D. Divan, "Feedback linearization of current regulated induction motors," Conference Record of *the 2001 IEEE Power Electronics Specialists Conference*, vol. 2, pp. 1173-1178, June 2001.
- [5.1] A. Kusko and D. Galler, "Control means for minimization of losses in ac and dc motor drives," *IEEE Transactions on Industry Applications*, vol. IA-19, pp. 561-570, July/August 1983.
- [5.2] D. S. Kirschen, D. W. Novotny and W. Suwanwittot, "Minimizing induction motor losses by excitation control in variable frequency drives," *IEEE Transactions on Industry Applications*, vol. IA-20, pp. 1244-1250, September/October 1984.
- [5.3] C. Mademlis, J. Xypteras and N. Margaris, "Loss minimization in surface permanent-magnet synchronous motor drives," *IEEE Transactions on Industry Applications*, vol. IA-47, pp. 115-122, February 2000.
- [5.4] E. Levi, "Impact of iron loss on the behavior of vector controlled induction machines," *IEEE Transactions on Industry Applications*, vol. IA-31, no. 6, pp. 1287-1296, November/December 1995.
- [5.5] T. Matsuo, A. El-Antably and T. A. Lipo, "A new control strategy for optimum efficiency operation of a synchronous reluctance motor," *IEEE Transactions on Industry Applications*, vol. 33, no. 5, pp. 1146-1153, September/October 1997.
- [5.6] H. G. Kim, S. K. Sul and N. H. Park, "Optimal efficiency drive of a current source inverter fed induction motor by flux control," *IEEE Transactions on Industry Applications*, vol. 20, no. 6, pp. 1453-1459, November/December 1984.

- [5.7] K. Matsuse, S. Tanguchi, T. Yoshizumi and K. Namiki, "A speed-sensor-less vector control of induction motor operating at high efficiency taking core loss into account," *IEEE Transactions on Industry Applications*, vol. IA-37, no. 2, pp. 548-558, March/April 2001.
- [5.8] D. Grenier, L. A. Dessaint, O. Akhrif, Y. Bonnassieux and B. Le Pioufle, "Experimental nonlinear control of a permanent magnet synchronous motor using saliency," *IEEE Transactions on Industrial Electronics*, vol. 44, no. 10, pp. 680-697, October 1997.
- [5.9] H. Lee, S. Kang and S. Sul, "Efficiency-optimized direct torque control of synchronous reluctance motor using feedback linearization," *IEEE Transactions on Industrial Electronics*, vol. 46, no. 1, pp. 192-198, February 1999.
- [5.10] O. Ojo, F. Osaloni and Z. Wu, "A control strategy for optimum efficiency operation of high performance interior permanent magnet motor drives," *Conference Record of the 2003 IEEE Industry Applications Conference*, pp. 604-610, October 2003.
- [5.11] M. P. Kazmierkowski, R. Krishnan and F. Blaabjerg, **Control in Power Electronics: Selected Problems**, Academic Press, Boston, 2002.
- [5.12] R. Marino and P. Tomei, **Nonlinear Control Design, Geometric, Adaptive and Robust**, Prentice-Hall, New York, 1995.
- [5.13] B. Friedland, **Control System Design, An Introduction to State-Space Methods**, McGraw-Hill, New York, 1986.
- [6.1] M-H Shin, D-S Hynn, S-B Cho and S-Y Choe, "An improved stator flux estimation for speed sensorless stator flux orientation control of induction motors," *IEEE Transactions on Power Electronics*, vol. 15, no. 2, pp. 312-317, March 2000.
- [6.2] F.-Z. Peng and T. Fukao, "Robust speed identification for speed-sensorless vector control of induction motors," *IEEE Transactions on Industry Applications*, vol. 30, pp. 1234-1240, September/October 1994.
- [6.3] M. W. Degner and R. D. Lorenz, "Position estimation in induction machines utilizing rotor bar slot harmonics and carrier frequency signal injection," *IEEE Transactions on Industry Applications*, vol. 36, no. 3, pp. 736-742, May/June 2000.
- [6.4] M. J. Corly and R. D. Lorenz, "Rotor position and velocity estimation for a salient-pole permanent magnet synchronous machine at standstill and high speeds," *IEEE Transactions on Industry Applications*, vol. 34, no. 4, pp. 784-789, July/August 1998.

- [6.5] H. Kubota, K. Matsuse, and T. Nakano, “DSP-based speed adaptive flux observer of induction motor,” *IEEE Transactions on Industry Applications*, vol. 29, pp. 344–348, March/April 1993.
- [6.6] G. Yang and T.-H. Chin, “Adaptive-speed identification scheme for a vector-controlled speed sensorless inverter-induction motor drive,” *IEEE Transactions on Industry Applications*, vol. 29, pp. 820–825, July/August 1993.
- [6.7] C. Schauder, “Adaptive speed identification for vector control of induction motors without rotational transducers,” *IEEE Transactions on Industry Applications*, vol. 28, pp. 1054–1061, September/October 1992.
- [6.8] M. Hinkkanen, “Analysis and design of full-order flux observers for sensorless induction motors,” *IEEE Transactions on Industrial Electronics*, vol. 51, no. 5, pp. 1033–1040, October 2004.
- [6.9] B. Friedland, **Control System Design: An Introduction to State-Space Methods**, McGraw-Hill, New York, 1986.
- [6.10] D. D. Siljak, **Nonlinear System: The Parameter Analysis and Design**, John Wiley & Sons, McGraw-Hill, New York, 1969.
- [6.11] P. Vas, **Electrical Machines and Drives, A Space-Vector Theory Approach**, Clarendon Press, Oxford, New York, 1992.
- [6.12] A. Netushil, **Theory of Automatic Control**, Mir Publishers, Moscow, 1978.
- [6.13] M. Rashed and A.F. Stronach, “A stable back-EMF MRAS-based sensorless low-speed induction motor drive insensitive to stator resistance variation,” *IEE Proceeding – Electrical Power Applications*, vol. 151, no. 6, pp. 685–693, November 2004.
- [6.14] Elena N. Gryazina, Boris T. Polyak, “Stability regions in the parameter space: D-decomposition revisited”, *Automatica*, vol. 42, no. 1, pp. 13-26, January 2006.
- [6.15] D. W. Novotny and T. A. Lipo, **Vector Control and Dynamics of AC Drives**, Clarendon Press, Oxford, New York, 1996.
- [6.16] S. Suwankawin and S. Sangwongwanich, “A speed-sensorless IM drive with decoupling control and stability analysis of speed estimation,” *IEEE Transactions on Industrial Electronics*, vol. 49, no. 2, pp. 444–455, April 2002.
- [6.17] J. Maes and J. Melkebeek, “Speed-sensorless direct torque control of induction motors using an adaptive flux observers,” *IEEE Transactions on Industry Applications*, vol. 36, no. 3, pp. 778–785, May/June 2000.

- [7.1] Vladimir Blasko, "Analysis of a hybrid PWM based on modified space vector and triangle comparison methods," *IEEE Transactions on Industry Applications*, vol. 33, no. 3, pp. 756-764, May/June 1997.
- [7.2] A. Hava, R. J. Kerkman and T. A. Lipo, "A high performance generalized discontinuous PWM algorithm," *IEEE Transactions on Industry Applications*, vol. 34, no. 5, pp. 1059-1071, September/October 1998.
- [7.3] K. Zhou and D. Wang, "Relationship between space-vector modulation and three-phase carrier-based PWM: a comprehensive analysis," *IEEE Transactions on Industrial Electronics*, vol. 49, no. 1, pp. 186-196, February 2002.
- [7.4] J. Holtz, W. Lotzkat and A. Khambadkone, "On the continuous control of PWM inverters in the over-modulation range including the six step mode," *IEEE Transactions on Power Electronics*, vol. 8, no. 4, pp. 546-553, October 1993.
- [7.5] A. M. Khambadkone, J. Holtz, "Compensated synchronous PI current controller in overmodulation range and six-step operation of space-vector-modulation-based vector-controlled drives," *IEEE Transactions on Industrial Electronics*, vol. 49, no. 3, pp. 574-580, June 2002.
- [7.6] A. M. Hava, S. Sul, R. J. Kerkman, T. A. Lipo, "Dynamic over-modulation characteristics of triangle intersection PWM methods," *IEEE Transactions on Industry Applications*, vol. 35, no. 4, pp. 896- 907, July/August 1999.

VITA

Gan Dong was born in Xishui, Hubei, China, in 1972. He got his Bachelor's and Master's degrees in Electric Power Engineering from Huzhong University of Science and Technology, Wuhan, Hubei, China, in 1993 and 1996. He has worked for Hubei Electric Power Testing & Research Institute from 1996 to 2001 and later got admission into Tennessee Technological University in August 2001 where he is a candidate for the Doctorate of Philosophy degree in Engineering. His research interests include power electronics, induction machine control and converter modulation techniques.